Thermal properties of solid-liquid nanocomposites

Xiaorui Wang

N°d'ordre NNT : 2022ISAL0085

THESE de DOCTORAT DE L'INSA LYON, membre de l'Université de Lyon

Ecole Doctorale N° EDA162
Mécanique, Energétique, Génie Civil, Acoustique

Spécialité/ discipline de doctorat :
Thermique/ Energétique

Soutenue publiquement le 06/10/2022, par :
Xiaorui WANG

Thermal Properties of Solid-Liquid Nanocomposites

Devant le jury composé de :

Evelyne MARTIN	Directrice de Recherche, Université de Strasbourg, CNRS	Rapporteure
Jérôme SAINT-MARTIN	Maître de conférence, Université Paris-Saclay, CNRS	Rapporteur
Gilles PERNOT	Maître de conférence, Université de Lorraine, CNRS	Examinateur
Samy MERABIA	Directeur de Recherche Université Claude Bernard Lyon 1, CNRS	Examinateur
Séverine GOMES	Directrice de Recherche INSA-Lyon, CNRS	Co-Directrice de thèse
Konstantinos TERMENTZIDIS	Directeur de Recherche INSA-Lyon, CNRS	Directeur de thèse

Département FEDORA – INSA Lyon - Ecoles Doctorales

SIGLE	ECOLE DOCTORALE	NOM ET COORDONNEES DU RESPONSABLE
CHIMIE	**CHIMIE DE LYON** **https://www.edchimie-lyon.fr** Sec. : Renée EL MELHEM Bât. Blaise PASCAL, 3e étage secretariat@edchimie-lyon.fr	**M. Stéphane DANIELE** C2P2-CPE LYON-UMR 5265 Bâtiment F308, BP 2077 43 Boulevard du 11 novembre 1918 69616 Villeurbanne **directeur@edchimie-lyon.fr**
E.E.A.	**ÉLECTRONIQUE, ÉLECTROTECHNIQUE, AUTOMATIQUE** **https://edeea.universite-lyon.fr** Sec. : Stéphanie CAUVIN Bâtiment Direction INSA Lyon Tél : 04.72.43.71.70 secretariat.edeea@insa-lyon.fr	**M. Philippe DELACHARTRE** INSA LYON Laboratoire CREATIS Bâtiment Blaise Pascal, 7 avenue Jean Capelle 69621 Villeurbanne CEDEX Tél : 04.72.43.88.63 **philippe.delachartre@insa-lyon.fr**
E2M2	**ÉVOLUTION, ÉCOSYSTÈME, MICROBIOLOGIE, MODÉLISATION** **http://e2m2.universite-lyon.fr** Sec. : Bénédicte LANZA Bât. Atrium, UCB Lyon 1 Tél : 04.72.44.83.62 secretariat.e2m2@univ-lyon1.fr	**Mme Sandrine CHARLES** Université Claude Bernard Lyon 1 UFR Biosciences Bâtiment Mendel 43, boulevard du 11 Novembre 1918 69622 Villeurbanne CEDEX **sandrine.charles@univ-lyon1.fr**
EDISS	**INTERDISCIPLINAIRE SCIENCES-SANTÉ** **http://ediss.universite-lyon.fr** Sec. : Bénédicte LANZA Bât. Atrium, UCB Lyon 1 Tél : 04.72.44.83.62 secretariat.ediss@univ-lyon1.fr	**Mme Sylvie RICARD-BLUM** Institut de Chimie et Biochimie Moléculaires et Supramoléculaires (ICBMS) - UMR 5246 CNRS - Université Lyon 1 Bâtiment Raulin - 2ème étage Nord 43 Boulevard du 11 novembre 1918 69622 Villeurbanne Cedex Tél : +33(0)4 72 44 82 32 **sylvie.ricard-blum@univ-lyon1.fr**
INFOMATHS	**INFORMATIQUE ET MATHÉMATIQUES** **http://edinfomaths.universite-lyon.fr** Sec. : Renée EL MELHEM Bât. Blaise PASCAL, 3e étage Tél : 04.72.43.80.46 infomaths@univ-lyon1.fr	**M. Hamamache KHEDDOUCI** Université Claude Bernard Lyon 1 Bât. Nautibus 43, Boulevard du 11 novembre 1918 69 622 Villeurbanne Cedex France Tél : 04.72.44.83.69 **hamamache.kheddouci@univ-lyon1.fr**
Matériaux	**MATÉRIAUX DE LYON** **http://ed34.universite-lyon.fr** Sec. : Yann DE ORDENANA Tél : 04.72.18.62.44 yann.de-ordenana@ec-lyon.fr	**M. Stéphane BENAYOUN** Ecole Centrale de Lyon Laboratoire LTDS 36 avenue Guy de Collongue 69134 Ecully CEDEX Tél : 04.72.18.64.37 **stephane.benayoun@ec-lyon.fr**
MEGA	**MÉCANIQUE, ÉNERGÉTIQUE, GÉNIE CIVIL, ACOUSTIQUE** **http://edmega.universite-lyon.fr** Sec. : Stéphanie CAUVIN Tél : 04.72.43.71.70 Bâtiment Direction INSA Lyon mega@insa-lyon.fr	**M. Jocelyn BONJOUR** INSA Lyon Laboratoire CETHIL Bâtiment Sadi-Carnot 9, rue de la Physique 69621 Villeurbanne CEDEX **jocelyn.bonjour@insa-lyon.fr**
ScSo	**ScSo*** **https://edsciencessociales.universite-lyon.fr** Sec. : Mélina FAVETON INSA : J.Y. TOUSSAINT Tél : 04.78.69.77.79 melina.faveton@univ-lyon2.fr	**M. Bruno MILLY** Université Lumière Lyon 2 86 Rue Pasteur 69365 Lyon CEDEX 07 **bruno.milly@univ-lyon2.fr**

*ScSo : Histoire, Géographie, Aménagement, Urbanisme, Archéologie, Science politique, Sociologie, Anthropologie

Acknowledgement

First and foremost, My first heartfelt thanks go to my supervisor, Dr. Konstantinos Termentzidis, who gave me a lot of patience and encouragement throughout my studies. He is my guide in the field of heat transfer of condensed matter at nanoscale, and always shared unreservedly his lecture and experience with me. His personality and diligence will continue to inspire me in my future life. I would like also to appreciate that my supervisor provided me with many opportunities to attend conferences and participate in the ANRs project, from which i benefited greatly.

Meanwhile, I appreciate sincerely to all the co-workers in the project, Dr. Séverine Gomès, Prof. David Lacroix, Dr. Mykola Isaiev, for their help and insightful discussion. I am also particularly indebted to my team partners, Dr. William Gonçalves and Dr. Paul Desmarchelier. It is my honor to work with you and i will treasure the days we stayed. Besides, many thanks to all the people of MINT group and other labmates in CETHIL, who gave always a warm response and sincerity to me.

I would like to express my appreciation to committee members. Thank you for your attendance at my defence and for your valuable advice on the revision of my thesis.

At last, my warm gratitude also goes to my friends for their continuous encouragement and companionship, Longkai Guo, Bao Chen, Xin Zheng, Lan Zhang, Wenxiang Sun, Xinke WANG, Zengqiang Zhai, Kevin Hao Hong, Guanfei Shen, my sisters Zuge, Bingnan, Xinxin, Emma Han and other friends in China. Also, I am thankful for my boyfriend Cong You and our pets YingmuHuadao and Yixiu. You are the one who free me of all the weight and pain of life. Finally yet importantly, I express deeply thanks to my parents, my family, particularly my late grandfather. Your support and love will always be the motivation of my life.

Abstract

The solid-liquid hybrid systems are extensively present in various industrial applications. Furthermore, with the rapid development of nanomaterials elaboration, it is possible to fabricate series of nanostructured and nanoporous materials with confined liquid. Consequently, the experimental and theoretical studies of the solid/liquid interface and their nanocomposites became increasingly necessary. Compared to the macroscale, their physical properties might be altered considerably, for example thermal properties of solid/liquid composites.

In this thesis, the thermal conductivity (TC) of solid-liquid hybrid nanocomposites is investigated, and more specifically for the dry and wet nanoporous crystalline silicon with the confined water. Several parameters have been studied in details. The thermal conductivity is calculated using Molecular Dynamics (MD) simulations, which are performed with LAMMPS. At first, a simulation cell of crystalline silicon with a spherical pore in the center is studied. The cases of dry and wet samples are compared. Using the Equilibrium Molecular Dynamics (EMD) simulations, the effects of temperature and effective density on the TC are examined, separately. I found that for certain temperature (at 300 K) or effective density (0.8 g/cm^3), a surprising maximum value of TC was obtained. Furthermore, a stratification of water molecules close to the solid/liquid interface is observed confirming in the literature. To clarify the physical mechanisms behind the thermal transport at solid/liquid interfaces and the intermolecular interaction of nanoconfined water, several structural and dynamical parameters of the nanoconfined water were explored: the radial distribution function, mean square displacements, water molecules orientation, and hydrogen bond networks. Additionally, the existence of new heat flux channels between a solid matrix and a nanoconfined liquid was proved, with clear signatures in the phonon density of states. In the second part of the thesis, the effects of spatial, size and the combined spatial/size distribution of pore on the TC of the wet nanoporous silicon are investigated. The new simulation cell is produced by replicating the cubic nanoporous silicon along the longitudinal direction. This part of the study, due to the modeling requests, has been done using the Non Equilibrium Molecular Dynamics (NEMD) simulations. This thesis contributed to the literature on the thermal properties of solid-liquid hybrid nanocomposites and also enriched the analysis of the interface between a solid and a liquid.

Keywords: Molecular Dynamics, Thermal Conductivity, Nanoporous Silicon, Nanoconfined Water, Solid/liquid Interface, Hydrogen Bond Networks

Resumé

Les systèmes hybrides solide-liquide sont largement présents dans diverses applications industrielles. De plus, avec le développement rapide de l'élaboration des nanomatériaux, il est possible de fabriquer une série de matériaux nanostructurés et nanoporeux avec un liquide confiné. Par conséquent, les études expérimentales et théoriques de l'interface solide/liquide et de leurs nanocomposites sont devenues de plus en plus nécessaires. Par rapport à l'échelle macroscopique, leurs propriétés physiques peuvent être considérablement modifiées, par exemple les propriétés thermiques des composites solide-liquide.

La thèse est dédiée à l'étude numérique des propriétés thermiques des nanocomposites hybrides solide-liquide, en particulier du silicium cristallin nanoporeux sec et humide avec l'eau confinée. Plusieurs paramètres ont été étudiés en détail avec des simulations atomistiques en utilisant le code de dynamique moléculaire LAMMPS : la conductivité thermique (TC), les densités d'états de phonons, etc. Premièrement, le silicium cristallin avec un pore sphérique au centre est modélisée et étudiée. Les cas d'échantillons secs et humides sont comparés. En utilisant les simulations de dynamique moléculaire à l'équilibre (EMD), les effets de la température et de la densité effective initiale sur la TC sont examinés, séparément. Pour une certaine température (à 300 K) ou une certaine densité effective (0,8 g/cm3), une valeur maximale de la TC a été obtenue. De plus, une stratification des molécules d'eau près de l'interface solide/liquide est observée et confirmée dans la littérature. Pour clarifier les mécanismes physiques derrière le transport thermique aux interfaces et l'interaction intermoléculaire de l'eau nanoconfinée, plusieurs paramètres structurels et dynamiques de l'eau nanoconfinée ont été explorés, la fonction de distribution radiale, les déplacements carrés moyens, l'orientation des molécules d'eau et les réseaux de liaisons hydrogène. De plus, l'existence de nouveaux canaux de flux thermique entre une matrice solide et un liquide nanoconfiné a été prouvée, par la densité d'états des phonons. Deuxièmement, les effets de la distribution spatiale, de la taille et de la combinaison espace/taille du silicium nanoporeux humide sont étudiés. La nouvelle cellule de simulation est produite en répliquant le silicium nanoporeux cubique dans la direction longitudinale. Cette partie de l'étude, en raison des demandes de modélisation, a été réalisée en utilisant les simulations de dynamique moléculaire hors-équilibre (NEMD). Cette thèse a contribué à la littérature sur les propriétés thermiques des nanocomposites hybrides solide-liquide et a enrichi l'analyse de l'interface entre un solide et un liquide.

Mots-clés : Dynamique Moléculaire, Conductivité Thermique, Silicium Nanoporeux, Eau Nanoconfinée, Interface Solide/liquide, Réseaux de Liaisons Hydrogène

Contents

List of Acronyms

List of Figures

List of Tables

Introduction

Both in the nature or in the modern industrial applications, it's easily to find the trace of the solid-liquid hybrid system. They are manifested in various ways: by the immersion of solids into liquids, or by the moisture absorption of solids, or by the artificial creation of their mixtures. It is undeniable that solid-liquid contact inevitably results in an interface, and the creation of an interface definitely has an impact on the overall physical properties of the material. Hence, from the last decade, an increasing interest regarding the solid liquid system and their interface has arisen. It is found to be able to tune the physical properties, of course the thermal properties. For example, superlattice-based materials which are constructed from alternated solid layers can display a much lower thermal conductivity than their bulk counterparts (Roy Chowdhury *et al.* 2021). It makes them to good candidates for efficient thermoelectric devices. Another example is nanowire, because of its high structural boundary scattering than bulk, it could has a high resistivity (Cheng *et al.* 2015).

Meanwhile, with the rapid development of the new nanomaterials elaboration, it is possible to fabricate series of nanostructured and nanoporous materials with confined liquid such as nanoporous materials filled with water. Currently, nanoporous materials are widely used in microelectronic devices, thermoelectronic devices, sensing applications, etc. We know that when operating nanodevices, the materials is possible to work under wet condition. During the loading and unloading of nanosize modules, the strong capillary interaction of the contact nanostructure caused by the size and surface effects induces a high adhesion force. This also results in the sharp increase in the friction force and really decrease its lifetime. Furthermore, the water condensation at a tribological interface may alter the wear mechanism. It also facilitates material failure. However, from another aspect, there is also some researches found that some vapor can be absorbed on the solid surface, then sustain a liquid layer finally maintain a lubricating property (Asay *et al.* 2008).

At nanoscale, the curvature of liquid in contact with the solid is no longer a thin film. Liquid forms a solid-like layer near the solid surface which cannot be neglected (Rajabpour *et al.* 2019). Compared to the macroscale, their thermal properties such as TC might be altered considerably.

Considering the thermal properties of solid liquid nanoporous materials, it is well-known that because of more boundary scattering, nanoporous materials has a significant reduction of thermal conductivity compared to the bulk ones. But when

the liquid is added in the pore, both the experiment and the simulations demonstrated that, the effective thermal conductivity of a nanoporous silicon filled with water can be enhanced up to a factor of 50%, compared to the same sample without water. Someone gave the explanation that, as the liquid density fluctuate close to the interface, a layer effect will affect the heat transfer (Isaiev *et al.* 2020).

From this point of view, the combination of solid and liquid can make unexpected changes in performance, and the existence of solid-liquid interface also produces many new scientific problems that need to be solved. The study concerning the solid liquid nanoporous material is not enough. especially most of them focus on the porosity effect under ambient conditions.

More and more experimental and theoretical studies are involved into the effect factors on their thermal conductivity. Among them, the porosity and the pore distribution show strong dependences of TC. Additionally, pressure, temperature and the strength of solid-liquid interactions are also important parameters to study.

In this thesis, the most common component solid crystalline silicon and water as component are used to study the role of confined liquid to the thermal properties of nanoporous materials. Considering the factor which affects seriously the water state, different conditions to simulate the real situation are chosen, which is temperature dependence and initial water density (called it effective density later). Another serious factor for the thermal properties of nanoporous materials is the pore distribution. So the size and spatial distribution effect is studied at the last part. All the simulations are carried out using atomistic molecular dynamics approach a open source software LAMMPS.

To clarify the physical mechanisms behind the thermal transport at solid/liquid interface and the intermolecular interaction of nanoconfined water, I explored several structural and dynamical parameters of the nanoconfined water. Using the radial distribution function, the structure of the water molecules near the interface are investigated. After that, by the means of mean square displacements and diffusion coefficient, the dynamical properties of nanoconfined water in the pore is analyzed. The orientation of water molecules and hydrogen bond networks, give us a deep understanding of heat transfer passway. Finally, the existence of new heat flux channels between a solid matrix and a nanoconfined liquid is proved, with clear signatures in the phonon density of states.

As a result, this thesis is organized into the following chapters:

- **1st Chapter:** I started from introducing the solid/liquid nanocomposites. The component selection, the nanostructure and solid-liquid interactions are presented in depth with reference to previous researches. The solid/liquid hy-

brid system is inevitable present in these materials. Thus in particular, the most important characteristic affecting the nanoproperties of the material are expanded, including surface effect, size effect, and wettability. After that, thermal properties and industrial applications are studied.

- **2nd Chapter:** the detailed process of MD simulation using LAMMPS is introduced, including the thermostat/barostat, boundary conditions, algorithm, etc. After that, interatomic potential functions needed in our simulations are presented. To calculated the thermal properties via LAMMPS, the EMD, NEMD and AEMD methods are expanded in the third section. Finally, several parameters need to be studied to explain the results of thermal properties and clarify the physical mechanisms. The characterization methods for this part are details at the end.

- **3rd Chapter:** this chapter focuses on the temperature dependence of the thermal conductivity of nanoporous materials with the confined water. Using Equilibrium Molecular Dynamics (EMD) simulations, I investigated the role of the temperature T (from 285 to 360 K) on the thermal conductivity enhancement of nanohybrid porous silicon and water system. By studying the mean square displacement, radial distribution functions, density of states and so on, several structural and dynamical phenomena are discussed to give physical point of views of the TC results.

- **4th Chapter:** this chapter focuses on the density dependence of the thermal conductivity of nanoporous materials with the confined water. Using the similar method with the previous chapter, I investigated the role of the effective density (from 0.1 to 1.2 g/cm^3) on the thermal conductivity enhancement of nanohybrid porous silicon and water system. The results are also analysed by means of the investigations in the previous section.

- **5th Chapter:** this chapter focuses on the effects of spatial, size and the combined spatial/size distribution of the pore on the TC of the wet nanoporous silicon, using Non Equilibrium Molecular Dynamics (NEMD) simulations. Furthermore the mean free path of phonon in the system is deduced, as well as the TC of the infinitely long system. The derived details are presented in the following section.

- In the appendix, i introduced the study on the thermal conductivity of nanoporous amorphous silica. The available interaction potential function

between silica and water are presented to inform the further study. Finally, the paper published about this thesis are listed at the end of the thesis.

CHAPTER 1

Solid-liquid nanocomposite

Contents

During the last decade, an increasing interest regarding the interactions between a confined liquid and solid surfaces at atomistic scales has arisen (Glicksman & Schaefer 1967; Tarazona *et al.* 1987). Meanwhile, with the evolution of the elaboration methods, new nanocomposite materials such as nanoporous materials are available nowadays with different internal surface of pores, to tune the physical properties of the matrix and the overall physical properties of the hybrid liquid/solid nanocomposites. In this chapter, I introduced solid-liquid nanocomposites from three aspects: types of materials, thermal properties and industrial applications. In particular, current status of research and effect factors on thermal properties are studied.

1.1 Introduction

The transformation and transmission of energy in this world is inseparable from the existence of the medium. These mediums can be roughly divided into three categories of solids, liquids, gas. Among them, compared with gas, solids and liquids have lower mobility and more controllable states. Undoubtedly, pure solid materials have been widely and skillfully used in the fields of energy power, electronic information, bioinformatics, aerospace, etc. However, solid materials have always been limited by various factors such as the limited raw materials, difficult mining, low production efficiency, and backward processing technology. On the contrary, liquid materials are usually easy to prepare and synthesize, but it is bound by its liquidity, easy leakage, poor controllability, weak mechanical properties and other shortcomings. It makes the development and applications of solid liquid system to be challenged. The mixture of the solid and the liquid earned more attention.

Over the years, many scholars have tried to give the solid and the liquid a clear definition. The most accepted explanation is that liquid molecules have a certain mobility, and solid atoms are arranged in a lattice of crystals with a consistent space. They are collectively called condensed matter. However, a strange rigid solid whose atomic arrangement pattern was not repeated at all was first discovered in the laboratory in 1982 and rediscovered in nature in 2009 (Alam & Alam). Just like glass, a substance that behaves like a liquid but has a stable atomic structure. Thereafter, three types of solids have been developed, namely amorphous, crystalline and quasi-crystal (Karuso *et al.* 2012). The similar thing happens with liquids. It was found that when the liquid is frozen at a certain moment, it is likely to exhibit amorphous properties. Hence, in addition to the three pure phase, there are other kind of states close to like-solid, or like-liquid. They provide a way to describe new characteristics.

Compared with solids, liquids have some specialities that solids don't have. Firstly, the pressure of the liquid is transmitted in all directions. It induces a new phenomenon near the liquid surface that can't observe in the bulk liquid. Due to the surface molecules possess the bond with inner molecule, a net force pulls these molecule inward. A form of energy, surface tension (Tyson & Miller 1977), with unit J/m^2, is explored to describe physically this phenomenon. It implies a tendency of liquid to minimize the surface area. A spherical drop and bubbles are formed from this reason. Many phenomena like surface waves, capillary action, drainage, can be attributed from it (Perlin & Schultz 2000;

Pan *et al.* 2020a). Many macro-models such as smoothed particle hydrodynamics (SPH) (Gingold & Monaghan 1977) and macro-scale pseudo-particle modeling (MaPPM) (Ge & Li 2001) support to precise the process of drop formation. Based on the characteristics of solids and liquids, solid-liquid composites are designed.

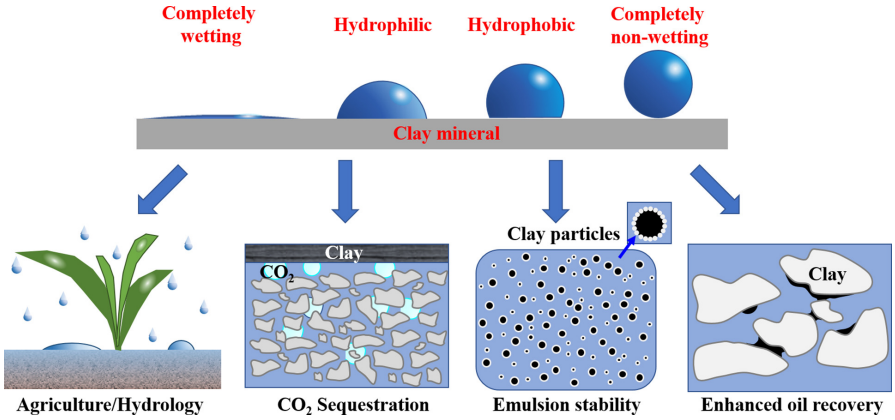

Figure 1.1: Schematic diagram of the capillary behavior of a liquid on a surface with different wettability, with clay mineral as an example from Ref.(Pan *et al.* 2020a)

1.2 Descriptions of solid-liquid nanosystem

Liquids, taking the advantages of the fluidity, compressibility, viscosity than solids, higher pre-determined mechanical or thermal properties could be expected by being compatible solid matrix with adjacent or attached materials. A useful method to predict the mechanical properties of solid-liquid isotropic multi-phase materials has been proposed, called Generalized Mixture Rule (GMR). It is appropriate for expressing the effective parameters, in terms of hardness, Young's modulus, viscosity, strength, etc. It can vary with the properties of component, volume fractions of each component, and their micro-structures. The GMR is expressed as (Ji 2004)

$$M^J = \sum_{i=1}^{N} (V_i M_i^J) \tag{1.1}$$

Where M is a specific mechanical property, J is a constant implying the effect of micro-structures, V is the volume fraction of component, and the subscript i represents the i^{th} phase. N is the total number of phase of composite consisting as:

$$\sum_{i=1}^{N} V_i = 1 \tag{1.2}$$

This means that the liquid and the solid have a comprehensive effect after the mixture and both of them result in an improved material properties. For example, Chuangguang WANG et al. (Wang *et al.* 2018) researched on adding liquid electrolytes (LE) at the interface to form a solid-liquid hybrid electrolyte in order to well reduce the interfacial resistance of Solid-State Lithium Batteries (SSLBs).

In addition to the change in properties, the solid-liquid contact also creates a new structure, which is the solid/liquid interface. In the vicinity of the interface, many physical quantities may undergo abrupt changes. This certainly makes the process of energy transfer more complex. As early as 2004, Xue. L et al. (Xue *et al.* 2004) were interested in the layer structure formed at the solid/liquid interface, and its effects on the interfacial thermal resistance. A discontinuous temperature change through the interface when the solid surface is wetted, shown in the Fig.1.2.

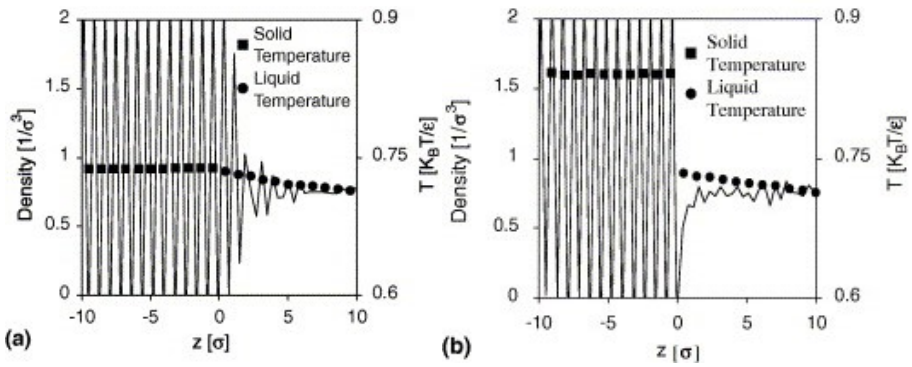

Figure 1.2: Atom number density profiles as solid lines and averaged temperature profiles of the atomic layers as dotted lines at the interface for (a) the wetting liquid (which means strong bonding between the solid and the liquid) and (b) the non-wetting liquid. The interface is depicted at the position $z = 0$

In addition, for nanocomposites, the size of the atoms is close to the coherence length of the electrons, which is likely to cause a strong correlation with electrons. This strong coherence will greatly affect the material properties. Moreover, its size is also close to the wavelength of light. Together with the special effects of the interface, the properties, such as melting point, magnetism, optical, thermal and electrical conductivity, are often different from those bulk counterparts.

1.2.1 Materials often used in solid/liquid nanocomposites

In general, a nanomaterial or a nanocomposite has characteristic size in the range from 1 to 100 nm. Solids can act as a matrix and liquids can be tiny droplets bound to the surface of the solid phase or inside voids, e.g. nanochannels with liq-

uid flow. Conversely, solid particles can also be incorporated in a liquid matrix, e.g. nanofluids. In the following paragraphs, the materials often used in the solid/liquid nanocomposites will be classified in two groups: solid and liquid.

1.2.1.1 Solids used in solid/liquid nanocomposites

Solids mainly provide inherent properties to the composite, such as strength, toughness. Solid materials used in solid/liquid system include mainly silicon and carbon systems, polymer, ceramic, metallic, and their hybrid systems.

1) **Silicon and carbon systems**

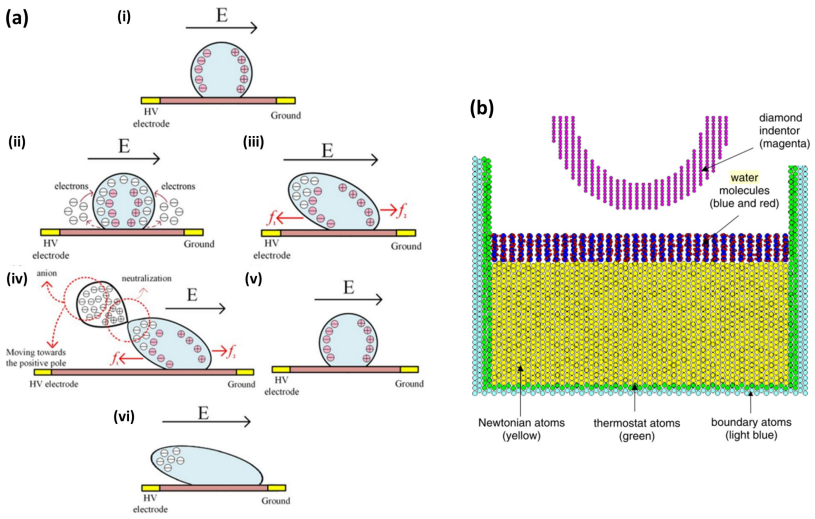

Figure 1.3: (a)The mechanism of the dynamic behaviors of direct current in water droplets and silicone rubber plate (Cao *et al.* 2021).(b) The configuration of nano-indentation with silicon nanocrystal, diamond indentor and water layers, in molecular simulations. Note that water molecules here are simulated in TIP4P models (Tang & Zhang 2004).

Silicon-based composites mainly consist of silicon, germanium silicon, organosilicon, porous silicon, crystalline silicon, and the substrate for heterogeneous epitaxy of other compounds. Among them, organosilicon refers to compounds that contain silicon-oxygen bonds and have at least one organic group that is directly connected to a silicon atom. It is also customary to treat those compounds that have organic groups connected to silicon atoms through oxygen, sulphur, nitrogen, etc, as organosilicon compounds. In recent years, a large number of silicon-based materials have been used as the core raw material for photovoltaic battery cells and microelectronic devices.

In particular, nanoporous silicon plays a significant role due to it takes good advantages of high surface-to-volume ratio, potentially efficient thermal control (Fang & Pilon 2011; Machrafi *et al.* 2016). Since these devices cannot operate in a fully virtual vacuum, it creates an opportunity for liquids to come into contact with solids by means of the absorption or moisture, thereby modifying the original properties of the materials. Many researches have also tended to study on the interaction between these non-metals with liquid molecules. Wen Cao studied the water impact on the surface properties of hydrophobic silicone rubber when it works as the insulation materials moistened by the fog or rain (Cao *et al.* 2021). As shown in Fig.1.3(a), the model schematics shows intuitively that a single water droplet on the silicone surface influences the performance of the electric field distribution, which also depends on the volume of the droplet. Indeed, the immersion of the liquid may be sometimes advantageous for the effective properties. For example, it has been proved that the lubrication with water reduces effectively the friction of the surface of the silicon nitride textured by the laser (Yamakiri *et al.* 2011).

Furthermore, silicon is the main material for manufacturing microelectronics and semiconductors. On the other hand, the water, as a clean and low-cost cooling liquid, performs a vital role in the process of silicon nanomachining process including heat dissipation and cleaning. In addition to the effect of moisture absorption, other studies have found that the nanostructure of silicon crystal is strongly affected by the water, which causes probably the damage and change of its surface in nano-indentations (Tang & Zhang 2004; Zarudi *et al.* 2004). As shown in Fig.1.3(b), a study by C. Y. Tang and L. C. Zhang (Zarudi *et al.* 2004) reproduced the process of nano-indentation with the help of molecular simulations, revealing that the cavities of the silicon substrate are invaded by the water molecules upon loading. Subsequently, damages occurred as a result of changing the structure of the residual deformation zone. A similar phenomenon but for the nano-indentation of ionic liquid film on silica was reported by P. Ballone (Ballone *et al.* 2012), using the computational experiment.

These observations seem to suggest that liquid molecules and silicon based materials have uncertain chemical effects at nanoscale. The explanation in this aspect is still insufficient.

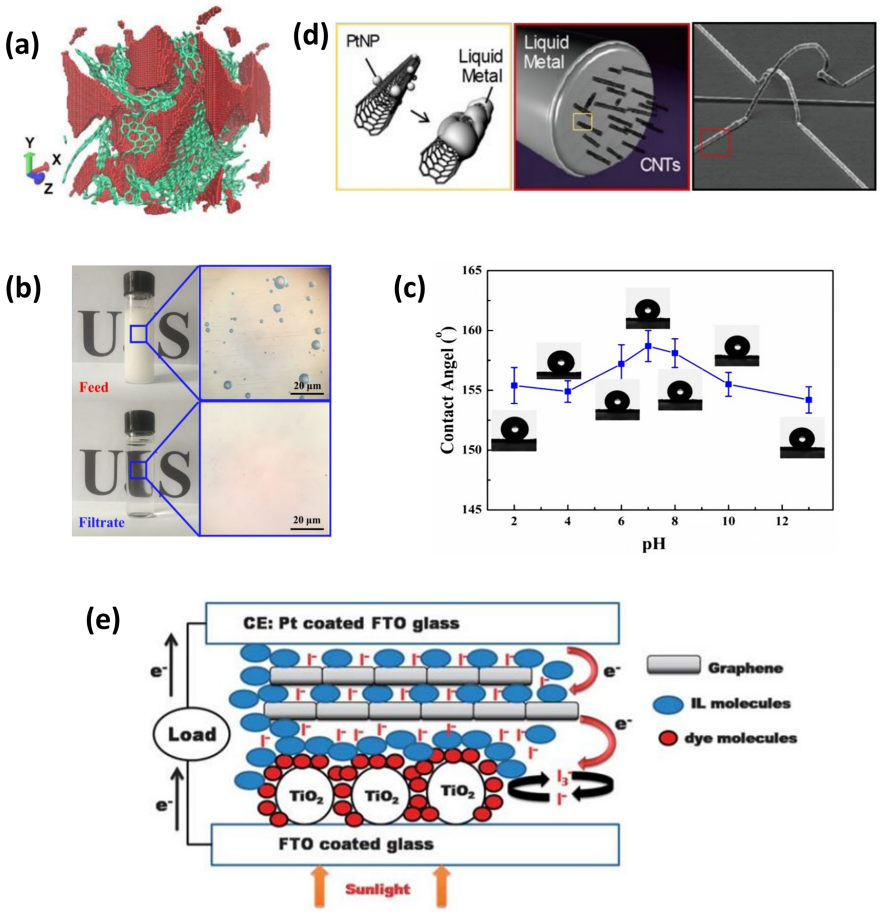

Figure 1.4: (a)Argon in red colour diffuses in the free space of SiC-DC in blue colour in the constructed model of HRMC (Farmahini & Bhatia 2016).(b) Before and after separation of water-in-toluene, and (c) contact angle of a water droplet with different pH values on the supershydrophobic HBCT aerogel (Yuan *et al.* 2018). (d) The sketch and SEM images of Pt-decorated carbon nanotube in liquid metal matrix (Park *et al.* 2019). (e) Scheme of a DSSC of graphene-ionic liquid based quasi-solid state electrolyte (Ahmad *et al.* 2011).

Carbon materials based on carbon atoms with other atoms or functional groups linked in chains, such as carbide-derived carbon, carbon aerogels, carbon nanotubes, onion-like carbon and graphene, can all be incorporated with liquids to form new materials.

Amir H. Farmahini (Farmahini & Bhatia 2016) found lower diffusion of argon liquid in the SiC-derived carbon (SIC-DC) compared to Ti_3SiC_2-derived carbon, using Hybrid Reverse Monte Carlo method (HRMC), illustrated in Fig.1.4(a). Dengsen Yuan (Yuan *et al.* 2018) demonstrated that when the biomass carbon aerogel is assembled with TiO_2 nanorods (HBCT), a hierarchi-

cal structure is found with the superhydrophobicity. It is an effective media to separate the emulsion. Details are shown in Fig.1.4(b) and (c).

In the carbon systems, Carbon nanotubes (CNTs) taking advantages of the high stability, high thermal conductivity, modifiability of functional groups, are one of the most representative carbon materials. It is proved that the suspension of liquid in CNTs is a good way to improve the mechanical and thermal properties of the composite, compared to the pure liquid matrix. Young-Geun Park et al. (Park *et al.* 2019) found a reinforced mechanical strength of Pt-decorated carbon nanotube in liquid metal matrix overcoming the limitation of liquid metal. The sketch and SEM images of this material are displayed in Fig.1.4(d). Moreover, the induced current density is much comparable to metal wire. Haifeng Jiang (Jiang *et al.* 2015) found that the CNTs-based nanofluid with a solid-like nanolayer can obtain a better heat transfer with the effective thermal conductivity increasing. Mixture of carbon solid and the liquid is a potential electrolytes applied in solar cells. Iftikhar Ahmad et al. (Ahmad *et al.* 2011) incorporated graphene, single wall carbon nanotubes (SWCNTs) into 1-methyl-3-propylimidazolium iodide (PMII) ionic liquid, which is used for dye sensitised solar cells (DSSCs), shown in Fig.1.4(e). The ionic liquid plays an important role in building a self-organised networks of graphene and SWCNT, contributing to an effective electron transfer. The carbon system also includes the formation of non-metallic inorganic substances with non-metallic elements, such as SiC, B_4C, etc. Xinrui. Zhang (Zhang *et al.* 2020) focused on the deionized water nanofluid dispersed with SiC particles in micro-cylinder-group which is used in cooling system. He investigated the effect of volume fraction of SiC on the Reynolds and Nusselt number of nanofluid, then found the greatest heat transfer performance at the specific volume fraction.

2) **Polymeric systems**

Polymers consist of thousands of atoms covalently bonded to each other to form organic compounds with particularly large relative molecular masses and repeating structural units. Commonly, thermoplastic polymers are flexible and they can be dissolved in suitable solvents. They soften when the temperature rises to a molten state, and then have a certain amount of fluidity. Therefore, polymers are often added to liquid matrices as reinforcing agents to form stretchable materials that enhance the physical properties and stability of the compound while maintaining softness. For example, Qiangbing Wei (Wei *et al.* 2020) reported a stable strategy to fabricate EGaIn nanodroplets sta-

bilized by polymer brushes, shown in Fig.1.5(a) and (b). EGaIn is regard as a kind of liquid metal alloy with metallic property and good fluidity. The dispersibility of nanoparticles in the solvent is well improved by good attachment of polymer brushes. The approach is extendable for fabrication of other polymer system and a wide range of aqueous system, as well as soft electronics, biomedicines (Malakooti *et al.* 2020). Polymer can be functionalized by water, by connecting through a crosslinking point, which is able to develop more complex systems from water-soluble polymers such as nanocomposite and hybrid adsorbents (Rivas *et al.* 2018). The diagram is shown in Fig.1.5(c). It overcomes the drawbacks of each separated components and enhances the overall performance.

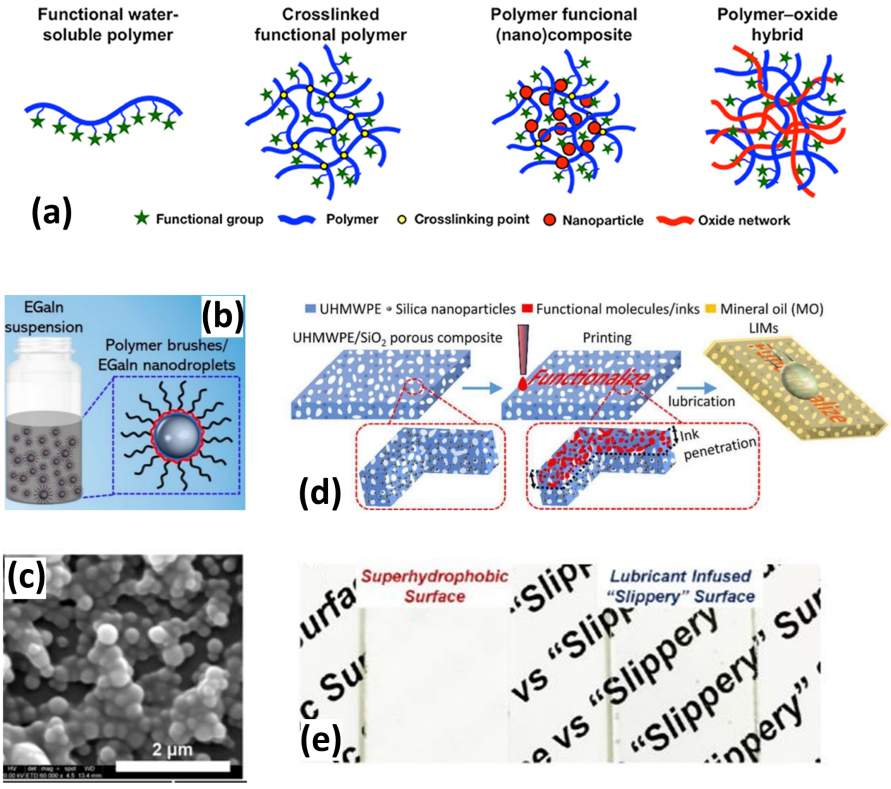

Figure 1.5: (a) Schematic illustration and (b) SEM image of the EGaIn nanodroplets stabilized by polymer brushes (Wei *et al.* 2020). (c)The adsorption processes for designing different polymer-based materials (Rivas *et al.* 2018). (d) Scheme of porous polymer nanocomposite functionalized by specific ink(He *et al.* 2018). (e) The optical images of the substrate composed of polymer and hydrophobic fumed silica before (left) and after (right) infusion of silicone oil. It shows a high transparency, which manifests that the text "Slippery" can be seen through the material(Cao *et al.* 2016).

Besides, interfaces formed by polymer solid-liquid composite are of great

importance for the application of anti-frosting/icing, antifouling, unidirectional transport, microreactor, and so on (Guo *et al.* 2021). Wenqing He et al. (He *et al.* 2018) introduced a porous polymer nanocomposite consisting of ultrahigh-molecular-weight polyethylene (UHMWPE) and SiO_2. The combination of non-polar polymer network and polar nanoparticles provides a controllable lubrication and surface slipperiness of mineral oil, shown in Fig.1.5(d). A wetting solid surface presents a higher transparency than the one non-wetted due to the low scattering rate of light. For example, a substrate composed of the hydrophobic fumed silica nanoparticle and poly dimethyl siloxane is tuned to be transparent after infusion of silicone oil in the study of Moyuan Cao (Cao *et al.* 2016), as shown in Fig.1.5(e).

3) **Metallic systems**

Metallic system has the advantages of good electrical conductivity, strong mechanical properties, electromagnetic shielding function, easy access to easy processing and so on. Therefore, metals are often involved in nanoelectronic devices, as well as microstructural evolution (such as solid-state phase transformation). The traditional metal materials like Cu, Al, are often used in the chips. Iron oxide particles dispersed in the nanofluids are promised to take an advantage of superparamagnetic behaviors (Abareshi *et al.* 2010). In addition, the alloys like Ni alloys, Mg alloys are also in a large number of applications in nano components. However, when these materials serve in non-vacuum conditions, being wetted by water molecules in the air or contacted with liquids happens frequently. Consequently, it is difficult to avoid the effect of such solid-liquid contact on energy transfer through the interface. The main influence on the heat transfer is the presence of the thermal resistance at the solid/liquid interface, resulting in a large temperature change. In recent years, a large amount of researches have been invested in the solid/liquid interface of metal-liquid interactions. Truong Quoc Vo et his partner (Vo & Kim 2015) used Non-Equilibrium Molecular Dynamics (NEMD) to investigate the Kapitza resistance, which is associated Kapitza length, between water and other 4 different metals: Au, Ag, Cu, Al. The kapitza length is defined as the equivalent thermal thickness of the fluid at the solid-liquid interface. They found that the kapitza length decreases exponentially with the interaction strength between the liquid and the metal increases, and the heat transfer at the interface increases. Jerry Vera (Vera & Bayazitoglu 2015) using the same method compiled the linear fit

coefficients for the Kapitza resistance as the function of the wall temperature and heat flux. Models simulated are shown in Fig.1.6(a). The expression obtained makes it possible to implement the thermal interfacial resistance of each metal and liquid depending on the temperature and heat flux. Although solid-liquid hybrid system causes interfacial problems, the incorporation of metal particles suspended in the liquid enhances the thermal conductivity of nanofluid (Balla *et al.* 2013). This kind of materials could be beneficial to biological system, for example cancer photothermal therapy based nanoparticles. A.Rajabpour (Rajabpour *et al.* 2019) using Steady-state NEMD (SNEMD) found that thanks to the metallic nanoparticles, the thermal conductivity of basefluid is 1.5 times more than bulk fluid. The temperature profiles of water shells surrounding the nanoparticles are shown in the Fig.1.6(b), exhibiting the higher value of the temperature for the first water shell near the center.

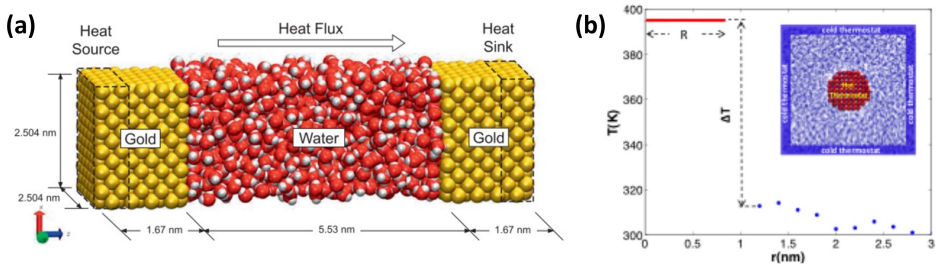

Figure 1.6: (a) The snapshot of the simulation configuration in MD to calculate the Kapitza resistance between gold (or Au, Ag, Al) and water (Vera & Bayazitoglu 2015). (b) The temperature profiles of the Ag/water nanofluid using SNEMD simulation (Rajabpour *et al.* 2019).

4) Ceramic systems

Ceramic materials such as clay, alumina, oxide besed Si, Ti, Zr exhibit excellent stability and chemical inertness. It is usually mixed with other elements like carbon, silicon, copper and so on, to ameliorate their poor thermal properties. Due to his low cost, it is also one of the most desirable class of nanofluid systems (Timofeeva *et al.* 2009; Buschmann 2012; Ehle *et al.* 2011). For instance, S. Suresh (Suresh *et al.* 2011) prepared the Al_2O_3-Cu/water nanofluid by dispersing the synthesized nanocomposites powder.

1.2.1.2 Liquids used in solid/liquid nanocomposites

In solid-liquid nanocomposite, the liquid can be mainly chosen from: inorganic solution (such as water, liquid metal, salt), organic solution, and hybrid solution.

1) **Inorganic solutions**

Water is the most commonly used and cheapest solvent, with acid and base properties, and also used as an oxidizing and reducing agent under certain chemical conditions. Water adsorption is a pervasive phenomenon in nature. Many studies investigating the moisture behaviors of water in the nanocomposites have been reported using both experiments (Ladhari *et al.* 2010; GHASEMI & Kord 2009) and simulations (Cheh *et al.* 2013). The main mechanism of water absorption on the macroscope mainly follows the kinetics of Fickian's diffusion (GHASEMI & Kord 2009), which means that the molar flux of solute through a unit area of the system is proportional to the concentration gradient. After moisture absorption, the mechanical, dielectric, surface charge and structure of the material are influenced. (Zhao & Li 2008; Ladhari *et al.* 2010; Du *et al.* 2016). For example, Jigger Cheh (Cheh *et al.* 2013) found the "ice-like" ordered structure of the monolayer water on the ionic substrate, which affects the heat transfer through the solid/liquid interface, shown in the Fig.1.7.

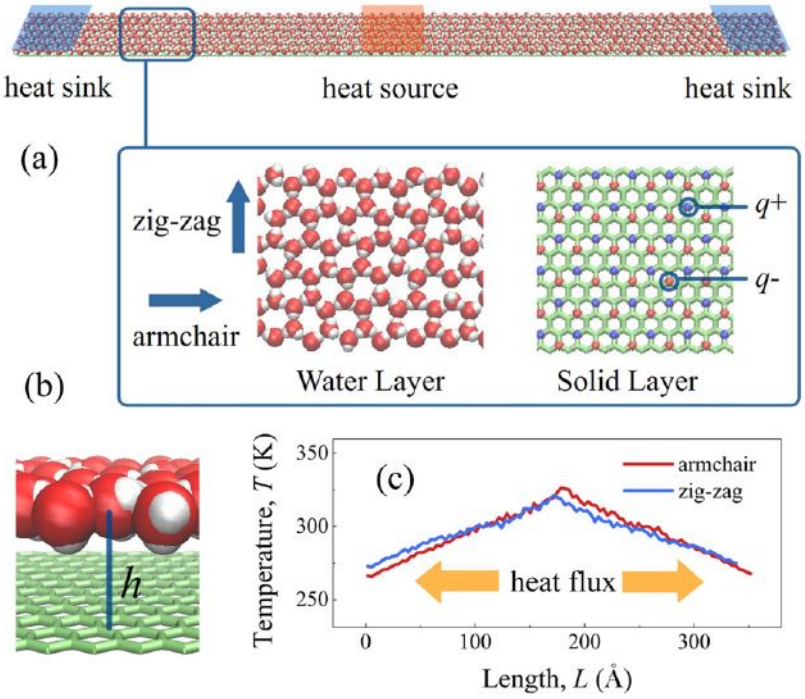

Figure 1.7: The "ice-like" ordered structure of the monolayer water on the ionic substrate (Cheh *et al.* 2013). (a) Water,solid layer and (b) the interface. (c) The heat flux between two heat sinks as a function of the length.

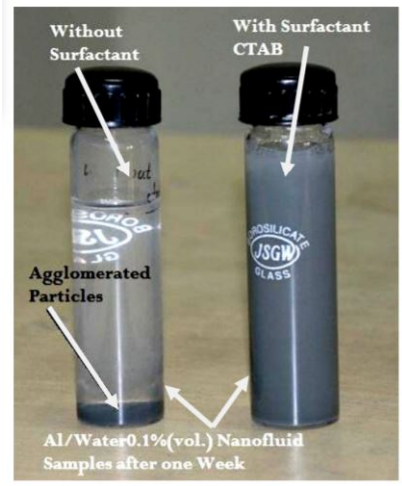

Figure 1.8: The Cu nanoparticles diffuse uniformly and stably in water in the presence of surfactants (Cetyl trimethylammonium bromide (CTAB)) (Sharma 2018).

Water is also designed as host liquid mixing with metal and their oxide like copper, gold, aluminium to compose the hybrid nanocompos-

ite (Kim *et al.* 2009; Lo *et al.* 2005; Abareshi *et al.* 2010). Shubham Sharma (Sharma 2018) used chemical process methods by adding 0.2% nanoparticles volume concentration of the particle size 75-135 nm into distilled water to fabricate Cu/water nanofluid, shown in Fig.1.8. Another example given by Maryam Abareshi et al. (Abareshi *et al.* 2010) proved that dispersing the Fe_3O_4 nanoparticles into water can obtain a better thermal performance than basefluid, as well as the magnetic property.

In addition of water molecules, other inorganic solutions such as liquid metal, salt, as well as some acid and base solutions are equally alternative to mixing with solids. Examples are given as follows. Compared with rigid solids, liquid metals have the advantages of flexibility, deformability and mechanical sensitivity at room temperature, broadening the wide range of applications for soft robots, wearable electronics (Dickey 2017; Kim *et al.* 2019). The alloys like Gallium–Indium (GaIn) can be a continuous matrix mixed with metallic nanoparticles or as a suspension dispersed in the soft polymer matrix (Liu *et al.* 2021). As shown in Fig.1.9(a), a biphasic GaIn is created by spray-print the GaIn nanoparticles onto a silicon wafer. Additionally, the industrial solution $CaCl_2$ mixing with nanoparticles can be made into phase change materials for supercooling by dissolving, stirring (Li *et al.* 2017), as shown in Fig.1.9(b).

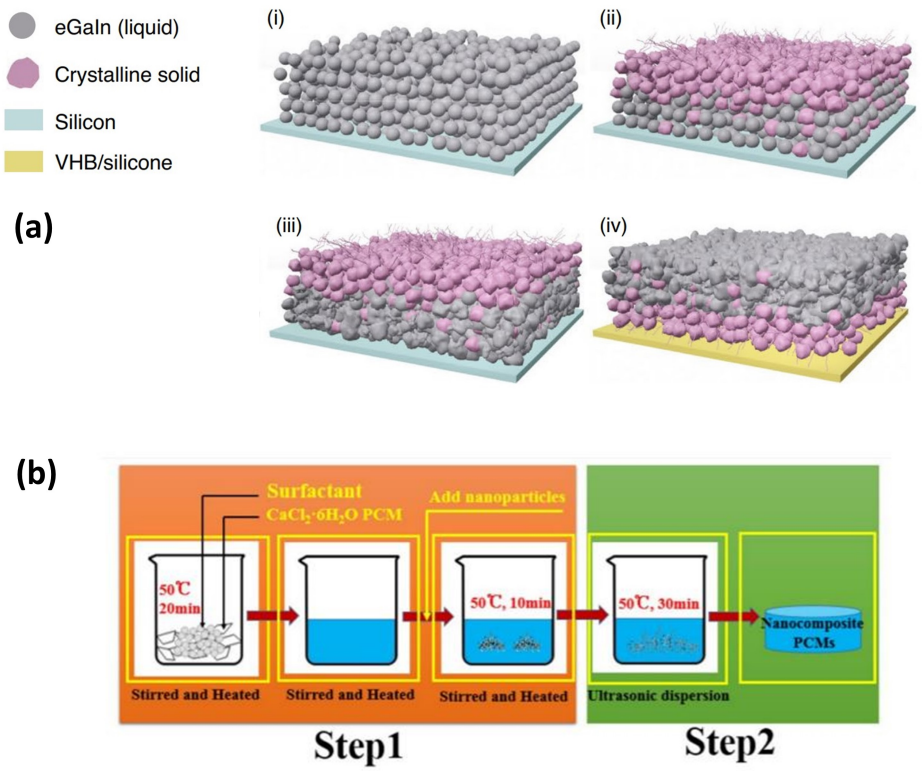

Figure 1.9: (a) The process to create biphasic GaIn (Liu *et al.* 2021). (b) Schematic of the preparation of $CaCl_2 6H_2O$ PCMs (Li *et al.* 2017).

2) Organic solutions

Organic solvents, as organic compounds that are widely used in life, can be mixed with various solids, such as olefins, alcohols, esters, phenols, aromatic hydrocarbons, and nitrogen and sulfur-containing compounds, etc. For example, the ethylene glycol nanofluid can be formed via the solvothermal method by being dispersed with carbon–copper oxide nanoparticles (Akilu *et al.* 2019). The samples for different nanoparticle concentrations of nanofluid are shown in Fig.1.10(b). A good synergistic of the nanoparticles and basefluid of the sample contributes to improving the thermal and viscous performance. Dun-Yen Kang et al. fabricated aluminosilicate single-wall nanotubes (SWNTs) dispersed in the liquid poly vinyl alcohol (PVA), as displayed in Fig.1.10(b) (Kang *et al.* 2012). The fabricated nanocomposites show an remarkable water transport behaviors and good selectivity of water and alcohol. This leads to the potential for the development of SWNTs liquid hybrid nanocomposites for water separation ap-

plications. In addition, the ester is also one of the top choice of basefluid. Lucian PD (Pîslaru-Dănescu *et al.* 2013) presented that a super-paramagnetic nanofluid (SMP-NF) based on colloidal nanoparticles Fe_3O_4 and transformer oil (TO), can perform well in the transformer and micro-actuator as a magnetic material.

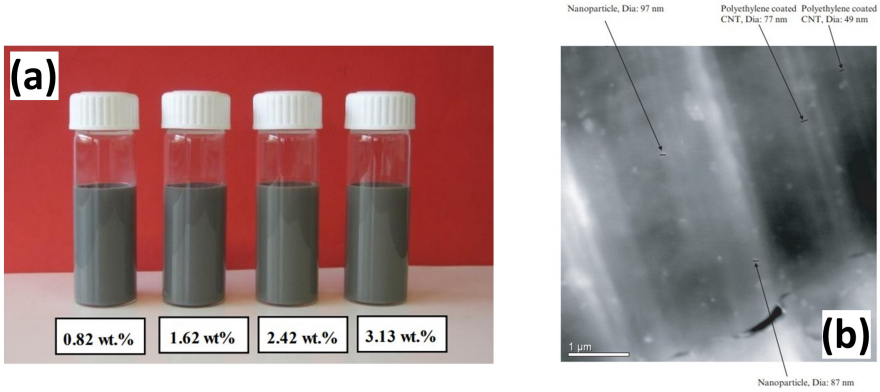

Figure 1.10: (a) Photos of different samples of SiC-CuO/C-ethylene glycol nanofluids at room temperature for 30 days (Akilu *et al.* 2019). (b) The SEM image and scheme of SWNTs in PVA nanocomposites (Kang *et al.* 2012).

1.2.2 Nanostructures presented in solid/liquid nanocomposites

Generally, solid-liquid hybrid nanocomposites could be achieved by all the materials presenting a solid/liquid interface: nanofluid (colloidal suspension of solid nanoparticles) (Kio 2014; Yang & Liu 2011), nanostructured matrix with liquid (Ong & Pop 2010), and the functionalized surface attached by liquid nanosystem (Yang & Liu 2011; Furchner *et al.* 2017), etc. The fabrication process and TEM images of fabricated nanofluids, and examples of functionalized nanosystem are displayed in Fig.1.11.

In 1995, the first concept of nanofluid built by Choi (Choi & Eastman 1995), was defined as an new generation of heat transfer fluids engineered by suspending metallic nanoparticles into the fluid. With the development of nano design and nanotechnology, the structure of suspending materials was extended in the variety of ways, like fibers, sheets or tubes with average size below 100 nm and less than 1 % volume concentrations of the dispersion (Choi 2009). One of the advantages of nanofluid is the high thermal conductivity of nanoparticles (usually in the range of 100-6000 W/m·K), which is also at least 2 magnitudes greater than that of conventional heat transfer nanofluid (minus 1 W/m·K). So the purpose of several study is finding a mean effective thermal conductivity of dispersion and fluid (Esfe & Afrand 2020; Sadeghinezhad *et al.* 2016). Because of the major brown

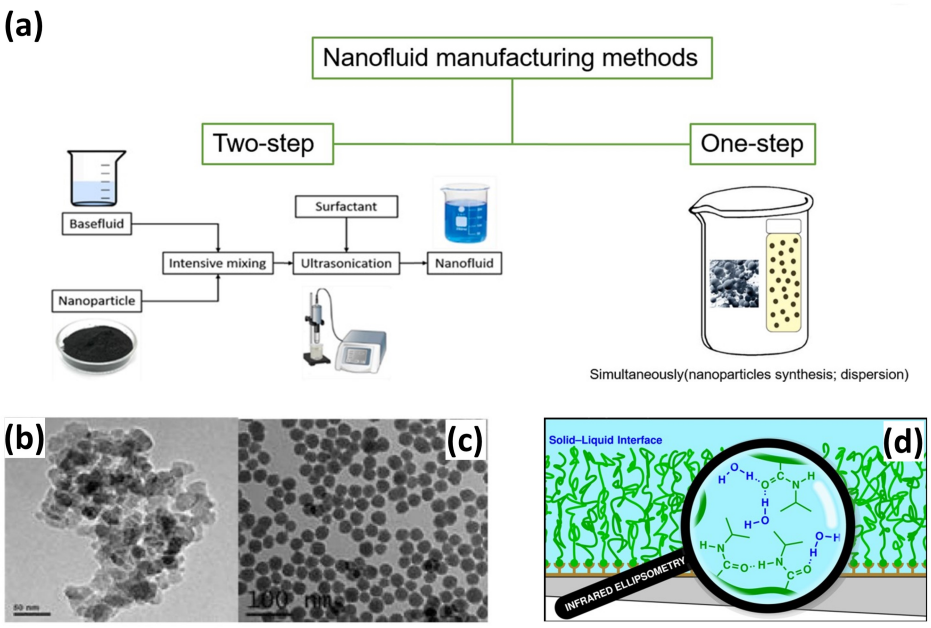

Figure 1.11: (a) The manufacturing methods classified as one and two steps of nanofluids (Narankhishig *et al.* 2021). The figure below is the TEM images of (b) the traditional silica/water nanofluid and (c) functionalized by silane (Yang & Liu 2011). (d) The scheme of ultrathin functional poly(N-isopropylacrylamide) brushes (Furchner *et al.* 2017).

motion of nanoparticles, the smaller size of suspended particle induces a faster heat transport in the nanofluid. This also means that nanoparticles suspending in the fluid are more stable than micro-particles or particle clustering, and enhance greatly to thermal conductivity of nanofluid (Daviran *et al.* 2017). Meanwhile, the structure of dispersion is also the research focus. The nanoparticle dispersed could be traditional structure of atoms such as metal atoms Cu, Al, Au, graphene, or nanostructured materials such as nanotube (Thomas *et al.* 2010; Carlborg *et al.* 2008). Accordingly, the base fluid can be water, Ethylene glycol (EG), Engine oil (EO) (Hu *et al.* 2016).

For the nanostructured matrix with liquid, most of examples signify that the liquid is invaded in the hole or empty space of available nanomaterial which constitutes a specific nanoscale repeatable structure (Lugger *et al.* 2018; Erlebacher 2018; Chen *et al.* 2016). 0D structures as nanoparticle (dispersed in the liquid to form nanofluids) and nanopore, 1D structures as nanochannel (Neek-Amal *et al.* 2016; Futamura *et al.* 2017; Zhang *et al.* 2019) , 2D structures as nanoshell (Yang *et al.* 2019b), nanomenbranes (layer confinement) (Yu *et al.* 2018a; Gravelle *et al.* 2016), nanofilm (Han *et al.* 2010; Smith *et al.* 2014), are good filled objects in the field of solid/liquid nanocompos-

ites. Some examples are shown in Fig.1.12. The empty space leads to a confinement of liquid filling in.

In addition to the manufactured solid/liquid nanocomposites, some inorganic minerals in nature (like shale mainly based on quartz nanopores) are inevitable to be permeated by liquid (liquid hydrocarbon, like octane), in the process of fuel exploitation (Wang *et al.* 2016). This gives an inspiration that the liquid permeability in nanostructured materials is an available way to alter the performance of these materials. Yu Qiao (Qiao *et al.* 2006) found through experiments that an external pressure can help water to infiltrate to the nanoporous (zeolyst ZSM-5 zeolite, with the silica/alumina), conversely to defiltrate at the low pressure. It was also reported that a similar approach for liquid wetting in nanochannels, i.e., reversible switching of water by external stimulation of temperature and voltage (Xie *et al.* 2018; Zhang *et al.* 2019). Wettability controlled by the nanostructured confinement is strongly affected the thermal conductivity. No accurate numerical relation of the thermal property between matrix and confined liquid is found that can well estimate the thermal properties of solid-liquid hybrid nanocomposites. The first reason is the variety of component types and structural features. Another important reason is the plenty of influence factor of solid/liquid interface, increasing the complexity of studies.

1.2.3 Solid-liquid interactions

Forces between a solid and a liquid are generally analysed in terms of short range and long range forces. The short range forces between a solid and a liquid are usually Van der Waals (VdW) force, describing the interaction between neutral molecules or atoms of a solid and a liquid. For the long range forces, most are caused by electrostatic nature. Among them, the most stronger one are coulombic forces, a kind of attractive forces inducing by any two static point charges. The next stronger interaction for molecule, is the bonding interaction and angle, which represents the connection and structural relationship of shared electron pairs. More narrowly, if more chemical bonds are connected by one atom, the dihedral torsion angle, bond angle bending, bond stretching, are also necessary to be considered. In addition the intermolecular interaction, non-bonding atoms in the chain also have the contributions of force.

When analysing molecular interactions, it is strictly necessary to analyse the atomic interactions of each different type atoms, and the chemical bonds and angles of their composition. It might be complex from macromolecular structure, but there are many methods to simplify the system. The first one is to regard

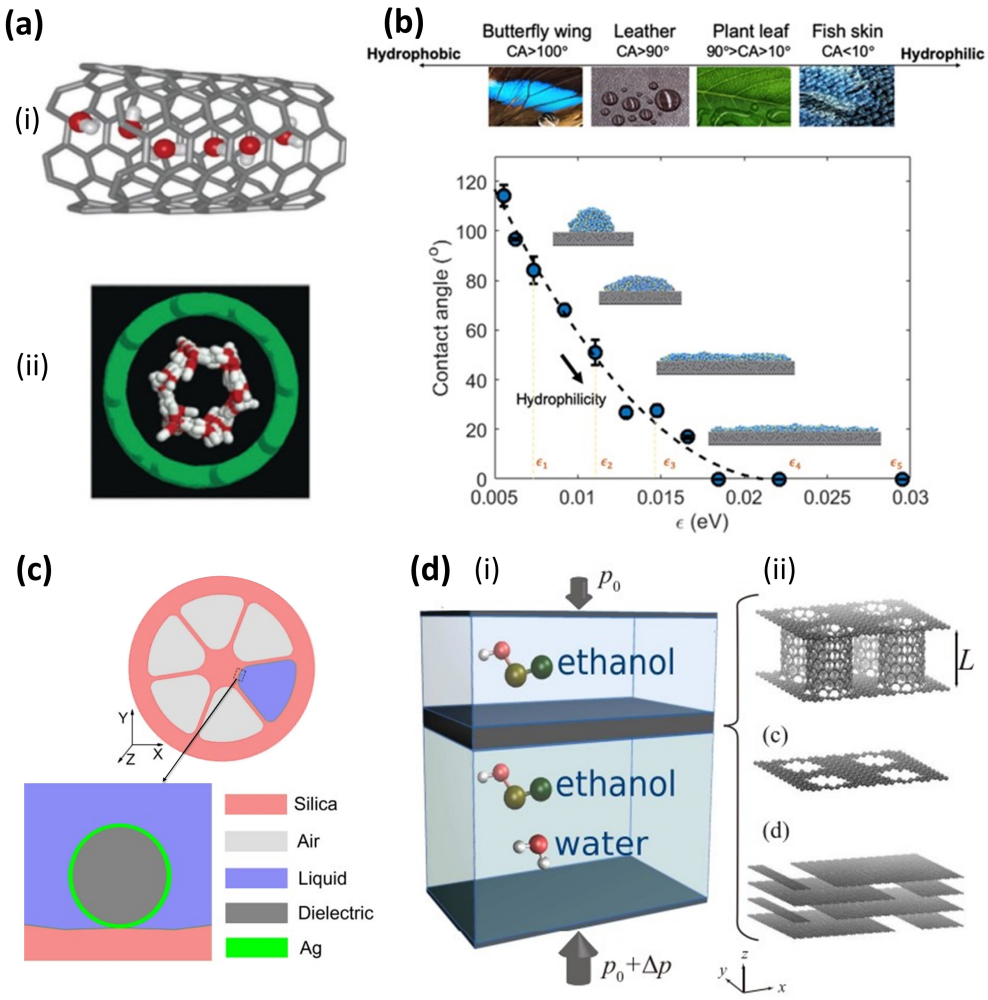

Figure 1.12: (a) The structure and cross section of water confined in CNT (Zhang *et al.* 2019). (b) Surface wetting properties of nanofilm from the hydrophobicity to hydrophilicity which are correlated with a wide range of biological applications (Montazeri *et al.* 2020). (c) The cross section of grapefruit fiber temperature sensor filled with a silver nanoshell and liquid (Yang *et al.* 2019b). (d) Carbon nanotube menbrane for water-ethanol separation (Gravelle *et al.* 2016).

the molecule model as a rigid body by fix the bonging energy and angle for each molecule (Burnham & Xantheas 2002). Then for the liquid containing representative functional groups, like CH_3, Ch_2 in ethanol, propylene, a united atom force field is employed by considering functional groups as a single pseudo atom.

What calls for special attention is that for water, there is a special force greater than VdW force and less than coulombic force, namely the force of hydrogen bond. With the advantage of having only one free electron in shell of hydrogen atom, the bond formed by an attraction between a hydrogen atom and a highly electronegative non-metallic element containing also a free electron, is stronger than normal bond (Legon & Millen 1987). Some solid atoms dissolve in the water through this bonding. Moreover, on account of the angular structure of water molecule and the electronegativity difference of hydrogen and oxygen atoms, the water molecule is polarizable and easier to attract other polar atoms.

In this aspect, many models of water are explored to represent the water molecule and express the interaction with other atoms or clusters as much as possible. They can be classified from three aspects: rigid or flexible, polarizable or non-polarizable, and the number of interaction points (Guo *et al.* 2002). Based on these three differences, amounts of the potential energy models of water molecules are established, commonly including SPC, TIP3P, TIP4P, BF, etc (Lee & Kim 2019; Bauer *et al.* 2012).

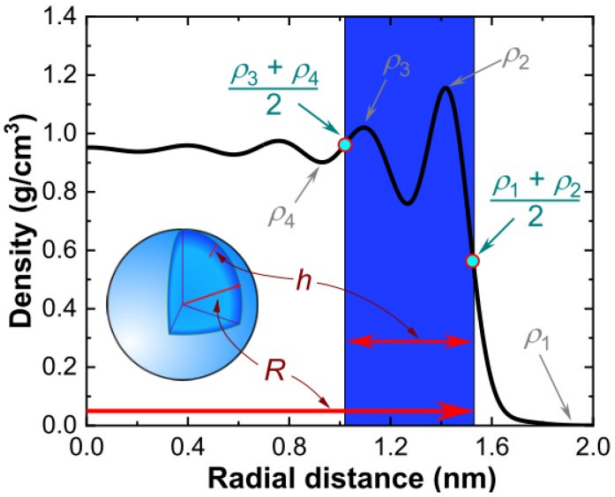

Figure 1.13: Scheme of the water density profile in the pore (Isaiev *et al.* 2020). ρ_1, ρ_2, ρ_3, ρ_4 represent the position of two maxima, one minimun and 0 value of density of water, respectively. And then the solid-liquid interfacial region could be defined, as indicated by blue region.

In the computational simulation at the nanoscale, the most common and effective physical parameter that characterizes the strength of the interaction is potential

energy, which is also the most important setting parameter in the simulation. The total energy is contributed from the short range interactions, the long range interactions and the inter- and intermolecular interaction of molecule (bonding and angle), expressed as:

$$E_{total} = E_{VdW} + E_{Coul} + E_{bond} + E_{angle} \tag{1.3}$$

Many models of potentials are discovered for the intermolecular potentials between atoms used in the simulation, commonly like Lennard-Jones potential, and Stillinger-Weber, Tersoff, COMB, AIREBO, and ReaxFF, etc (Choudhary *et al.* 2017) (introduced in Chap.2.2).

To understand the responsibility of the mechanism for the impact of liquid confined in solid matrix on thermal conductivity, Keblinski et al.(Loulijat *et al.* 2015) have suggested four potential mechanisms: effects of nanoparticles clustering, molecular-level layering of the liquid at the nanoparticle surface, nature of heat transport in nanoparticles, and Brownian motion of nanoparticles.

A large number of studies showed the liquid stratification close to the solid surface. That pointed out the solid/liquid interface plays an increasingly important role in understanding the thermal transport mechanism of solid-liquid hybrid composites (Harikrishna *et al.* 2013; Zhang Jun 2017). TQ Vo et al. (Vo & Kim 2015) found that liquid molecules form a layered structure near the solid surface. Similarly a temperature jumps in the study due to using two parallel solid walls separated by liquid water, holding each solid wall at a different temperature. In our previous study (Isaiev *et al.* 2020), we investigated the water density profiles of the solid/liquid interface of nanoporous silicon with the confined water, and calculated successfully the thickness of the thin layer near the liquid with higher density, illustrated in Fig.1.13.

The thermal properties of the solid and the liquid are modified in close proximity to the interface, at both hydrophilic and hydrophobic surfaces (Xue *et al.* 2003b), attributed by different liquid-solid interaction strength. In the study of Mykola Isaiev, the interaction strength expressed by the parameter of Lennard-Jones of the potential between the solid and the liquid, can be confirmed directly by the contact angle of liquid.

1.2.4 Main characteristics of solid/liquid interfaces

1.2.4.1 Contact angle

The solid/liquid interface is a problem that needs to be solved in many practical applications. It is well known that the solid-liquid interaction occurs mainly at the

interface. Research in this area can be traced back to the way of liquid wetting the solid surface. It starts from a liquid droplet spreading extensively on the solid surface at the macroscale. Further, it needs to improve macro description of the physical expression at the nanoscale, so as to clarify the interaction between the solid and the liquid.

Many phenomenons of confined liquid, such as the meniscus and the curved solid/liquid interface, can be explained by capillarity, which is defined as a tendency of absorption in the confinement. The most common supporting theory at the macroscale is Young-Laplace equation (Young 1805). The Young-Laplace equation is the main building stone to represent quantitatively the pressure drop across the curved interface (Van Honschoten *et al.* 2010). It describes the relation of the wetting angle of a macroscopic droplet θ and the surface tension γ_{ij} of two different phases of substance:

$$\cos\theta_{Young} = \frac{\gamma_{vs} - \gamma_{ls}}{\gamma_{vl}} \tag{1.4}$$

The illustration of coefficients is shown in Fig.1.14. It is suitable for a mechanical equilibrium condition for two homogeneous phases separated by an interface with an assumption of no thickness of the interface. But at the nanoscale, the curvature of liquid in contact with the solid is no longer a thin film. Liquid forms a solid-like layer near the solid surface which cannot be neglected (Rajabpour *et al.* 2019). So in the study of Mykola Isaiev and his co-workers, a modified Young-Laplace equation was introduced to explain the influence of the Gibbs adsorption on the nanodroplet volume contraction using molecular dynamics (Isaiev *et al.* 2018).

In addition to surface tension, the liquid also gives a tension acting along the tangents to the curved line. It is called 'line tension τ'. So the Young-Laplace

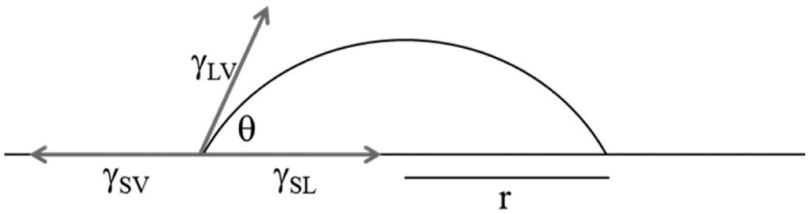

Figure 1.14: The illustration of the cross section of a liquid droplet on solid surface related to the coefficients of Young-Laplace equation (Heim & Bonaccurso 2013).

equation was elevated by adding a term of line tension (Heim & Bonaccurso 2013):

$$\cos\theta_{Young} = \frac{\gamma_{vs} - \gamma_{ls}}{\gamma_{vl}} - \frac{\tau}{\gamma_{vl} \cdot r'} \tag{1.5}$$

where r' is the radius of the contact line. Based on this equation, a complete calculation process of surface energy of substance was given in the article of A. I. Hienola (Hienola *et al.* 2007). This equation can be regarded as the connection between the interface at macro and nano scale, which can be reflected by the contact angle and the surface/line tension, respectively.

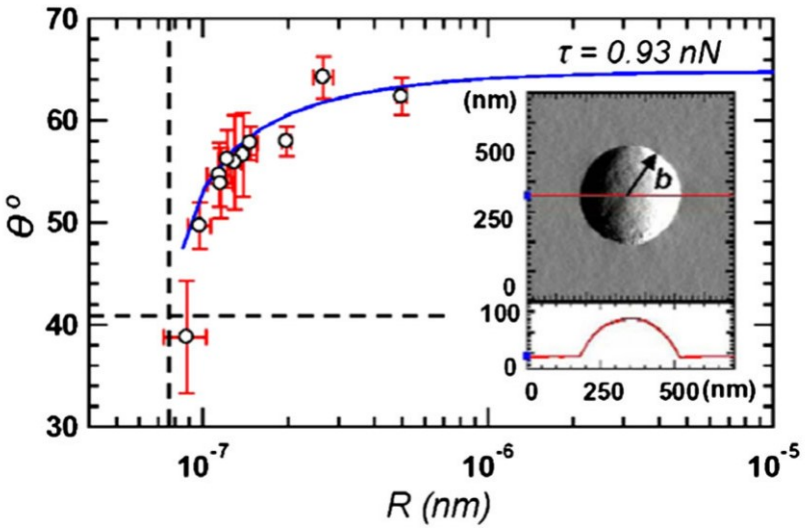

Figure 1.15: Contact angle θ as a function of the radius R of liquid particle, with the line tension $\tau = 0.93nN$ (McBride & Law 2012).

The contact angle, is easily to be measured using goniometer system controlled by computer (Ogwu *et al.* 2012), AFM (Isaifan *et al.* 2019), or a long range microscope (First Ten Angstroms FTA100) (McBride & Law 2012). There are also some researchers using simulation to calculate the contact angle, together with the value of tension. It is also proved that with the reduction of the size of liquid particle, the contact angle decreases (McBride & Law 2012), as detailed in the Fig.1.15. Fernando Bresme and Nicholas Quirke studied the liquid lens at the solid/liquid interface. They brought in Neumann's equation (Weil 1984) which is similar to Young-Laplace equation as follow, but neglected the effect of line tension, then calculated the contact angle by computative model.

$$\cos 2\theta = 0.5\left(\frac{\gamma_{vs}\gamma_{vs}}{\gamma_{vl}\gamma_{sl}} - \frac{\gamma_{vl}}{\gamma_{sl}} - \frac{\gamma_{sl}}{\gamma_{vl}}\right) \tag{1.6}$$

It indicates that this equation can describe accurately the wetting behavior of liquid lens with the nanometer size.

On the other hand, ever since the advent of AFM in 1986, the adhesive force between the tip and surface has become a hot research topic (Sirghi *et al.* 2000). Before the formal experiment, it is the basis of accuracy of data to clarify and calibrate the errors in this aspect. The effect of water meniscus formed between samples and tips, and local curvature of the sample surface on account of capillary are inevitable in AFM measurement in air (Woodward & Zasadzinski 1994). The interaction between solid (tip or sample surface) and liquid (H_2O molecule in the air) may make an impact and is difficult to measure quantitatively in the results of AFM, especially for Scanning Thermal Microscopy (SThM) mode. Evaporation and condensation of water molecules can affect energy transfer when testing thermal properties (He *et al.* 2001). So many scholars used numerical equations and simulations to obtain a quantitative expression. Luo et al. (Luo *et al.* 1997) proposed an equation to give a conductance of water meniscus adding into the whole conductance calculation. The article of Ali Assy (Assy *et al.* 2014) discovered also a methodology (for Wollaston probe) to correlate the thermal conductance of meniscus. He calculated the thermal conductance of the sample in the air conductance term, and determine the final value according to the size of meniscus. In addition, Claire K et al.(Fang & Pilon 2011) used the Edgertronic high speed camera to describe the interface curvature of droplet vaporization on superhydrophilic nanoporous thin layers on a macroscopic scale.

The contact angle even surface wettability can be also studied by Molecule Dynamics (MD)(Yang *et al.* 2019a; Zhang *et al.* 2016) where a clear figure change of three phases can be found. It chooses usually the position of average density of liquid and vapor (i.e. for water at ambient temperature 0.5 g/cm^3) as their interface as a basis of curvature calculation. Around the year of 2010, some articles were reported about the molecular dynamics of AFM to investigate the meniscus shape. Choi Hojin (Choi *et al.* 2008a) built the model of the hydrophobic flat surface and a hydrophilic tip above which is designed almost as a spherical surface at the top. It is found that with the increase of the flat surface energy, the shape of the water meniscus changed from convex to concave. The capillary force and meniscus are not the unique two factors that affect the surface energy and heat transfer path. There are also other reasons like hydrophilic/hydrophobic surface, roughness of surface (Ko *et al.* 2010), and the relative humidity (Korayem *et al.* 2018). Later years, less research or simulation has been done in this domain. Here, it is surmised that some experimental data showed that compared with the heat loss to the air, the

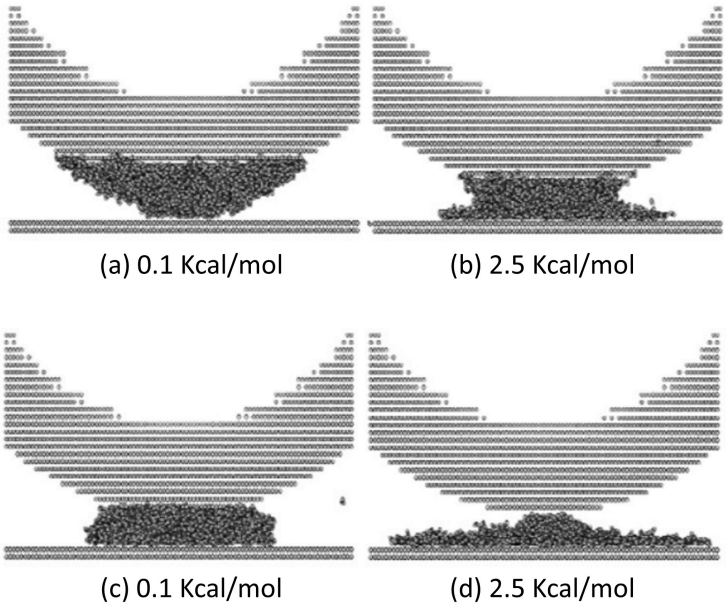

Figure 1.16: The geometries of water meniscus on the AFM (a) and (b) hydrophobic, (c) and (d) hydrophilic tips with two different surface energies (Choi *et al.* 2008a).

effect of water meniscus could be negligible (Shi & Majumdar 2002). In addition, more and more experiments required a vacuum environment to eliminate the effect of air. Even so, it needs also stress the importance of this part.

1.2.4.2 Wettability

The hydrophilicity even superhydrophilicity of a substance could be roughly divided into hydrophobicity and hydrophilicity, which are distinguished by contact angle (Drelich 2019), as shown in Fig.1.17. Generally with the help of the ionized or polar groups, the hydrophilic surface attracts the dipoles and quadrupoles of water to obtain consequently a affinity for liquid (Lu & Berkowitz 2006). Here it can be simply understood as the more attractive of interaction, the more hydrophilic (Melillo *et al.* 2011). The hydrophilicity of a surface determines the wettability, film stability and contact angle of the surface.

Matsumoto, S. M. T. K. S (Matsumoto & Kimura 1998) studied the phase transition behavior of droplets on solid surface. Two layers of solid molecule were set at the bottom and top of the calculation box. The higher temperature of the solid surface at the bottom and the lower temperature at the top provide conditions for evaporation and condensation. Finally, the velocity profile and temperature distribution of evaporation and condensation droplets are

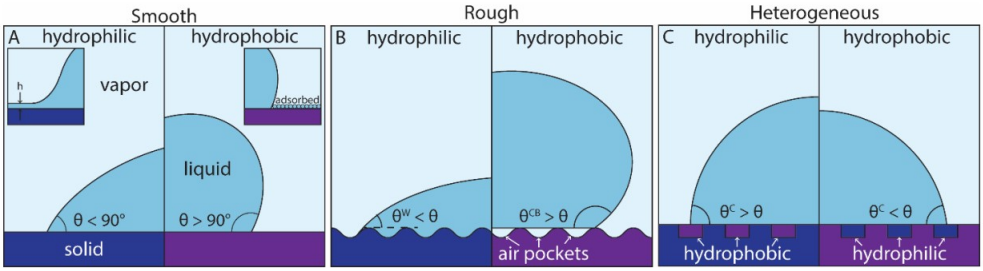

Figure 1.17: Schematics of water on the different surfaces : (a) smooth, (b) rough, (c) heterogeneous (Drelich 2019). h is the thickness of the liquid film, θ^W, θ^{CB}, θ^C is the Wenzel contact angle, Cassie Baxter contact angle, Cassie contact angle, respectively.

calculated, exhibiting a layered change near liquid/vapor interface. Mastumoto (Sinha 2004) found the pre-diffusion behavior of solid-liquid-gas three-phase contact line. The results showed that there are a lot of molecular diffusion occur at the solid/liquid interface and some of them pass through the interface. In the study of Nakabe(Nakabe *et al.* 1999), comparing the micro-scale droplet behavior on smooth and rough planes, it concluded that the contact angle on smooth and rough planes decreases with the increase of potential well parameters. When the parameters of potential wells are the same, the contact angle of rough surface is larger than that of smooth surface. It indicates that the surface micro-scale rough structure is beneficial to improve the hydrophobicity of surface.

The solid-liquid contact can likewise be dynamic. Thompson (Thompson & Robbins 1989) studied liquid flow on solid surface using molecular dynamics simulations. He found that the slip phenomena of determining fluid on the surface of the material type are closely related to the potential energy action and wettability of the fluid on the solid surface. The flow of liquid on the hydrophobic surface has obvious slip, while on the hydrophilic surface it may be non-slip or even "negative slip"(Nagayama & Cheng 2004). The statistical density of liquid molecule is in the range of several molecular diameters near the solid wall surface. Because of the influence of the wall potential energy, the statistical density of liquid molecule is in a layered spatial fluctuation distribution. Furthermore, for the liquid flow in nanochannels, it is found that there is a critical velocity shear rate. Under this critical vale, the slip length is only related to the properties of the fluid and the wall and accords with the slip law. When the shear rate is higher than the critical velocity, the slip length increases rapidly (Wagemann *et al.* 2017).

1.2.4.3 Size effect

Since crystals are periodic, we can usually convert particle motion inside a crystal into particle motion within a cell. However, if the particle size is comparable or smaller than the size of physical features, the periodic boundary variation of the crystal will be broken (Arora 1981). They could be the Broglie wavelength of electron conduction, the wavelength of light waves, the wavelength of phonons, and the transmission length. For a bulk system consisting of an infinite number of atoms, its physical properties may greatly change, compared with the limited particles. They include, but are not limited to the magnetic properties, internal pressure, light absorption, thermal resistance, chemical activity, catalytic properties and melting point. For example, gold block is very stable under normal conditions, but gold nanoparticles play a key catalytic role in many chemical reactions (e.g.carbon monoxide oxidation). Due to the comparable size, more interfaces are induced. When solid-liquid composites are reduced to the nanoscale in a specific dimension, or when the solid-liquid particle motion is limited to the nanometer size, the most significant change is the increase in the ratio of surface particles, and thus the increase in the specific surface area of the solid/liquid interface. Based on this, a possible tunable role played by the interface in the energy transfer process is crucial.

Rajabpour (Rajabpour *et al.* 2019) proposed a equation to calculate the interfacial thermal conductance G between the nanoparticle and surrounding water, as follows:

$$G = \frac{|dE/dt|}{A\Delta T} \tag{1.7}$$

where dE/dt and ΔT present the heat flux, G depends strongly the surface area of the nanoparticles and A is the surface of cross section . It is obvious that the specific surface area increases leading to the thermal conductance decreases. Graphene, a two-dimensional sheet of carbon atoms with only one carbon atom thickness, having a larger specific surface area, is often chosen to introduce into PCMs to improve the thermal properties of PCMs (Dao & Jeong 2015). In addition to adjusting the particle size, delicately changing the nanostructure is also a way to make changes in the specific surface area. This involves the addition of nanoscale pore. For nanoporous materials, more interfaces are created, inducing more boundary scattering of phonons. It is proved that the thermal conductivity evolution is controlled by the limited mean free path of phonons, which is related to the specific surface area of pore (Jean *et al.* 2014). Geometrically, it corresponds to the specific poros-

ity. Even in the same porosity, The thermal conductivity of materials with different specific surface areas also differs greatly (Dettori *et al.* 2015).

Another effect caused by small size is the quantum energy level effect. The bulk material is considered as a limit of an infinitely large system, corresponding to the continuous spectrum of states of electrons. So we can approximate that a continuous energy level is formed from infinitesimal energies. But if the size of material or the particle size is limited, the states are discrete, rather than continuous, shown in Fig.1.18. The averaged difference between each successive energy level is expressed by Kubo gap δ, equal to $4E_f/3N$ (Rao *et al.* 2000). E_f is the Fermi energy, the topmost energy potential of electrons at zero temperature, and N is the number of valence electrons. It verifies that for the infinitely large system, δ tends to 0, and the energy level seems continuous. At the nanoscale, the energy level changes from a continuous structure to a split structure, which leads to sorts of characteristics for nanomaterials. Keith T. Butler (Butler *et al.* 2019) using Density Functional Theory (DFT) designed the band gap, band alignment of interface between materials to tune electronic properties, predicting the performance of photovoltaic (PV), and photocatalytic (PC) devices. In the study of transport properties of materials, such as electrical and thermal conductivity, the energy level structure is always a very complex issue and is the basis for the study of density of states. The split energy bands allow the control of the frequency band of the absorbed waves, which makes the application of the material more relevant in specific areas. For example, the wavelength range of near-infrared light can pass through human skin and deep body tissues without causing damage. Therefore, when designing a photo-thermal nanomaterial, the material absorbs infrared light in a specified frequency band and converts the light energy into heat energy. Consequently, it results in high local temperatures that kills tumor cells (Zhang *et al.* 2018a).

1.3 Thermal properties of solid-liquid nanosystem

1.3.1 Thermal properties studies

The presence of a solid/liquid interface allows for a richer variation in heat transfer through the material, which in turn mainly changes the thermal conductivity, interface thermal resistance. Other properties of the material can also be altered in certain conditions, such as higher thermal insulation, tunable thermal radiation, thermal rectification, surface wettability even new utility as thermal transparency.

The image of solid-liquid surface modeled and the spatial heat conduction dis-

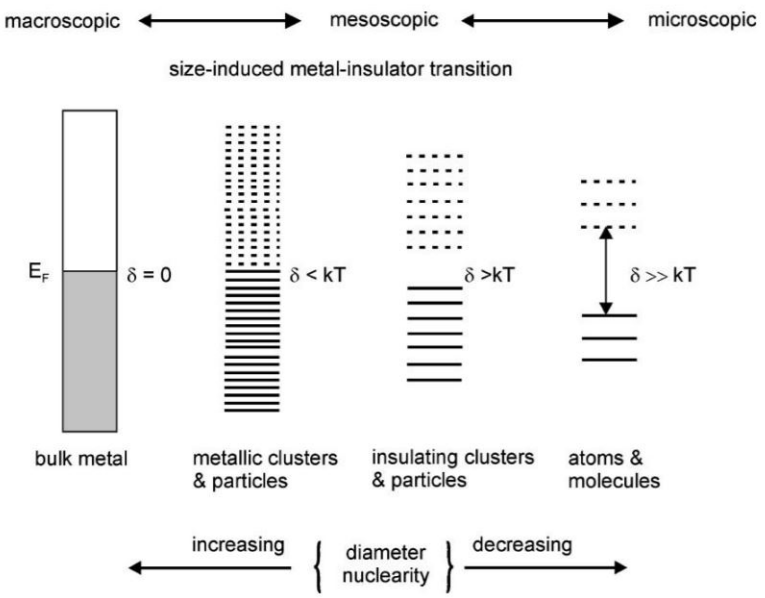

Figure 1.18: Evolution of Kubo gap in different scales (Roduner 2006).

tribution could help to explain thermal transport phenomenon of nanofluid. Mississippi Missouri Bhunia studied the thermal property of 2D dielectric nanomaterial: amorphous graphene Sheets in transformer oil (TO) (Bhunia *et al.* 2018). He found that a higher thermal conductivity of nanofluid is contributed by the lattice vibration and cluster formation, compared with the basefluid. As well, a electrical insulting performance is visible when the temperature increases. The co-existence of high electrical insulation and high thermal conductivity give TO an attractive improved overall property.

To the thermal transport of solid-liquid nanomaterials, thermal conductivity becomes a more and more significant investigated parameter. Many researches have demonstrated that the combination of the solid and the liquid in nanofluid produces a higher thermal conductivity, even with a very low particles volume percentage. Mostly a lower thermal resistance for solid/liquid interface makes it possible to reduce heat loss (Vo & Kim 2015; Wemp & Carey 2019).

To investigate the thermal conductivity of solid-liquid composite, experimentally, Photo Thermal (PT) method was used due to a high sensitive signal to thermal-induced pressure rising on the liquid (Andrusenko *et al.* 2012), as shown in Fig.1.19(a). Lishchuk et al.(Lishchuk *et al.* 2015) used this technique, finding that the thermal conductivity of a nanoporous silicon filled with oil is twice as large as the dry simple. Beside these, Patrick E. Hopkins et al. (Hopkins *et al.* 2011) applied Time Domain Thermoreflectance (TDTR) (in Fig.1.19(b)) to measure the

thermal conductivity of a series of single crystalline silicon phononic crystals (PnCs), which is over an order of magnitude lower than those obtained for bulk Si. For nanoparticle suspension (Cardellini *et al.* 2016), by effectively controlling the geometrical, chemical or physical parameters, the thermal conductivity can be enhanced, meanwhile a good compromise with viscosity. From other type of materials, like nanofluids, It is also revealed that a mixture of a solid and a liquid have a great promotion to thermal properties. Honorine Angue Mintsa et al. (Mintsa *et al.* 2009) studied the alumina/water and copper oxide/water nanofluid. A relative increase of thermal conductivity is found in the high temperature range.

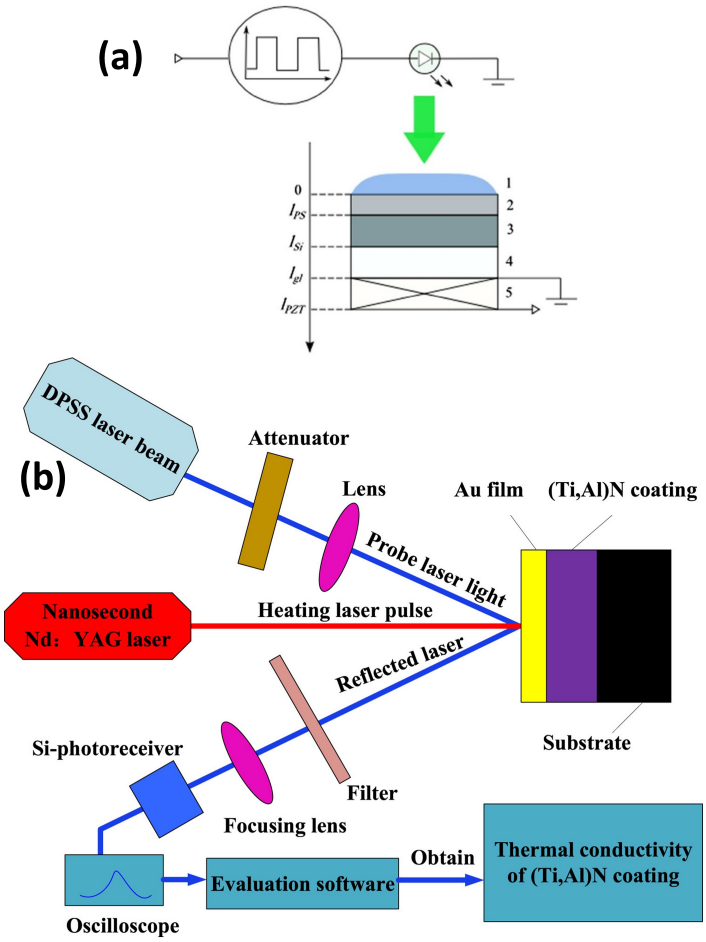

Figure 1.19: The test methods for the measurement of thermal conductivity. (a) Scheme of photo thermal method (Andrusenko *et al.* 2012). The layers 1 to 5 refer in order to: a liquid droplet, porous silicon layer, bulk silicon substrate, buffer glass-ceramic layer, and piezoelectric transducer. (b) Scheme of time domain thermoreflectance (TDTR) (Zhao *et al.* 2019).

From these results, the thermal conductivity of solid-liquid hybrid composite

is more excessive than the sum of thermal conductivity of the solid (matrix) and liquid, if proposed by macroscopic models like Effective Medium Approach (EMA) (Termentzidis *et al.* 2018). That indicates the significant meaning of interface and complexity of solid-liquid coupling. Moreover, it failed to capture the variation of the thermal conductivity at nanoscale by traditional macroscopic methods. To specify these mechanisms, the modeling and simulation techniques can be investigated to understand many properties on the microscopic scale. Molecular dynamics (MD) simulations are generally applied in many areas to obtain structural and thermal properties with better accuracy (Lee *et al.* 2007; Fang & Pilon 2011). In this context, Brownian dynamics simulations, based on equilibrium Green–Kubo approach (Allen & Tildesley 2017), have been interested in calculating the effective thermal conductivity of confined water in crystalline silicon matrix. The Green-Kubo method allows one to extract transport properties while carrying out the simulation at equilibrium. It has been shown to be reliable and accurate for Lennard-Jones liquid (Vogelsang *et al.* 1987) as well as solid systems (Li *et al.* 1998; Schelling *et al.* 2002).

Using micro time domain thermoreflectance and Monte Carlo simulations can find the similar results in the study of Maxime Verdier (Verdier *et al.* 2017). The boundary scattering is enhanced when adding the aligned and staggered hole in the nanomaterials, which induces a strong reduction of thermal conductivity.

Dezhao Huang et al. (Huang *et al.* 2018) found that there is a collaborative effect from the electrostatic interactions and the Lennard-Jones (LJ) interactions (especially the repulsive part). The electrostatic interactions, which are between the polar functional groups of self-assembled mono-layers (SAMs) and water, attract water molecules closer to the SAM surface, leading both the electrostatic and L-J interactions to have larger effective forces across the interfaces. This increases the power exchanged between solid and water atoms, enhancing the thermal energy transport. Harikrishna et al. (Harikrishna *et al.* 2013) using the same method investigated the interface thermal conductance between water and SAMs modified gold substrates. They reported an interface thermal conductance for a hydrophilic Au surface in water of 190630 $MW/m^2 \cdot K$. L. Sarkisov et al. (Sarkisov & Monson 2000) found that the hysteresis loops obtained in the molecular dynamics calculations are essentially identical to those obtained in GCMC simulations of the same system. Jun Zhang et al. (Zhang Jun 2017)demonstrated that for the nanodroplets spreading on the surfaces, applying a dynamic contact angle model is not sufficient to pick up the molecular effects. It is helpful to use the VOF method accounting for slip across the entire solid/liquid interface, in particular the

large slip behaviour at the contact-line. Ruixia Su et al. (Su & Zhang 2018) studied the size-effect impact of suspended and supported graphene.It is found that the thermal conductivity value would converge to a constant value as further increasing size. The underlying physics of the size effect on both suspended and supported graphene is investigated and presented in terms of phonon transport analysis.

1.3.2 Parameters that influence the thermal properties

Both from the experimental (Kokate & Sonawane 2019) and theoretical (Achhal *et al.* 2018) study on the thermal transport of nanofluid, it is found that the thermal conductivity in nanoparticle suspensions is strongly dependent on the size of the particles, where the thermal conductivity increases for smaller particles. But for nanoporous materials, it exhibited the opposite conclusion with larger pore size and lower thermal conductivity (Antidormi *et al.* 2018).

The thermal conductivity of solid-liquid nanoporous composites is controlled by the type of materials of liquid and solid (inclusion and matrix), the characteristics of the pores (porosity, size, position), also by the simulated conditions. Among them, the impact of porosity is the most severe. Many studies have already reported in this point. Fang et al. (Fang & Pilon 2011) investigated the impact of system length and pore diameter on the effective thermal conductivity of crystalline nanoporous silicon at 500 K. J.-H. Lee et al. (Lee *et al.* 2007) calculated the lattice Thermal Conductivity (TC) of Si with nanometer sized pores along the [001] direction as a function of pore diameter and pore spacing. What's more, he found that TC across pores is smaller than the bulk value by over two orders of magnitude at room temperature. Our previous study (Isaiev *et al.* 2020) showed that the thermal conductivity of porous silicon without water has decreased by nearly an order of magnitude compared to the bulk value, and much greatly when the pore size increases, which is consistent with the literature results on porous systems(Mortazavi *et al.* 2019; Yousefi *et al.* 2020a). M. Verdier added an amorphous silicon nanoinclusion in the inside nanopore of nanocrystalline silicon to prove its same effect on thermal conductivity as the nanopore. Two key parameters proposed as a function in his study to summarize the behavior of TC: the "non-crystalline" fraction and the surface to volume ratio (Verdier *et al.* 2016).

For temperature factor, only a few results have carried considering the dependence of the effective thermal conductivity values on temperature for nanoporous materials (Cui *et al.* 2018) and also nanofluid(Xing *et al.* 2006). For example, El Mehdi Achhal et al. (Achhal *et al.* 2018) found on the thermal conductivity of Au-Cu nanofluid with argon-based fluid and suspended copper nanoparticles,

which increases when the temperature increases in temperature range from 86 K to 102 K. For solid-liquid system, more researchers focus on the strong temperature dependence of thermal resistance of the interface (Yousefi *et al.* 2020b; Xue *et al.* 2003a). But when the liquid is confined in a mesoscale even nanoscale region, due to the extremely small size constraints, the interface is difficultly to define. (Achhal *et al.* 2018). Trend results are readily available. But for effective thermal conductivity, it lacks of analytical models for description and analysis of reason.

1.4 Thermal applications of solid-liquid nanosystem

Solid-liquid can take the advantages of the counterpart. Combining with the flow, diffusion and self-adaptive properties of liquid can help the new material having much stable composite properties. Numerous reviews (Wen *et al.* 2009; Senthilraja *et al.* 2010; Senthilraja *et al.* 2010; Wong & De Leon 2010; Yu & Xie 2012) published around 2010 introduced the preparation, fabrication, current and future development of applications of these materials. This shows that solid-liquid mixture in the field of nanomaterials has received great attention and developed greatly in these 20 years. Some examples involving in electronic devices, fuel cells, soft materials, thermal energy control, and biomedical therapy are taken in the following subsections.

As shown in Fig.1.20(a), Alan Molinari et al. (Molinari *et al.* 2019) tuned the interplay between electric and magnetic degrees of freedom at the interface of all-solid-state and solid/liquid state for magnetoelectric composites. In the Fig.1.20(b), Zhou Y et al. (Zhou *et al.* 2017) proposed to add the solid electrolyte LAGP in tetraethylene glycol dimethyl ether (TEGDME) electrolyte to obtain a sandwich structure hybrid electrolyte, which can effectively stabilize the electrode-electrolyte interface of Li-Se battery, limit the shuttle of polyselenide, inhibit the formation of lithium dendrites, and improve the electrochemical performance of Li-Se battery. In the Fig.1.20(c), Xiying Li and co-workers (Li *et al.* 2019) used the multimaterial microfluidic 3D printing platform to induce thermally flower-shaped complex with the two-layer beam structures, whose beam could maintain the shape after fast cooling to the room temperature, providing a new insight for soft robotics design. Xiaohu Yanga et al.(Yang *et al.* 2019c) demonstrated experimentally that the involvement of open-cell metal foam embedded into paraffin (phase change materials) can greatly reinforce efficiency of thermal energy storage, due to the reduction of the thermal interfacial resistance of metal form, shown in Fig.1.20(d).

Finally, Qi Wu et al.(Wu *et al.* 2019) found a high stretchability and self-healing of "solid–liquid" elastomers (SLEs) by interpenetrating polyborosiloxane (PBS) with polydimethylsiloxane (PDMS).

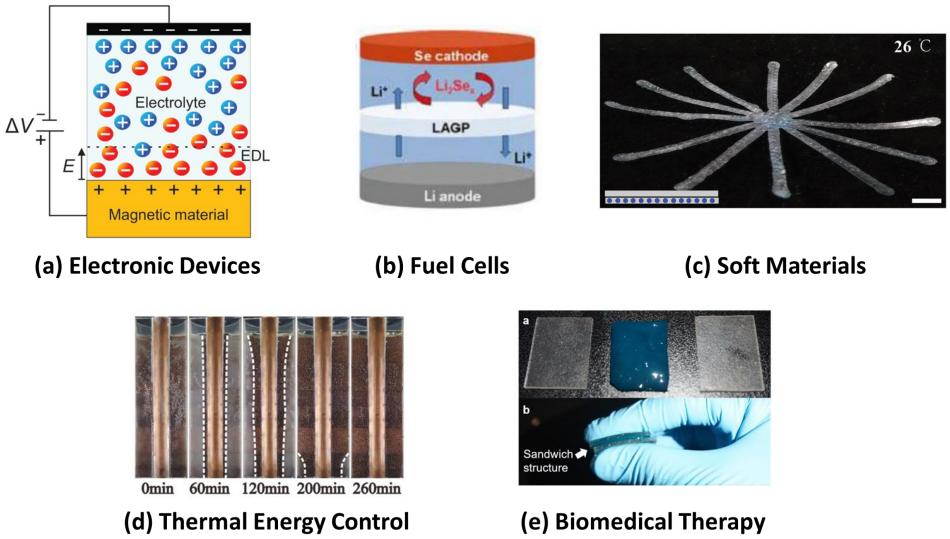

Figure 1.20: Examples involving in electronic devices, fuel cells, soft materials, thermal energy control, and biomedical therapy.

Due to the diversity of material types, quantum effects of atoms, structural versatility, the complexity of the interface, the applications of solid-liquid nanocomposites in micro devices are diverse and involve many fields, including microelectronics heat dissipation, thermal energy conversion, thermal storage and thermal control.

1.4.1 Microelectronics heat dissipation

One common solution to the problem of heat dissipation in microelectronic devices is the liquid flow cooling. As shown in Fig.1.21(a), the coupling of the heat conduction and heat transfer convection solid/liquid interface induces the continuity of heat flux dissipation in the single rectangle microchannel (Al-Neama *et al.* 2017). Moreover, it is proved that the nanofluids such as Al_2O_3-H_2O can employ successfully based heat sinks cavities in microelectronic packages, providing an excellent local heat exchange capability (Selvakumar & Suresh 2012). However, when the heat transfers through the radiator and heat source, the interface between them often restrict the heat dissipation, on account of the thermal contact resistance (TCR). It is so sensitive and influenced by many factors, like temperature, pressure. The phase change thermal interfacial

materials (PH-TIMs) is proposed as times require, as shown in Fig.1.21(b). When the PH-TIMs changes the phase from solid state to molten state, the wettability of two contact surfaces also changes from solid-solid to solid-liquid contact. It induces the great reduction of the TCR. In the report of Changqing Liu et al., they designed a novel PH-TIMs, graphene/olefin block copolymer/paraffin, which helps the TCR decrease with a drop of two orders of magnitude (Liu *et al.* 2020), shown in Fig.1.21(c).

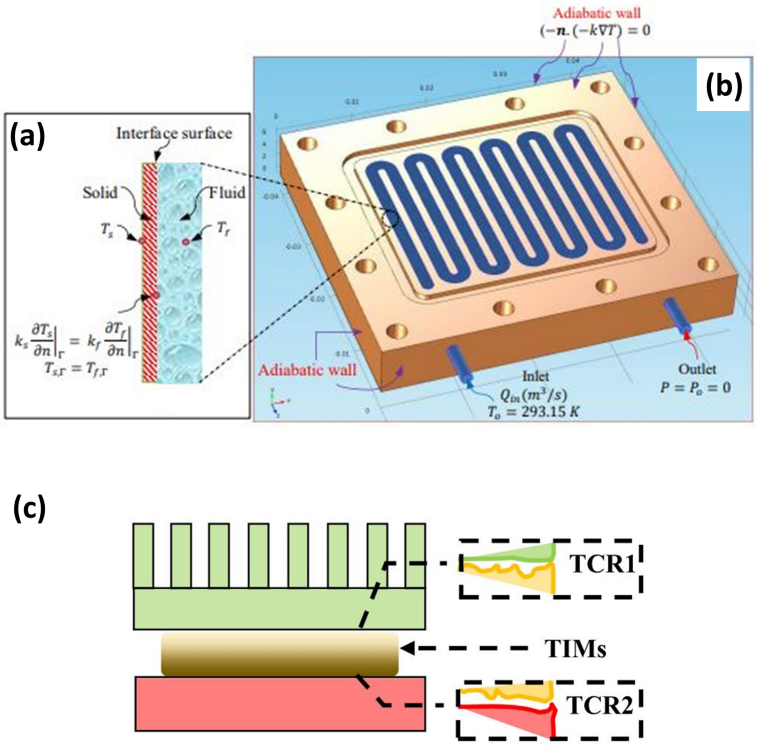

Figure 1.21: (a) 3D schematic of single rectangle microchannel heat sink with the physical explanation of solid-liquid boundary conditions (Al-Neama *et al.* 2017), and (b) stacked microchannel. (c) The phase change thermla interfacial materials applied in the microelectronic device (Liu *et al.* 2020).

1.4.2 Thermal energy conversion

Solid-liquid nanocomposites can also make the conversion of heat and light, electricity, magnetism, and mechanical energy through their tunable thermal properties, and they are extensively adopted in thermoelectric devices(Ohta *et al.* 2008), photo-thermal, solar-thermal devices(Duan & Lieber 2000; Huang *et al.* 2018), etc.

To convert directly the thermal energy into electricity in thermoelectric device, thermoelectric material contribute a sustainable and environmentally kind conversion. However, some of them such as Bi_3Ti_3, PbTe are toxic, with high cost and low efficiency. Note that the efficiency is generally evaluated by the dimensionless factor called figure of merit Z, expressed as:

$$ZT = \sigma S^2 T / \lambda \tag{1.8}$$

where T, λ and S are the Seebeck coefficient, the temperature, the thermal conductivity, respectively, as well as σS^2 the power factor (PF). Lourdes Márquez-García found that the PF can be significantly enhanced by a solid-liquid hybrid system based on a porous solid permeated by a liquid with the salt dissolved inside. An improved eletrostatic environment of solid was built by the ions at solid/liquid interface (Márquez-García *et al.* 2018). The conceptual and actual schematics of the solid-liquid hybrid system are shown in Fig.1.22(a) and (b). In addition, the PCM embedded the Graphene nanoplatelets and solid–Liquid In4Se3-In composite are also good choices of thermoelectric materials to provide an efficient thermo-electric conversion as well as energy harvesting (Yu *et al.* 2021; Luu *et al.* 2019).

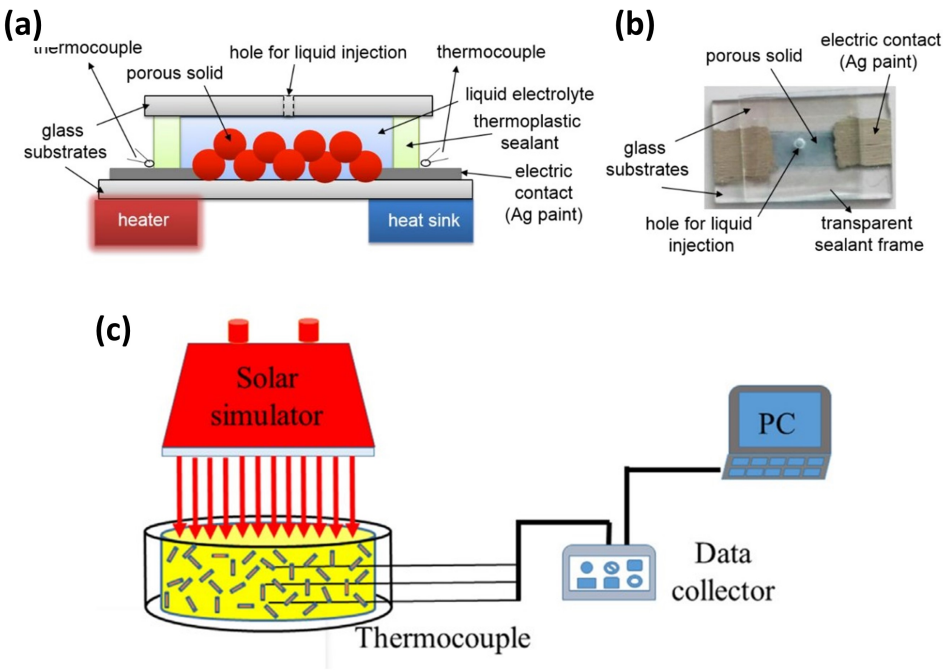

Figure 1.22: The (a) conceptual and (b) actual schematics of the solid-liquid hybrid system in the thermoelectric device (Márquez-García *et al.* 2018). (c) The diagram of solar transition of carbon-based nanofluid (Chen *et al.* 2018).

It is a well-known fact that solar energy is a very clean, environmentally friendly and easily accessible green energy source both in civil and industrial use. Solar energy can be converted into heat energy directly or indirectly by absorption. The energy efficiency is affected significantly by both the capture and conversion of solar energy. The diverse structures of energy collectors such as sheets, layers, and grids offer the possibility to increase the efficiency of solar energy capture. The efficiency of the energy converter, however, depends mainly on the photo-thermal properties of the liquid. A kind of solid-liquid nanocomposites is suggested to provide the potential of increasing the efficiency of direct solar-thermal conversion (Chen *et al.* 2018; Soltani *et al.* 2017; Mu *et al.* 2009). Nanofluids play a significant role among them. Fig.1.22(c) shows the diagram of solar transition of carbon-based nanofluid. The nanoparticles, fibers, or tubes are suspended into the conventional basefluids such as water, oil, etc (Soltani *et al.* 2017; Li *et al.* 2020). Jia-Sheng Li et al. (Li *et al.* 2018) proposed a solid-liquid hybrid state quantum dots LED (QD-LED) to achieve higher conversion efficiency of LED, by integrating liquid solution (like methyl-terminated polydimethylsiloxane) into solid-state matrices (like ethylene-terminated polydimethylsiloxane).

1.4.3 Thermal storage and thermal control

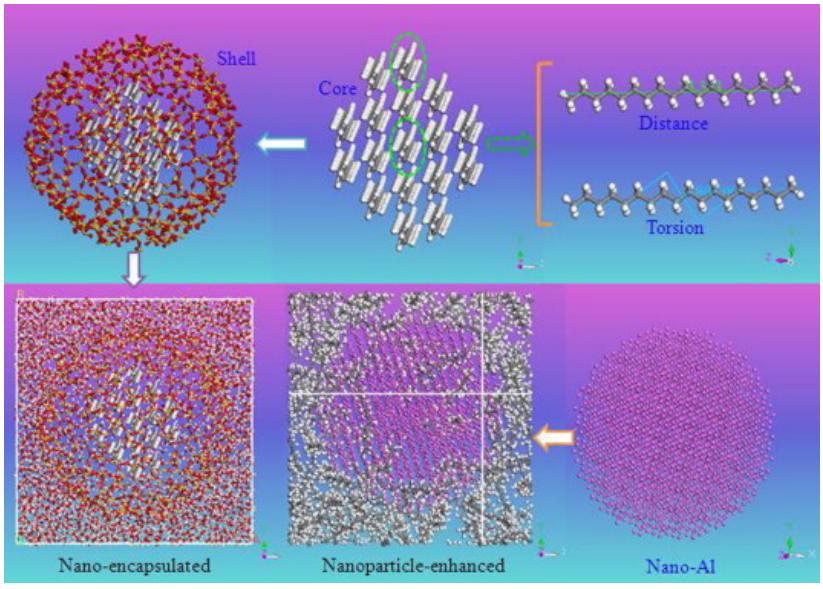

Figure 1.23: Two Typical types of phase change materials simulated: nano-encapsulated structure (n-octadecane as core, SiO_2 as shell in this figure), and nanoparticle-enhanced structure (SiO_2 enhanced by aluminium)(Rao *et al.* 2013).

Numerous types of solid-liquid PCMs have been researched for thermal en-

ergy storage applications (TESS) (Su *et al.* 2015). Through the phase transformation, it is the storage and consumption of energy that is out of sync with time (Rao *et al.* 2013). Examples for PCM structure simulations are shown in Fig.1.23.

Compared with traditional energy storage systems, the PCMs material weight and volume required for storing the same capacity are smaller. Energy can be stored at a stable or near phase transition temperature (Agyenim *et al.* 2010). So in solar absorption refrigeration systems, electronics thermal management, industrial waste heat recovery and off peak electricity storage systems (Merlin *et al.* 2016; Khan *et al.* 2017), the use of PCMs is highly recommended.

CHAPTER 2

Molecular dynamics

Contents

Molecular dynamics (MD) is an effective approach to calculate the thermodynamic quantities and other macroscopic properties of the systems. In this study, the main purpose of MD is to estimate the thermo-physical properties, for instance the heat flux, thermal conductivity, thermal motion of atoms and so on. It provides

the visualisation and process means to properly understand and analyze the microscopic reactions. So in this chapter, the detailed process of MD simulation using LAMMPS is introduced, including the thermostat/barostat, boundary conditions, algorithm, etc. After that, interatomic potential functions needed in our simulations are presented. To calculated the thermal properties via LAMMPS, the EMD, NEMD and AEMD methods are expanded in the third section. Finally, several parameters need to be studied to explain the results of thermal properties and clarify the physical mechanisms. The characterization methods for this part are details at the end.

2.1 Introduction

Molecular dynamics simulates the motion of individual atoms in a large collection of particles (solid, liquid, gas) combining the physics, the mathematics and the chemistry. It relies on the Newtonian mechanics to simulate the motion of molecular system in order to take samples in the different states of molecular systems, thus calculating the motion behaviors of the whole system, further the calculations of thermodynamic quantities and other macroscopic properties of the system.

Molecular Dynamics (MD) simulation is simply to solve the N-body problem through the numerical method. It aims at exploring the following motion of molecules based on the initial position, velocity, mass of N-body in classical Newtonian mechanics case. The most important role evolves into the linking of the single-particle dynamics to the collective state of the system, which attempts to explain the dynamics of systems of large collections of particle by examining the motion of individual atoms. Molecular dynamics has been used in many research fields such as high molecular chemistry, material science, molecular biology and condensed matter physics, etc.

In this study, MD is used mainly for thermodynamic calculation, which has high accuracy and validity in the calculation of macroscopic properties. MD simulations are conducted with the open source code Large-scale Atomic Molecular Massively Parallel Simulator (LAMMPS) (Plimpton 1995a). The effective thermal conductivity has been computed with the Equilibruim Molecular Dynamics (EMD) methodology. In the following paragraphs, details of the modeling and the simulatations are given.

2.1.1 Simulation process

Molecular dynamics can be carried out in roughly the following steps.

1) Determine the starting configuration

   A well-structured starting 3D configuration is the first step in performing MD simulations. The starting configuration of biological macromolecules are mainly derived from experimental data.

2) Choose appropriate force field and simulation software

   The selection of an appropriate force field is the basis for conducting MD simulations. Different force fields have different applicability and limitations and need to be selected appropriately according to the system and problem under study. When using multiple force fields at the same time, attention should be paid to the compatibility between the used force fields. The choice of the force field is closely related to the accuracy of the final simulation results. The choice of software is often related to the force fields used and should focus on the required algorithms, the speed of operation of the software and parallel computing capabilities.

3) Building system and energy minimization

   The starting configuration of the target molecule is already available, and then the simulation system has to be constructed according to the environment in which the target is located. The size of the system and the shape of the simulated cells depend on the specific system and need to be balanced with the rationality and the feasibility.

4) Equilibrium process

   After the system is constructed, the initial velocity of each atom is given, and the velocity of motion of each atom is adjusted so that the sum of the kinetic energies of the system in general in all directions is zero. NVT and NPT conditions control the temperature, pressure and density of the system. This process requires monitoring the energy, temperature, pressure, and density of the system to see if it converges until the system reaches equilibrium.

5) Data acquisition process

   After the system has reached equilibrium then a long simulation can be performed and samples can be taken from this process for analysis. The macroscopic physical quantities needed are output according to the research needs. Simulations should be as long as possible to be sure that the phenomenon or property under study can be observed, and the reproducibility of the occurrence of this phenomenon needs to be ensured.

6) Analysis of MD results

The result analysis is mainly to obtain macroscopic physical quantities that can be compared with experimental results by means of coefficient averaging. There are many tools available for data analysis. The analysis methods include: average energy, average atomic coordinates of the system, geometric structure, dynamic mechanical properties, etc.

2.1.2 Cutoff radius settings

In order to save computational resources, the potential energy needs to be cut at a suitable distance. In molecular dynamics, potential energy is often cutoff and shifted so that the potential energy at the cut-off radius is zero.

$$u_c(r) = \begin{cases} u(r) - u(r_c), & r \leq r_c \\ 0, & r > r_c \end{cases} \tag{2.1}$$

To ensure the continuity of the force and to eliminate the jump in energy at the cutoff radius, molecular dynamics chooses to add a shift potential u' to the above equation Eq.2.2. It ensures that both force and potential energy are continuous. For the potential energy of metals and semiconductors, they are designed with the cutoff radius is taken into account, so the potential energy and the first and second order derivatives are zero at r_c.

$$u_c(r) = \begin{cases} u(r) - u(r_c) - u'(r_c)(r - r_c), & r \leq r_c \\ 0, & r > r_c \end{cases} \tag{2.2}$$

2.1.3 System control

After the energy minimization, the molecular velocity needs to be initialized. Usually, the initial velocity is chosen according to the Maxwell-Boltzmann velocity distribution of the Gaussian distribution random number generator is chosen. It is usually obtained from the initial temperature corresponding to of the Maxwell velocity distribution to ensure that the initial velocity distribution corresponds to the set initial temperature of the system.

After the system is constructed, an initial velocity is assigned to each atom, after which equilibration is performed to ensure that the system has no translational displacement. The initial velocities are usually generated at low temperatures (to avoid excessive initial temperatures, which can cause atomic collisions, system

instability, etc.), and then the particles are restrained for a gradual ramp-up under NVT conditions. After ramping up to the desired temperature, the simulation is then performed under NPT conditions to adjust the pressure and density of the system.

Applying Hamilton's formula, the momentum is summed over 3N. N is always degrees of freedom of the system.

$$\sum_{i=1}^{3N} \langle \frac{p_i^2}{2m_i} \rangle = \frac{3N}{2} k_B T \tag{2.3}$$

where p_i and m are the momentum and mass of atom i, k_B is Boltzmann constant. From Eq.2.3, the instantaneous temperature of the system is proportional to the instantaneous kinetic energy, while the kinetic energy is related to the square of the velocity, which leads to the possibility of temperature controlled by regulating the velocity of particle motion. The molecular dynamics approach to temperature optimization at target temperature T_D can be understood as adding a resistance term to the equation of motion.

$$\ddot{\vec{r}}_i = \frac{\vec{F}_i}{2m_i} - \frac{\alpha}{m_i} \varepsilon(T, T_D) \dot{\vec{r}}_i \tag{2.4}$$

where $\ddot{\vec{r}}_i$ is the acceleration of atom i, α is a coupling parameter describing the intensity of heat exchange between the system and the heat source, and $\varepsilon(T, T_D)$ is a function of temperature, which will be defined later. Obviously, ε is positive when the instantaneous temperature is greater than the target temperature, and negative when the opposite is true. Different thermostats have different methods of calculating the resistance, just the calculation of ε.

The Langevin thermostat is a stochastic method that associates the equations of motion with the thermostat by adding a random force. the Lanvegin equations of motion can be expressed as

$$\ddot{\vec{r}}_i = \frac{\vec{F}_i}{2m_i} - \gamma_i \dot{\vec{r}}_i + F_o(t) \tag{2.5}$$

Here, γ_i is damping factor of atom i, $F_o(t)$ is the random time-varying forces. If γ_i is too small, it weakens the control of temperature and then slow down the equilibrium process. If being too large, it makes the random forces more influential than the interatomic forces, and the motion of the atoms will be closer to Brownian motion. Another type of temperature relaxation is called Berendsen thermostat, where

the damping factor is defined as:

$$\varepsilon_{Berendsen}(T, T_D) = 1 - \frac{T_D}{T} \tag{2.6}$$

These two thermostats can both adjust the temperature so that it is close to the target temperature, but time-irreversible. To solve this problem, Nose-Hoover thermostat, which introduces an additional parameter to Langevin thermaostat to achieve a constant temperature.

$$\vec{F_i} = -\frac{\partial U(\vec{r^N})}{\partial \vec{r_i}} - \varepsilon \dot{\vec{r}_i} m_i \dot{\varepsilon} = \frac{1}{Q}(\sum_i \frac{\vec{P_i}^2}{m_i} - \frac{3}{2} N k_B T) \tag{2.7}$$

where $U(\vec{r^N})$ is the total potential energy of the system at a given moment, Q is analogous to a mass parameter that represents the strength of the coupling between the system and the environment. The greatest advantage of the Nose-Hoover thermostat is the ability to obtain the correct process quantities, such as the thermostatic diffusion coefficient. The coupling strength Q has very little effect on these quantities.

The fatal flaw of Nose-Hoover thermostat is that when the system is subjected to external forces (i.e. external potential energy), Nose-Hoover thermostat does not give the correct phase trajectory, seriously violating ergodicity and eventually giving wrong results (Another thermostat called Andersen Thermostat could be still applicable in this case). The solution to this problem is to use a series of coupled Nose-Hoover Thermostats to satisfy the ergodicity.

For barostats, the two main methods, Berendsen barostat and Andersen barostat are introduced here.

$$\dot{\vec{r}_i} = \frac{\vec{P_i}}{m_i}(1 - \frac{\beta}{\tau_P}(P_D - P(t))) \tag{2.8}$$

where τ_p is the relaxed time, β is the compression factor. Like the method of thermostat, When the instantaneous pressure $P(t)$ is greater than the target pressure P_D, the value in parentheses is greater than 1 and vice versa.

Another method is called Andersen barostat, which is similar to Nose Hoover thermostat. It sets additional kinetic and potential energy terms to relate the equations of motion to the moveable piston. However, the physical meaning of the coupling strength of the system to the environment is not clear enough in this method, so it isn't accurate enough in calculating the physical quantities of the process, such as the diffusion rate.

2.1.4 Ensembles

The statistical ensemble is a fundamental concept introduced when statistical methods are used to describe the statistical regularity of a thermodynamic system. The ensemble is not an actual object, but rather a formulation of statistical theory, and the system that constitutes the ensemble is the actual object. In EMD, the statistical ensembles commonly used in EMD research include Microcanonical ensemble (NVE), Canonical ensemble (NVT), and Isothermal-isobar ensemble, etc.

1) Microcanonical ensemble

   The atomic number N, volume V and energy E of the system remain constant. Also is called the NVE system. It is an isolated, conserved system. In general, precise initial conditions for the energy cannot be obtained, so the energy can only be adjusted by regulating the velocity and achieving the equilibrium of the system by iterative relaxation.

2) Canonical ensemble

   The number of atoms of the system N , the volume V , the temperature T remain constant and the total momentum remains constant. This is also called the NVT system. By keeping the temperature virtual heat bath and thus keeping the kinetic energy of the system fixed, the atomic velocity scale is achieved. This system is the best choice to measure the behavior of the system at constant temperature.

3) Isothermal-isobar ensemble

   This includes the isothermal isobaric (NPT) and isobaric isoenthalpic (NPH) systems. The system atomic number N , pressure P , and temperature T remain constant, also known as the NPT synthesis. Since the pressure and volume are conjugate, the volume of the system can be scaled for the purpose of pressure control. NPH is a system where the atomic number N, the pressure P, and the enthalpy $H = E + PV$ remain constant.

2.1.5 Boundary conditions

Boundary conditions are divided into the following three cases. The illustrations are shown in Fig.2.1

1) Periodic boundary conditions

   When the molecule moves beyond the i-directional edge outside the i-direction boundary, the molecule will be moved from the -i direction in the

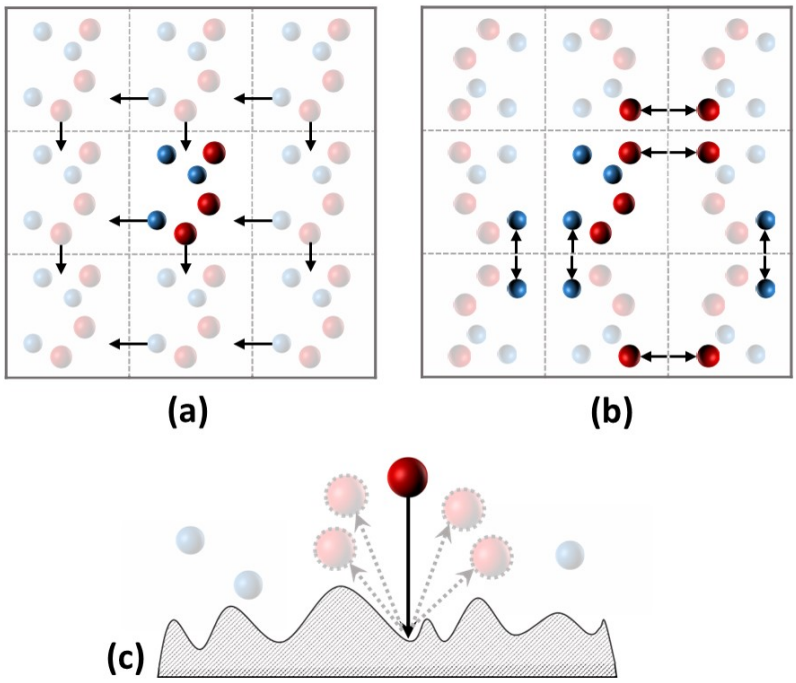

Figure 2.1: The schematic illustrations of the three boundary conditions: (a) periodic, (b) mirror, (c) diffusion reflection boundary condition.

current time. The length of the system in direction i is set as l_i, so as the displacement could be:

$$\vec{r}_i(t+\Delta t) = \vec{r}_i(t) \pm \vec{l}_i \tag{2.9}$$

2) Mirror boundary conditions

When the molecule moves beyond the i-direction boundary, the i-direction position coordinates of the molecule are reset by multiplying the adjustment factor a, and the i-direction velocity is reversed in the current time step.

$$\vec{r}_i(t+\Delta t) = a_{l_i}/2 \tag{2.10}$$

$$\dot{\vec{r}}_i(t+\Delta t) = -\dot{\vec{r}}_i(t) \tag{2.11}$$

3) Diffuse reflection boundary conditions When the molecule moves beyond the i-direction boundary, the i-direction position coordinate and velocity vector of the molecule are reset in the current time. The velocity components of the reflected particles are obtained from the Maxwell velocity distribution cor-

responding to the boundary temperature, chosen randomly, and the velocity direction is guaranteed to point inside the system. This boundary condition is usually used to simulate a constant temperature boundary with a wall. The boundary treatment takes into account the energy exchange. The molecules are considered to have the same temperature as the solid wall when they are emitted from the boundary back inside. However, this method does not arrange the actual solid atoms and does not consider the flow-solid potential.

2.1.6 Algorithms

Molecular dynamics simulations are based on the numerical integration of the equations of motion of hundreds or even thousands of molecules, taking advantage of the high speed and accuracy of modern computers. There are many different integration methods to integrate second-order ordinary differential equations. The following two most commonly used methods are described here.

2.1.6.1 Verlet algorith

This it the most widely used algorithms in molecular dynamics. The start of the algorithm follows the following steps:

1) Specify the initial position,
2) Specify the initial velocity,
3) Perturbing the initial position, $\vec{r}_i(\Delta t) = \vec{r}_i(0) - \vec{v}_i(0)\Delta t$
4) Calculate the force of the n^{th} step,
5) calculate the position of the $(n+1)^{th}$ step, $\vec{r}_i(t+\Delta t) = \vec{r}_i(t) - \vec{r}_i(t-\Delta t) + \vec{a}_i(t)\Delta t^2$
6) Calculate the velocity of the n^{th} step,
7) Repeat 4^{th} to 6^{th} steps.

The calculation of the particle position follows the Taylor expansion and the calculation of the acceleration follows Newton's second law.

$$\begin{aligned} \text{Position:} \quad \vec{r}_i(t+\Delta t) &= \vec{r}_i(t) + \vec{v}_i\Delta t + \frac{1}{2}\vec{a}_i(t)\Delta t^2 \\ \vec{r}_i(t-\Delta t) &= \vec{r}_i(t) - \vec{v}_i\Delta t + \frac{1}{2}\vec{a}_i(t)\Delta t^2 \end{aligned} \tag{2.12}$$

$$\text{Velocity :} \qquad \vec{v}_i(t) = \frac{\vec{r}_i(t+\Delta t) - \vec{r}_i(t-\Delta t)}{2\Delta t} \tag{2.13}$$

$$\text{Acceleration :} \qquad \vec{a}_i(t) = \frac{\vec{F}_i}{m_i} \tag{2.14}$$

The Advantages of verlet are only one force is calculated for each integration and time reversible. But the velocity calculated has a large error (Δt^2) according to Taylor expansion. Meanwhile, the trajectory is not related to the velocity and cannot be coupled with the heat bath.

2.1.6.2 Leap-frog algorithm

Leap-frog Algorithm firstly uses the acceleration at the current moment to calculate the velocity after half a time step, and then calculates the position at the next time step to infer the velocity at the current moment, shown as following. This operator takes an advantage of improved accuracy than verlet above, and it could be coupled with a heat bath because of the speed-dependent trajectory. Relatively, it takes more time and is less efficient.

1) Specify the initial position,
2) Specify the initial velocity,
3) Perturbing the initial position, $\vec{v}_i(\Delta t) = \vec{v}_i(0) - \vec{a}_i(0)\Delta t/2$
4) Calculate the force of the n^{th} step,
5) calculate the velocity of the $(n+\frac{1}{2})^{th}$ step, $\vec{v}_i(t+\frac{1}{2}\Delta t) = \vec{v}_i(t-\frac{1}{2}\Delta t) + \vec{a}_i(t)\Delta t$
6) calculate the position of the $(n+1)^{th}$ step, $\vec{r}_i(t+\Delta t) = \vec{r}_i(t) + \vec{v}_i(t+\frac{1}{2}\Delta t)\Delta t$
7) Calculate the velocity of the n^{th} step,
8) Repeat 4^{th} to 7^{th} steps.

2.1.7 Output of molecular dynamics

Using the above calculation methods, the position, velocity, and acceleration of the particles are calculated, and when the system reaches the specified moment, the molecular information is sampled and the specified macroscopic physical quantities are output according to the research needs.

The output data processed in LAMMPS is divided into three main sections:

1) Breakpoint data

   It uses mainly the commandes like 'restart','writerestart' to output in stages. In order to prevent accidents in the simulation process, such as a sudden power failure in the laboratory or machine room, errors in some phases of the program, the generated breakpoint data helps that the calculation can be continued from the intermediate process to improve efficiency.

2) The output of the thermodynamic quantities of the system, which are generally the collective behavior of the individual atoms in the system, such as temperature, pressure, etc. This kinds of output values are for the entire system, instead of a group, an atom. The main commands include 'thermo', 'thermo_style', etc. Other commands like 'fix ave/time','fix ave/spatial','compute reduce' could set the region of particles and frequency of data sampling, and the name of output files. The clever use of these commands can greatly improve output efficiency, reduce the pressure of post-processing data, and enrich the variety of output data.

3) The detailed information of each atom, such as trajectory of atom, using the command like 'dump','dump_modify'.

The above is only the most basic output of molecular dynamics software, on which I perform post-processing and complex operations to meet our needs for calculating more complex physical quantities.

2.2 Interatomic potential functions

A potential function is a mathematical function that represents the value of physical potentials. It gives the energy of a molecule as a function of its geometry. It describes generally the strength of interactions changing with the position of atoms. The accuracy of the interaction potential between molecules or atoms has a great influence on the accuracy of the calculation results, but the research on the interaction potential between atoms has been developing slowly, which has restricted the application of predictive dynamics in practical research to a certain extent.

There are three different classes of atomic potentials used in molecular dynamics simulations: pair potentials, many body potentials, and bond order potentials.

1) Pair Potentials

Many potentials such as Lennard-jones potential, Morse potentials are widely used in Molecular dynamics, with quicker computations. It performs feasibly the Coulomb's law in electromechanics, Newton's law in mechanics and so on. It is also the most common and typical choice for liquid and gas models. Pair potentials is a function which depicts the potenitial energy of two interacting particles. The total energy of a atom (e_i) is the sum of pair energies, f, as a function of distance, r_{ij}, between the atom (i) and all other atoms:

$$e_j = \sum_{j \neq i} f(r_{ij}) \tag{2.15}$$

The pair function f often decays quickly with disctance, and then the scope is limited by a cutoff radius for numerical efficiency.

2) Many-body Potentials

Many-body potential is more complicated and computationally expensive, but describes the physical properties of particles more accurately with higher fidelity than pair potential. It depicts three of more objects interacting with each others. Lots of simulations for metals and polymers choose to use many-body potentials, such as embedded-atom method (EAM) (Sheng *et al.* 2011), Environment-Dependent Interatomic Potential (EDIP) (Keblinski *et al.* 2002), Tersoff potential (Ohira *et al.* 1994), Moment Approximation (TBSMA) (Rousset *et al.* 1995) and so on. In the model of many-body potentials, except for pairwise interactions, global terms related to the surrounding atoms also occur through the particles. The total energy cannot be summed over the pair potential of atoms. It includes mostly a explicit combination of high order terms. An example of a many-body term for the total energy of atom e_i is shown as following:

$$e_j = \sum_{j \neq i} \sum_{i, j \neq k} f(r_{ij}, r_{ik}, r_{jk}) \tag{2.16}$$

3) Bond Order Potentials

Bond order potentials such as Tersoff potentials and Brenner potentials (Brenner *et al.* 1991), reflect not only the pair or many-body informations, but also several different bonding states of an atom, consequently to extend to describe the chemical reactions. The chemical bonds can depend on non-pair interactions like dihedral angles. Each bond order potential develops independently the strength of bonds. Different bonding environment including

the angle and length of bonds, the number of them are reflected in the body order potentials. The total energy of an atom e_i is based on a combination of pair or many-body term and a term of chemical bonds. From a simple case based on the concept of Linus Pauling (Abell 1985), the bond order potential for three atom interactions can be written as a simple pair potential with a modified term of bond order function b_{ijk}:

$$e_j = \sum_{j \neq i} f_{repulsive}(r_{ij}) + \sum_{i,j \neq k} b_{ijk} f_{attractive}(r_{ij}) \tag{2.17}$$

2.2.1 Lennard-Jones potential

Lennard-Jones potential (LJ) is a typical representative of continuous pair potential. It starts with the assumption that two particles at infinite distance from each other and don't interact. LJ consists mainly of the repulsion force proportional to the n-th power of the reciprocal distance of the atom and the force produced by the instantaneous dipole induced by the paired atom. Due to the computational expediency, LJ is usually represented by 12-6 Lennard-Jones model, given by the following equation:

$$U(z) = 4\varepsilon \left[\left(\frac{\sigma}{r} \right) - \left(\frac{\sigma}{r} \right)^6 \right] \tag{2.18}$$

where ε is well depth of energy between solid and liquid to explain the stronger attraction of two particles., σ is the distance parameter when the bonding potential is equal to 0. The potential energy and interaction force between molecules are shown in the Fig.2.2 (Kittel *et al.* 1996). When the particle are brought closer from infinitely long distance, they are attractive with each other. This attractive force makes them even further closer until they reach an equilibrium distance with their minimum bonding potential $U(z) = \varepsilon$ with $z = 2^{1/6}\sigma$. And then the distance continues to decrease, the particles overlap, the repulsive force acts and pushes them further apart.

Sikkenk, J. H (Sikkenk *et al.* 1987) found the wetting and drying behavior of solid surface by using Young's equation. All atoms are LJ atoms. Two kinds of molecules were simulated, including three layers of solid wall molecules and molecules constituting fluids. Fluid molecules are located between two solid walls at a certain simulated temperature, and the parameters of solid-liquid σ_{sl} and liquid-liquid σ_{ll} change. According to $\sigma_r = \sigma_{sl}/\sigma_{ll}$, three phenomena can be observed.

If the potential energy function of all atoms in a plane is integrated for fcc(111) plane, the following potential function can be obtained (Sun & Ebner 1992). σ_{sl}

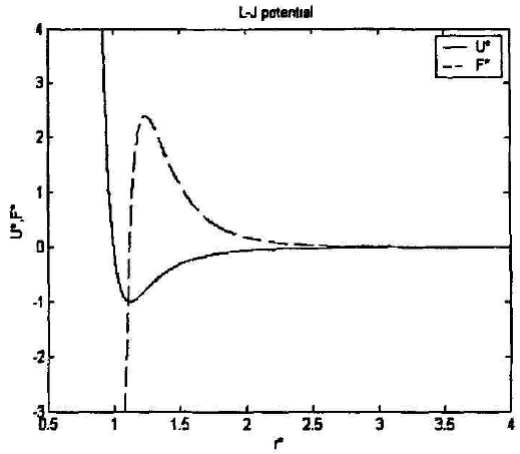

Figure 2.2: The potential energy and interaction force of LJ potential, where U is the interatomic potential, F is the interatomic force.

and ε_{sl} represent the atomic lattice parameters on the solid wall. z represents the vertical distance from liquid molecules to the solid wall. From the above formula, I can get the minimum of the potential function when $z = \sigma_{sl}$.

$$U_{min} = -\frac{4\sqrt{3}\pi}{5}(\frac{\sigma_{sl}}{\sigma_z})^2\varepsilon_{sl} \tag{2.19}$$

Assuming that the solid wall is infinite, the potential function of an arbitrary liquid atom is that of a solid wall atom. The integral in a semi-infinite space is expressed as

$$U(z) = \frac{2\sqrt{2}\pi}{45}\frac{\varepsilon_{sl}\sigma_{sl}^3}{\sigma_z^3}[2(\frac{\sigma_{sl}}{z})^9 - (\frac{\sigma_{sl}}{z})^3] \tag{2.20}$$

1) When $\sigma_r < 0.54$, the liquid layer is kept in the middle of the system, both sides are covered by gas molecules. In this case, there are two solid-gas and two liquid-gas interfaces. Solid walls are dry and not wetted.

2) When $0.54 < \sigma_r < 0.78$, the liquid is adsorbed to a solid surface and the other solid surface is dry and not wetted. In this case, the solid-liquid, liquid-vapor and solid-vapor interfaces have one each.

3) When $\sigma_r > 0.78$, both solid walls are covered with liquid.In this case, there are two solid-liquid and liquid-gas interfaces, and the solid surface is completely wetted.

In molecular dynamics simulation, except for LJ potential function, other forms of continuous pair potential function are also used, such as Born-Mayer-

Haggins (BMH) potential[9], Morse potential[10], Johnson potential[11]. In general, the LJ potential function is used to describe the interaction between inert gas molecules, as well as the interaction between chromium, tungsten and other body-centered cubic transition metals and molecules, mainly dispersive and repulsive materials. BMH potential is mainly used to characterize the atomic or intermolecular interaction potential of alkali metal halides and alkali earth metal halides. Morse potential and Johnson potential are often used to describe metallic solids.

2.2.2 Potential models for water

Water models have been maturely applied in the simulation of molecular dynamics. Models about liquid water, gaseous water, water clusters and aqueous solutions can better respond to the thermal dynamics, structural as well as mechanical dynamic properties of water under different conditions. These models are obtained through quantum mechanics, molecular mechanics, experimental results and have been revised and updated over the years. These models can be divided into three main categories: rigid water, flexible water and water subject to polarization. Based on this, it has been shown that as of 2002, as many as 46 molecular models of water have been established (Guillot 2002).

The process of constructing a model requires a trade-off between model complexity and the time scale and system size and complexity that can be simulated. A system containing large number of molecules (> 10,000 molecules) or taking long periods (above dozen nanoseconds) fits mostly into simple water models, while complex but more accurate models (e.g. ab initio methods) can only be used for relatively small systems (100-1000) and short simulation timescales (picosecond magnitude).

Classified by the number of sites, the water molecule model can be divided into 3 site (as TIP3P (Li *et al.* 2021), SPC (Hu & Jia 2021), SPC/E), 4-site (as TIP4P/2005 (Yagasaki *et al.* 2020), OPC3 (Xiong *et al.* 2020)), 5-site (as BNS(Pan *et al.* 2020b) TIP5P (Kasahara *et al.* 2020)) and 6-site (Nada 2016)water models. Parameters of some common water models are shown in Table.2.1, collected by Ref.(Brini *et al.* 2017).

Table 2.1: Parameters of Some Water Molecular Models. Note that iAMOEBA is a polarizable water model.

Model	SPC	SPC/E	TIP3P	iAMOEBA	TIP4P
Type	a	a	a	a	b
σ/Å	3.166	3.166	3.15061	3.6453	3.15365
$\varepsilon/J \cdot mol^{-1}$	0.65	0.65	0.6364	0.8235	0.648
l_1/Å	1	1	0.9572	0.9584	0.9572
l_1/Å	-	-	-	-	0.15
q_1/e_0	0.41	0.4238	0.417	0.29701	0.52
q_1/e_0	-0.82	0.8476	-0.834	-0.59402	-1.04
$/deg$	109.47	109.47	104.52	106.48	104.52
δ/deg	-	-	-	-	52.26
	TIP4P-Ew	TIP4P/2005	ST2	TIP5P	TIP5P-Ew
Type	b	b	c	c	c
σ/Å	3.16435	3.1589	3.1	3.12	3.097
$\varepsilon/J \cdot mol^{-1}$	0.680946	0.7749	0.31694	0.6694	0.7448
l_1/Å	0.9572	1	0.9572	0.9572	
l_1/Å	0.125	0.1546	0.8	0.7	0.7
q_1/e_0	0.52422	0.5564	0.24357	0.241	0.241
q_1/e_0	-1.04844	-1.1128	-0.24357	-0.241	-0.241
$/deg$	104.52	104.52	109.47	104.52	104.52
δ/deg	52.26	52.26	109.47	109.47	109.47

A water molecule consists of three atoms, so the main parameters of water models should be the mass of each atom, the power, the length of the hydrogen-oxygen bond and the bond angle of H-O-H. The rigid water models represents that all these parameters are fixed such as SPC, SPC/E, TIP3P, contrarily the ones of the flexible models could be alterable. These two models take the same the atomic mass and the electric charge. The only difference is that the H-O-H bond angle of TIP3P is smaller than the theoretical value of 109.47°, which is 104.52°. These two water models only have Van Der Waals coefficients for oxygen atoms, and zero for hydrogen atoms.

The above two models have corresponding improved models. The improved model of SPC is SPC/E. It makes the total energy of the solution system multiplied by 5.22 kJ/mol, which can make the SPC solution properties closer to the experimental value. The improvement of TIP3P in the CHARMM force field is to give the hydrogen atom a certain Van Der Waals coefficient (Ong & Liow 2019), so that the calculation of the results corresponds to the complex.

The real case of the water molecule's electric distribution is not exactly on the atom, such as the oxygen atom part of the negative electric energy on the

diagonal of H-O-H, and two electron pairs in the H-O chemical bond extension line. In order to obtain a more realistic model of the water molecule, models with more than four particles are applied to molecular dynamics simulations. Among them, the most famous one is the TIP4P model. This model has an extra point in the middle of the three atoms, on the diagonal of the H-O-H chemical bond, which contains no mass, only electric quantity. In many protein simulations, the combination of TIP4P and all-atom optimized potentials is used with good results (Jorgensen & Tirado-Rives 1988).

2.2.3 Interatomic potential functions for silicon and silicon/Water

The crystal silicon has a directional character of covalent bonds which is highly dependant on the atomic environment. To describe simply the pair potential of silicon atoms, PN Keating (Keating 1966) built an interatomic potential with elasticity consideration on the bonds in 1966. In 1986, Stillinger and Weber(Fang & Pilon 2011; Stillinger & Weber 1985) proposed another potential taking the two-body and three-body into contributions for solid and liquid silicon model. With this potential, the total energy E includes two-body and three-body interactions:

$$E = \sum_{i<j} \varepsilon \psi_2(r_{ij}) + \sum_{i\neq j, j<k} \varepsilon \psi_3(r_{ij}, r_{ik}, \theta_{ijk}) \tag{2.21}$$

$$\tag{2.22}$$

where Ψ are the function of two- and three-body:

$$\psi_2(r_{ij}) = A[B(\frac{\sigma}{r_{ij}})^p - (\frac{\sigma}{r_{ij}})^q]exp(\frac{1}{r_{ij}/\sigma - a}) \tag{2.23}$$

$$\psi_3(r_{ij}, r_{ik}, \theta_{ijk}) = \lambda(cos(\theta_{ijk}) + \frac{1}{3})^2 exp(\frac{\gamma}{r_{ij}/\sigma - a})exp(\frac{\gamma}{r_{ik}/\sigma - a}) \tag{2.24}$$

Using this potential, the thermal conductivities of bulk silicon, at room temperature, have been successfully retrieved (Schelling *et al.* 2002).

Moreover, an effective improvement of this potential was developed by L. Pizzagalli in 2012 (Pizzagalli *et al.* 2013). It retained the original feature like elasticity and point defects of SW potential, while improved the modeling behavior in the case of dislocation, amorphous structure and threshold displace energy, etc. The comparable parameter of the original and improved (called SW_{im} here) SW potential are shown in the table 2.2, accompanying with the parameters of an-

other alternative potential presented by Vink and co-worker (called VBWM here) (Vink *et al.* 2001).

The interactions between silicon-oxygen and silicon-hydrogen are modeled using a L-J potential, which is sufficient and physically meaningful for many relevant applications (Sachdeva 2009; Lennard-Jones 1924). The interactions between hydrogen and silicon atoms are neglected. More detailed interatomic parameters are displayed in Table 2.2. Considering the contact angle 87.5°of water droplet on the silicon surface (Isaiev *et al.* 2016), the LJ value for Si-O are chosen as: $\varepsilon_{Si-O} = 15.75$ meV and $\sigma_{Si-O} = 2.6305$ Å. The cut-off distance beyond which the interatomic potential vanishes has been chosen to be 2.5 σ.

2.3 Methodologies to study thermal conductivities

LAMMPS provides at least four methods that can be used to measure the thermal conductivity of a material. For a simple Lennard-Jones fluid model, the KAPPA catalogue is consulted and four methods are discussed here.

The heat conduction tensor *kappa* is a measure of the propensity of a material to transfer heat energy in a diffuse manner given by Fourier's law

$$J = -k\nabla(T) \tag{2.25}$$

where J is the heat flux per unit energy unit per time zone, and $\nabla(T)$ is the spatial gradient of temperature. Therefore, thermal conductivity has an energy unit per distance per degree K, and is generally approximated as an isotropic quantity, as a scalar quantity.

Firstly, two methods for calculating thermal conductivity using NEMD are presented. The first method is to set two constant temperature zones at two sides of the simulation box, as shown in Fig.2.3(a). By keeping the two zones at different temperatures through thermostatic fixation, the energy added to the hot region should be equal to the energy subtracted from the cold region and the difference is proportional to the heat flux moving between the two zones. For details on this idea, see the papers by K. Konashi (Konashi *et al.* 2003) and Hafskjold (Hafskjold *et al.* 1993) and Wirnsberger et al (Wirnsberger *et al.* 2015). One notes that several thermostat commands (such as 'fix nvt', 'fix langevin', and 'fix temp/rescale') help to store the accumulated energy added or subtracted.

In a second method, shown in Fig.2.3(b), a fixed heating or fixed flux command can be used instead of the thermostat on each of the two regions. Subsequently, the specified amount of energy is added/subtracted to or from the two regions.

Table 2.2: Interatomic potential parameters of Stillinger-Weber(SW), SW_{im}, VBWN potentials, and Lennard-Jones(LJ) (Horn *et al.* 2004) used in the molecular dynamics simulation

	ε(eV)	σ (Å)	a	λ	γ	A	B	p	q
SW	2.1683	2.0951	1.80	21.0	1.20	7.0496	0.6022	4.0	0.0
SW_{im}	1.04190	2.128117	1.80	31.0	1.10	19	0.65	3.5	0.5
VBWM	1.64833	2.0951	1.80	31.0	1.20	7.0496	0.6022	4.0	0.5

	ε_{ij}(kcal/mol)	σ_{ij}(Å)	$q_{ii}(e)$	d_{ij}(Å)	$\theta_{iji}(^\circ)$
O-H	0	0		1.0	109.47
O-O	0.1553	3.166	-0.8476		
H-H	0	0	0.4238		
O-Si	0.3632	2.6305	0		

Similarly with the previous one, a temperature gradient is imposed inside. In both cases, it can use the calculate 'temperature/area' command to monitor the final temperature of the two regions, and use 'fix ave/chunk' and 'ke/atom' to monitor the temperature value of the middle region.

The third method is to use the fixed 'thermal/conductivity' command to perform a reverse unbalanced MD simulation, which implements Muller-Plathe's model using the Reverse Non Equilibrium Molecular Dynamics algorithm (rNEMD). In the Fig.2.3(c), It allows to exchange kinetic energy between atoms through multiple layers in two different temperature layers of the simulation box. This will create a temperature gradient between the two layers. This correction is consistent with the cumulative energy transfer that it performs. More details can be seen in the manual page of 'fix thermal/conductivity' command in LAMMPS.

The fourth method is based on the Green-Kubo (GK) formula, which relates to the heat flux to the overall average of the autocorrelation of kappa. A general configuration is shown in Fig.2.3(d). The heat flux can be calculated by the fluctuation of the per-atom potential and kinetic energy and per-atom stress tensor in the steady-state equilibrium simulation. This is in contrast to the previous two non-equilibrium methods, in which energy flows continuously between thermostats. This equilibrium method (EMD) needs a long time to equilibrium in order to get a homogeneous value in three directions. That's also what I use mainly in the study.

In the following section, details about these simulation methods are expanded. Based on them, a more efficient simulation method AEMD is also suggested in Sec.2.3.3.

2.3.1 EMD

The thermal conductivity is then computed using the Green-Kubo (Che *et al.* 2000; Baroni *et al.* 2020) formula:

$$k = \frac{1}{3k_B V T^2} \int_0^\infty \langle J(0)J(t)\rangle \, dt \tag{2.26}$$

where J denotes the heat flux vector.

$$\begin{aligned} J &= -k\nabla(T) \\ J(t) &= \sum_{i=1}^{N} \sum_{j=1, j\neq i}^{N} [\frac{1}{2} r_{ij} \cdot (F_{ij} \cdot v_i) \\ &+ \frac{1}{6} \sum_{k=1, k\neq i,j} (r_{ij} + r_{jk}) \times (F_{ijk} \cdot v_i)] \end{aligned} \tag{2.27}$$

V is the volume of the particle, T is the equilibrium temperature, k_B is the Boltzmann constant, r_{ij} is given by $r_{ij} = |r_i - r_j|$. F_{ij} and F_{ijk} are the two and three-body forces, respectively. For an homogeneous system, the thermal conductivity is reduced to:

$$k = \frac{1}{k_B V T^2} \int_0^\infty \langle J_x(0)J_x(t)\rangle \, dt \tag{2.28}$$

averaged over all the three components (k_x, k_y, k_z).

Using EMD simulations, a long run is necessary to obtain a convergence of the thermal conductivity. Though usually the thermal conductivity fluctuates in a small range after about 50 ns, a longer equilibrium period (NVE run) for 70 ns is applied in my study, to avoid a high dispersion of the results. After convergence, the final value of thermal conductivity can be obtained.

2.3.2 NEMD

Non-equilibrium molecular dynamics is also a very effective method for calculating the thermal conductivity of a material. Even when the system is in quasi-equilibrium, it can calculate the gradient of the change in physical quantities and consequently the thermal conductivity of the material.

Depending on the boundary conditions, there are two method setups proposed for NEMD, one is the period boundary, the other is fixed sides. In this study, I adopted the second one that the both sides are fixed adjoined with two thermostats. According to the definition of thermal conductivity in Eq.2.27, thermal conductivity is related to heat flow and temperature gradient. The system heat flux J is

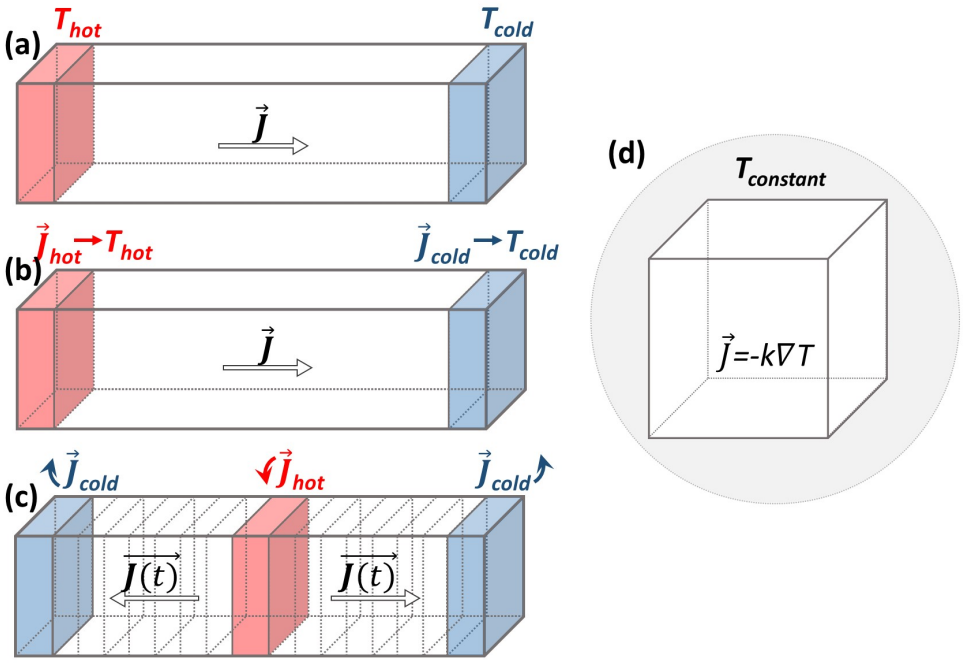

Figure 2.3: The configuration of different methods to calculate the thermal conductivity. The temperature directly are set in the hot and cold sink in the (a). By fixing (a) the temperature or (b) the heat flux, a temperature gradient are give using NEMD. (c)The reverse NEMD proposed by the Muller-Plathe model. (d) EMD

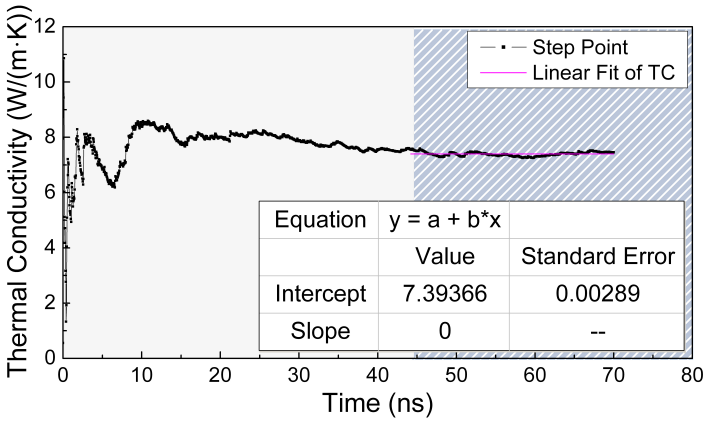

Figure 2.4: Time evolution of the thermal conductivity data profile of nanohybrid water-nanoporous silicon system at 300 K. The duration of EMD simulation is 70 ns. Each TC in this paper is calculated using the linear fit during the final equilibrium stage of 20 ns.

generated internally by the different thermostats ∇T on both sides. The heat flow can be calculated by the amount of energy transfer through the system section per unit time as:

$$J = \frac{\Delta\varepsilon}{A\Delta t} \tag{2.29}$$

where the A is the surface of cross section affected by the heat flux, $\Delta\varepsilon/\Delta t$ is the transfer energy rate added or subtracted from the both sides. Since the model simulated in this study contains pores, non-homogeneous material and the temperature gradient vary unevenly in different regions, the temperature gradient is approximated as $\nabla T = \Delta T/L$. Here, L is the length of main part of system. From the above formulas, the thermal conductivity λ is driven to be:

$$\lambda = \frac{\Delta\varepsilon}{\Delta t}\frac{L}{A\Delta T} \tag{2.30}$$

In this work, the whole system is divided into 200 bins along the longitudinal direction. After reaching the equilibrium state, the energy transfer is obtained by fitting linearly the energy change of each slab.

Except for the thermal conductivity calculations, NEMD is also used as one of the effective means to calculate the interface thermal resistance. When the heat flows through the solid/liquid interface, because of the interface at the solid lattice interruption, the hot carrier (phonon, electron) instantaneously changes in propagation. It does not allow all carriers to pass through the interface, called also the interface defects. At the same time, two temperature differences are formed on both sides of the interface. Especially in the temperature gradient curve, the temperature changes abruptly. At this point, the interface thermal resistance can be calculated by the ratio of the interface temperature difference and heat flow density.

2.3.3 AEMD

With an insight into the EMD and NEMD approach, their shortcomings are clearly being exposed. First of all, to achieve a sufficient converged value of thermal conductivity for EMD simulations, several millions of the simulation timesteps are required. Meanwhile, for NEMD simulation, it takes also a long time to reach a stable condition after imposing the initial temperature gradient or heat flux. Both methods require long computational times and indeed limit their applications on the large atomic systems or the complicated nanostructure. From this aspect, an Approach-to-Equilibrium Molecular Dynamics (AEMD) came out for the purpose of reducing the computational cost and accelerating the progress. AEMD describes

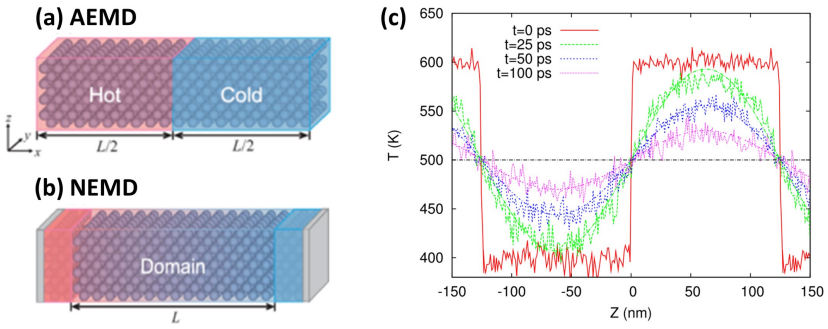

Figure 2.5: (a) and (b) The simulation diagrams of AEMD and NEMD, respectively (Sheng *et al.* 2022). The system for AEMD is divided into two parts with each size of $L/2$. (c) The time evolution of temperature profiles (0, 25, 50, 100 ps) for the bulk crystalline silicon system with the half length of 125 nm, including the direct MD calculation with noisy color lines and smooth lines fitted to the equation (Palla *et al.* 2019).

helpfully the transport phenomena and extracts thermal properties from different thermal transport systems in a much efficient way. This approach is usually applied in a large system and has been already used to investigate the thermal conductivity of various bulk materials (Lampin *et al.* 2013; Melis *et al.* 2014). The simulation diagram of AEMD compared with the NEMD are shown in Fig.2.5(a) and (b) (Sheng *et al.* 2022). It is obvious to see that two different temperatures in AEMD simulation are set on two regions in contact, rather than on the two separated outer sides in NEMD. Furthermore, unlike the continuous non-equilibrium in NEMD, the AEMD is initially established a transient thermal conduction regime by imposing a temperature different in the left and right regions at the beginning of the simulations. And then the system could reach quickly the equilibrium state during NVE run in just a few tens or hundreds of ps. Fig.2.5(c) is helpful to describe visually the time evolution of the temperature difference (Palla *et al.* 2019). In this example, the temperature profile turns into a smooth sinusoidal curve in the left and right homogeneous regions during 100 ps, instead of the initial step-like profile, which is much faster than EMD simulations. Moreover, the authors Claudio Melis et al. have also estimated the lattice thermal conductivity dependence of the crystalline and amorphous silicon on the sample cross section, initial temperature settings and the sample length. It gives the beneficial evidence of the theoretical robustness and numerical accuracy.

Due to the original ballistic phonon transport in AEMD, the thermal conductivity is mostly contributed by the phonons with short mean free paths. In the AEMD simulation, less phonon with long MFP contributes to thermal conductivity, com-

pared to NEMD simulations with the same size(Sheng *et al.* 2022). When the heat carrier MFP are larger than the simulation cell, the size effect need to be taken into account. Hayat Zaoui et al.(Zaoui *et al.* 2016) found a strong length dependence of thermal conductivity in the AEMD simulations, deriving from an origin the cut-off on the maximum of MFP. In the study of Thuy-Quynh Duong and co-workers (Duong *et al.* 2019), the length dependence is effectively considered in the thermal conductivity calculation of $GeTe_4$. By differ the size of the computational cell, the propagation of heat carriers is at least up to a distance of 6 nm.

2.4 Mechanisms and physical properties studied in this work

2.4.1 Definition of stratified water layers near solid/liquid interface

In order to output the specified parameters, the pore region is divided into 100 spatial spherical bins with a thickness of 0.2172 Å from the center to the edge. The property of the interface is characterized correctly with the help of these small bins, especially the fluctuations. The density and the pressure inside of each bin are calculated and averaged. As shown in Fig.2.6, the density profile of water nanoporous silicon system at 300 K is plotted as a function of distance from the pore center, averaged every 20 ns. According to the density profile, I separated the nanoconfined water into two regions: the core and the shell. The core contains all the water molecules within a distance of 9 Å from the center of the pore. The edge of the core is determined as 9 Å, where the middle value of the second maximum and minimum value is found. The shell corresponds to the region from the edge of the core to the edge of pore 14.48 Å in Fig. 2.6, where the strong fluctuations of the density and two obvious maxima value are observed close to the solid surface. The structural and dynamical properties of water are compared between these two regions.

The density and pressure profiles are calculated from 100 spherical bins with the size of 0.2172 Å. The pressure value is calculated by summing the stress tensor for all atoms in the specific region and divided by the corresponding volume, using the command "compute stress/atom" in LAMMPS. Here, the pressure profile is consist of the values of each bin.

2.4.2 Radial distribution function

The radial distribution functions (RDF) describes the probability of the distribution of particles in space, and then the study of the ordering of matter, and can

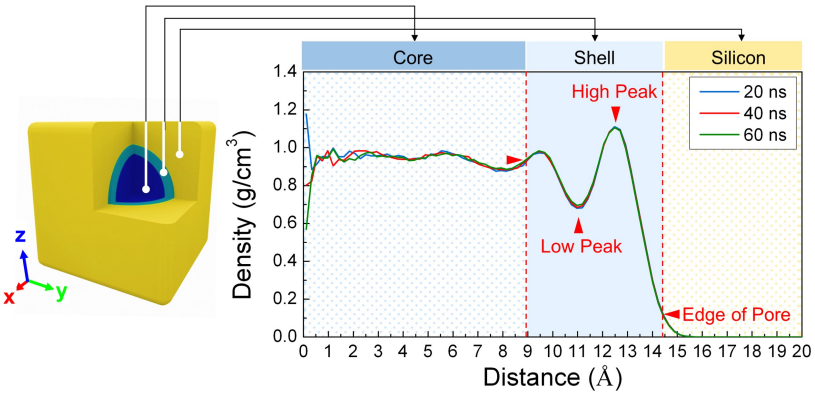

Figure 2.6: Density profiles of water nanoporous silicon system at 300 K, averaged every 20 ns. The core and shell region of the nanoconfined water are defined and marked in the figure.

also be used to describe the correlation of electrons. RDF can be understood as the ratio $g(r)$ of the local density of a molecule ρ_0 with respect to the bulk density ρ_s at a distance r around a central molecule, expressed by the following formula:

$$g(r) = \frac{\rho_0(r)}{\rho_s(r)} = \frac{n_0(r)}{4\pi r^2 r} \times \frac{1}{V/N} \tag{2.31}$$

N and V are the total number of silicon atoms in the pore and volume of the pore, respectively. The number of particles contained at dr is calculated by the above equation, and then normalized by the average density of the system (the average number of particles contained in this volume), which gives $g(r)$.

In general, when the particle is far enough from the central particle, the local density of the particle should be equal to the average density of the overall system, thus $g(r)_\infty = 1$. However, in the study of the confined system, due to the limited size of the system, there are no more particles at a certain distance from the central particle. By calculating the normalization, $g(r)$ decreases gradually for larger r until it becomes 0. Therefore, in this paper, a finite distance is intercepted and normalized again. Only the relative difference is compared in different cases, rather than the absolute value of $g(r)$.

Another parameter derived from RDF can likewise express the local characteristics of the particle distribution, called the coordination number N. It computes the number of atoms around the central atom of compound. The expression is introduced as:

$$N = 4\pi\rho \int_0^r r^2 g(r) dr \tag{2.32}$$

from this expression, it is seen that the coordination number can also be computed by the integration of RDF profile.

In this paper, I focus on the RDF of water molecules. I studied the RDF for only oxygen atoms, and only hydrogen atoms separately, finding that their RDF all remain consistent. Therefore, all the RDF studies in this paper are based on the oxygen atoms of water molecules, which is also called partial RDF. It is worth mentioning that, the RDF in this work is studied for water molecules in different regions under the same system, such as the core and shell of the pore. In order to ensure the rationality of the study, the referenced atom is chosen in the specified region when calculating the RDF, and the other atoms surrounded by this atom are chosen from all water molecules in the pore.

Usually there are many post-processing software such as VMD, OVITO, Material Studio, which can calculate the RDF from the particle information output by Lammps. However, due to the special region choice in my system, the calculations of RDF studies are completed through the code.

2.4.3 Mean square displacement and diffusion coefficient

Known from the kinetic energy expression, the thermal conductivity is related to the velocity of atoms. Therefore, the dynamical properties of nanoconfined water are investigated.

The diffusion coefficient is calculated from the Mean Square Displacement (MSD) of the atoms using the Einstein relation (Allen 1987):

$$D = \lim_{t\to\infty} \frac{1}{6t} \langle |r(t) - r(0)|^2 \rangle \tag{2.33}$$

Where r is the position of the atom of a water molecule at time t and D is the diffusion coefficient. The orientation of the water molecules is measured by computing the angle, θ, which is between the radial direction of the oxygen atom (determined from the oxygen atom and pore center coordinates) and the angle bisector of the water molecule.

2.4.4 Hydrogen bond networks

Other structural and topological analysis methods are implemented in the *ChemNetworks* software package (Ozkanlar & Clark 2014). Hydrogen bond networks can be observed as sub-structures in water (Ozkanlar & Clark 2014). The number of Hydrogen bonds and the geodesic length of the network can be com-

puted to further characterize the nano-confined water. As suggested by Ozkanlar et al. (Ozkanlar & Clark 2014), a H-bond is defined by the distance of H and O atoms from two different molecules within a distance of 2.5 Å and a O-H-O angle ψ between 145°and 185°, as shown in Fig.2.7. The cutoff distance is chosen at 10 Å. The geodesics (gd) is the shortest continuous path formed connecting any two water molecules, which indicates that the extent of localisation of network of any water.

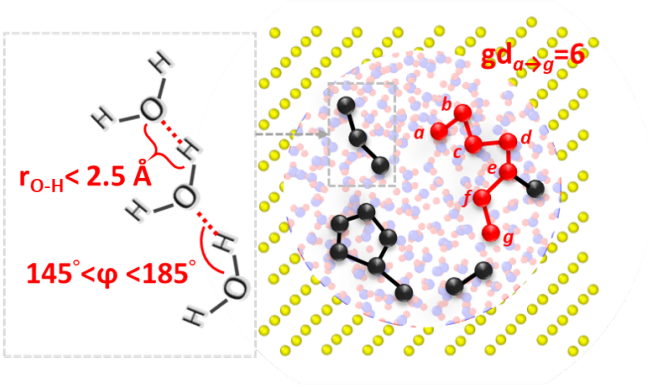

Figure 2.7: The left figure shows the definition of the intermolecular hydrogen bonds for water and the right one is the illustrations of geodesic length between any two water molecules.

2.4.5 Density of states

The aim of the vibrational density of states (VDOS) study is to identify possible heat flow channels through the dense water layer close to the solid surface, which might explain the enhanced thermal conductivity of the hybrid nanosystem. Because it is more intuitive, it is more widely used in the discussion of phonon density.

It is obtained via the Fourier transform of the velocity autocorrelation function (VACF) (Owens & Daniels 2013). The system is thermalized at 300 K for 500 ps with Nosé-Hoover thermostat. An average for temporal VACF over the initial time and all the particles in specified group is extracted every 0.01 ps. The Fourier transform is applied to VACF to obtain DOS as following Eq.2.34. After that, the results are smoothed by Savitzky-Golay filter (Press & Teukolsky 1990). This statistical method provides a better performance for long-time simulation of large systems (Desmarchelier *et al.* 2020).

$$DOS(\omega) = \int \frac{\langle \sum_i \vartheta_i(t_0) \cdot \vartheta_i(t_0+t) \rangle}{\langle \sum_i \vartheta_i(t_0) \cdot \vartheta_i(t_0) \rangle} e^{-2\pi i \omega t} \tag{2.34}$$

where t_0 is the different starting time, t is the correlation time.

CHAPTER 3

Temperature Dependence of Thermal Conductivity of Nanoporous Crystalline Silicon via EMD

Contents

This chapter focuses on the effect of the temperature on the thermal conductivity of the hybrid solid-liquid nanocomposites based on the silicon crystalline nanoporous matrix. Using Molecular Dynamics simulations, the role of the temperature T (from 285 to 360 K) on the thermal conductivity enhancement of nanohybrid porous silicon and water system is investigated. By studying the mean square displacement, radial distribution functions, density of states and so on, several structural and dynamical phenomena are discussed to give physical point of views of the TC results. Note that molecular Dynamics (MD) simulations are conducted

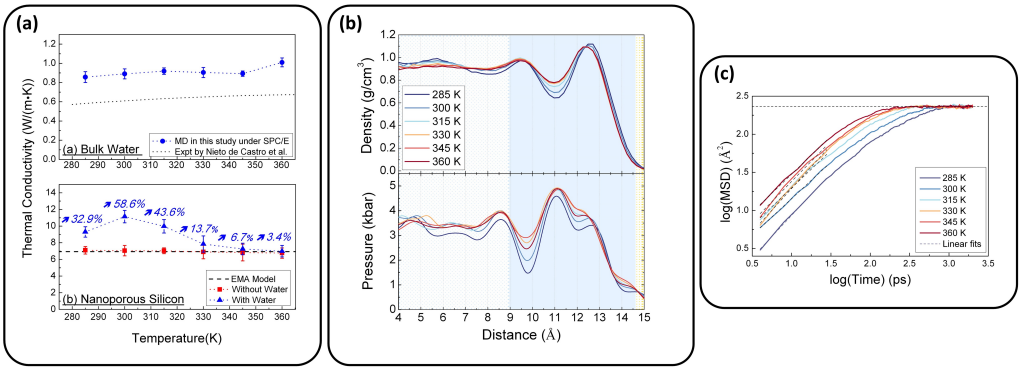

Visual Abstract: (a) the thermal conductivity of nanoporous materials, (b) the density and pressure profiles and (c) mean square displacement of the water molecules confined in nanoporous materials.

using the open source code LAMMPS (Large-scale Atomic/ Molecular Massively Parallel Simulator) (Plimpton 1995b). The effective thermal conductivity is computed using Equilibrium Molecular Dynamics (EMD) methodology.

3.1 Simulation details

The configuration is determined firstly. Then the system is built by defining the force field, the environmental factor, the boundary conditions, etc. In the following subsections, the details about the simulation methods are provided.

3.1.1 Determination of the configuration

The bulk system, the most simplest cubic system, is regard as the basic model for study. According to the lattice constant of silicon $a_0 = 5.43$ Å, I generated firstly the bulk crystalline silicon system with dimensions of $8a_0 \times 8a_0 \times 8a_0$ ($a_0 =$ 5.43 Å), which corresponds to a cubic sample of 43.4 Å size length. And then, a sphere of atoms within a radius of 14.48 Å is extracted from the simulation box center to finally catch a porosity of 15.51%. The dry nanoporous crystalline silicon system is obtained. For immersing the water molecules, a spherical volume of water with the same radius size of the pore is considered. The water molecules are set to be 'crystalline-like' with a lattice constant of a_0^w. In the study of temperature

dependence, the a_0^w is equal to 3.1 Å to obtain the desired density of water of 1 g.cm^{-3}.

From this configuration, the porosity is introduced by removing a sphere of atoms from the center. Some authors (Mirmohammadi *et al.* 2018; Van Norren *et al.* 2009) observed that above a porosity of 15%, the measurement of thermal conductivity exhibits large fluctuations which is not the case at low porosity level. This is attributed to the dominating role of boundary effect over phonon scattering.

In this chapter, the temperature dependence of thermal conductivity in the ranger from 285 K to 360 K is investigated, in which range the bulk water molecules stay in the liquid state. The target temperatures for equilibrium T_{eq} are set to six values of 285, 300, 315, 330, 345 and 360 K. For each set of parameters, at least six parallel simulations with different initial velocities, which is adjusted by the random number of seeds in LAMMPS, have been performed to decrease the uncertainty of the results.

Fig.3.1 summarizes the simulated configurations. Fig.3.1 (a) shows the dimensions of the dry nanoporous crystalline silicon from the front of view. In Fig.3.1(b) and (c), the crystalline water is initially introduced inside of the nanoporous silicon. Then after equilibrium shown in Fig.3.1(d), it is observed that the water molecules aggregate in groups within the confinement of the pore, and keep rotating inside the pore. The water molecules gather inhomogeneously inside the pore, instead of spreading evenly. These snapshots are produced using the post-processing visualization software OVITO (Stukowski 2009).

3.1.2 System equilibrium and characterization

All the configurations studied here are simulated under periodic boundary conditions. First of all, the velocity of each atom is initialized using a Maxwell- Boltzmann distribution set by different random number of seeds. Then, the system is relaxed in the NVT ensemble for at 10 K, and at the temperature T_{eq} for 200 ps for each temperature. Verdier et al. (Verdier *et al.* 2016) successfully obtained relaxed nanoporous crystalline silicon following this method. Finally, a NVE run is imposed during 70 ns for producing the equilibrium run to compute the thermal conductivity using EMD method (introduced in Sec.2.3.1). The thermal conductivity of nanoporous silicon system with the confined water evolved by the time at 300 K is shown in Fig.2.4.

The TC data displays a strong fluctuation at the beginning of the simulation becaused of NVT ensemble application. At about 45 ns, the system tends to the

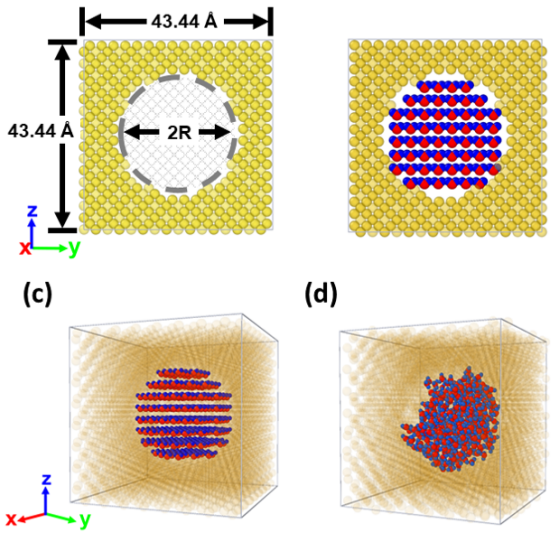

Figure 3.1: The simulation models with the dimensions of the unit cell $8a_0 \times 8a_0 \times 8a_0$: (a) Cross-section at the middle of the simulation cell of the dry nanoporous silicon system with the specific sizes; (b) and (c) initial configuration of the nanohybrid system (water and silicon) with crystalline water filling the porous; (d) nanohybrid system after equilibrium.

equilibrium state and the data starts to converge. The data after this moment shown in the blue shade part in the figure, is fitted to a constant value to represent the final value of thermal conductivity.

3.2 Results

3.2.1 Temperature vs Thermal conductivity

The thermal conductivities of (a) crystalline silicon, (b) bulk water and (c) dry and wet nanoporous silicon system are depicted in Fig.3.2 within the temperature range: 280 to 360 K. For comparison, the effective medial approach (EMA) is also introduced in the figure to estimate the thermal conductivity. Several repetitions for each temperature provide the results much good statistics and acceptable uncertainty of less than 2%. The general calculation for the mixture thermal conductivity. For comparison, the thermal conductivity with EMA model has been estimated with the Eq.3.1. In addition, the thermal conductivities of bulk water calculated here and taken from experimental data (Nieto de Castro *et al.* 1986) are plotted for the same temperature range in Fig.3.2.

First of all, for silicon, the recommended curves from reference in the tem-

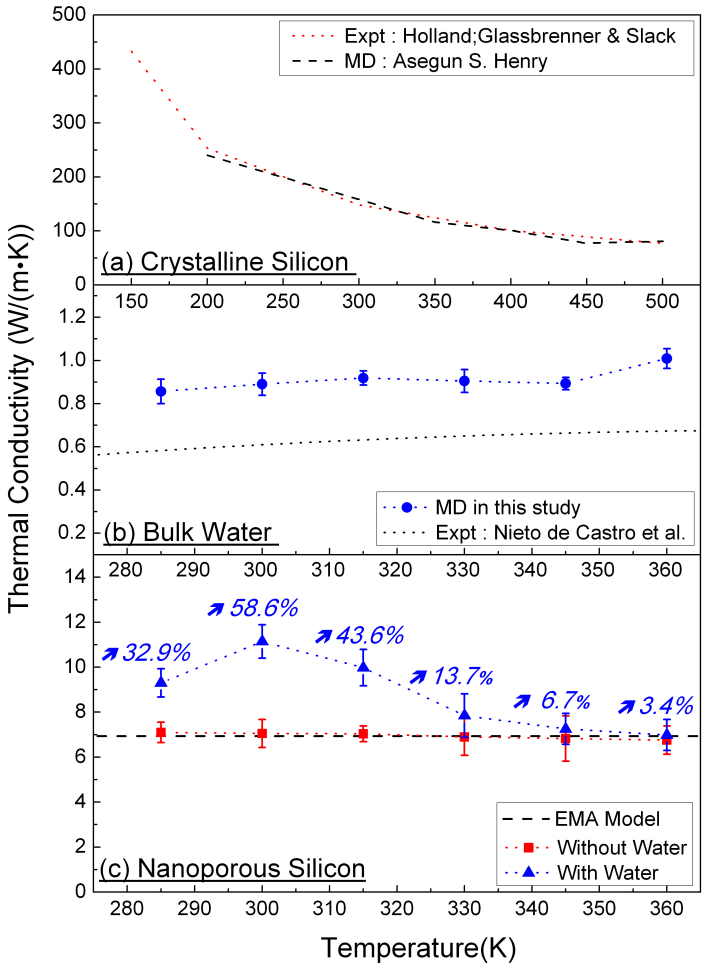

Figure 3.2: Thermal Conductivity of (a) crystalline silicon, (b) bulk water and (c) dry and wet nanoporous silicon with porosity of 15.51 % as a function of the temperature.

perature range 150-500 K are plotted with dotted line in the upper panel. Both in the experiment and MD simulations, the thermal conductivities of bulk silicon show the negative dependence on the temperature (Glassbrenner & Slack 1964; Henry & Chen 2008). It varies from 148 W/(m·K) at 300K to 99 W/(m·K) at 400K according to 1/T law (Callaway 1959). To present, studies on the thermal conductivity of monolithic silicon have been well established. From 1960s, many authors have conducted experiments and proposed analytical models to explore the variations of thermal conductivity of bulk silicon as a function of temperature. At low temperature region below 30 K, bulk silicon increases with the temperature augment, until reaches a maximum value of 5500 W/(m·K) at 30 K (Asheghi *et al.* 1998; Touloukian 1970). Above 30 K the thermal conductivity of bulk Si decays gradually with raising temperature (Kazan *et al.* 2010).

For the bulk water, from the middle panel, the thermal conductivities under SPC/E model are calculated, and took experimental data from Ref.(Nieto de Castro *et al.* 1986). Both of them display an increasing trend with the temperature augment. The result here illustrates a general trend of thermal conductivity of water at low temperature range. This dependence on the temperature is a common behavior for liquid systems, which could easily be found in other liquids such as oil (Keblinski *et al.* 2005), ethylene glycol or methanol (Guevara-Carrion *et al.* 2008). Note that at approximately greater than 600 K, the TC of water shows a opposite trend (Römer *et al.* 2012)), that a decline of TC with higher temperature. The thermal conductivity simulated in this study under the SPC/E model is 0.87 ± 0.051 W/(m·K), 20% higher than the experimental value of about 0.61 W/(m·K) at the room temperature (298 K) (Nieto de Castro *et al.* 1986; Abdulagatov & Azizov 2005; Huber *et al.* 2012). The comparable values from previous reports are shown in Table 3.1. For example, the thermal conductivity of the bulk water simulated in this study under the SPC/E model is 0.87 ± 0.051 W/(m·K) at 300 K, while the experimental value is about 0.61 W/(m·K) at the room temperature (298 K) (Nieto de Castro *et al.* 1986; Abdulagatov & Azizov 2005; Huber *et al.* 2012). It proves that our results have a good agreement with previous reported values under the same model (Zhao *et al.* 2020).

Then, I focus on the thermal conductivity of solid liquid hybrid system in the Fig.3.2(c). Firstly concerning the result for the dry nanoporous silicon, the thermal conductivity for each temperature is about 7 W/(m·K), an order of magnitude smaller than the one of bulk crystalline without the pore. The pore addition has a strong effect on the bulk silicon. In nanoporous systems, the boundary scattering is

the predominant scattering event being responsible for the reduction of the thermal conductivity (Ong & Pop 2010) compared to the bulk value. The thermal conductivity of dry nanoporous silicon is strongly related to the phonon scattering at the pores surfaces. In addition, the result almost stays constant on the average value of 6.9 ± 0.11 W/(m·K) for different temperature, meaning that the TC for dry sample is independent on the temperature.

For the wet nanoporous silicon system, MD simulations are used. It is found that an increase with temperature from 285 K reaching a maximum at 300 K, then a decline from 300 K reaching the same value as the dry system for temperatures greater than 345 K. A well known method to calculate the effective thermal conductivity of porous matrix with inclusions is developed, called the 'Effective Medium Approach' (EMA). It permits to evaluate easily and fast the thermal property of 3D porous media, taking into account the porosity and interfacial thermal resistance . It performs as a excellent reliable approach on the macroscopic (Hui *et al.* 1999). It helps us to understand the inherent factors affecting the thermal conductivity of solid liquid hybrid system. Ref (Nan *et al.* 1997) provides a general expression of EMA. Based on the silicon solid matrix and the confined liquid water, the expression of k_{eff}^{EMA} is deduced as follows:

$$k_{eff}^{EMA} = k_{Si}^{m} \frac{k_{H_2O}^{b}(1+2\alpha) + 2k_{Si}^{m} + 2f_v[k_{H_2O}^{b}(1-\alpha) - k_{Si}^{m}]}{k_{H_2O}^{b}(1+2\alpha) + 2k_{Si}^{m} - f_v[k_{H_2O}^{b}(1-\alpha) - k_{Si}^{m}]} \tag{3.1}$$

where k_{Si}^{m} and $k_{H_2O}^{b}$ represent the bulk TC of crystalline Si matrix and bulk water, f_v is the porosity of system, while α is a dimensionless parameter defined as:

$$\alpha = R_K^{Si/H_2O} k_{Si}^{m} / r \tag{3.2}$$

here the r is the radius of nanoinclusion and R_K^{Si/H_2O} is the Interface Thermal Resistance (ITR) (or Kapitza resistance) between silicon and water. From this expression, it is easily known that the most important parameters for TC is the TC of silicon matrix and water, and the ITR between them. In general, the TC of bulk silicon is taken as about 150 W/(m·K) at ambient temperature (Fang *et al.* 2006). But in this framework, the pore present in the silicon matrix are so small enough to achieve the nanoscale. It induces that the mean free path of bulk crystalline silicon which is of the order of hundreds nanometer (335 nm (Yang & Dames 2013)) is too large compared to the pore size (1.448 nm). So I borrowed from Minnich and Chen model (Minnich & Chen 2007) to express numerically the impact of pore. So the matrix thermal conductivity is deduced as:

$$k_{Si}^{m} = \frac{k_{Si}^{b}}{1 + \xi l_{MFP}/4} \tag{3.3}$$

where the k_{Si}^{b} is the TC of bulk silicon, the l_{MFP} is the phonon mean free path in the matrix, the ξ represent the specific surface area of the pore defined as $\xi = S_{pore}/V_s$, S_{pore} is the surface area of pore, the V_s is the volume of the simulation box. Here, the k_{Si}^{b} is caught from Ref. evaluated by EMD for bulk silicon at different temperature using S-W potential (Henry & Chen 2008). The l_{MFP} is estimated as 460 ± 20 nm as (Isaiev *et al.* 2020). By calculating the Eq.3.3, the final k_{Si}^{m} is taken from 8.8 to 5.1 W/(m·K) in the studied temperature range. The $k_{H_2O}^{b}$ is calculated in this study shown in the Fig.3.2.

The R_K^{Si/H_2O} is deduced as 6.8×10^{-8} K·m^2/W, from the heat flux provided in Ref.(Pham *et al.* 2014). The interfacial resistance, regarded as the kapitza resistance, is introduced by its similar term Kapitza length. Murat Barisik et al. (Barisik & Beskok 2014) calculated the Kapitza length as a function of the temperature, showing a mild dependence of Kapitza length on the temperature. Similarly, it is clear that the R_K^{Si/H_2O} could be considered as a constant in a small range of temperature variation. So the R_K^{Si/H_2O} is deduced as 6.8×10^{-8} K·m^2/W , from the heat flux provided in Ref.(Pham *et al.* 2014).

As a result, the TC using EMA is shown in Fig.3.2(b) by the black dashed line. The effective thermal conductivity of the wet nanoporous silicon calculated by EMA is constant around 7 W/(m·K) in the studied temperature range.

Except for EMA model, well-known model called Maxwell-Eucken model (ME) is also introduced here, which assume that the dispersed component intrudes randomly and uniformly in the continuous phase component or in the opposite situation (Hashin & Shtrikman 1962). Note that it is not a function of the temperature. For our case, the continuous phase of water is immersed in the dispersed silicon particles. So using this model, the thermal conductivity of nanoporous silicon with the confined water is evaluated as

$$k_{eff}^{ME} = k_{H_2O}^{b} \frac{2k_{H_2O}^{b} + k_{Si}^{b} - 2(k_{H_2O}^{b} - k_{Si}^{b})(1 - f_v)}{2k_{H_2O}^{b} + k_{Si}^{b} + (k_{H_2O}^{b} - k_{Si}^{b})(1 - f_v)} \tag{3.4}$$

I substituted the value of 150 W/(m·K) for k_{Si}^{b} as mentioned above, and the MD value of 0.87 W/(m·K) for $k_{H_2O}^{b}$, in comparison to the experimental value of 0.61 W/(m·K) for the bulk water. The thermal conductivity of the present sample at 300 K is calculated to be 14.09 W/(m·K) using EMA model, and 10.08 W/(m·K) using ME model. The result shows bad agreement with our MD result.

Consequently, it is concluded that the macroscopic theories and models for thermal conductivity apply no longer properly to the case of solid liquid hybrid nanoporous system.

Going back to the results in Fig.3.2(c), the thermal conductivity of the wet nanoporous silicon shows an increase from 9.30 W/(m·K) at 285 K, and reaches a maximum value of 11.18 W/(m·K) at 300 K. The enhancement percentage of the effective thermal conductivity as a function of the temperature is also depicted. The enhancement at this temperature window of 285 K to 300 K is the order of 40 %. The enhanced thermal conductivity of the wet samples has been simulated recently (Isaiev *et al.* 2020) and there are evidences of thermal enhancement of solid-liquid systems experimentally (Lishchuk *et al.* 2015). Then the TC decreases from 300 K, and for the temperature greater than 345 K, the thermal conductivity becomes independent of the presence of the water.

How to understand the TC results of nanoporous silicon system is particularly important. The water addition is the main reason for the enhancement of the TC of the dry system. And when the temperature increases, the movement of liquid molecules becomes much vigorous, leading to the initial augment from 285 to 300 K of TC. The decrease of TC after 300 K might be due to the boundary scattering which dominates over phonon-phonon umklapp scattering.

A consideration from multiple aspects to address the observed phenomenon is taken here. As demonstrated in the previous study (Isaiev *et al.* 2020), the liquid density fluctuation close to "solid/liquid interface" causes the layering effect, which inducing a significant difference for more than two folds of thermal conductivity of pristine porous silicon and "porous silicon liquid – composite".

On the other hand, the thermal conductivity of a solid material is controlled by the heat capacity, the average velocity and the Mean Free Path (MFP) of phonon (Yang & Dames 2013). In the high temperature range, the heat capacity is less affected by temperature, so the sensitivity of the average velocity and MFP to temperature is interpreted critically in some models. Furthermore, in the Fig.3.1(c), the water molecules exhibits an uneven distribution in the pore. The change in local density and pressure is possible to incite the phase transition of water, which is likely to cause surprising changes in TC. Therefore, from several considerations, the structure and dynamical properties of water molecules are studied in the following subsections.

Table 3.1: Thermal conductivity data for MD simulations of different water models SPC/E, TIP3P, TIP4P, TIP4P/2005, TIP5P obtained from Ref.

Model	$T_{ave}(K)$	$k_{MD}(W/(m\cdot K))$	Ref.
SPC/E	298	0.93 ± 0.016	(Mao & Zhang 2012)
TIP3P	298	0.88 ± 0.019	(Mao & Zhang 2012)
TIP3P	298	0.608	(Sedighi & Mohebbi 2014)
TIP4P	298	0.82 ± 0.015	(Mao & Zhang 2012)
TIP4P/2005	298	0.91 ± 0.014	(Mao & Zhang 2012)
TIP5P	298	0.68 ± 0.007	(Mao & Zhang 2012)
SPC/E	300	0.87 ± 0.051	This study
SPC/E	300	0.808 ± 0.038	(Zhao *et al.* 2020)
TIP4P	300	0.641	(Lee & Kim 2019)
SPC/E	315	0.92 ± 0.032	This study
TIP4P/2005	324	0.85	(Römer *et al.* 2012)
SPC/E	325	0.87	(Römer *et al.* 2012)

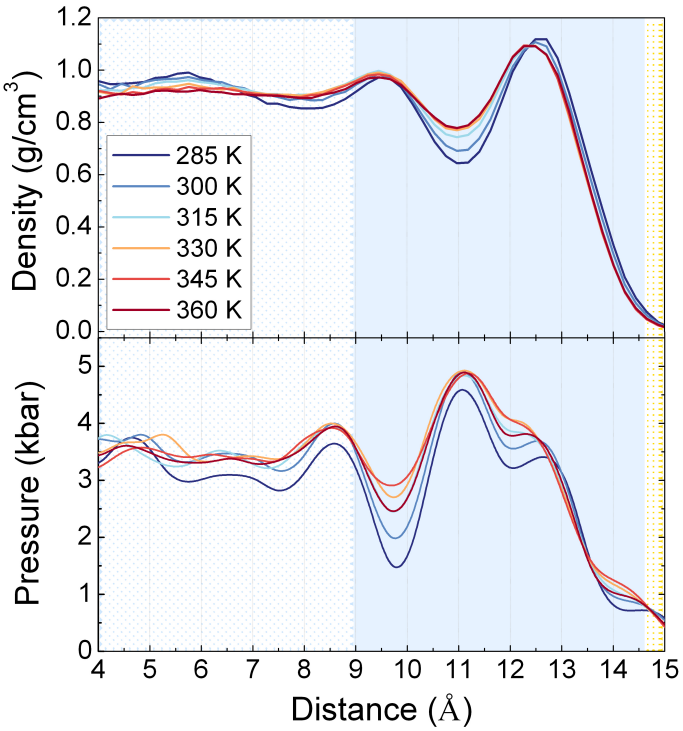

Figure 3.3: Density and pressure profile of nanohybrid water-nanoporous silicon system as a function of distance from the center of the system to the edge along radial direction. The center of the system is set as the zero point. To simplify the figure, the part from 15 Å to the edge of the system is omitted, where there isn't any water molecules inside. All of profile are averaged over 200 ps and output at 60 ns of simulation.

3.2.2 Density and pressure profiles

The primary study to understand thermal conductivity results, is the investigations of the interfacial structure. The local density and pressure along the radial direction of the pore are analysed. The profiles of water from the center to the edge of the interface are calculated and shown in Fig.3.3. The density changes dramatically at the 0 Å position, and the variation in the central region from 0 to 9 Å can be approximated as fluctuating around a desired density value 1 g/cm^3. Then, there are several extreme values observed near the solid/liquid interface, including three maxima and two minima. This is a phenomenon already observed at solid/liquid interfaces at atomic scale (Yu *et al.* 2018b). And then, near the edge of pore, few value of density is observed revealing that just some water molecules penetrate through the edge of the pore into the silicon matrix. For large distance, when the distance is greater than 15 Å, no water molecules is found, with the vanish of density value to zero. This phenomenon is also observed in the Fig.3.1(d).

In the density profiles, the depth of the minimum decreases with increasing the temperature is also observed. It is expected that the thermal agitation becomes severe when the temperature is raised. To depict numerically the dependence of the density peaks with the temperature, the values of high peak and low peak marked in Fig.2.6 are plotted in Fig.3.4 gives the density peak values, as well the interface thickness. With the temperature increases, the high peak value changes slightly, but the low peak shows a increasing trend. The averaged shell thickness is calculated to be 4.76 Å. The peak values shows a linear variation with temperature, changing from about 0.65 to 1.25 g/cm^3.

The pressure profiles in Fig.3.2 exhibits the internal pressure of water molecules in each chosen bin (a sphere with the thickness of 0.2172 Å) given by the two neighbor bins. The figure unfolds a clear comparison between the density and pressure. The region with the higher pressure given by the adjacent bins corresponding the lower density, and vice versa. In additions, it reveals a remarkable change in the interface position in the range of 1 to 5 kbars. Referred to the phase diagram of water (Chaplin 2015; Arsiccio & Pisano 2020), there is no phase transition in 1-5 kbar pressure range.

3.2.3 Radial distribution function

The Radial Distribution Functions (RDF) is a concept frequently used in statistical physics of equilibrium states, where microscopic physical states can be correlated with macroscopic physical quantities through the calculation of Density

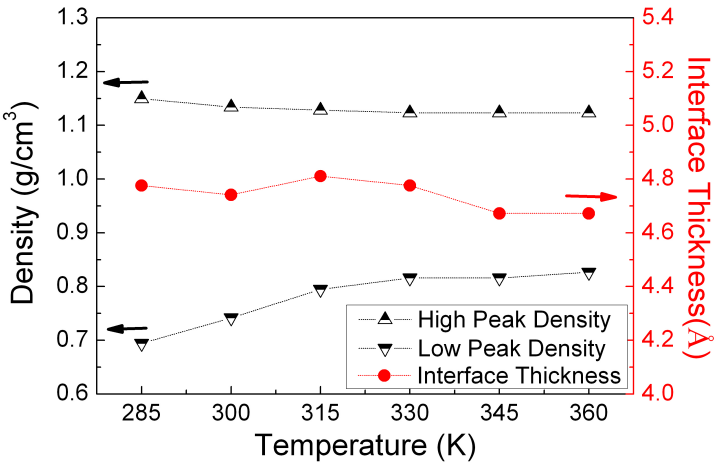

Figure 3.4: The interface thickness and density value of high and low peak in the interface as a function of temperature.

number of atoms. In this study, it describes well the localized distribution of atoms near the interface, then represents numerically the ratio of the local density of a molecule relative to the bulk density at a distance r around a central molecule.

The RDF of bulk water, and water in the core and shell for two different temperatures (300 K, 360 K) are depicted in Fig.3.5 to check for definitive phase transition of water. The position of the first neighbor peak for both the bulk water and confined water locates around 2.75 Å. Meanwhile, it has no significant change for the core and shell water molecules compared to the bulk water and then it is temperature independent. It is necessary to notice also here that the RDF for confined water decays gradually to 0 from 7 Å until the edge of pore (omitted in the figure). It has already been observed in previous studies that RDF for nanoconfined liquids don't attend the value of 1 as anticipated for bulk liquids (Giovambattista *et al.* 2006; Da Silva 2014). Another argument worthy discussing is that the temperature effect on the density of the g(r) and the Structural characteristics of water in different regions (core and shell) inside the pore.

The higher temperature induces the decrease of the intensity of the RDF peak by 10%-15%. Different temperature has the same effect on both core, shell and bulk water without changing the distance of first peaks. The first peak for both core and shell appears near 2.7 Å, in agreement with bulk water. Within a short area (under 3 Å), the water in core shows a same distribution with bulk water. Rather in the shell, more water molecules gathers together which becomes more pronounce as the temperature rises. For the shell water molecules, the RDF is almost double

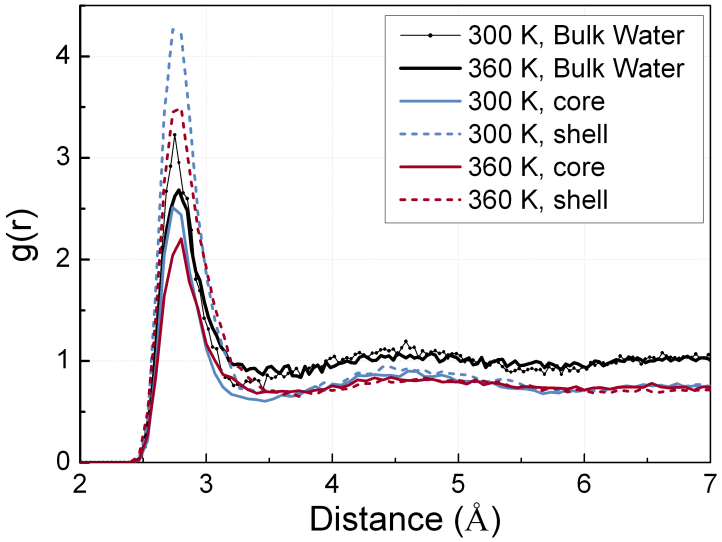

Figure 3.5: The partial Radial Distribution Functions (RDF) of oxygen-oxygen atoms for different parts (core and shell) of nanohybrid water-nanoporous silicon system under different temperature. The core and shell contain all the O atoms. The core is a sphere with a radius of 9 Å centered at box. The shell surrounds the core as a spherical shell from the 11 to 15 Å from the center of core. When we calculate RDF, a reference O particle is chosen from the core or shell, another O is chosen from all of O atoms.

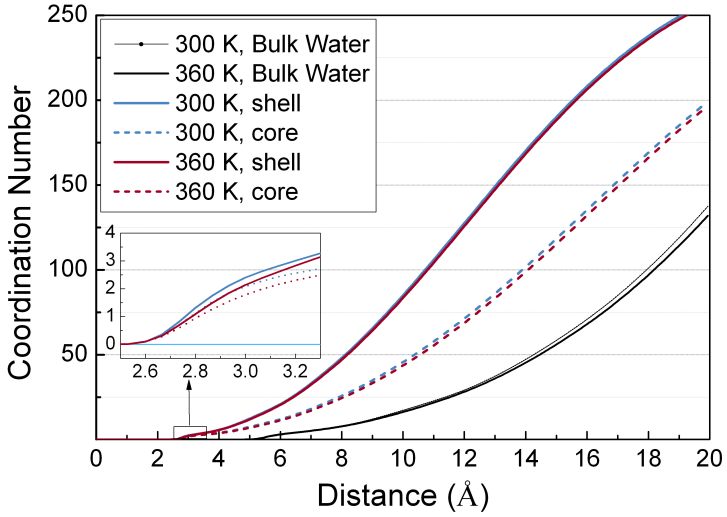

Figure 3.6: The coordination number of oxygen atoms for different parts (core and shell) of nanohybrid water-nanoporous silicon system under different temperature.

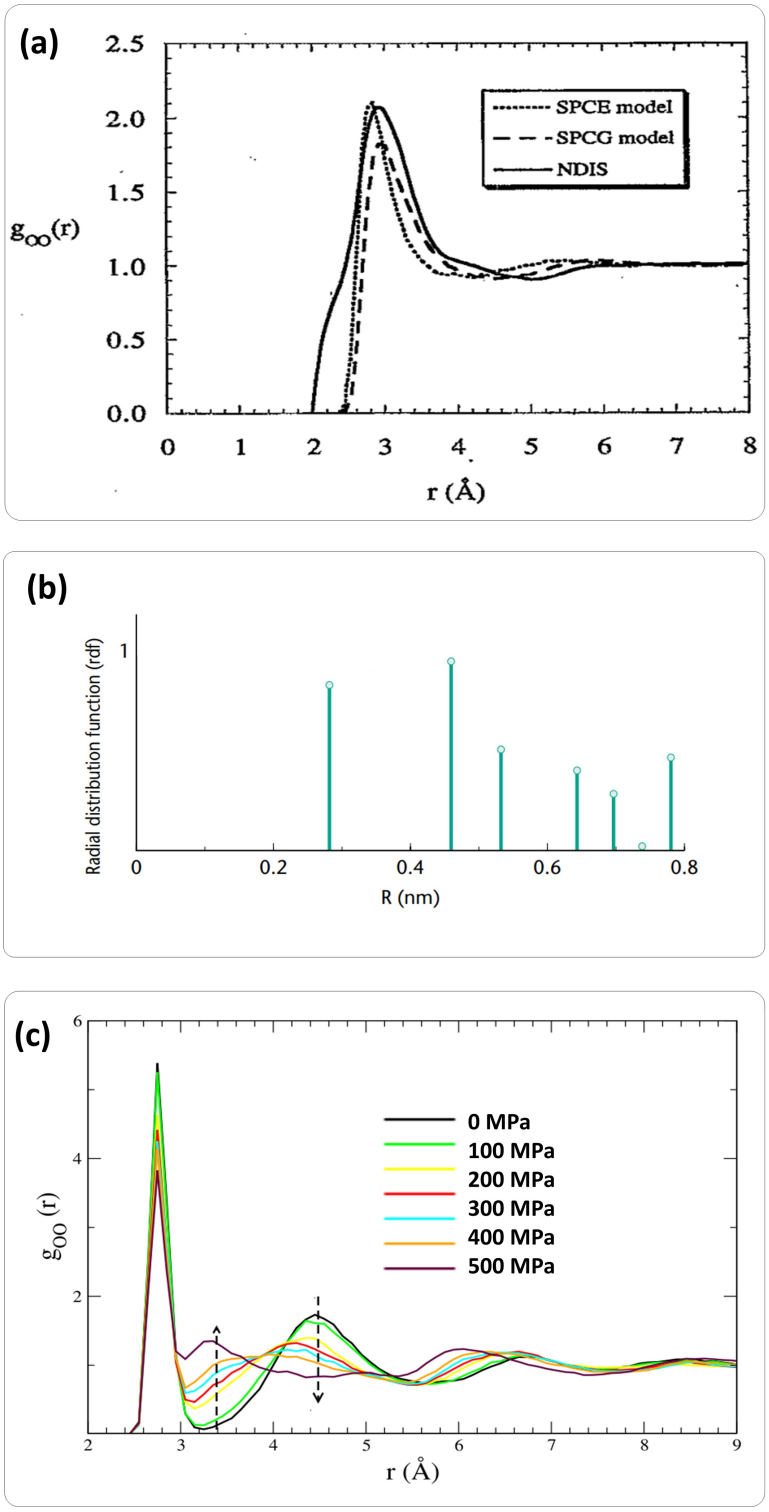

Figure 3.7: Radial distribution functions of oxygen-oxygen atoms of water molecules under different states. (a) The RDF of SPC/E and SPCG under supercritial condition at T=573 K and the density of 0.72 g/cm^3, including the comparison between the e Neutron diffraction with isotopic substitution xperiment (NDIS) with solid line and the simulations with dotted line and dashed line (Chialvo & Cummings 1994). (b) The RDF of Ice. Use the lines for the experimental data and circles for computer simulation data (Sharp 2001). (c) The RDF of amorphous ice during cooling cycles at 160 K under different pressures, with SPC/E model using MD (Duki & Tsige 2018).

than one in the core, meaning that the shell molecules are much more ordered and this persists even at higher temperatures. The reason for this has to do with the greater water density in this region. The discrepancy gets more important for the shell water molecules compared to the core ones. The RDF at higher temperatures (360 K) contains the similar observation but it is less evident.

By computing the coordination number of atoms around the central atom, called the coordination number, I can more clearly distinguish the distribution of water molecules at different locations and temperatures. The result is shown in Fig.3.6. The zoom figure shows that the values of the coordination number of the core and the shell begin to differ at the position of first peak. For long distance, higher number of water molecules gather in the shell than the ones in the core.

Based on these results, a brief research about RDF of different states of water has been done, to clarify the generation of phase transition. The radial distribution functions of oxygen-oxygen atoms of water molecules under different states are shown in Fig.3.7. At this point I tried to comment on the possible phase transition. From Fig.3.7(a) (Chialvo & Cummings 1994), it can be seen that the RDF for gas-like atoms would be accompanied with a much broaden first peak and then a constant value attending to 1 for long distance, rather than multiple peaks for bulk liquid water. Fig.3.7(b) displays an quite obvious comparison with ice, which shows discontinuous intermittent changes (Sharp 2001). In consequence, a possible ice formation is also removed. Another special state of water which has the potential to perform a compact structure is amorphous ice. From the Sec.3.2.2, I has discussed that the studied range of pressure in the pore in our study is from 1 to 5 kbar (100-500 MPa). So I consulted the study on the RDF of amorphous ice at different pressures during isobaric cooling cycle from Ref.(Duki & Tsige 2018). In the Fig.3.7(c), it is observed that the RDF for amorphous ice reflects a significant change in the second nearest neighbors of the oxygen atoms. Moreover, the greater the pressure, the deeper the drop. This kinds of behaviors has been detected for liquid water. To sum up, we conclude that no phase transition is observed in our system further with no powerful effect on thermal conductivity under the temperature changing in the range of 285-360 K.

3.2.4 Velocity and motion displacement

Thermal conductivity depends on velocity and motion displacement in a sense that in general the enhanced motion of liquid enhances the thermal transport value (Ju & Yang 2018; Sachdeva 2009). To check the effect of the motion of the nanoconfined water on the thermal properties, the Mean Square Displacement

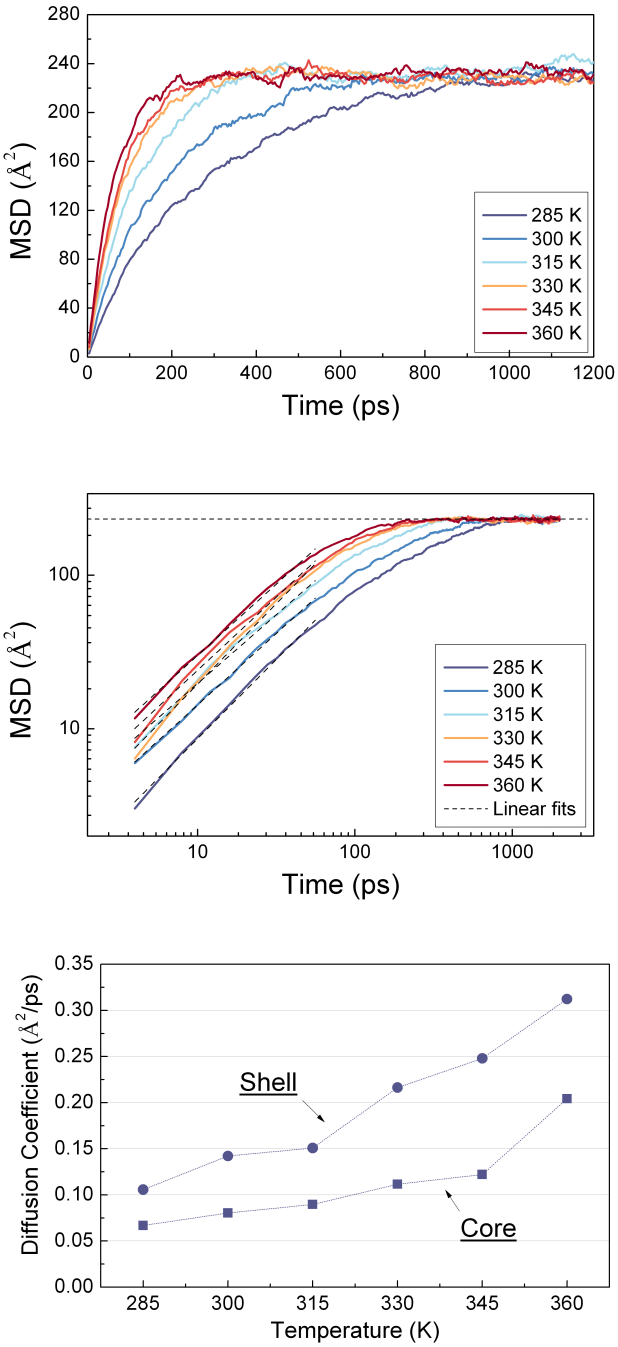

Figure 3.8: Mean Square Displacement Function(MSD) and its log-log plot, and diffusion calculated using MSD as a function of temperature

(MSD) was studied, further with estimating the diffusion coefficient. The diffusion coefficient is obtained using the slopes of MSD profile. Using the mean square displacement (MSD) to describe the water molecule motion, the results of MSD are shown in Fig.3.8.

For 285, 300, 360 K, it is observed that the water molecule shows the same shape of displacement. Before 200 ps, an approximate linear variation of the MSD profile appears. Then, the profiles vary slowly to attend a saturation between 300 to 1000 ps, depending on the temperature. After 1000 ps, the MSD profiles for all the temperatures become flat systematically to the value of about 232 $Å^2$, which is easily to observe that this value is independent of the temperature. To sum up, it is said that under the sufficient confined size, the MSD profiles of water are no longer linear to delay time over the long term. Mosaddeghi (Mosaddeghi *et al.* 2012) also observed the similar platform for the MSD of the nanoconfined water between parallel graphite plates, which occurs only when the inter-wall distance minus 7 Å.

This kind of anomalous diffusion has already discussed by other researches and among them, Vincent Tejedor et al. (Tejedor *et al.* 2010) have introduced an exponent α to well express the motion of atoms. It is redefined the relation of MSD and diffusion coefficient D in Eq.2.33, expressed as:

$$MSD = 2NDt^{\alpha} \tag{3.5}$$

where the N is still the dimensions. So the time required to implement MSD accords to the power law relationship with MSD (Chubynsky & Slater 2014). Based on this power law relationship, the diffusion state is characterised by comparing the value of α with 1, in details: α>1 for superdiffusion, α<1 for subdiffusion, α=1 for normal diffusion, and α tends gradually to 1 for confined diffusion. So the log-log of MSD is plotted in the Fig.3.8 to express schematically α, as well as the linear fitted lines. The diffusion coefficients are calculated from the intercept of these fitted lines, and reported in Table.3.2 with the slope of the curves.

The value $\alpha \approx 1$ indicates a classical Brownian motion at the first 100 ps. Furthermore, the slopes before 50 ps of MSD profile show a strong dependence on the temperature. With the temperature increasing, the slope becomes larger with the faster movement of water. And then, a decline of the slope decrease starts with the time until about 200 ps, after that stabilizes and remains to zero. It is the symbol of a non Brownian diffusion, attributed by the confined geometry. A similar diffusion has been reported in the study of S. Chakraborty (Chakraborty *et al.* 2017). It is found that when a single line of water molecules are confined inside a short, open-ended carbon nanotubes, they move collectively as a single unit because of

the presence of strong hydrogen bonding between adjacent water molecules. A normal simple one-dimensional random diffusion is presented here, called Fickian diffusion (Mukherjee *et al.* 2007).

In Table.3.2, the simulated diffusion coefficients of the nanoconfined water in a pore with radius of 14.48 Å is of the order of magnitude of 10^{-9} $m^2{\cdot}s^{-1}$. The values increase from 0.20 Å^2/ps at 285 K, to 0.58 Å^2/ps at 360 K. So the diffusion coefficient is enhanced by the augment of the temperature. In the case of bulk water, the value of 0.16 Å^2/ps at 276 K and 0.23 Å^2/ps at 290 K demonstrate the same growth trend (Qvist *et al.* 2011). Compared the nanoconfined water with the bulk water, it is concluded that The effect of temperature on the diffusion coefficient of nanoconfined water is greater than that of bulk water. Note that the finite size effect of diffusion (Yeh & Hummer 2004) doesn't take into account. Moreover, it is also possible that the diffusion of particles in the confined area has the directional character of the confined area (Cui 2005). It will be expected that different characteristics compiled by MSD can be found in radial and tangential directions in the spherical pore. This can be carried out in follow-up studies.

3.2.5 Orientation of water molecules

The hydrogen bond, as the most important bond in the water molecule, confers many unusual properties to the water molecule. The strength, density and distribution of H-bonds might affect seriously on the scattering of phonons and then on thermal conductivity. So in the following paragraph, the orientation dynamic, the density and geodesic length of H-bond network are carried out.

To explore the translational and rotational states of water molecules, the orientation of H-bonds angle between between the molecular dipole moment and the radial direction of oxygen atom from the same water molecule, is studied under different temperature, shown in Fig.3.9. The angle degree conforms to Gaussian distribution with the mean over 90° for both core and shell. Compared them, it reveals that oxygen atoms closer to the interface have a stronger preference for silicon while remaining almost independent of temperature, being less free to spin

Table 3.2: Diffusion coefficient for different temperatures of the nanoconfined water extracted by Fig.3.8

Temperature (K)	285	300	315	330	345	360
Slope	1.03	0.93	0.89	1.04	0.95	0.93
D (Å^2/ps)	0.20	0.27	0.41	0.29	0.44	0.58

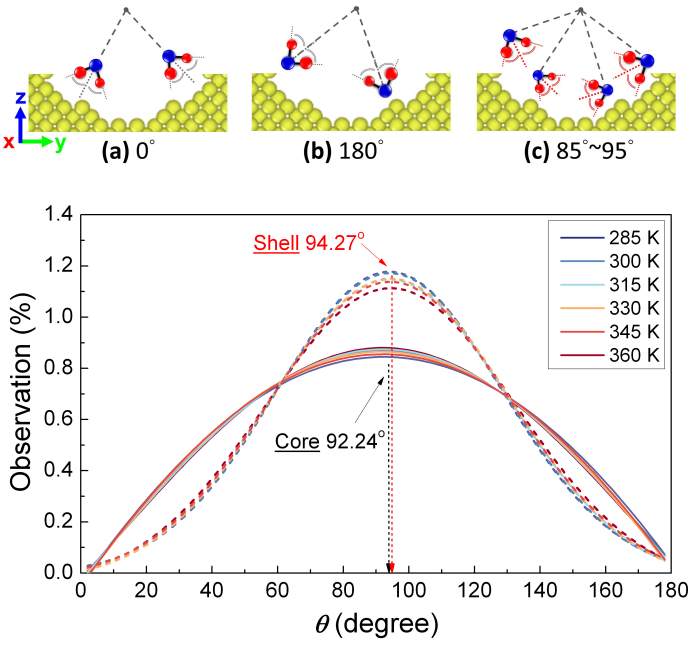

Figure 3.9: The Angle between the molecular dipole moment and the radial direction of oxygen atom in the same water molecule as a function of temperature. The radial angle value for center and shell region are both subject to the amplitude version of Gaussian peak function (GaussAmp) under different temperature conditions.

than the inner molecules. It is related to the van der Waals force between O and Si atoms. The most likely angle between radial direction and the angle bisector of hydrogen bond in the center and shell region, are 92.24° and 94.27°, which occur with the possibility of 0.86% and 1.17%, respectively. This phenomenon appears to be independent of temperature, at least for the core molecule, and for the molecules in the shell, a slight decline is observed in the peak with increasing temperature, which seems reasonable considering that temperature increases thermal agitation.

3.2.6 Hydrogen bonds network

ChemNetworks is considered as a post-processing package of *LAMMPS* in this study, to provide topological analysis of H-bonds networks. The averaged number of water molecules connected with a central water molecule through hydrogen bonds as a function of temperature are shown in Fig.3.10. The data in core, shell and in the both of them, is compared with bulk system with the aim of illustrating the dynamic behavior of the resulting intermolecular network. The first figure for analyzing all H-bonds in the pore, displays the large concentration of waters with the variation trend of H-bonds. For example, at 300 K, no zero number is observed,

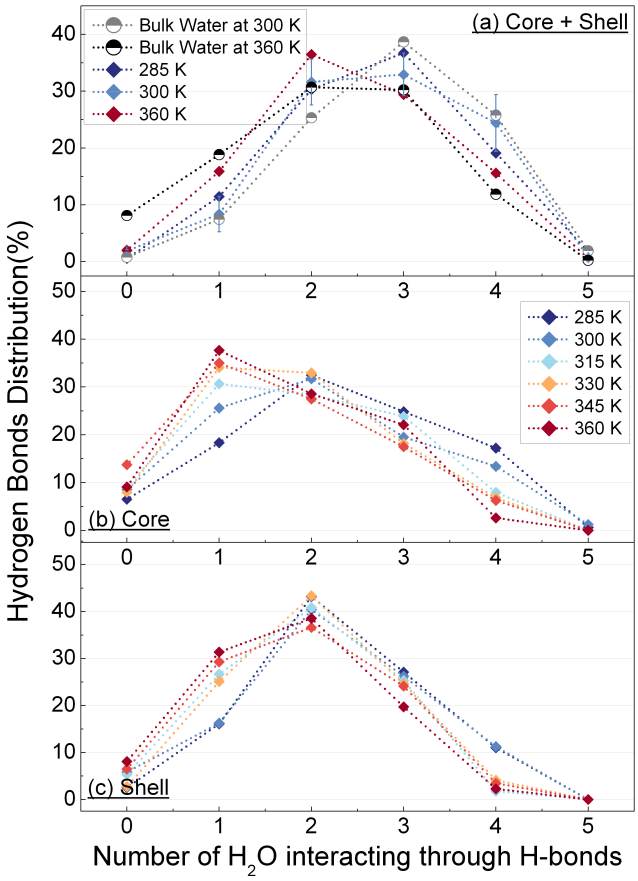

Figure 3.10: Hydrogen bonds (water water H-bonds) distributions for different temperatures in different region in the pore contributed from the interaction of water and its neighbor water molecules within 10 Å. From the top to bottom of the figure, the region studied are the whole pore (all waters in the core and shell),the core and shell.

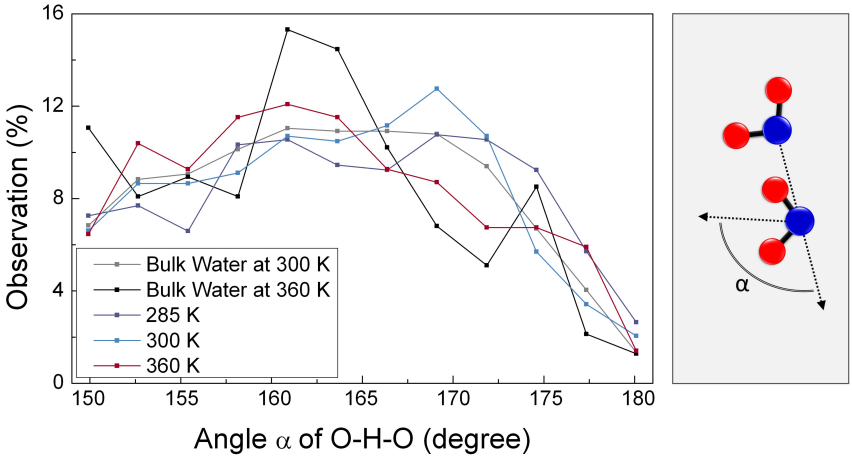

Figure 3.11: Dipole angle distribution α of bonds O-H-O for one water molecule and its neighbor water.

accompanied by few number of independent water molecules. Then a large number of network are interacted through 2, 3 and 4 H-bonds, consequently 3, 4 or 5 water molecules connect together. The distribution of H-bonds for bulk water at 300 K reveals that 8 % for 1 H-bonds, 23 % for 2 H-bonds, 38 % for 3 H-bonds, 26 % for 4 H-bonds and minus 1 % for 0 and 5 H-bonds, agreeing very well with SPC/E sites in other references (Wang *et al.* 2014; Ozkanlar & Clark 2014). At 360 K, the majority of H-bonds (3, 4, 5 H-bonds) decrease, with conversely the proportion of more independent H-bonds (minus 2 H-bonds) increases. Also a higher value of almost 9 % for 0 H-bonds is observed obviously, which means more isolated water molecules are found at higher temperature. That signifies that the raising temperature isn't conductive to the formation of much dense hydrogen network.

For nanoconfined water, similar trends for 285, 300, 360 K that at each temperature high densities value for 2-4 bonds, smaller values for shorter 0-1 and larger 5 H-bonds are discovered. That corresponds the designated criterion for the H-bond defined in the Sec.2.4.4, under which the unphysical over-coordination (more than 5 H-bonds) are prevented. The reference state that has been utilized is a "perfect" network wherein each H_2O has exactly 4 H-bonds, as in prior work (Speedy *et al.* 1987). At 300 K, the distributions show less isolated H-bonds and about 5 % higher distributions than 285 K (10 % higher distributions than 360 K) for 4 bonds. It could be roughly concluded that a much probable "perfect" network is found at 300 K though hydrogen bonds network, meaning that the greater H-bonds distribution value, leading to the greater thermal conductivity. Then as temperature increases, the percentage of hydrogen bonds formed with a small number H-bonds increases, which indicates that the distance between the intermolecular hydrogen-oxygen bonds gradually increases and the molecular forces decrease.

To further analyze of the H-bonds distribution of different region in the pore, a comparison of observation data from center and shell is shown in the Fig.3.10(b) and (c). Obviously, there are more isolated water molecules in the core. That proves that the water in the core is occupied with less water molecules in the neighbor, which hinder the propagation of heat. Compared with the core, higher number of H-bonds are found in the shell. a more stable hydrogen bonding network is formed, in favour of the heat propagation.

In Fig.3.11, the dipole angle distributions α of bonds O-H-O between two water molecules for bulk water and confined water at 285, 300, 360 K are shown. It is attempt that the librational motion of H-bonds can be understood by the variation of dipole angle. It is widely believed that the motion in water, especially the librational motion, induces the noticeable breakage and reforming of H-bonds in a short

time scale (Ozkanlar *et al.* 2014). So it is proved that the librational motion is the primary cause for the disruption of short H-bond persistence on a subpicosecond timescale (Luzar & Chandler 1996; Ozkanlar *et al.* 2014). The most likely location for water molecule adsorbed by another is found for angles in the range of 160° to 170°. With the temperature increased, the distribution of angle is a little shifted to lower value.

The grade of connectivity within the H-water network was evaluated by analysis of geodesic length, shown in Fig.3.12. As observed in Fig.3.12(a), the distribution of gd's in the bulk water is mainly Gaussian in shape, with a peak at 8, an average length of 12. Under different temperature conditions, the gd profile for temperature less than 300 K has a normal and narrow distribution of geodesics centered around the mean value of 9 H-bonds. From 315 K to 360 K, the distributions become much broader with significant populations of geodesics of length greater than 10 meaning that more contiguous hydrogen bonded paths are promoted. The same results in Fig.3.12(b) are also equally applicable for water molecules in the core and shell, respectively.

With the measurement of euclidean distance, the hydrogen bonding network can be depicted more graphically, as illustrated in Fig.3.13. For 300 K, an average euclidean distance having 9 H-bonds for confined water is of 18 Å. Therefore, that means each water molecule is connected to other water molecules through 9 contiguous H-bonds from 18 Å away on average. At 285, 300, 360 K, the most distant water molecules are each connected by 15, 14, 18 continuous H-bonds on average, respectively, making them near 28 Å apart. The extension over Euclidean space increases with the number of contiguous H-bonds as well as temperature dependant. It is reflective of the complexity of the H-bond network, where the shortest H-bond pathway with longer gd length between waters can be circular ring, an extended or twisted chain, or a mixture of the two in complex three-dimensional shapes.

3.2.7 Density of states

Phonon density of states (DOS) of the nanoporous silicon and the water confined in hybrid nanoporous materials are shown in FIG.3.14. The aim of the DOS study is to identify possible heat flow channels through the dense water layer close to the solid surface, which might explain the enhanced thermal conductivity of the hybrid nanosystem.

Similar to the bulk silicon, the DOS for nanoporous silicon with water exhibits two peak value at about 6 THz and 17 THz. Because of the solid-liquid interaction,

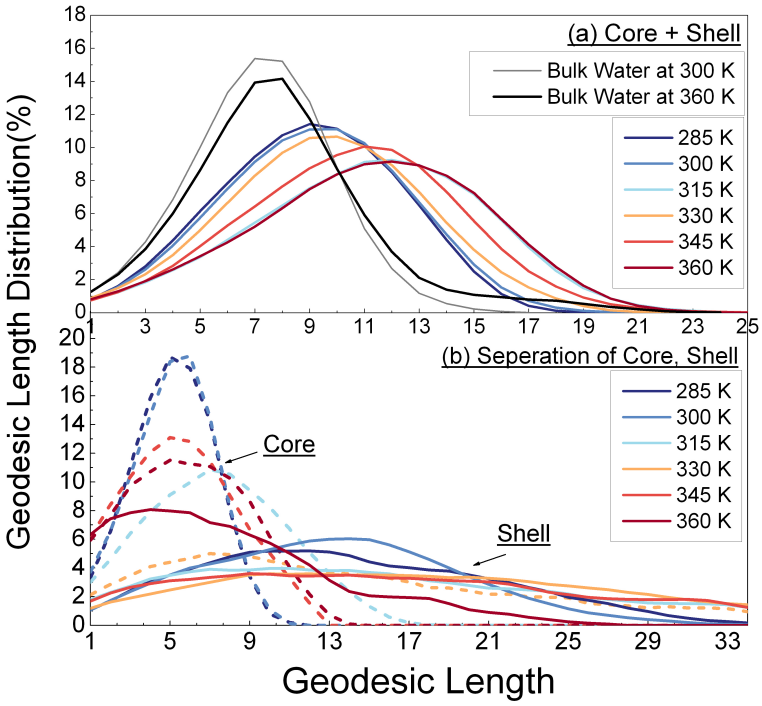

Figure 3.12: Distribution of geodesic (gd) lengths found of water (a)in the pore, (b)core and (c)shell.

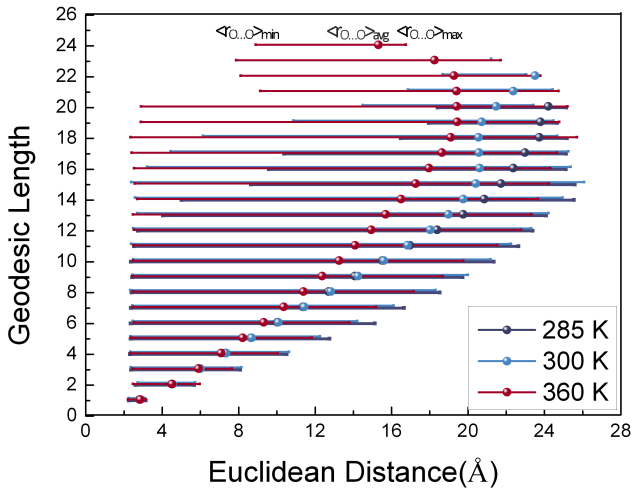

Figure 3.13: The averaged euclidean distance for each geodesic length for 285, 300, 360 K.

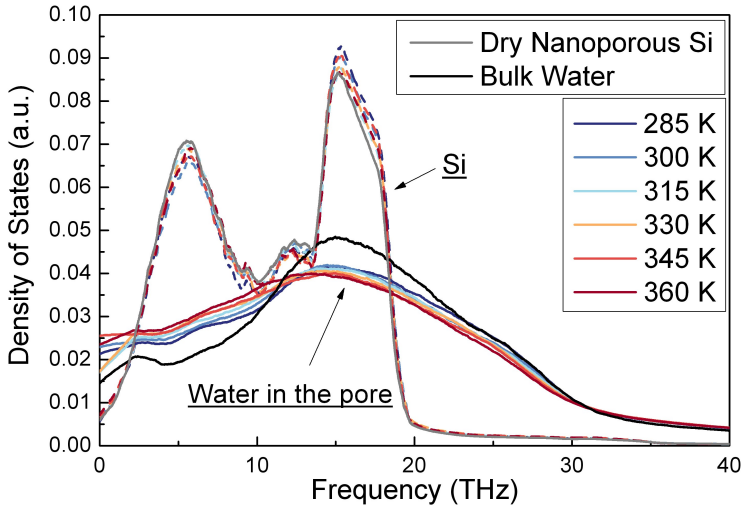

Figure 3.14: Density of States for bulk water with black continuous line, nanoporous silicon without water with the grey continuous line, the one with confined water with water pointed lines, and the nanoconfined water in the pore with continuous lines, for different temperatures.

a red shift of the transverse optical peak of the silicon atoms compared to the bulk-like silicon, secondly an hybridisation of the optical and acoustic longitudinal peaks (second and third peak) as something that has been observed previously on other systems for the surface atoms of silicon (Verdier *et al.* 2018) and finally a softening of all modes.

Compared to the bulk water, confined water has a higher value at low frequency. It follows that the density of states of confined water has a lower peak value at lower frequency. Moreover, there is a softening of the modes at higher frequencies corresponding to the longitudinal peak of silicon, and furthermore a creation of an extra DOS change for the nanoconfined water compared to the bulk water at around 6 THz which is at the same window frequency as the transverse acoustic silicon atoms modes. Fig.3.14 gives also the comparisons of density of states of solid-liquid nanohybrid system under different temperatures. For water molecules, phonons with high frequency in the librational modes contribute the most to heat transfer (Yu & Leitner 2005). In this figure, a higher temperature induces a higher value of DOS in low frequency range for water. Meanwhile, a redshift appears clearly with the temperature decline. It has been reported that the critical decline of the high frequency phonons gives a good contribution to the reduction of the thermal conductivity. Conversely, a high value is observed in the figure around 15 THz, verifying a higher thermal conductivity.

B. Kim (Masuduzzaman & Kim 2020) studying the confined water between

solid wall in the nanochannel, defined the wettability through the integral ratio of the interfacial liquid and solid DOS, shown in Fig.3.15. A higher ratio implies a greater overlap between the spectra, and a higher wettability, this stronger vibrational coupling results in reduced interfacial resistance and enhanced heat transfer. But in our study, no change was found in this ratio with temperature, which may means that the vibrational coupling of water molecules in the nanopore less depends on the temperature.

What we can conclude from this figure is that the modification of the DOS of the hybrid system is in the direction of expanding the area where the DOS for the silicon and the water overlap. Qualitatively this increase of the common surface support the idea that the heat can travel easier between the solid and the liquid as their DOS are modified respectively in a way to create heat flux channels. It is also worthy noticing that our water DOS has similar shape as those of other hydrophilic surfaces in the literature, such as hydrophilic peptide (Russo *et al.* 2011).

3.3 Conclusions

In this chapter, an enhancement of the effective thermal conductivity of wet nanoporous samples at different temperature is evaluated here. The underlying mechanisms are related to the stratification of the water molecules at the vicinity of the solid/liquid interface. This enhancement is much more important than the one that can be predicted by using macroscopic effective models. Furthermore, a maximum of the thermal conductivity of the solid/liquid nanohybrid system at 300 K was observed at first time, which vanishes for temperatures greater than 345 K. To understand this non-monotonic behavior, several structural and dynamical properties of the nanoconfined water, separated in a core water molecules (bulk-like) and shell water molecules (dense water layer close to the solid/liquid interface) have been studied numerically.

Density and pressure profiles helps to understand the structure near the interface. The water molecule density followed a stratification effect close to the solid interface and the water density fluctuations decreased in increasing the temperature. The average value of density of the maximum peak is around 1.15 g/cm^3 and this does not change with the temperature. In contrast, the value of the minimum peak at 285 K is 0.7 g/cm^3 and it increases with the temperature reaching the value of 0.85 g/cm^3 at 360 K. Furthermore, secondary peaks disappear in increasing the temperature. Nevertheless, the density variations cannot be connected to the maximum effective thermal conductivity at 300 K, as this variation is rather monotonic.

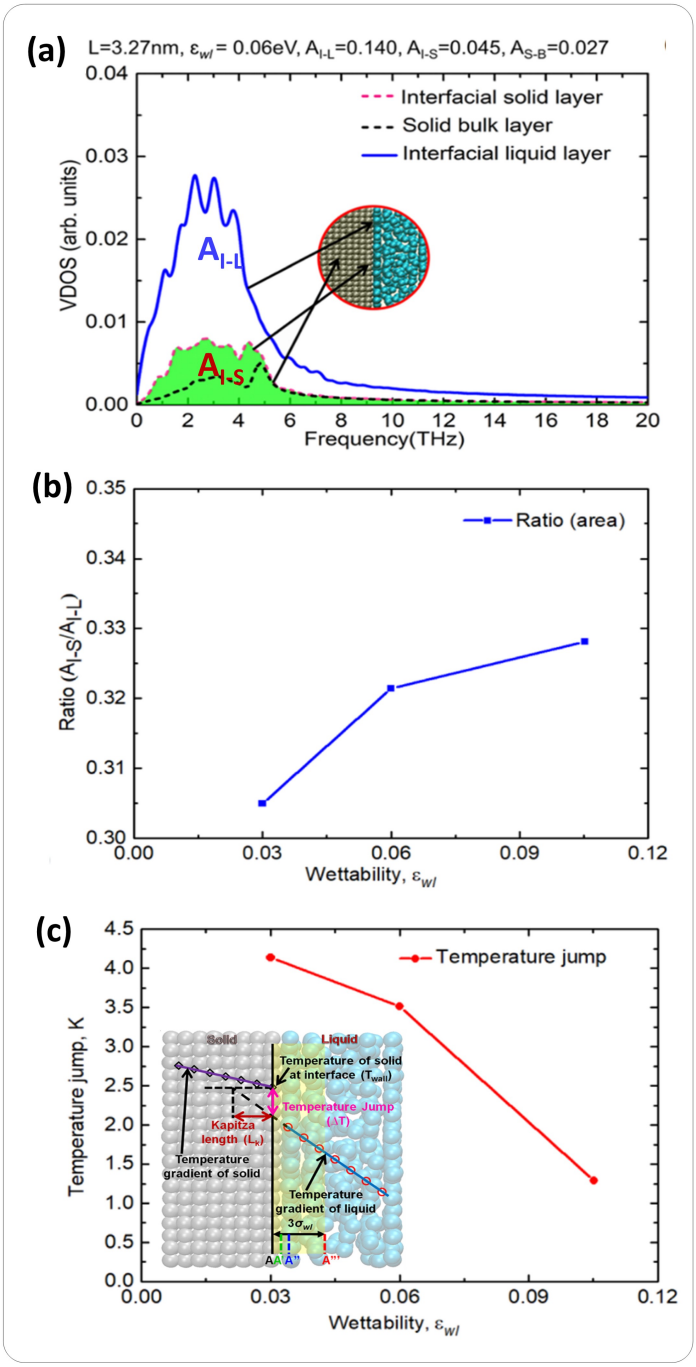

Figure 3.15: (a) Vibrational density of states of the confined water and solid wall at the interface in the nanochannel. (b) The relation of the wettability with the ratio of the integration of interfacial solid and liquid area. (c) The temperature jump defined in the inset, as a function of wettability.

Then with RDF analysis, it is advised to think about more physical insights concerning the maximum of the effective thermal conductivity: At 300 K the shell water molecules is much more ordered than the ones in the core.

On the other hand, dynamical features such as the mean square displacement and the diffusion coefficient showed a saturation of movement over a long period of observation. An uncorrelated Brownian motion of nanoconfined water is observed at the beginning of the observation, followed by a confined diffusion. The diffusion coefficient shows that nanoconfined water depends more strongly on the temperature than the bulk water. Concerning the orientation of water molecules, It is observed that oxygen atoms close to the solid/liquid interface are more rigid compared to the inner water molecules, but this phenomenon is independent of temperature. The hydrogen bond networks study for nanoconfined water reveals that the majority of molecules preserves similar networks to the bulk water and that the temperature does not have a systematic effect on the H-bond networks. The overall distribution of the number of long hydrogen bonds for the shell is much more than the one for the core. More connections of networking in the shell might be correlated to our remark that the high density water layer close to the solid/liquid interface has potential to cause the higher thermal conductivity of hybrid nanosystems. This conclusion is also supported by the tendency of water molecules to create shorter networks in increasing the temperature, corresponding to the decrease of the effective thermal conductivity of the hybrid nanosystems upon increasing the temperature. The geodesic length profiles of the nanoconfined water for temperature less than 300 K is a bit shifted compared to the bulk water to higher geodesic lengths, having a quite narrow distribution. For temperatures higher than 315 K, the distributions became much broader, with significant population of geodesic lengths greater than 10. The shell water molecules behaved more contiguous than the core molecules. Last but not the least was that the DOS of the silicon pores atoms and the nanoconfined water molecules increased their juxtaposed areas and this qualitatively means that new heat flux channels are established between the solid matrix and the nanoconfined water, but without explaining the maximum of the thermal conductivity at 300 K.

To sum up, I give physical insights of the observed phenomena with structural and dynamical aspects. Only a small amount of evidence explains the maximum value of thermal conductivity at room temperature. It is known from the hydrogen bonding network that, water molecules can have an impact on the thermal conductivity with their minor structural changes at different temperatures. However, this also demonstrates the complexity of confined water molecules at the nanoscale. In

the future study, the solid-liquid hybrid system can be explored with the help of more complex models and research methods in a greater depth.

Synthesis of the Chapter

- An enhancement of TC is evaluated.
  - Nanoconfined water contributes to a remarkable enhancement to TC.
  - A surprising maximum value of TC of nanoporous silicon with the confined water is found at room temperature (300 K), which cannot be predicted using macroscopic effective models.
- Density and pressure profiles provide a deep understanding of nanostructure near the interface.
  - A stratification effect is observed close to the solid interface
  - The maxima peaks do not change with the temperature, but the mimima peaks show a monotonic variation with the temperature.
- At 300 K the shell water molecules are much more ordered than the bulk water, also than the ones in the core.
- The dynamical properties of the water molecules inside the pore are investigated.
  - The water molecules move in the core, showing an uncorrelated Brownian motion at the beginning of diffusion.
  - And then, it is followed by a saturation of movement over a long period.
  - The nanoconfined water depends more strongly on the temperature than the bulk water.
- According to the radial angle of dipole moment of the water molecules, the oxygen atoms near the interface are much more rigid than the inner ones.
- The hydrogen bond networks reveal the effect of the localized interaction of hydrogen bonds on the TC.
  - The water molecules create shorter networks, corresponding to the decrease of the effective thermal conductivity in increasing the temperature.
  - More connections of networking in the shell might signify that the high density water layer close to the solid/liquid interface has potential to cause the higher TC.
- The juxtaposed areas are increased for the DOS.
  - The new heat flux channels are established between the solid matrix and the nanoconfined water, and
  - A higher value of DOS at high frequency verifies a higher value of TC, but cannot explain the maximum of TC at 300 K.

CHAPTER 4

Density Dependence of Thermal Conductivity of Nanoporous Crystalline Silicon via EMD

Contents

This chapter focuses on the effect of the initial water density (also called the effective density) on the thermal conductivity of the hybrid solid-liquid nanocomposites based on the silicon crystalline nanoporous matrix. Using Molecular Dynamics simulations, the role of the effective density (from 0.1 to 1.2 g/cm^3) on the thermal conductivity enhancement of nanohybrid porous silicon and water system is investigated. By studying the mean square displacement, radial distribution functions, density of states, several structural and dynamical phenomena are discussed to give physical point of views of the TC results. The effective thermal conductivity is also computed here by using Equilibrium Molecular Dynamics (EMD) methodology.

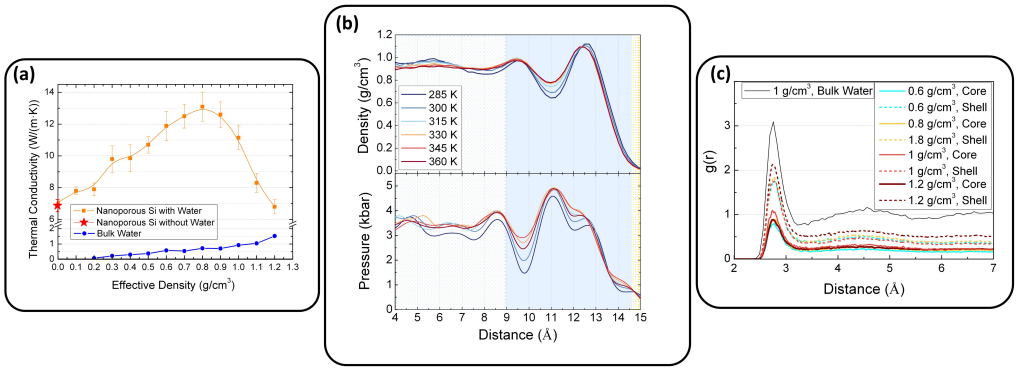

Visual Abstract: (a) the thermal conductivity of nanoporous materials, (b) the density and pressure profiles and (c) radial distribution function of the water molecules confined in nanoporous materials.

4.1 Simulation details

4.1.1 Determination of the configuration

The same dimension of the bulk crystalline silicon with dimensions $8a_0 \times 8a_0 \times 8a_0$ ($a_0 = 5.43$Å) has been generated, which corresponds to a cubic sample of 43.4 Å size length. The porosity of the studied system is set to 15.51%. The water molecule is constructed as a simple cubic structure at the beginning of the modeling. The effective density of water ρ_{eff}, is the averaged density of water in the pore. It is controlled by the initial distance of oxygen atoms d_{O-O} as:

$$\rho_{eff} = \frac{M_{H_2O}}{V_{H_2O}} = \frac{18}{\frac{4}{3}\pi d_{O-O}^3} \tag{4.1}$$

where M_{H_2O} is the molar mass of the water. It is adjusted from 0.1 to 1.2 g/cm^3. The configurations are displayed in Fig.4.1 with the details listed in the following table. For each set of parameters, six simulations with different initial conditions have been performed to decrease the uncertainty of the results.

In the Fig.4.1, according to the set density, different numbers of water particles formed as a sphere are dropped into the porous silicon. The radius of the pore is

Table 4.1: The details of configuration

ρ_{eff} (g/cm^3)	0.1	0.2	0.3	0.4	0.5	0.6	0.7	0.8	0.9	1.0	1.1	1.2
Number of Water	31	69	104	135	168	196	236	259	305	343	370	409
d_{O-O} Å	6.69	5.30	4.64	4.21	3.91	3.68	3.50	3.34	3.12	3.10	3.00	2.92

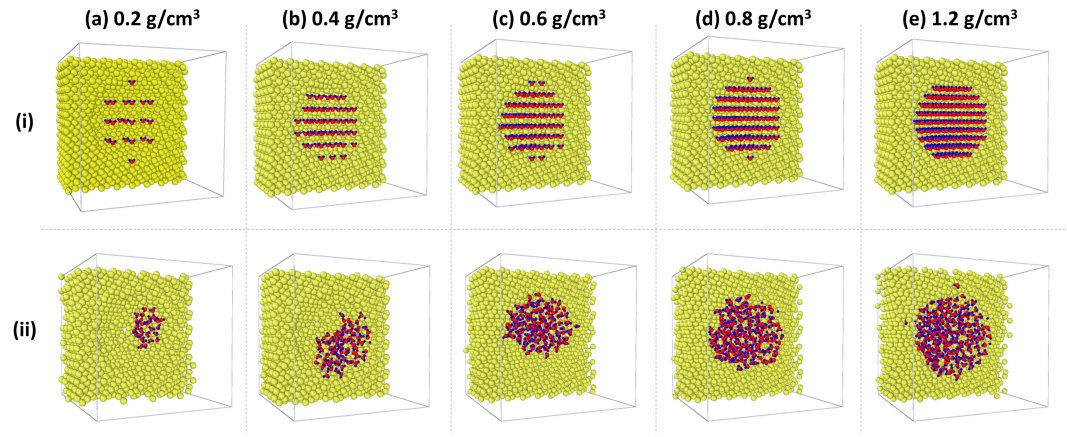

Figure 4.1: The simulation models for the different densities of (a) 0.2, (b) 0.4, (c) 0.6, (d) 0.8, (c) 1.2 g/cm^3. The upper and lower configurations (i) and (ii) represent the initial and equilibrium states of the system at the corresponding densities, respectively.

always 14.48 Å to obtain the same porosity.

4.1.2 System equilibrium and characterization

The velocity of each atom is initialized using a Maxwell-Boltzmann distribution, relaxing the system in the NVT ensemble for 200 ps at the temperature T_{eq}. Then, a NVE run is imposed during 70 ns where the thermal conductivity is computed using EMD method (see section 2.3 for more details). All the configurations studied here are simulated using periodic boundary conditions.

The bulk system is divided into 100 spatial spherical bins with a thickness of 0.2172 Å defined from the center to the edge of the pore. A small bin size is chosen to correctly characterize the fluctuations at the interface. The density and the pressure inside of each bin are calculated and averaged. The profiles are then plotted as a function of distance from the center of the pore.

4.2 Results

4.2.1 Effective density vs Thermal conductivity

Fig.4.2 shows the thermal conductivity of bulk water and the confined water in the nanoporous silicon as a function of density. For bulk water in the figure, the TC is featured by a moderated increase with the density, increasing from 0.05 W/(m·K) at 0.2 g/cm^3 to 1.5 W/(m·K) at 1.2 g/cm^3. At room temperature, a density of 1.2 has 30 times thermal conductivity than the one at 0.2 g/cm^3. In marked contrast,

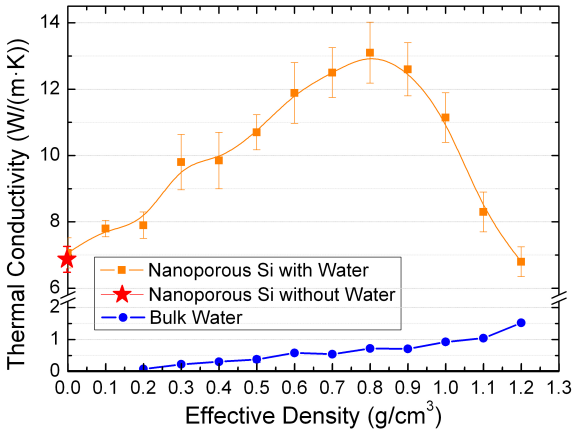

Figure 4.2: Thermal Conductivity of nanohybrid water-nanoporous silicon system as a function of effective density (initial density of water), with the MD data of bulk water

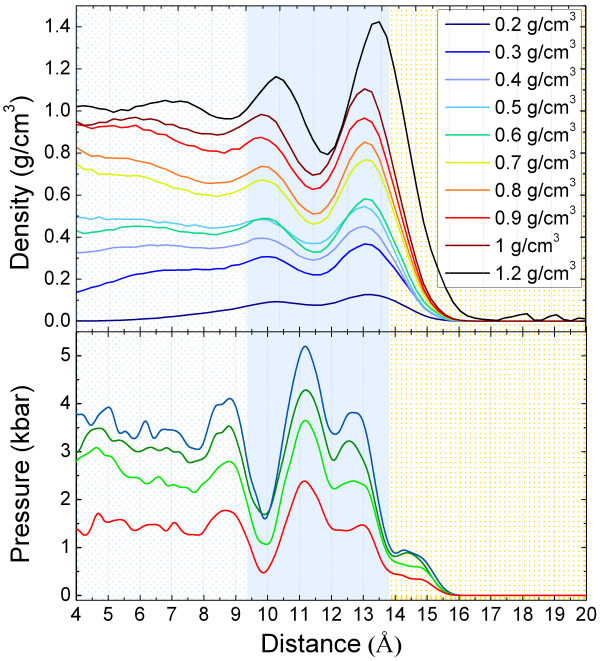

Figure 4.3: Density and pressure profile of nanohybrid water-nanoporous silicon system along radial direction under different effective densities of water immersed.

the thermal conductivity of nanoporous silicon with the confined water exhibits a distinct trend (orange line in the figure). The red star point with the value of 7 W/(m·K) represents the TC of dry sample (water density is 0 g/cm^3). The TC profile reveals that the TC of hybrid system follows two stages. The first stage corresponds to the density below 0.8 g/cm^3. With increasing density, the thermal conductivity displays an approximately linear increase until the value about 13 W/(m·K) at the density of 0.8 g/cm^3. Almost doubled value here is found compared with the dry sample. After an upward, the second stage starts with a downward trend instead of a monotonous trend like bulk water. Moreover, after 1 g/cm^3, it declines speedily with decreasing density of water.

From the above results, it seems that the thermal conductivity of nanoporous silicon undergoes a substantial change with the effective density of water molecules inside the pore. A maximum value is proved to appear near the density of 0.8 g/cm^3.

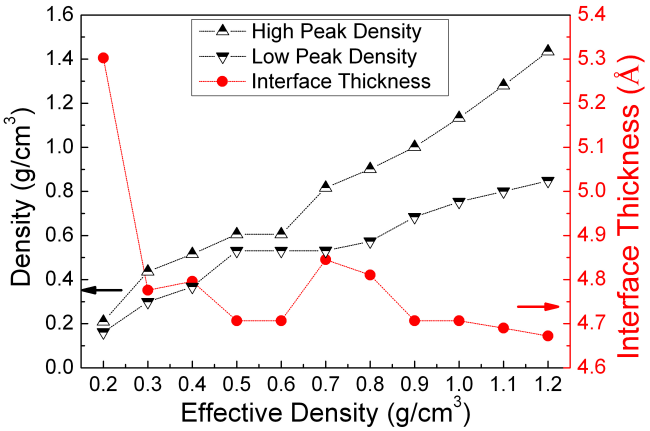

Figure 4.4: The interface thickness and density value of high and low peak in the interface calculated through density profile as a function of effective density

4.2.2 Density and pressure profiles

It is well known that a change in the density of water at room temperature is necessarily accompanied by a change in pressure, even leading to a phase change. It means that an accurate study of density and pressure profiles is quite crucial in understanding the water molecules in the confined system.

The density and pressure profiles for different effective densities are shown in Fig.4.3. The profiles reflect similar trends at different densities, with subtle differences. The density profile starts from the center of the pore. When the effective

density is below 0.6 g/cm^3, the density in the center is lower than the corresponding effective density. In contrast, a higher density value compared with the corresponding effective density occurs at 0 position when the effective density is high than 0.7 g/cm^3. Then, I focus on the interface region. From 0.2 to 0.6 g/cm^3, only two maxima and one minimum are obviously observed. Due to the limited number of water molecules and swirling as clusters in the pore, the interface boundaries adjacent to the core are very difficult to define, resulting in an illusion of a larger solid/liquid interface at low effective density. The thickness interface is crudely estimated in the Fig.4.3. We can also say that the traditional obvious interface no longer exist at low density range. At the density higher than 0.7 g/cm^3, the density profiles near the interface change considerably. Particularly at the density of 1.2 g/cm^3, it soars quickly from the minimum to maximum value. Such an extremely rapid change in density causes the water molecules to show a clear stratification at the interface, impeding the transfer of heat.

The numerical value of high and low peak, as well as the shell thickness defined are shown in the Fig.4.4. The density of high and low peak grow moderately with effective density of nanohybrid water-nanoporous silicon. The difference between them becomes higher and higher starting from the density of 0.6 g/cm^3. The most higher difference at the density of 1.2 g/cm^3 reaches 0.6 g/cm^3. The shell thickness shows an abnormal high value in the range of 0.6 to 0.9 g/cm^3, while a slight decline with the effective density follows after the density higher than 0.9 g/cm^3.

The snapshots in the Fig.4.1 give us a most direct approach to understand the complex behaviors observed for the confined water. What we observed is that in the low density states, the water molecules is not distributed homogeneously and most of them shows a discontinuous states. So instead of the overall pressure of water, the pressure profiles is a much more effective to express the localized pressure in the pore. To simplify the simulation, the pressure profiles of the effective density from 0.6 to 1.2 g/cm^3 are extracted, presented below in Fig.4.3. It shows that the pressure in each region of the system is positively correlated with effective density. At the density of 1.2 g/cm^3, the pressure changes sharply near the interface.

Actually, in the study of confined water inside carbon nanotubes, a special behavior of pressure profile as a function of water has been observed (Sadeghi & Parsafar 2013). As shown in the Fig.4.5, several distinct regimes could be concluded. The first one is from 0.1 to 0.55 g/cm^3, less change is shown in the low density range. From 0.55 to 0.88 g/cm^3, the pressure value rises and falls twice, explained by the formation of much ordered phases in the reference. Above

0.9 g/cm^3, the pressure rise with the same rate until the end. The change of pressure in the range of 0.6 to 1.2 g/cm^3 in my study reveals that the molecular arrangement is strongly altered, affecting the thermal transport. It's even possible that a phase transition of water occurs.

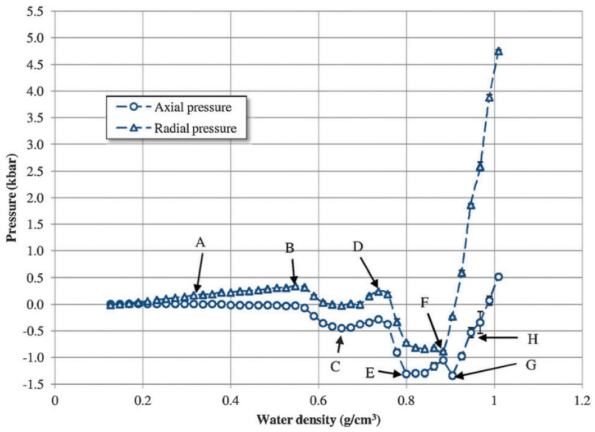

Figure 4.5: Axial and radial pressure profiles as a function of water density for the water confined in the carbon nanotube with the diameter of 1.28 nm (Sadeghi & Parsafar 2013).

4.2.3 Radial distribution functions

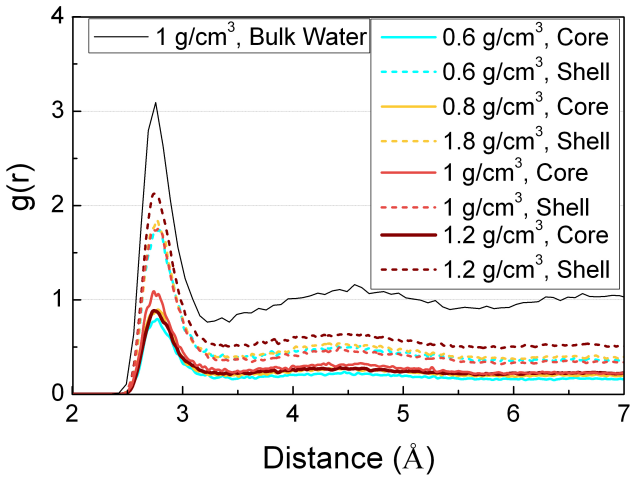

Figure 4.6: The Partial Radial Distribution Functions of O-O pair for different parts (core and shell) of nanohybrid water-nanoporous silicon system under different effective densities.

The radial distribution functions of water in the core and shell for different effective densities(0.6, 0.8, 1, 1.2 g/cm^3) are depicted in Fig.4.6. To remain the

original difference, the normalization of the RDF profiles have not been done here. The shapes between different densities are quite similar to each other. Only one obvious peak at 2.7 Å is observed. The position of the first neighbor peak is independent on the effective density. As the distance being longer than 3.2 Å, the RDF for different densities don't show much differences. The density of the g(r) for the shell is generally higher than the core due to more ordered structure in the shell. With the density increases, the peak of the g(r) for the shell is broader than the core, with a higher maximum value, meaning that more ordered phases of water are formed in this region.

4.2.4 Velocity and motion displacement

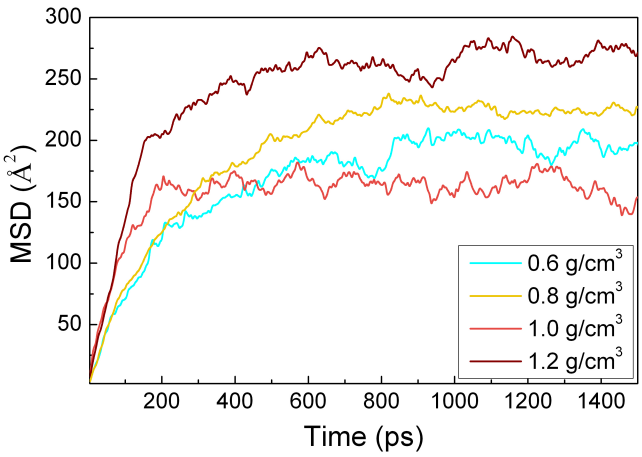

Figure 4.7: Mean Square Displacement Function(MSD) and diffusion calculated using MSD as a function of effective density

To check the effect of the motion of the nanoconfined water on the thermal properties, the Mean Square Displacement (MSD) is studied, further with estimating the diffusion coefficient. The diffusion coefficient is obtained using the slopes of MSD profile. The results of MSD are shown in Fig.4.7.

It is observed that the MSD for all cases follow the same trend with the ones for the case of temperature, as discussed in Sec.3.2.4. A classical Brownian motion is displayed at the first 100 ps. The slopes in this region are dependent strongly on the effective density, being much greater for higher density. Furthermore, after 200 ps, the MSD values show a non Brownian diffusion reaching a saturation with the slope of 0.

The results of diffusion coefficient are shown in the Table.4.2, calculated us-

ing Eq.2.33. The value of α is equal around 1, indicating that the normal diffusion occurs for different densities. In Table.4.2, the values increase from 0.21 Å^2/ps at 0.6 g/cm^3, to 0.27 Å^2/ps at 1 g/cm^3, followed by a sharp decrease to 0.1 Å^2/ps at 1.2 g/cm^3. In consequence, the diffusion coefficient is limited in the high density region, and enhanced in the certain effective density region where the thermal conductivities also show an enhancement.

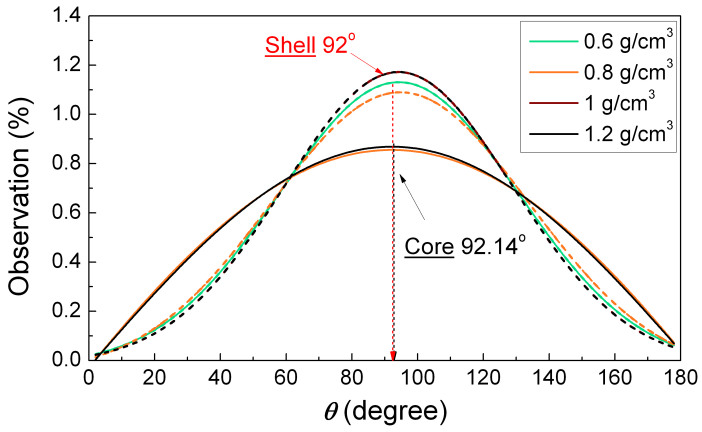

Figure 4.8: The Angle between the molecular dipole moment and the radial direction of oxygen atom in the same water molecule as a function of effective density. The radial angle value for center and shell region are both subject to the amplitude version of Gaussian peak function (GaussAmp) under different densities conditions. These values are quitely similar with the results of temperature effect.

4.2.5 Orientation of water molecules

For the orientational dynamic analysis, to simplify the comparison, the results with the density greater than 0.6 g/cm^3 are calculated, shown in Fig.4.8. At any density ranging from 0.6 to 1.2 g/cm^3, the angles between the molecular dipole moment and the radial direction of oxygen atom in the same water molecule reveal the similar trend. Conforming with the Gaussian simulation, the most likely angle from the center of the system to the solid/liquid interface, are 92.14°and 92°, which

Table 4.2: Diffusion coefficient for different effective densities of the nanoconfined water extracted by Fig.4.7

Density (g/cm^3)	0.6	0.8	1.0	1.2
Slope	0.99	0.98	0.93	1.03
D (Å^2/ps)	0.21	0.25	0.27	0.1

occur with the possibility of 0.87% and 1.13%, respectively.

4.2.6 Hydrogen bonds network

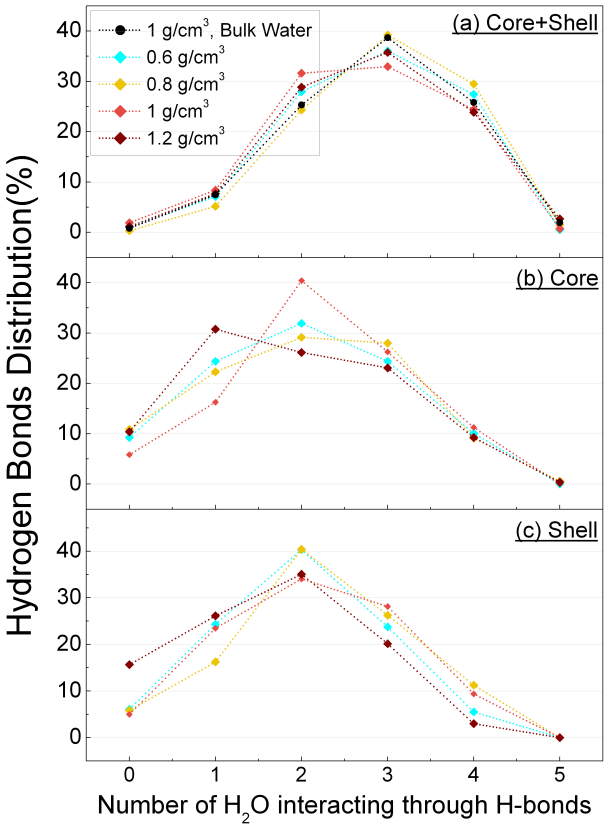

Figure 4.9: Hydrogen bonds (water water H-bonds) distributions for different effective densities in different region in the pore contributed from the interaction of water and its neighbor water molecules within 10 Å. From the top to bottom of the figure, the region studied are the whole pore (all waters in the core and shell),the core and shell.

To provide topological analysis of H-bonds networks, the averaged numbers of water molecules connected with a central water molecule through hydrogen bonds for different effective densities are shown in Fig.4.9. The connected hydrogen bonds numbers in core, shell and in the both of them, are compared with bulk system with the aim of illustrating the dynamic behavior of the resulting intermolecular network. The first figure for analyzing all H-bonds in the pore, displays the large concentration of waters with the variation trend of H-bonds. Compared to the bulk water, the water molecules in the pore at the density of 0.6 and 0.8 g/cm^3 have a lower value for shorter H-bonds, and higher value for 4 or 5 H-bonds. It reveals that the confined space improves the formation of H-bonds of water. No

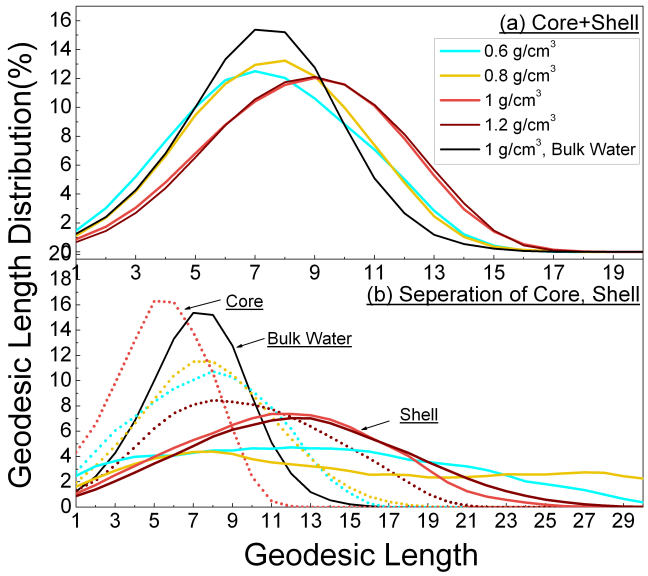

Figure 4.10: Distribution of geodesic (gd) lengths found of water with different effective densities (a)in the pore, (b)core and (c)shell.

longer than 5 number of H-bonds is observed in any case of effective density. I can also said that the independent H-bonds (0 H-bonds) and much longer H-bonds (5 H-bonds) is insensitive in the density. The hydrogen bond being reformed or broken are connected through 2, 3, 4 and 5 numbers of bonds. For nanoconfined water, similar trends for 0.6, 0.8, 1.0, 1.2 g/cm^3 that at high densities, smaller values for shorter 0-1 and larger 5 H-bonds are discovered. Especially at the density of 0.8 g/cm^3, which corresponds the density with the highest thermal conductivity, few number of water molecules are interacted through 1, 2 H-bonds, consequently 2, 3 water molecules connect together. The distribution of H-bonds at the density of 0.8 g/cm^3 is almost 40% for 3 H-bonds, and 30% for 4 H-bonds, 5% higher than the ones at 1.2 g/cm^3. A "perfect" network is found here at 0.8 g/cm^3 though hydrogen bonds network.

To further analyze of the H-bonds distribution of different region in the pore, the observed data for the water molecules in the core and shell are compared in the Fig.4.9(b) and (c). Obviously the water molecules in the core with high effective densities, show more shorter H-bonds connecting water molecules in the core, with higher values for 1 and 2 H-bonds. It proves that the water in the core is occupied by fewer water molecules in the neighbors, which hinders the propagation of heat. The number of H-bonds in the shell is higher compared to the core. A more stable hydrogen bonding network is formed, which facilitates the heat propagation.

Fig.4.10 shows the analyse of geodesic length to evaluate the grade of connectivity within the hydrogen bond networks. As observed in Fig.4.10(a), the distribution of geodesic length for all cases are always in Gaussian shape, being same with the results in previous chapter. At the low density of 0.6 g/cm^3, the gd profile has a peak value of 7 H-bonds with the distribution value of 12%, which is smaller than the other densities. For 0.8 g/cm^3, the gd exhibits a higher and narrow distribution of geodesics centered around the mean value of 8 H-bonds. Associated with the results of thermal conductivity, a specific density of nanoconfined water which has a concentrated distribution of gd is conducive to heat propagation. In the contrast, the gd distribution for the higher effective densities becomes much broader with larger number of geodesics length greater than 10. It indicates that hydrogen bonds with much dispersed length of pathway is formed at high effective density. A comparison of the geodesic length for the water molecules in the core and shell can be found in the Fig.4.10(b). Basically, the water in the core are connected through the shorter hydrogen bonds pathway, which is accordance with the lower value observed of hydrogen bonds numbers in the core. The extremely dispersed value for the shell at 0.6 and 0.8 g/cm^3, I think that it is caused by the low number of water molecules in the shell region after dividing two regions. So it takes a long pathway of hydrogen bonds to connect each other.

4.2.7 Density of states

Phonon density of states (DOS) of the nanoporous silicon and the water confined in hybrid nanoporous materials are shown in FIG.4.11. The DOS for nanoporous silicon exhibits always two peak value at about 6 THz and 17 THz. Compared to the bulk water, almost no shift of optical and acoustic peak of the silicon atoms is observed for different effective densities. Specifically, the DOS for 1.2 g/cm^3 has a higher value for acoustic peak and lower value for optical peak. Especially, the effective densities of 1 and 0.8 g/cm^3 keep higher peaks for transverse optical mode. This important increase of high frequency phonons contributes to an augment of thermal conductivity, which has also been proven in the literature (Hu *et al.* 2011).

Compared to the bulk water, confined water has a higher value at low frequency. I point out that the DOS at 0.6 and 0.8 g/cm^3 from 5 to 9 Thz create an extra change, rather than a decline for bulk water in the same window frequency. It is argued here that this is a signature of overlap of the confined water and the transverse acoustic mode of silicon atoms, which might promote the thermal conductivity.

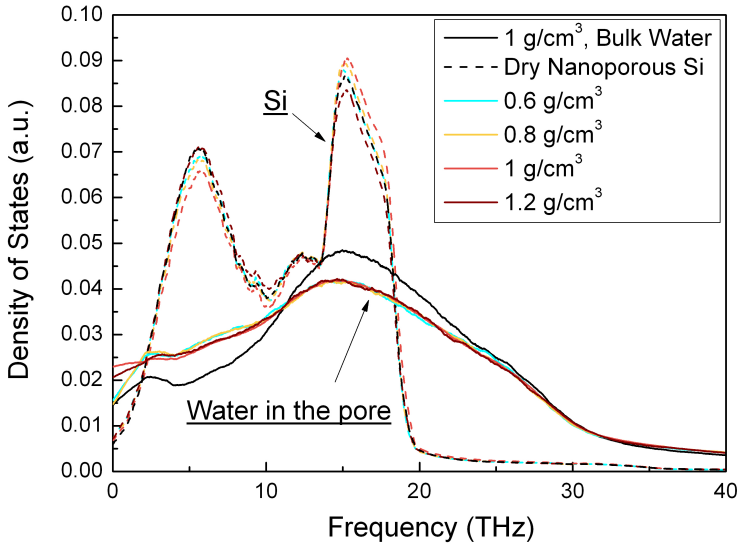

Figure 4.11: Density of States for bulk water with black continuous line, nanoporous silicon without water with the grey continuous line, the one with confined water with water pointed lines, and the nanoconfined water in the pore with continuous lines, for different effective densities.

4.3 Conclusions

In this chapter, the effect of effective density from 0.2 to 1.2 g/cm^3 on the thermal conductivity of wet nanoporous samples was investigated here. a maximum value of TC at the density around 0.8 g/cm^3 was found for the first time. The TC increases gradually from the density of 0.2 g/cm^3, then reaches a peak at 0.8 g/cm^3, after which the TC decreases sharply along with the increase of the effective density until the value of 1.2 g/cm^3. The underlying mechanisms are also related to the stratification of the water molecules at the vicinity of the solid/liquid interface.

To understand the non-monotonic change of thermal conductivity as a function of effective density, several structural and dynamical properties of the nanoconfined water, separated in a core water molecules (bulk-like) and shell water molecules (dense water layer close to the solid/liquid interface) have been studied numerically. When the effective density is high than 0.7 g/cm^3, huge density difference between two peaks near the interface cause lower TC. Also the shell thickness for these densities are much larger, compared to other density values not in this range. A dramatic change of pressure near the interface is found for the density of 1.2 g/cm^3. With the analysis of RDF, no phase transition is observed in the density range of 0.6 to 1.2 g/cm^3.

From another point of view, dynamical features such as the mean square displacement mentioned that the water molecules at the higher density move faster at the beginning of diffusion. And then, the movement of water molecules reaches to a platform, which is dependant on the corresponding effective density. Concerning the orientation of water molecules, the Angle between the molecular dipole moment and the radial direction of oxygen atom are independent of the effective density both in the core and shell. The hydrogen bond networks study for nanoconfined water reveals that longer hydrogen bond pathways with the number of 3 and 4 are found, at the density of 0.8 g/cm^3, corresponding to the highest thermal conductivity. With increasing the effective density, the tendency of water molecules creating shorter networks in increasing the density, leads to the decline of the effective thermal conductivity of the hybrid nanosystems. The geodesic length profile of the nanoconfined water for the density of 0.8 g/cm^3 has a higher and quite narrow distribution. For densities higher than 0.8 g/cm^3, the distributions became much broader, with significant geodesic lengths greater than 10. Last but not the least was that the DOS of the silicon pores atoms and the nanoconfined water molecules overlaps at the low frequency, inducing a increased juxtaposed areas and this qualitatively means that new heat flux channels are established between the solid matrix and the nanoconfined water.

To sum up, the maximum value of the thermal conductivity at 0.8 g/cm^3 are explained. I gave physical insights of the observed phenomena for the density from 0.6 to 1.2 g/cm^3 with structural and dynamical parameters. Hydrogen bonding network proved that, minor structural changes of water molecules can have an impact on the thermal conductivity at different densities. Combined with the conclusion of previous sections, the main reason giving rise of higher thermal conductivity is much clear in our framework.

Synthesis of the Chapter

- The effective thermal conductivities as a function of the effective initial density of wet nanoporous samples are depicted.
  - The TC of nanoporous silicon with the confined water increases gradually from the density of 0.2 g/cm^3.
  - An surprising maximum value is found at 0.8 g/cm^3.
  - And then, the TC decreases sharply along with the increase in the density until the value of 1.2 g/cm^3.
- Density and pressure profiles provide the complex behavior for the density range of 0.7 to 0.9 g/cm^3 near the interface.
  - For low effective density, the interfacial region is blurred.
  - For high effective density, huge density difference between two peaks near the interface causes lower TC
  - The shell thickness for these densities are much thicker, compared to other density values not within 0.7 to 0.9 g/cm^3.
  - A dramatic change of pressure near the interface is found for the density of 1.2 g/cm^3.
- No phase transition is observed from RDF for the density range of 0.6 to 1.2 g/cm^3.
- By mean square displacement and diffusion coefficient, the movements of the water molecules inside the pore are investigated.
  - Both normal diffusion and confined diffusion are observed.
  - The water molecules at the higher density move faster at the beginning of diffusion.
  - Nanoconfined water depends strongly on the effective density.
- The hydrogen bond networks reveal the effect of the localized interaction of hydrogen bonds on the TC.
  - Water molecules create shorter networks, corresponding to the decrease of the effective TC in increasing the density.
  - Longer hydrogen bond pathways with the number of 3 and 4 are found, at the density of 0.8 g/cm^3, corresponding to the highest TC.
- The juxtaposed areas are increased for the DOS at the density of 0.8 g/cm^3.
  - The new heat flux channels are established between the solid matrix and the nanoconfined water.
  - A higher value of DOS overlaps at the low frequency, inducing a increased juxtaposed areas.

CHAPTER 5

Size and spatial distribution of nanoporous silicon with confined water on the effective thermal conductivity via NEMD

Contents

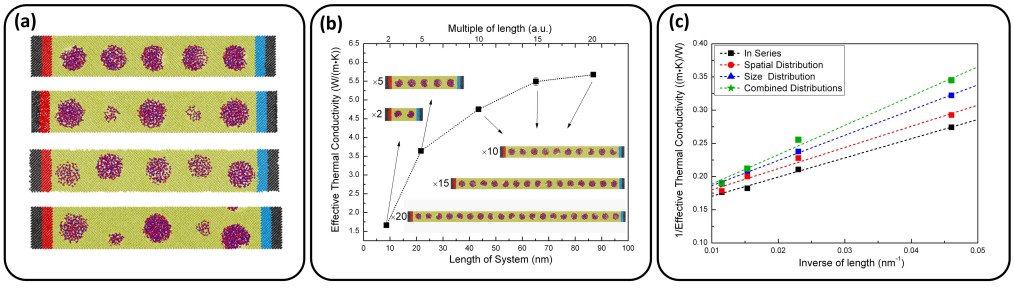

Visual Abstract: (a) the simulated configurations for pore distribution, (b) the effective thermal conductivity of nanoporous silicon as a function of length and (c) the inverse of TC to calculate the TC for the infinitely long system.

This chapter focuses on the effect of pore position and pore size on the nanoporous silicon with the confined water. Using Non Equilibrium Molecular Dynamics (NEMD) simulations, the role of the position and the size of the pore on the thermal conductivity have been investigated. This has also been done for several lengths of system to obtain the thermal conductivity of infinitive size systems. The total porosity content has always remained constant. Furthermore the mean free path of phonon in the system is deduced, as well as the TC of the infinitely long system. The derived details are presented in the following section.

5.1 Simulation details

Compared to the sustainable equilibrium state in the Equilibrium Molecular Dynamics (EMD), Non Equilibrium Molecular Dynamics (NEMD) simulations is carried out in a non-equilibrium state by imposing a stable and uniform distribution of heat flow. In general, the model in NEMD extends in one direction to allow for conveniently applying heat flow from both sides. The configuration in this study is designed based on this thought, then the system is built by defining the force field, the environmental factor, the boundary conditions, etc. In the following subsections, the details about the simulation methods are provided.

5.1.1 Determination of the configuration

5.1.1.1 Materials and interaction potentials

Following previous chapters, the new configuration is produced by replicating the cubic monoporous silicon along the longitudinal direction. The new simulation cell illustrated in Fig.5.1, consists of nanoporous silicon, the confined water, and two crystalline silicon walls. Depending on the length of the system, the main simulated cell of the simulation contains different numbers and sizes of pores. By varying the position and the size of pores, the spatial distribution and the size distribution are realized. Moreover, by tuning both the size and position of the pore,

the combined distribution on the TC is also investigated. The interatomic potentials obey the Lennard-Jones potential for water, Stillinger-Weber for Si-Si interactions, as elaborated in the previous chapters.

5.1.1.2 Size of the configuration

I varied the length of the main simulated cell of the system to $2\times, 5\times, 10\times, 15\times$ and $20\times$ of the unit cell in the longitudinal direction. The unit cell takes the same size length as the cubic crystalline silicon in the previous chapter, with 43.44 Å in three directions. There are two additional walls on the both sides, each of which has a thickness of $4a_0 = 21.72$ Å. Each of them contains two parts of the same thickness: the fixed one as the first outer layer, and the non-fixed one as the second outer layer for imposing the high and low temperature heat source to the system.

The overall porosity of the system remains 15.51%, and the density of confined water remains 1 g/cm^3. The spatial distribution is obtained by varying the position of pores. The center position of each pore varies randomly in the range of 21.72 ± 17.40 Å in the three directions. The size distribution is realized by changing the radius of each pore in the range from 10.86 to 16.29 Å. The details for the size of configuration are listed in Table.5.1.

Table 5.1: The simulated details for the NEMD configurations.

Porosity(%)	Repetitions of the unit cell	Length thermostat(Å)	Total Length(Å)	Total Number of Atoms
15.51	2	86.88	130.32	13056
	5	217.2	260.64	26496
	10	434.4	477.84	48896
	15	651.6	695.04	71296
	20	868.8	912.24	93696

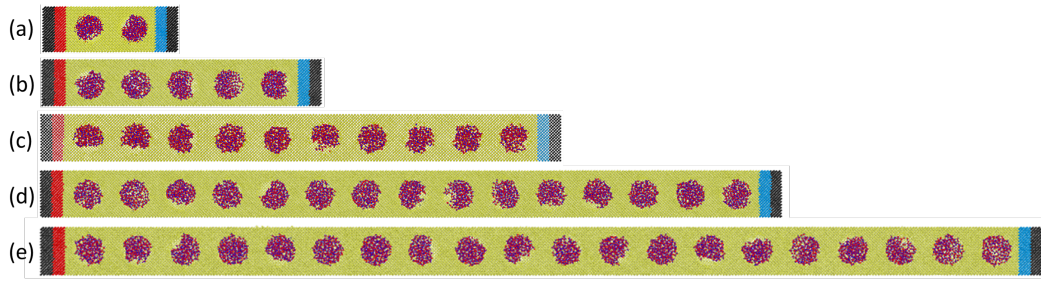

Figure 5.1: The configuration of longitudinal nanoporous silicon with the confined water in this chapter. The system is available in different length by replicating different times of cubic monoporous silicon. From (a) to (e), the multiple time of pore is clearly seen as 2, 5, 10, 15, 20, respectively. More details correspond to the Table.5.2.

5.1.2 System equilibrium and characterization

Table 5.2: The illustrations of NEMD configurations corresponding with the length of system.

Name	Illustration
In Series (labeled as 'ins')	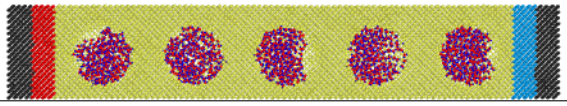
Size distribution (labeled as 'size')	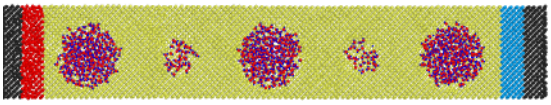
Spatial distribution (labeled as 'spatial')	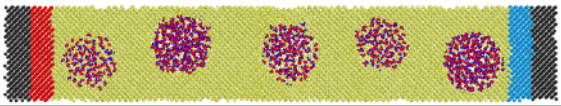
Combined spatial/size distributions (labeled as 'combined')	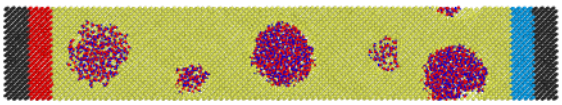

The periodic boundary condition is applied in the vertical and lateral directions. In the longitudinal direction, fixed boundary conditions are achieved by forcing the inner atoms not interacting with outside of system in this direction.

All atoms are firstly set by an initial velocity at 300 K using Maxwell-Boltzmann distribution. Then with Nose-Hoover thermostat, NVT ensemble for 300 K is applied during 0.5 ns to reach an isothermal stable state. After that, the atoms in the first outer layers on the both side are fixed, while the ones in the second outer layers are still under NVT ensemble. The Nose-Hoover thermostat are

applied at different temperature 270 K and 330 K on the left and right second outer layers, to induce the heat flux through solid/liquid interface. Finally, the rest silicon atoms and the confined water molecules in the main simulated cell are under NVE ensemble. The whole system is performed under the above heat flux during 40 ns (4×10^7 timesteps) to reach equilibrium state.

To get the computational results, the system is divided into 100 slab bins with different sizes, which vary with the length of the system. The desired properties are averaged over every 0.1 ns and caught out in the file every 1 ns.

5.2 Results

5.2.1 Length effects on thermal conductivity

Firstly, NEMD simulations for the model with five straight-line aligned pores are performed. The Fig.5.2 shows the variation of transfer energy rate that added into the system from the hot side and removed to the cold side. Heat flow is measured as a positive value at the high temperature side, and reversely it is negative at the low temperature side. As shown in the figure, the transfer energy rate changes linearly with increasing time and the curve is symmetrical along the 0-axis, which corresponds well to the system energy conservation. According to the Eq.2.29, the heat flow or energy power provided by the bath thermostat can be obtained by dividing the transfer energy rate by the cross-section area of system. Thereby, the effective thermal conductivity of the nanoporous crystalline silicon with the confined water can be achieved by Eq.2.30.

The thermal conductivities of nanoporous silicon with the confined water varing with the length are shown in the Fig.5.3. A range of the length of system between 8.8 nm to 88 nm helps to investigate the length effect at room temperature 300 K. Due to the fixed atom at both sides, phonons are constrained under the limitation of the boundary for the small length of system. Therefore, few thermal conductivity is found for the smaller length. And then, what we can clearly observe from the figure is that the thermal conductivity increases non-linearly with the growth of the system length. When the system contains two pores with a length of 8.7 nm, its thermal conductivity is about 1.6 W/(m·K). The thermal conductivity of the system with a length of about 21.7 nm increases to 3.6 W/(m·K). After that, the thermal conductivity continually grows. Until the system contains 20 pores, of which the length is 86.9 nm, the thermal conductivity reaches about 5.7 W/(m·K).

In this solid-liquid hybrid system, the effect of system length is positive. On

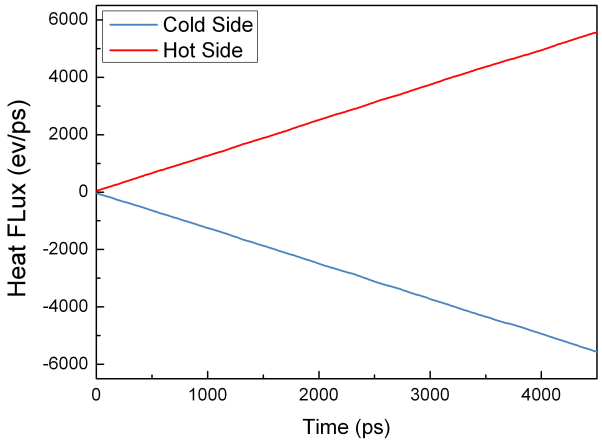

Figure 5.2: The transfer energy rate added into the nanoporous silicon with the confined water from the hot side and removed to the cold side.

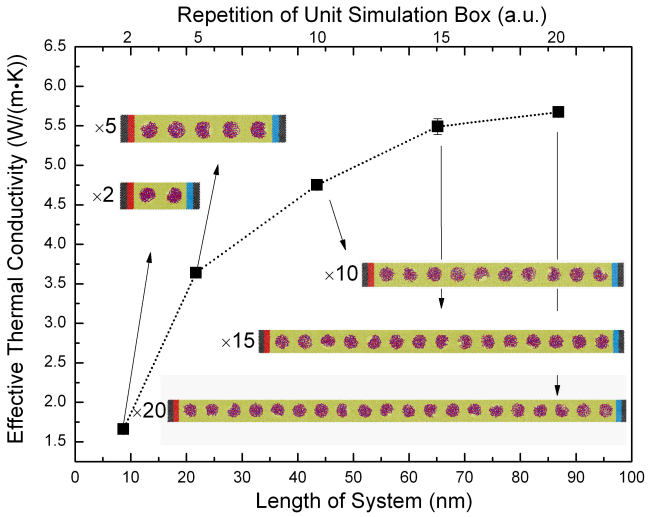

Figure 5.3: Thermal conductivity of the nanoporous silicon with the confined water with different length in one direction at room temperature, as well as the fitting curve.

account of the increase of the length, the possibility of the phonons to travel further grows and more phonons are involved, enhancing the efficiency of the heat transfer. That's the reason for the significant rise of thermal conductivity with the length augment until 50 nm. However, when the length of system is greater than 50 nm, the magnitude of improvement becomes smaller. That's because at constant porosity, the presences of more voids and interfaces make the system more defective and the chances of phonons not being able to pass through the defects are greater. Moreover, the phonons interact with each other more often. As the length increases, the negative effect of length on thermal conductivity gradually dominates. This makes the thermal conductivity reach a platform value instead of following the continuous growth when the length reaches a certain value (Mortazavi *et al.* 2016; Felix & Pereira 2018).

An theoretical model suggested by Sellan et al. (Sellan *et al.* 2010) is usually possible to predict successfully the thermal conductivity k_l as a function of length. It followed the Matthiessen's rule and applied the Boltzmann transport equation in order to express the size dependence on TC. It can be described as:

$$\frac{1}{k_l} \propto \frac{1}{L} + \frac{1}{k_{bulk}} \tag{5.1}$$

k_l converges to k_{bulk} as the length of system is infinite. By substituting our results into the above equation, it can be easily verified that this approach is not applicable in the model of this study. When the solid liquid system is taken into account, the simple relationship between the relaxation time and frequencies of phonons in the original model is not accurate. In addition, some assumptions about phonons dispersion, which are only suitable for the simple system such as single-element crystal Si, are no longer reasonable (Sellan *et al.* 2010). So far, although many researches have been carried out on the prediction of thermal conductivity of two phase materials, they are mostly applied to bulk systems. Taking the system dimension into account, many methods reveal significant shortcomings. Hence, a simple model or prediction procedure relating the thermal conductivity of solid liquid system with the size dependence need more attention.

5.2.2 Pore position and size distributions on thermal conductivity

In this subsection, the effects of the size and position of the pore on the thermal conductivity of the material are investigated and the results are shown in Fig.5.4. Again, it is emphasized that all cases are kept at the same porosity of 15.51%. It is clear from the histogram that compared to the one of in series, the thermal

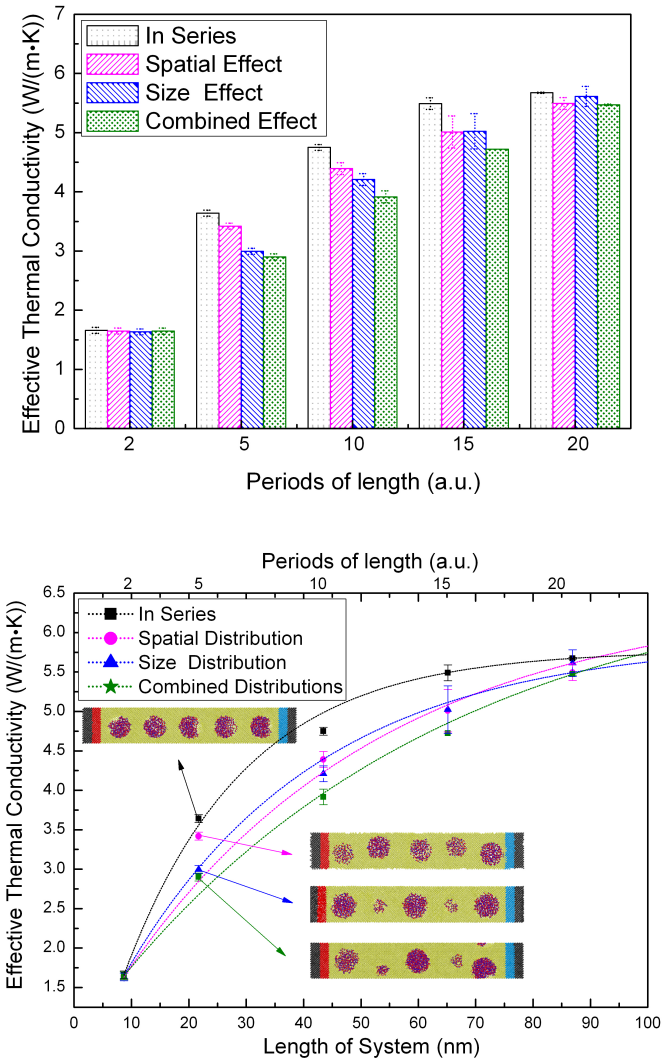

Figure 5.4: Thermal conductivity of the nanoporous silicon with the confined water for different distribution of pores at room temperature, as well as the fitting curve.

conductivity has certain attenuation at a given length under the two effect factors of the position and size of the pore. Taking the system length of 43 meters as an example, compared to the one of in series, the thermal conductivity decreases by 7% when only changing the spatial arrangement of the pores and by 11% when only changing the size of the pores. The largest decrease of 17% was observed when the both acted together. It can also be noticed that varying the pore size affects the thermal properties of the material more severely than spatially varying the pore arrangement position. It can be imagined that the combined distribution of the pore is the greatest obstacle to heat propagation . As shown in the figure, it leads to the declines about 20%, 17%, 14%, and 7% for lengths of 21.7 nm ($\times$5), 43.4 nm ($\times$10), 65.1 nm ($\times$15), and 86.9 nm ($\times$20), respectively.

However, this remarkable decrement of the thermal conductivity has not been observed for the similar study of the micro pore materials. M. Zhang et al. (Zhang *et al.* 2018b) investigated the TC of ceramic closed-cell foams with multi-scale pores. The result which can be compared with our study is that when the porosity is 18%, the decay of thermal conductivity is less than 10% by changing the pore distribution. Comparative studies of nanoporous materials on different scales suggests that the pore nanostructure as a crucial and complex factor, affects the material properties, which depends on the pore size, the position, even the morphology.

The thermal conductivity behaviour is also analysed in the lower figure in Fig.5.4. The trend of the thermal conductivity with the length of the system is evident. The thermal conductivity increases non-linearly with increasing length in all cases of distributions. The TC shows a continuous growth, but the growth rate of TC decreases with the length augment. When the system is small enough (less than 8 nm here), the thermal conductivity of the system basically does not vary with neither the pore size nor the position. In this study, the ballistic regime could be defined for the length minus to 40 nm, where the TC shows a linear positive correlation to the length. In this region, the MFP of phonons is larger than the system size. After that, accompanying with the larger length of system, the MFP becomes much comparable. Consequently, the ballistic regime starts to transit to the diffusive regime. Here, this transition is roughly defined in the range of 44 nm to 88 nm. In the case of length greater than 88 nm, where the MFP is much smaller than the system size, TC shows almost an independence with the length. The fitted lines are performed with small uncertainties, with which the TC of infinitely long system and MFP can be obtained in the following subsection.

Regarding the porous materials with two phase, several models are avail-

able to predict the pore distribution of the thermal conductivity. Most of them have been proved to be suitable for the cubic bulk system in the macroscope (Yuan & Sundén 2013; Zhang *et al.* 2018b). In the 3.2.1, two mathematical methods EMA and ME are presented. EMA is a useful tool to forecast the thermal conductivity, which fully considers the contribution of the interface. ME model is designed for macroscopically isotropic, homogeneous materials with two phases, the continuous one and the dispersed one. However, these two models have not reached an adequate consideration of pore features, such as the morphology and the position.

Hence, Cirillo Atzeni (Atzeni *et al.* 2008) presented a fractal procedure called Intermingled Fractal Units model (IFU), which is useful to reproduce any type of pore and consequently possible to predict the thermal conductivity for any porous materials. Giorgio Pia (Pia *et al.* 2016) applied it to calculate the TC of Yittria-stabilized zirconia (YSZ). The result is more consistent with experimental data. It is quiet capable of exhibiting the dependence of thermal conductivity with different pore features, than the two methods mentioned above.

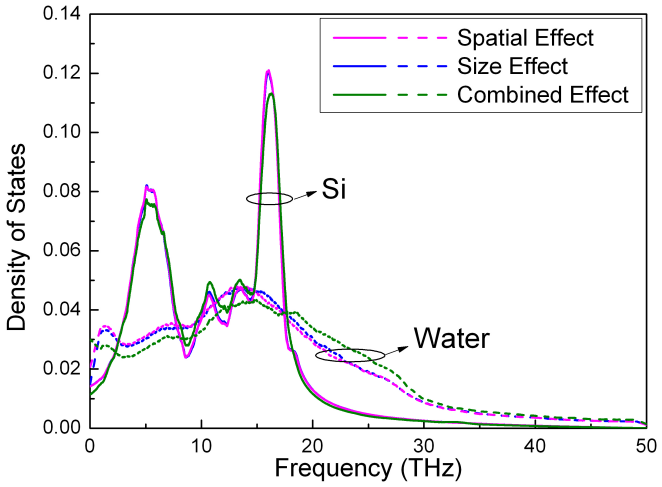

Figure 5.5: Density of stats for the nanoporous silicon with the confined water for different distribution of pores

It is well known that the thermal conductivity is affected by both the frequencies of phonons, as well as the mean free path of phonon. Here, the density of states for the system with the length of 15×43.44 Å are studied. A unit cell in the middle position (the eighth pore) with the size of $43.44 \times 43.44 \times 43.44$ Å^3 is chosen. In this cubic cell, the size and position of the pore are always the same in

all cases. The velocity data for DOS calculation is extracted from this cell. Fig.5.5 displays the results of DOS. What is directly seen that the DOS of both silicon and water exhibit the bulk behaviours. Following the trends and peaks of DOS profiles, the characteristic features of phonon DOS are independent of pore distribution. Furthermore, both for the silicon and the water, the DOS for spatial and size distribution have the same consistence. So what stands out is the difference between them and the combined distribution case. For silicon, the peaks around 7 and 17 THz possess greater heights for the spatial and size distribution. Correspondingly, for their DOS of the water, the amplitude in the low frequency range 0-17 THz are also higher compared with the combined one. These important overlaps of the available states of phonons promote phonons carrying heat, which can contribute to the increase of their thermal conductivity (Cao *et al.* 2018).

Another noteworthy feature displayed for the DOS of the water is that for combined distribution case, more available states of phonons are found for a range of frequencies larger than 17 THz. It indicates more phonons in the water are involved in the vibration at high frequencies. The insightful augments raised by Giri and Hopkins help to interpret an increase in the amplitude of DOS (Giri & Hopkins 2014): it can be attributed to the vibrational mode which prevent the phonons from transferring to the adjacent phases. So i thought that high frequency phonons with a larger DOS value decrease the thermal conductivity of the material. In addition, for solid liquid systems, many findings pose as evidence that the phonons in low frequency benefit to the energy transmission. It has been verified by the carbon nanotubes (Carlborg *et al.* 2008; Thomas *et al.* 2010), as well as the SAM/water system (Goicochea *et al.* 2011). So here less involvement of phonons in low frequency regions accounts also for the lower TC in the combined distribution case. Finally, we tried to understand the results from structural aspect. G. Corongiu et al. (Corongiu & Clementi 1993) gave a general augment about it. They proposed that the intermolecular water-water interaction dominate the low frequency region, conversely the intramolecular motions among the single water molecules dominate the high frequency region.

Therefore, an expected conclusion for the case of combined distribution is that When the pore is arranged randomly, less intermolecular interaction of water is involved to transfer the heat, accounting for the reduction of the thermal conductivity in the case of combined distribution.

5.2.3 Thermal conductivity of infinite system and MFP

There is finite-size effect when the mean free path of phonon is competitive to the length of simulation system ($l_m/L \ll 1$). The most obvious result is that the scattering occurs at the interface near the heat and sink source. Consequently, the thermal conductivity is also limited by the system size. Casimir limit is well known for this regime (Casimir 1938). Based on this limit, Patrick K. Schelling (Schelling *et al.* 2002) has presented the equation for the mean free path l_m and infinite thermal conductivity λ_∞ in 2001. The common thermal conductivity is recalled firstly given by the kinetic theory:

$$\lambda \approx \frac{1}{3} c v l_m \tag{5.2}$$

where the c is the specific heat capacity of phonons, v is the group velocity of an acoustic branch, and l_m is the mean free path of phonons. For each atom, the total energy U in three degree of freedoms in thermal equilibrium is averaged as $3/2k_BT$. With the assumption that acoustic branches carry the majority part of heat and have a larger group velocity than optical branches, the contribution of optical branch to the heat transfer is neglected here. It means that every degree of freedom contributes $3/2k_B$ to the system's heat capacity. The specific heat for the whole system is given by:

$$c = \frac{\partial U}{\partial T} = \frac{3}{2} k_B n \tag{5.3}$$

here, the n is the number density of atoms. To relate to the λ_∞, it is necessary to firstly specify the MFP of infinity l_∞ from the effective mean free path (Poetzsch & Böttger 1994; Schelling *et al.* 2002):

$$\frac{1}{l_\infty} = \frac{1}{l_m} - \frac{4}{L} \tag{5.4}$$

where the L is equal to the length of system cell, the factor of 4 represents the position of the last scattering at the averaged distance $L/4$ when the phonons pass through the system from the heat source to sink. It indicates that for either the hot or the cold source, a random portion of phonons occurs the last harmonic scattering at a distance of $L/4$. Here it is assumed that there is only ballistic heat transfer in the system. So the Eq.5.2 is evolved as:

$$\frac{1}{\lambda_\infty} = \frac{2}{k_B n v} \cdot \frac{1}{l_\infty} \text{ (Infinitely long system)}$$

$$\frac{1}{\lambda} = \frac{a_0^3}{4k_B v}\left(\frac{1}{l_\infty} + \frac{4}{L}\right)$$

where $n = 8/a_0^3$ for a unit cell with a length of a_0. The thermal conductivity of infinitely long system can be calculated as (Schelling *et al.* 2002):

$$\frac{1}{\lambda} = \frac{1}{\lambda_\infty}\left(\frac{l_m}{L} + 1\right) \tag{5.5}$$

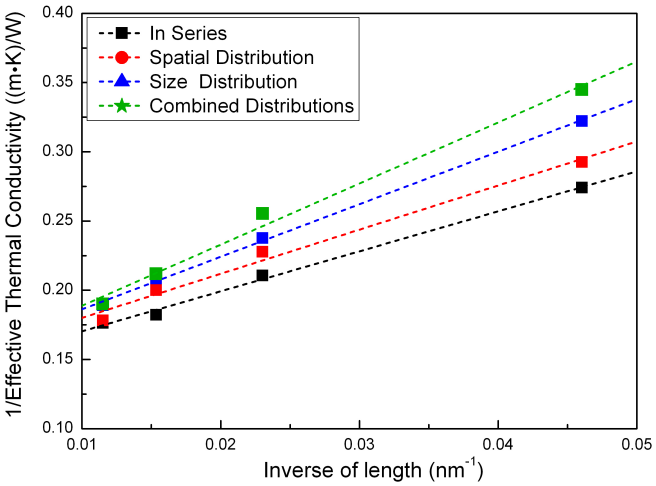

Figure 5.6: Inverse Thermal conductivity of the nanoporous silicon with the confined water as a function of inverse of system length for different distribution of pores, as well as the fitting curve for infinitely long system.

Table 5.3: The thermal conductivity for the infinitly long system and the corresponding mean free path.

	Spatial distribution	Size distribution	Combined distribution
TC of Infinite Length (W/(m·K))	6.75	6.744	6.9
MFP of Infinite Length (nm)	24.1	25.6	30.5

Therefore, the inverse of thermal conductivities of the nanoporous silicon with the confined water with different length from 8 nm to 88 nm are plotted in the Fig.5.6, as a function the inverse of length. The inverse of TC varies linearly with the length of system, conforming well to the previous equation, in all cases. Because the system with a length of 8 nm is too tiny, the fitted line is considered from the length longer than 21.7 nm to the 86.9 nm. As the equation proposed by Patrick

K, the TC of infinitely long system is obtained when the inverse of length is equal to 0, referring to the intercept of the fitted lines.

The final value of thermal conductivity of infinitely long system, is also called intrinsic thermal conductivity. The detailed results for infinite system are exhibited in the Table.5.3. The intrinsic thermal conductivity of nanoporous crystalline silicon with the confined water for 4 cases is averaged to be about 6.9 W/m·K.

By substituting the result data to the Eq.5.5, the averaged effective MFPs as a function of length are calculated, shown in the second line of the Table.5.3. There is a positive correlation between the MFP and the system length. The mean free path for nanoporous silicon with the confined water under different distributions of pore is averaged over 25 ± 4 nm. The complicate distribution of pore has high thermal conductivity for long infinitely system, less hindering the propagation of atoms. There is no evidence to suggest that which of the position or size of the pores plays a dominant role in heat transport.

5.3 Conclusions

In this chapter, the thermal conductivity of the nanoporous silicon with the confined water were investigated. The simulation cell is produced by replicating the cubic nanoporous silicon along the longitudinal direction. At first, the effect of the system length is studied. The result showed a nonlinear change of TC with the length of the system. The TC increases rapidly with the length increasing until 50 nm, due to more phonons are involved and travel further. Then the TC increases gradually with the length longer than 50 nm, and because of the hindrance of the voids and the interfaces.

Afterward, the effects of spatial, size and the combined spatial/size distribution of pore on the TC of the wet nanoporous silicon are studied. Only the position and size of pore are changed to obtain the different distribution of pore under the same porosity. The trends of the thermal conductivity for all cases with the length are much similar. The thermal conductivity increases nonlinearly with increasing length in all cases. When the system is small enough (less than 8 nm here) the thermal conductivity of the system basically does not vary with neither the pore size nor the position. The results of DOS show less involvement of phonon in the low frequency region. The intrinsic thermal conductivity of nanoporous crystalline silicon with the confined water is calculated as about 6.9 W/m·K. The averaged MFP is calculated to be $25 \pm 4nm$. The complicate distribution of pore has high thermal conductivity for long infinitely system, less hindering the propagation of

atoms. There is no evidence to suggest which of the position or size of the pores plays a dominant role in heat transport.

To sum up, I extended the previously studied model to investigate the effect of the system length, the position and size distribution of the pores on the thermal conductivity. And based on the length effect, I comprehensively exhibited the calculation process of thermal conductivity for infinitely long systems, and then derived the mean free range of phonons in the nanoporous silicon with the confined water. The entire framework is underlined by this chapter with the improved generality.

Synthesis of the Chapter

- The thermal conductivity of the nanoporous silicon with the confined water shows the nonlinear effect of the length of the system.
  - The TC increases rapidly with the length increasing until 50 nm.
  - Then the TC increases gradually with the length longer than 50 nm, and reaches a plateau value because of the hindrance of the voids and the interfaces.
- The effects of position and size of pore as well as their combined distribution are studied.
  - The trends of the thermal conductivity for all cases with the length are quite similar. The thermal conductivity increases nonlinearly with increasing length in all cases.
  - When the system is small enough (less than 8 nm here) the thermal conductivity of the system basically does not vary with neither the pore size nor the position.
  - The DOSs for each cases remains highly consistent.
- The intrinsic thermal conductivity of nanoporous crystalline silicon with the confined water is about 6.9 W/m·K.
  - The complicate distribution of pore has high thermal conductivity for long infinitely system, less hindering the propagation of atoms.
  - The averaged MFP for four cases is calculated to be 25 ± 4 nm.

Conclusions

In this thesis, the thermal conductivity (TC) of solid-liquid hybrid nanocomposites was investigated, especially for the dry and wet nanoporous crystalline silicon with the confined water. Meanwhile, a deep understanding in solid/liquid hybrid system has been developed. The thermal conductivity is calculated using Molecular Dynamics (MD) simulations, which are performed with LAMMPS. The study is composed by two parts. The first focuses mainly on the influence of two parameters on the thermal properties: the effect of temperature and the effective density of water on the TC of nanoporous silicon with the confined water, which is calculated using the Equilibrium Molecular Dynamics (EMD) methodology. In the second part, the effects of spatial, size and the combined spatial/size distributions of the wet nanopores on the TC of silicon are investigated. This part of the study, due to the modeling requests, has been done using the Non Equilibrium Molecular Dynamics (NEMD) simulations.

In the first part, an enhancement of the effective thermal conductivity of wet nanoporous samples at the temperature spectra of 285-360 K is evaluated. A surprising maximum of the thermal conductivity of the solid/liquid nanohybrid system at 300 K is observed here for first time, which then vanishes for temperatures greater than 345 K. The underlying mechanisms are related to the stratification of the water molecules at the vicinity of the solid/liquid interface. This enhancement is much more important than the one that can be predicted by using macroscopic effective models. To understand this non-monotonic behavior, several structural and dynamical properties of the nanoconfined water, separated in a core water molecules (bulk-like) and shell water molecules (dense water layer close to the solid/liquid interface) have been studied numerically.

- Density and pressure profiles help to understand the water molecules structure near the interface. The water molecule density follows a stratification effect close to the solid interface and the water density fluctuations decreases in increasing the temperature.
- With RDF analysis, at 300 K the shell water molecules is much more ordered than the ones in the core.
- Dynamical features such as the mean square displacement and the diffusion coefficient showed a saturation of movement over a long period of observation. An uncorrelated Brownian motion of nanoconfined water is observed

at the beginning of the observation, followed by a confined diffusion. The diffusion coefficient shows that nanoconfined water depends more strongly on the temperature than the bulk water.

- Concerning the orientation of water molecules, I have observed that oxygen atoms close to the solid/liquid interface are more rigid compared to the inner water molecules, but this phenomenon is independent of temperature.
- The hydrogen bond networks for the total nanoconfined water reveal that the majority of molecules preserve similar networks to the bulk water and that the temperature does not have a systematic effect on the H-bond networks. If we separate the nanoconfined water to shell and core water molecules, then we observe that more networking connections are present in the shell and this might be correlated to our remark that the high density water layer close to the solid/liquid interface has potential to cause the higher thermal conductivity of hybrid nanosystems. This conclusion is also supported by the tendency of water molecules creating shorter networks in increasing the temperature, corresponding to the decrease of the effective thermal conductivity of the hybrid nanosystems upon increasing the temperature.
- Last but not the least was that the DOS of the silicon pores atoms and the nanoconfined water molecules increases their juxtaposed areas compared to the bulk state and this qualitatively means that new heat flux channels are established between the solid matrix and the nanoconfined water.

Secondly, the same methodology has been used as in the first part, to investigate the influence of the effective density from 0.2 to 1.2 g/cm^3 on the thermal conductivity of wet nanoporous samples. A similar maximum value of TC at the effective density around 0.8 g/cm^3 is found. The TC increases gradually from the density of 0.2 g/cm^3, then reaches a peak at 0.8 g/cm^3, after which the TC decreases sharply along with the increase in the effective density until the value of 1.2 g/cm^3. We found that:

- A higher density value at the center of pore is observed for effective densities in the range of 0.7 to 0.9 g/cm^3 compared to the initial effective density. Furthermore, the shell thickness for these densities are much larger compared to other density values. Moreover, a dramatic change of pressure near the interface is found for the density of 1.2 g/cm^3.
- Similar results of RDF with the first part (temperature dependence) and thus it can be concluded that no phase transition is observed.

- The MSD profiles reveal that the saturation of movement over a long period of observation differs for the different densities. This indicates that the diffusion coefficient of nanoconfined water depends strongly on the effective density.
- We do not observe important modifications of the orientation of water molecules in the core and the shell upon the effective density.
- The hydrogen bond networks for nanoconfined water reveal that water molecules create shorter networks, corresponding to the decrease of the effective TC in increasing the density. Longer hydrogen bond pathways with the number of 3 and 4 are found, at the density of 0.8 g/cm^3, corresponding to the highest TC.
- The DOS of the silicon pores atoms and the nanoconfined water molecules overlaps at the low frequencies, inducing an increased of the juxtaposed areas, resulting new heat flux channels established between the solid matrix and the nanoconfined water.

At the last part, the simulation cell switches from a cubic to a longitudinal model. Here we wanted to study the influence of the size, spatial and the size/spatial distribution of the wet pores on the thermal conductivity of the nanoconfined water in porous silicon system. The thermal conductivity of nanoporous silicon with confined water shows a nonlinear dependence in increasing the length of the system. The TC increases rapidly with the length, until the system reaches 50 nm, and then reaches a plateau around 70-80 nm. Then, the effects of different features of the pore on the effective thermal conductivity are studied. The trends of the thermal conductivity for all cases with the length are quite similar. The thermal conductivity increases nonlinearly with increasing length in all cases. When the system is small enough (less than 8 nm here) the thermal conductivity of the system basically does not vary with neither the pore size nor the location. The intrinsic thermal conductivity of nanoporous crystalline silicon confined with water is calculated as about 6.9 W/(m·K). The averaged MFP for all cases is calculated to be 25 ± 4 nm. The complicate distribution of pore has high thermal conductivity for long infinitely system, less hindering the propagation of atoms.

To sum up, I gave physical insights of the observed phenomena with structural and dynamical aspects. Only a small amount of evidence explains the maximum value of thermal conductivity at room temperature. Through multiple research approaches I have used, the complexity of confined water molecules at the nanoscale is much clear in our framework. The entire framework is also underlined by the last part with the improved generality.

In this thesis, the role of solid liquid interface for the important enhancement of the effective thermal conductivity of a nanoporous silicon filled with water is argued, compared with the dry one. However, the density profiles results can not explain the maximum value of thermal conductivity at certain temperature or effective densities. This suggests that there are still limitations to the current density profiles for interface characterisation that have been done. As our research shown that the broken and rebuilding of hydrogen bonding network are the main reason giving rise of higher thermal conductivity. So much complex models such as 4-sites model of water, should be taken into account in the future study, for expressing specifically the interaction of the solid and the liquid. The current used model in this thesis have not attained an adequate understanding of the water molecules, for example in the aspect of representing the polarity changes, spin motion, dipole moment, etc. All of them are related to the solid/liquid interaction, the hydrophilicity of the surface, consequently the thermal properties. Meanwhile, it is also meaningful to extend the run period to study the life time of H-bonds (femtoseconds). In addition, too little attention has been paid to the density of states for solid/liquid nanocomposites, which is one of the most important approach to analyze the thermal transports. The effect of the overlapping area of the solid and the liquid are still not clear.

As a more general prospective, there are also other points which are worthy studying in the future. For instance, it is intriguing to see how temperature and density will affect nanoporous amorphous silica and whether similar extreme values would still exist. Such system would be more realistic taking into account the oxidation occurring in all silicon nanomaterials. Another perspective is to study the impact of the shape of the pore on the the effective thermal conductivity by modeling cylindrical or polygonal pores which are closer to the real nanoporous systems.

Appendices

APPENDIX A

Thermal conductivity of nanoporous amorphous silica

The solid liquid system of silica and water will be much complex due to the different oxygen atoms from silica and water. It's a pity that the study of the thermal conductivity on the nanoporous amorphous silica confined with the water didn't be completed in the period of PhD. We started from the TC of bulk and nanoporous amorphous silica. In this appendix, the calculation of their thermal conductivities is explored using molecular dynamics simulations. The following subsections represent the simulation details including the simulated configurations, the interatomic potentials, the system equilibrium, and the results. In the future, works on follow-up can build on this base.

A.1 Introduction of nanoporous amorphous silica

As the definition of nanoporous silicon, nanoporous silica consist of amorphous silica matrix with a larger number of nano-sized pore (0.1 nm-1 um). Taking the advantages of the low density, stable thermal properties, high thermal insulation, low dielectric and tunable refractive index and so on, the nanoporous amorphous silica are explored in the field of in the detectors, MEMS devices, filters and sensors (Yang *et al.* 2022; Zhu *et al.* 2020; Choi *et al.* 2008b; Coquil *et al.* 2011). Therefore for these applications, the knowledge of the thermal conductivity of amorphous silica is significant for the design of these devices.

En general, the presence of the pore leads to the degradation of the thermal transport of amorphous silica, caused by the boundary scattering. However, M.Y.Yang et al. studying the thermal insulation of nanoporous silica aerogels, found that the water molecules can deduce effectively the phonon scattering and promote the heat transfer by filled the molecular defects (Yang *et al.* 2022). This certainly contributes to the complexity of the prediction of the thermal conductivity of nanoporous silicon and liquid system. Furthermore, due to their disordered structure and the ambiguous interfacial area at the pore boundary, it is also a chal-

lenge to define precisely the interface between an amorphous silica and liquid, which is related to the thermal transport, thereby, the effective thermal conductivity. We have proved in the main content that the well-known approach, effective medium approximation, is no longer applicable for the case of the solid and liquid system with the nanosized pore. Another classical method, molecular dynamical simulations, came into the mind. It is capable to simulate directly the motion process of atoms, then extract the physical properties with certain assumptions. It can be helpful for us to investigate the complex solid/liquid system.

Besides, the effect of pore features on the thermal conductivity of amorphous silica cannot be disregarded as well. As in the systematic study carried by Thomas Coquil et al, the results of MD simulations confirms quantitatively the strong dependence of the porosity on the TC of nanoporous amorphous silica, but no dependence of the pore size. Hence, a deep understanding in this domain is still required.

A.2 Methodology of EMD

A.2.1 Interatomic potentials

A.2.2 Interatomic potential functions for silica and silica/water

Silicon dioxide (or silica) is a tetrahedron formed by silicon atoms and four oxygen atoms, which can be divided into two categories: crystalline and amorphous forms. There are many different potentials recommended for bulk silica. The most widely used are the BKS potential(Van Beest *et al.* 1990) and Tersoff. potential(Tersoff 1988).

A.2.2.1 BKS potential

The name of BKS potential is made up of the initials for its inventors Beest, Kramer and van Santen(Van Beest *et al.* 1990). It takes fully account of the ab initio calculation and classical lattice dynamics. It is frequently applied for amorphous silica, also nanoporous silica films. Through BKS potential, the structural and thermodynamic properties, such as radial distribution functions , thermal conductivity, specific heat, are predicted with reliable accuracy. Compared with many body potential such as tersoff, BKS potential takes a good advantage of being a two-body potential, which is more efficient. This allows to work in longer run, and thus to study the system under low temperature. So it is an attractive potential function for silica for computer simulation.

The BKS potential take into account two parts: the Coulomb and the Buckingham interactions. The interaction between two atoms i and j in BKS potential is expressed as:

$$\begin{aligned}\Phi(r)^{BKS} &= \Phi(r)^{Coul} + \Phi(r)^{Buck} \\ &= q_i q_j e^2 V(r) + A_{ij} exp^{-B_{ij} r} - \frac{C_{ij}}{r^6}\end{aligned} \tag{A.1}$$

where q_i and q_j are the charges of atoms, the r is the separation distance, A_{ij}, B_{ij} and c_{ij} are the different constants for different pairs of atom i and j. For example, there are three different pairs of silica, Si-Si, Si-O and O-O. The first term $V(r) = 1/r$ in Eq.A.1 represents the contribution of long-range Coulombic interaction, which could be further approximated by finite range potentials. The second and third one are defined for the short-range attraction and repulsion of atoms, respectively(Yeo *et al.* 2013).

In 1996, Katharina Vollmayr (Vollmayr *et al.* 1996) discovered that the original BKS proposed by Van Santen cannot perform in the short and medium structure of amorphous BKS. A truncation of potential need to be considered. It is found that a practical method, presented and developed by D.Wolf in 1992 and 1999, enables to extract the energy, force and stress from a spherically truncated environment (Wolf 1992; Wolf *et al.* 1999). It is readily implemented on MD simulations of amorphous silicon. Combined with this model, the Eq.A.1 can be deduced as:

$$\begin{aligned}\Phi(r)_W^{Coul} &= q_i q_j e^2 V(r) \\ &= q_i q_j e^2 \left((\frac{1}{r} - \frac{1}{r_{c,Coul}}) + \frac{1}{r_{c,Coul}^2}(r - r_{c,Coul}) \right), \quad r < r_{c,Coul}\end{aligned} \tag{A.2}$$

$$\Phi(r)_W^{Buck} = A_{ij} exp^{-B_{ij} r} - \frac{C_{ij}}{r^6} - (A_{ij} exp^{-B_{ij} r_{Buck}} - \frac{C_{ij}}{r_{c,Buck}^6}) \tag{A.3}$$

where the $r_{c,Coul}$ and r_{Buck} are the cut-off for the Comlomb potential and Buckingham potential, respectively. $r_{c,Coul}$ is determined as 10.17 Å, which has been demonstrated that it is representative of the behavior of the Coulomb potential in real space part in the study of Antoine Carré (Carré *et al.* 2007). Furthermore, for the cutoff of non-Coulomb interaction, the finding of Vollmayr found that r_{Buck} shifted at a distance of 5.5 Å, made the simulations agree well with real experiments (Vollmayr *et al.* 1996). It means that only the particles with a distance of 0.55 nm interact with each other. This term makes it possible to have a more re-

alistic and effective expression of the BKS potential for those systems of length greater than $r_{c,Coul}$.

However, there is an initial problem of Wolf model is that this truncated potential in Eq.A.3 leads to the discontinuous forces, which is not accepted for MD simulations. Hence, in the Ref.(Carré *et al.* 2007), the author multiplied the following function so as to make it continuous at $r_{c,Coul}$ and $r_{c,Buck}$:

$$\Phi(r)^{BKS} = f(r)\Phi(r)_W^{Coul} + g(r)\Phi(r)_W^{Buck} \quad (A.4)$$

$$f(r) = exp\left(-\frac{h_{Coul}^2}{(r - r_{c,Coul})}\right) \quad (A.5)$$

$$g(r) = exp\left(-\frac{h_{Buck}^2}{(r - r_{c,Buck})}\right) \quad (A.6)$$

where the constant h_{Coul} and h_{Buck} were set to 0.5 (Mantisi *et al.* 2012).

Based on these considerations, B. Mantisi improved the Eq.A.6, by adding a repulsive part in order to avoid the collapse of atoms at short range $r_{c,Rep}$ at high pressure or temperature. The final potential established was proved to be useful to emulate the main feature and structure of amorphous silica glass both the elastic and plastic regime, under shear and pressure (Mantisi *et al.* 2012). Consequently, in his model, the BKS potential is described as:

$$\Phi(r)^{BKS} = f(r)\Phi(r)_W^{Coul} + g(r)\Phi(r)_W^{Buck} + \Phi_{ij}^{Rep}(r) \quad (A.7)$$

$$\Phi_{ij}^{Rep}(r) = (\frac{D_{ij}}{r})^1 2 + E_{ij}r + F_{ij} \quad (A.8)$$

A.2.2.2 Tersoff potential

The Tersoff potential function is used for many-body systems and is widely used for such as C-Si, Si-O interatomic interactions. It has been shown that the reparameterized Tersoff reproduces the bulk thermal properties better than the BKS potential(Van Beest *et al.* 1990), while being a much capable in the area on reproducing density of states (DOS) of bulk amorphous silica (Munetoh *et al.* 2007). The arithmetic expressions of its potential function are as following:

$$E = \frac{1}{2}\sum_i \sum_{j \neq i} V_{ij} \quad (A.9)$$

$$V_{ij} = f_C(r_{ij})(f_R(r_{ij}) + b_{ij} f_A(r_{ij})) \tag{A.10}$$

$$f_C(r_{ij}) = \begin{cases} 1, & r < R - D \\ \frac{1}{2} - \frac{1}{2} sin(\frac{\pi r - R}{2D}), & R - D < r < R + D \\ 0, & r > R - D \end{cases} \tag{A.11}$$

$$f_R(r_{ij}) = Aexp^{(} - \lambda_2 r_{ij}) \tag{A.12}$$

$$f_A(r_{ij}) = -Bexp^{(} - \lambda_1 r_{ij}) \tag{A.13}$$

$$b_{ij} = (1 + \beta^n \psi_{ij}^n)^{-\frac{1}{2n}} \tag{A.14}$$

$$\psi_{ij} = \sum_{k \neq i,j} f_C(r_{ik}) g(\theta_{ijk}) \times exp^{[} \lambda_3^m (r_{ij} - r_{ijk})^m] \tag{A.15}$$

$$g(\theta_{ijk}) = \gamma_{ijk}(1 + \frac{c^2}{d^2} - \frac{c^2}{(d^2 + (\cos\theta - \cos\theta_0)^2)}) \tag{A.16}$$

This potential takes into account of all j and k atoms within the cut-off of $R+D$ to i atom. The θ is the angle between bonds of atom i,j and i,k.

A.2.2.3 Potentials of the silica/water

Note that We have not conducted Silica/water studies. So this part is only for knowledge and hopefully it will be beneficial for the further research.

Since silica is an atomic crystal, the oxygen and silicon atoms occupying each lattice point act through covalent bonds, and there are no intermolecular forces. Therefore, when considering the role of water and silica, we can also consider only the interaction potential of the H, O atoms of the water molecule on the Si, O atoms of silica. Eduardo R.Cruz-Chu (Cruz-Chu *et al.* 2006) developed a potential function compatible with the CHARMM force field, which can take account into the stretching and bending contribution of bonds and angles, the VdW and electrostatic non-bonded atomic interactions. Under this force field, he found the sensitive control of electrostatic interaction between amorphous silica and water.

Duin et al.(Van Duin *et al.* 2003) first applied ReaxFF force field on the structural properties of pure silica and water systems. Based on this force field, chemical reactions between silica surface and water are described(Fogarty *et al.* 2010). A proton-transfer process that hydrogen atoms pass through the silica surface by associating and dissociating with O atom within bulk water, could be observed, leading to an electric potential difference within the solid/liquid interface. More potentials are presented in the table A.1.

Table A.1: The interatomic potentials referenced for silica and water

Year	Author	Water	Silica	Notes
2000	Tiffany R.Walsh(Walsh *et al.* 2000)	SPC	PIM, TTAM	
2006	Cruz-Chu et al.(Cruz-Chu *et al.* 2006)	TIP3P	CHARMM water contact(CWCA)	Bonds, Angles, VdW, Coulomb
2010	P A Bonnaud et al.(Bonnaud *et al.* 2010)	SPC	PN-TrAZ(2002)	Born-Mayer for short-range repulsion, dispersion interaction, coulomb
2010	Joseph C et al.(Fogarty *et al.* 2010)	SPC/E	ReaxFFSi/O/H	Chemical interaction between Si/O/H
2012	Ian C. Bourg et al.(Bourg & Steefel 2012)	SPC/W	LR, CLAYFF, JA, LRL	Rigid model for Si/O/H
2014	Fateme S et al.(Emami *et al.* 2014)	TIP3P	CHARMM, CVFF, AMBER (12-6 LJ)	Bonded, non-bonded term
2014	Zambrano (Zambrano *et al.* 2014)	SPC/E	Modified BKS	Coulomb, Buchkinghum
2020	H. Gokberk Ozcelik et al. (Ozcelik *et al.* 2020)	SPC/E	Becke-Johnson (BJ)	Combination 12-6 LJ of O-O and O-Si

A.2.2.4 Summary

The importance and the originality of the BKS potential is that it explores an good structure properties of amorphous silica both in mechanical and dynamical aspects, which shows consequently a high compatibility with the experimental results (Yuan & Huang 2012; Kerrache *et al.* 2006; Hemmati & Angell 1998). And the final BKS potential in Eq.A.6 enables to work effectively for large samples.

However, in the studies on the thermal properties of amorphous silica, it has been proved that BKS potential provided a poor estimation of bulk thermal conductivity, and vibrational density of states (Yeo *et al.* 2013). So we wanted to change the potential for the thermal property study. Comparison the finding with those of Tersoff potential conformed that the bulk thermal characteristics of amorphous silica can be successfully reproduced accurately by Tersoff with great accuracy.

Therefore, at first in our study, we used the modified BKS potential in Eq.A.6 to generate the amorphous silica from the crystalline state. The parameters used are shown in Table.A.2. Then, the potential was replaced by the Tersoff in order to calculate much correctly the thermal conductivity of bulk and nanoporous amorphous silica. The parameters for Tersoff potential could be directly extracted from the Ref.(Dmitriev *et al.* 2018).

A.2.3 Determination of the configuration

At first, a bulk system is under the consideration with the length larger than 5.5 Å to avoid the finite effect during the amorphous silica formation. According to the structure of -Christobalite cell, the cubic length in each direction is set as $a = 7.46$ Å, as shown in Fig.A.1(a). So we generated firstly the bulk crystalline

Table A.2: Interatomic potential parameters of BKS in the upper panel (Mantisi *et al.* 2012).

	O-O	Si-O	Si-Si
$A_{ij}(eV)$	1388.773	18003.7572	872360308.1
$B_{ij}(\text{Å}^{-1})$	2.7601	4.8733	1522.0
$C_{ij}(\text{eV}\cdot\text{Å}^6)$	175.0	133.5381	23.299907
$D_{ij}(\text{Å}\cdot eV^{-12})$	142.383338	1.42402882	0.0
$E_{ij}(\text{eV}\cdot\text{Å}^{-1})$	-14.97811134	-3.24749265	0.0
$F_{ij}(\text{eV})$	39.0602602165	-15.86902056	0.0
$r_{c,Rep}(\text{Å})$	1.75	1.27	0.0
q_{ij}	$q_{Si} = +2.4e$	$q_O = -1.2e$	

silica system by replicating the -Christobalite cell, with dimensions of$6a \times 6aa$, which corresponds to a cubic sample of $L = 44.76$ Å size length, as illustrated in Fig.A.1(b).

After the formation of Silica, a sphere of atoms within a radius of $R = 14.92$ Å is extracted from the simulation box center to finally catch a porosity of 15.51%. The dry nanoporous amorphous silica system is obtained, as displayed in Fig.A.1(c). Fig.A.1(d) and (e) are the nanoporous amorphous silica configuration in the perspective and front view, respectively.

From this configuration, the porosity is introduced by removing a sphere of atoms from the center. Some authors (Mirmohammadi *et al.* 2018; Van Norren *et al.* 2009) observed that above a porosity of 15%, the measurement of thermal conductivity exhibits large fluctuations which is not the case at low porosity level. This is attributed to the dominating role of boundary effect over phonon scattering.

A.2.4 Melt-quench process

In order to prepare an amorphous silica, a initial crystal silica are successively heated, melted, and quenched, to achieve an final amorphous state. Known that the density of amorphous silica is 2.2 g/cm^3 (Structures 1963), we chose the *beta*-Christobalite with the same density as its. The whole process is always under the periodic boundary condition.

First of all, the atom velocities are initialized using a Maxwell- Boltzmann distribution set by different random number of seeds. Then, the bulk *beta*-Christobalite sample is heated in NVT ensemble, from 300 K to 6000 K during 100 ps. After that, the system need to evolve at 6000 K and at 1 atm during 10 ns (10 000 timesteps) to make sure that all atoms are fully melted into the liquid state. It is followed by a quenching of system from 6000 K to 300 K with a cooling rate of 5.7 K/ps during 1 ns. Finally, the system is still thermalized at 300 K for another 100 ps to achieve the equilibrium state of amorphous silica. In this process, the temperature and the pressure are controlled by the Langevin thermostat (Schneider & Stoll 1978) and Berendson barostat (Berendsen *et al.* 1984), respectively, to generate the positions and velocities of atoms as implemented by LAMMPS.

Once the Tersoff potential is defined in LAMMPS, the BKS potential will be replaced.. Aiming to bring the system back to equilibrium with the new potentialthe system is performed under a local energy minimization using conjugate gradient (CG) algorithm. Finally, it is allowed to relax further at 300 K at 0 pressure for 20

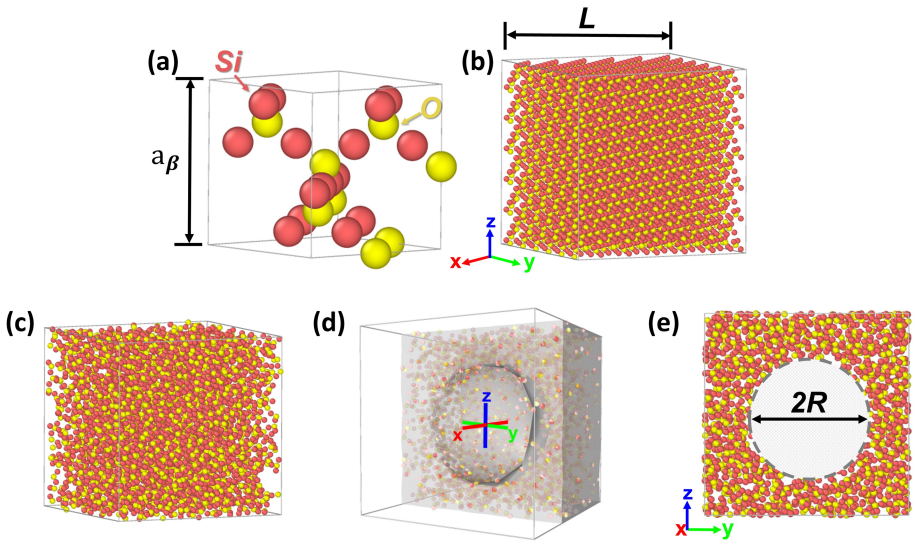

Figure A.1: The simulation models for crystal and amorphous silica: (a) the unit cell of -Christobalite with the length of $a = 7.46$ Å, (b) the bulk system of crystal silica with the length of $L = 44.76$ Å, (c) the bulk and nanoporous amorphous silica in the (d) perspective and (e) front view after equilibrium.

ps to be well prepared for EMD simulations.

A.2.5 System equilibrium for EMD

The method for EMD is quiet similar as the description in Sec.3.1.2. All the configurations studied here are simulated under periodic boundary conditions. All the velocities are integrated by the velocity-Verlet integration algorithm for the atomic motion with the timesteps of 0.5 fs. To make sure that the system has been fully relaxed after the potential switching, we still relax the system at 300 K in the NVT ensemble at zero pressure for 200 ps, and then imposed the NVE run during 70 ns to compute the thermal conductivity using EMD method (introduced in Sec.2.3.1).

A.3 Results

A.3.1 Characterization of the amorphous silica

A random and disordered silica in amorphous state are obtained after the above melt-quench process. In this amorphous stage, the density of the final sample here is calculated as 2.22 g/cm^3, which is consistent with the referenced data (Structures 1963). Besides, it's also necessary to check the structure properties of

the sample to ensure the accuracy of the thermal conductivity calculation. We took firstly into account the pair Radial Distribution Functions (RDF) to specify numerically the bond length of silica atoms. Fig.A.2 provides the results of the pair RDF of the amorphous silica after the melt-quench process and the change to Tersoff potential at 300 K and 0 pressure . What we can observe is that, the first peak of O-O, Si-O and Si-Si atoms appear at 2.58, 1.61 and 3.14 Å, respectively. Comparison of the interatomic lengths for all sizes with those of the others studies confirm that our RDF distributions are in accord with both the experimental (Vollmayr *et al.* 1996) and simulated results (Mantisi *et al.* 2012; Issa *et al.* 2020). The same agreement can be also attained for subsequent peaks in Fig.A.2.

On the other side, the bond angle, which is correlated strongly with the bonding state, is also an important parameter to deliberate the glass network (Liu *et al.* 2022). With the aide of angle distributions of silicon and oxygen atoms, the distributions of O-Si-O and Si-O-Si angles are illustrated in the Fig.A.3 below. The angle distribution concentrated in certain range as an approximated Gaussian distributions. And the maximum values of O-Si-O and Si-O-Si are about 112 °and 152 °. These results match consistently those observed in previous study (Ndour *et al.* 2021). With the aid of these distributions, it is encouraging to summarize that our amorphous silica sample is reliable and realistic for MD simulations.

A.3.2 Results of the thermal conductivities

The thermal conductivities of bulk nanoporous silica , compared with nanoporous crystalline silicon, are studied here. It indicates that the great attenuation of the TC because of the existence of the pore both for the crystalline silicon and for the amorphous silica. The TC of the nanoporous silica decline from 1.12 to 0.65 $K \cdot m^2/W$, after the addition of the pore. It can be seen that the pore has less influence on the thermal properties of amorphous silicon dioxide compared to the crystalline silicon.

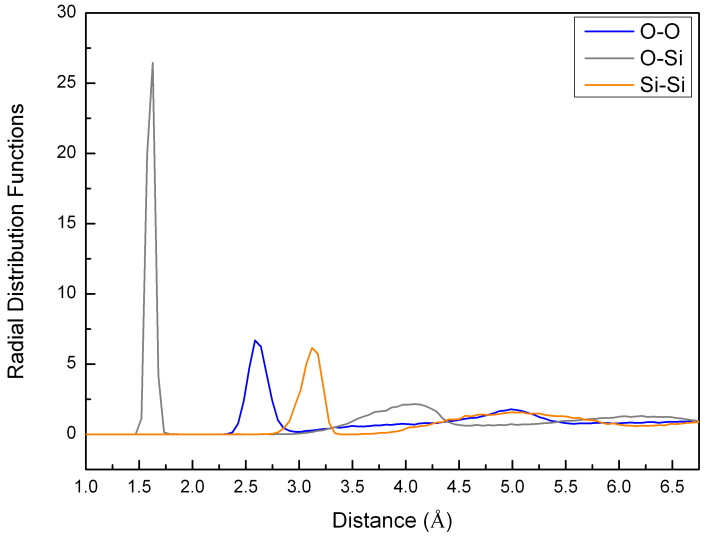

Figure A.2: The radial distribution functions of the nanoporous amorphous silica

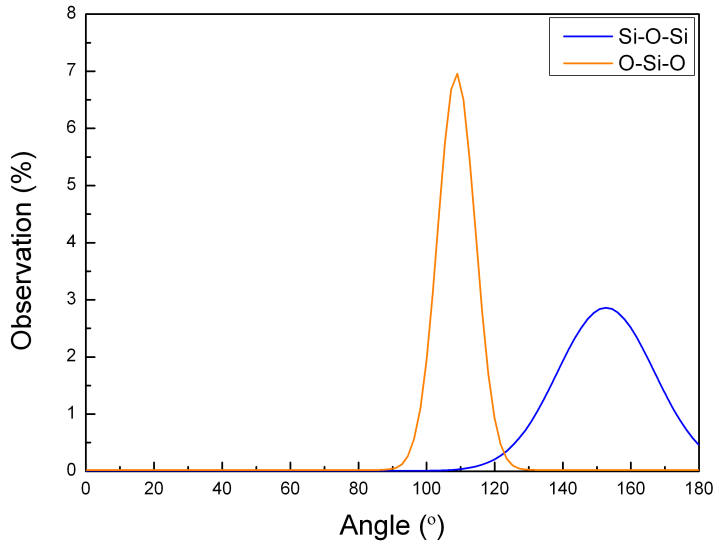

Figure A.3: The bond angle of Si-O-Si and O-Si-O atoms of the nanoporous amorphous silica.

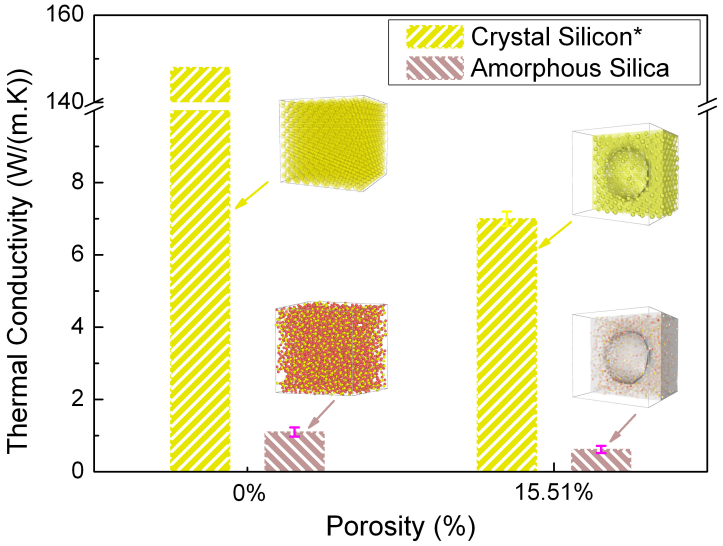

Figure A.4: Thermal Conductivities of nanoporous amorphous silica, compared with nanoporous crystalline silicon. The porosities are set as 0% (without pore) and 15.51 %. The label '*' signifies the value of bulk crystalline silicon is extracted from the Ref.(Callaway 1959), as same as the value in Sec.3.2.1

Publications List

Published Articles

- *Thermal transport enhancement due to confined water in hybrid nanocomposite*, Mykola ISAIEV, Xiaorui WANG, Konstantinos TERMENTZIDIS and David LACROIX. Applied Physics Letters, 2020, 117(3): 033701.

  https://doi.org/10.1063/5.0014680

- *Thermal conductivity temperature dependence of water confined in nanoporous silicon*, Xiaorui WANG, William GONÇALVES, David LACROIX, Mykola ISAIEV, Séverine GOMÈS and Konstantinos TERMENTZIDIS, Journal of Physics: Condensed Matter, 2022, 34: 305701.

  https://doi.org/10.1088/1361-648X/ac664b

Posters

- *Thermal conductivity of 'porous silicon–water' nanocomposite with molecular dynamics*, Xiaorui WANG, Mykola ISAIEV, Séverine GOMÈS, David LACROIX and Konstantinos TERMENTZIDIS. E-MRS Fall Meeting 2019. Warsaw

Project Funded

- Project UT-INSA of Chinese Scholarship Council
  - obtained from 2018 September to 2022 March

Bibliography

[Abareshi *et al.* 2010] Maryam Abareshi, Elaheh K Goharshadi, Seyed Mojtaba Zebarjad, Hassan Khandan Fadafan and Abbas Youssefi. *Fabrication, characterization and measurement of thermal conductivity of Fe3O4 nanofluids*. Journal of Magnetism and Magnetic Materials, vol. 322, no. 24, pages 3895–3901, 2010.

[Abdulagatov & Azizov 2005] IM Abdulagatov and ND Azizov. *Thermal Conductivity and Viscosity of Aqueous K 2 SO 4 Solutions at Temperatures from 298 to 575 K and at Pressures up to 30 MPa*. International journal of thermophysics, vol. 26, no. 3, pages 593–635, 2005.

[Abell 1985] GC Abell. *Empirical chemical pseudopotential theory of molecular and metallic bonding*. Physical Review B, vol. 31, no. 10, page 6184, 1985.

[Achhal *et al.* 2018] El Mehdi Achhal, Hicham Jabraoui, Soukaina Zeroual, Hamid Loulijat, Abdellatif Hasnaoui and Said Ouaskit. *Modeling and simulations of nanofluids using classical molecular dynamics: Particle size and temperature effects on thermal conductivity*. Advanced Powder Technology, vol. 29, no. 10, pages 2434–2439, 2018.

[Agyenim *et al.* 2010] Francis Agyenim, Neil Hewitt, Philip Eames and Mervyn Smyth. *A review of materials, heat transfer and phase change problem formulation for latent heat thermal energy storage systems (LHTESS)*. Renewable and sustainable energy reviews, vol. 14, no. 2, pages 615–628, 2010.

[Ahmad *et al.* 2011] Iftikhar Ahmad, Umar Khan and Yurii K Gun'ko. *Graphene, carbon nanotube and ionic liquid mixtures: towards new quasi-solid state electrolytes for dye sensitised solar cells*. Journal of Materials Chemistry, vol. 21, no. 42, pages 16990–16996, 2011.

[Akilu *et al.* 2019] Suleiman Akilu, Aklilu Tesfamichael Baheta, Sujan Chowdhury, Eswaran Padmanabhan and KV Sharma. *Thermophysical profile of SiC–CuO/C nanocomposite in base liquid ethylene glycol*. Powder Technology, vol. 354, pages 540–551, 2019.

[Al-Neama *et al.* 2017] Ahmed F Al-Neama, Nikil Kapur, Jonathan Summers and Harvey M Thompson. *An experimental and numerical investigation of the*

use of liquid flow in serpentine microchannels for microelectronics cooling. Applied Thermal Engineering, vol. 116, pages 709–723, 2017.

[Alam & Alam] SN Alam and Syed Samsul Alam. *Daniel Shechtman, Quasicrystals, and Golden Ratio: A Review of the Great Discovery*.

[Allen & Tildesley 2017] Michael P Allen and Dominic J Tildesley. Computer simulation of liquids. Oxford university press, 2017.

[Allen 1987] MP Allen. *DJ Tildesley Computer simulation of liquids*, 1987.

[Andrusenko *et al.* 2012] Dmitriy Andrusenko, Mykola Isaiev, Andrey Kuzmich, Vladimir Lysenko and Roman Burbelo. *Photoacoustic effects in nanocomposite structure 'porous silicon-liquid'*. Nanoscale Research Letters, vol. 7, page 411, 2012.

[Antidormi *et al.* 2018] Aleandro Antidormi, Xavier Cartoixà and Luciano Colombo. *Nature of microscopic heat carriers in nanoporous silicon*. Physical Review Materials, vol. 2, page 056001, 2018.

[Arora 1981] Vijay K Arora. *Quantum size effect in thin-wire transport*. Physical Review B, vol. 23, no. 10, page 5611, 1981.

[Arsiccio & Pisano 2020] Andrea Arsiccio and Roberto Pisano. *The ice-water interface and protein stability: a review*. Journal of Pharmaceutical Sciences, vol. 109, no. 7, pages 2116–2130, 2020.

[Asay *et al.* 2008] David B Asay, Michael T Dugger and Seong H Kim. *In-situ vapor-phase lubrication of MEMS*. Tribology Letters, vol. 29, no. 1, pages 67–74, 2008.

[Asheghi *et al.* 1998] M Asheghi, MN Touzelbaev, KE Goodson, YK Leung and SS Wong. *Temperature-dependent thermal conductivity of single-crystal silicon layers in SOI substrates*. 1998.

[Assy *et al.* 2014] Ali Assy, Stéphane Lefèvre, Pierre-Olivier Chapuis and Séverine Gomès. *Analysis of heat transfer in the water meniscus at the tip-sample contact in scanning thermal microscopy*. Journal of Physics D: Applied Physics, vol. 47, no. 44, page 442001, 2014.

[Atzeni *et al.* 2008] Cirillo Atzeni, Giorgio Pia and Ulrico Sanna. *Fractal modelling of medium–high porosity SiC ceramics*. Journal of the European Ceramic Society, vol. 28, no. 14, pages 2809–2814, 2008.

[Balla *et al.* 2013] Hyder H Balla, Shahrir Abdullah, Wan Mohd Faizal WanMahmood, M Abdul Razzaq, Rozli Zulkifli and Kamaruzaman Sopian. *Modelling and measuring the thermal conductivity of multi-metallic Zn/Cu nanofluid*. Research on Chemical Intermediates, vol. 39, no. 6, pages 2801–2815, 2013.

[Ballone *et al.* 2012] P Ballone, MG Del Popolo, S Bovio, A Podestà, P Milani and N Manini. *Nano-indentation of a room-temperature ionic liquid film on silica: a computational experiment*. Physical Chemistry Chemical Physics, vol. 14, no. 7, pages 2475–2482, 2012.

[Barisik & Beskok 2014] Murat Barisik and Ali Beskok. *Temperature dependence of thermal resistance at the water/silicon interface*. International Journal of Thermal Sciences, vol. 77, pages 47–54, 2014.

[Baroni *et al.* 2020] Stefano Baroni, Riccardo Bertossa, Loris Ercole, Federico Grasselli and Aris Marcolongo. *Heat transport in insulators from ab initio Green-Kubo theory*. Handbook of Materials Modeling: Applications: Current and Emerging Materials, pages 809–844, 2020.

[Bauer *et al.* 2012] Brad A Bauer, Shuching Ou, Sandeep Patel and Karthik Siva. *Dynamics and energetics of hydrophobically confined water*. Physical Review E, vol. 85, no. 5, page 051506, 2012.

[Berendsen *et al.* 1984] Herman JC Berendsen, JPM van Postma, Wilfred F Van Gunsteren, ARHJ DiNola and Jan R Haak. *Molecular dynamics with coupling to an external bath*. The Journal of chemical physics, vol. 81, no. 8, pages 3684–3690, 1984.

[Bhunia *et al.* 2018] Mississippi Missouri Bhunia, Karamjyoti Panigrahi, Swati Das, Kalyan Kumar Chattopadhyay and Paramita Chattopadhyay. *Amorphous graphene–transformer oil nanofluids with superior thermal and insulating properties*. Carbon, vol. 139, pages 1010–1019, 2018.

[Bonnaud *et al.* 2010] Patrick Alain Bonnaud, Benoît Coasne and R JM Pellenq. *Molecular simulation of water confined in nanoporous silica*. Journal of Physics: Condensed Matter, vol. 22, no. 28, page 284110, 2010.

[Bourg & Steefel 2012] Ian C Bourg and Carl I Steefel. *Molecular dynamics simulations of water structure and diffusion in silica nanopores*. The Journal of Physical Chemistry C, vol. 116, no. 21, pages 11556–11564, 2012.

[Brenner *et al.* 1991] DW Brenner, JA Harrison, CT White and RJ Colton. *Molecular dynamics simulations of the nanometer-scale mechanical properties of compressed Buckminsterfullerene*. Thin Solid Films, vol. 206, no. 1-2, pages 220–223, 1991.

[Brini *et al.* 2017] Emiliano Brini, Christopher J Fennell, Marivi Fernandez-Serra, Barbara Hribar-Lee, Miha Luksic and Ken A Dill. *How water's properties are encoded in its molecular structure and energies*. Chemical reviews, vol. 117, no. 19, pages 12385–12414, 2017.

[Burnham & Xantheas 2002] Christian J Burnham and Sotiris S Xantheas. *Development of transferable interaction models for water. III. Reparametrization of an all-atom polarizable rigid model (TTM2–R) from first principles*. The Journal of chemical physics, vol. 116, no. 4, pages 1500–1510, 2002.

[Buschmann 2012] Matthias H Buschmann. *Thermal conductivity and heat transfer of ceramic nanofluids*. International journal of thermal sciences, vol. 62, pages 19–28, 2012.

[Butler *et al.* 2019] Keith T Butler, Gopalakrishnan Sai Gautam and Pieremanuele Canepa. *Designing interfaces in energy materials applications with first-principles calculations*. npj Computational Materials, vol. 5, no. 1, pages 1–12, 2019.

[Callaway 1959] Joseph Callaway. *Model for lattice thermal conductivity at low temperatures*. Physical Review, vol. 113, no. 4, page 1046, 1959.

[Cao *et al.* 2016] Moyuan Cao, Dawei Guo, Cunming Yu, Kan Li, Mingjie Liu and Lei Jiang. *Water-repellent properties of superhydrophobic and lubricant-infused "slippery" surfaces: A brief study on the functions and applications*. ACS applied materials & interfaces, vol. 8, no. 6, pages 3615–3623, 2016.

[Cao *et al.* 2018] Bing-Yang Cao, Ji-Hang Zou, Guo-Jie Hu and Gui-Xing Cao. *Enhanced thermal transport across multilayer graphene and water by interlayer functionalization*. Applied Physics Letters, vol. 112, no. 4, page 041603, 2018.

[Cao *et al.* 2021] Wen Cao, Hao Xue, Wei Shen, Hao Yang, Long Zhao and Yang Wang. *The effect of dynamic behaviours of the water droplet on DC/AC flashover performance on silicone rubber surface: Experiment, simulation and theoretical analysis*. High Voltage, vol. 6, no. 4, pages 637–646, 2021.

[Cardellini *et al.* 2016] Annalisa Cardellini, Matteo Fasano, Masoud Bozorg Bigdeli, Eliodoro Chiavazzo and Pietro Asinari. *Thermal transport phenomena in nanoparticle suspensions*. Journal of Physics: Condensed Matter, vol. 28, no. 48, page 483003, 2016.

[Carlborg *et al.* 2008] Carl Fredrik Carlborg, Junichiro Shiomi and Shigeo Maruyama. *Thermal boundary resistance between single-walled carbon nanotubes and surrounding matrices*. Physical Review B, vol. 78, no. 20, page 205406, 2008.

[Carré *et al.* 2007] Antoine Carré, Ludovic Berthier, Jürgen Horbach, Simona Ispas and Walter Kob. *Amorphous silica modeled with truncated and screened Coulomb interactions: A molecular dynamics simulation study*. The Journal of chemical physics, vol. 127, no. 11, page 114512, 2007.

[Casimir 1938] HBG Casimir. *Note on the conduction of heat in crystals*. Physica, vol. 5, no. 6, pages 495–500, 1938.

[Chakraborty *et al.* 2017] Sudip Chakraborty, Hemant Kumar, Chandan Dasgupta and Prabal K Maiti. *Confined water: structure, dynamics, and thermodynamics*. Accounts of chemical research, vol. 50, no. 9, pages 2139–2146, 2017.

[Chaplin 2015] Martin Chaplin. *Water structure and science. 2016*. Available online: www1. lsbu. ac. uk/water/water_vibrational_ spectrum. html (accessed on 20 June 2020), 2015.

[Che *et al.* 2000] Jianwei Che, Tahir Cagin and William A Goddard III. *Thermal conductivity of carbon nanotubes*. Nanotechnology, vol. 11, no. 2, page 65, 2000.

[Cheh *et al.* 2013] Jigger Cheh, Yi Gao, Chunlei Wang, Hong Zhao and Haiping Fang. *Ice or water: thermal properties of monolayer water adsorbed on a substrate*. Journal of Statistical Mechanics: Theory and Experiment, vol. 2013, no. 06, page P06009, 2013.

[Chen *et al.* 2016] I-Tzu Chen, David A Sessoms, Zachary Sherman, Eugene Choi, Olivier Vincent and Abraham D Stroock. *Stability limit of water by metastable vapor–liquid equilibrium with nanoporous silicon membranes*. The Journal of Physical Chemistry B, vol. 120, no. 23, pages 5209–5222, 2016.

[Chen *et al.* 2018] Yanfeng Chen, Qi Zhang, Xiaoyan Wen, Huibin Yin and Jian Liu. *A novel CNT encapsulated phase change material with enhanced thermal conductivity and photo-thermal conversion performance*. Solar Energy Materials and Solar Cells, vol. 184, pages 82–90, 2018.

[Cheng *et al.* 2015] Zhe Cheng, Longju Liu, Shen Xu, Meng Lu and Xinwei Wang. *Temperature dependence of electrical and thermal conduction in single silver nanowire*. Scientific reports, vol. 5, no. 1, pages 1–12, 2015.

[Chialvo & Cummings 1994] Ariel A Chialvo and Peter T Cummings. *Hydrogen bonding in supercritical water*. The Journal of chemical physics, vol. 101, no. 5, pages 4466–4469, 1994.

[Choi & Eastman 1995] Stephen US Choi and Jeffrey A Eastman. *Enhancing thermal conductivity of fluids with nanoparticles*. Technical report, Argonne National Lab., IL (United States), 1995.

[Choi *et al.* 2008a] Hojin Choi, Jung Yun Kim, Seungdo Hong, Joonkyung Jang and Man Yeong Ha. *Characteristics of the Water Meniscus at AFM Tip for Various Surface Energy*. In ASME 2008 6th International Conference on Nanochannels, Microchannels, and Minichannels, pages 1005–1011. American Society of Mechanical Engineers Digital Collection, 2008.

[Choi *et al.* 2008b] Sun Gyu Choi, Tae-Jung Ha, Byoung-Gon Yu, Seung Pil Jaung, Ohmyoung Kwon and Hyung-Ho Park. *Improvement of uncooled infrared imaging detector by using mesoporous silica as a thermal isolation layer*. Ceramics International, vol. 34, no. 4, pages 833–836, 2008.

[Choi 2009] Stephen US Choi. *Nanofluids: from vision to reality through research*. Journal of Heat transfer, vol. 131, no. 3, 2009.

[Choudhary *et al.* 2017] Kamal Choudhary, Faical Yannick P Congo, Tao Liang, Chandler Becker, Richard G Hennig and Francesca Tavazza. *Evaluation and comparison of classical interatomic potentials through a user-friendly interactive web-interface*. Scientific data, vol. 4, no. 1, pages 1–12, 2017.

[Chubynsky & Slater 2014] Mykyta V Chubynsky and Gary W Slater. *Diffusing diffusivity: a model for anomalous, yet Brownian, diffusion*. Physical review letters, vol. 113, no. 9, page 098302, 2014.

[Coquil *et al.* 2011] Thomas Coquil, Jin Fang and Laurent Pilon. *Molecular dynamics study of the thermal conductivity of amorphous nanoporous silica*.

International Journal of Heat and Mass Transfer, vol. 54, no. 21-22, pages 4540–4548, 2011.

[Corongiu & Clementi 1993] Giorgina Corongiu and Enrico Clementi. *Molecular dynamics simulations with a flexible and polarizable potential: density of states for liquid water at different temperatures*. The Journal of chemical physics, vol. 98, no. 6, pages 4984–4990, 1993.

[Cruz-Chu *et al.* 2006] Eduardo R Cruz-Chu, Aleksei Aksimentiev and Klaus Schulten. *Water- silica force field for simulating nanodevices*. The Journal of Physical Chemistry B, vol. 110, no. 43, pages 21497–21508, 2006.

[Cui *et al.* 2018] Liu Cui, Sanqiang Shi, Zhao Li, Gaosheng Wei and Xiaoze Du. *Reduction of thermal conductivity in silicene nanomesh: insights from coherent and incoherent phonon transport*. Physical Chemistry Chemical Physics, vol. 20, no. 42, pages 27169–27175, 2018.

[Cui 2005] ST Cui. *Molecular self-diffusion in nanoscale cylindrical pores and classical Fick's law predictions*. The Journal of chemical physics, vol. 123, no. 5, page 054706, 2005.

[Da Silva 2014] Leandro Barros Da Silva. *Structural and dynamical properties of water confined in carbon nanotubes*. Journal of Nanostructure in Chemistry, vol. 4, no. 2, page 104, 2014.

[Dao & Jeong 2015] Trung Dung Dao and Han Mo Jeong. *Novel stearic acid/graphene core–shell composite microcapsule as a phase change material exhibiting high shape stability and performance*. Solar Energy Materials and Solar Cells, vol. 137, pages 227–234, 2015.

[Daviran *et al.* 2017] Samaneh Daviran, Alibakhsh Kasaeian, Hamed Tahmooressi, Alimorad Rashidi, Dongsheng Wen and Omid Mahian. *Evaluation of clustering role versus Brownian motion effect on the heat conduction in nanofluids: A novel approach*. International Journal of Heat and Mass Transfer, vol. 108, pages 822–829, 2017.

[Desmarchelier *et al.* 2020] Paul Desmarchelier, Konstantinos Termentzidis and Anne Tanguy. *Vibrational density of states of free and embedded semiconducting GaN nanoparticles*. Semiconductor Science and Technology, vol. 35, no. 9, page 094001, 2020.

[Dettori *et al.* 2015] Riccardo Dettori, Claudio Melis, Xavier Cartoixa, Riccardo Rurali and Luciano Colombo. *Model for thermal conductivity in nanoporous silicon from atomistic simulations*. Physical Review B, vol. 91, no. 5, page 054305, 2015.

[Dickey 2017] Michael D Dickey. *Stretchable and soft electronics using liquid metals*. Advanced Materials, vol. 29, no. 27, page 1606425, 2017.

[Dmitriev *et al.* 2018] Andrey I Dmitriev, Anton Y Nikonov and Werner Österle. *Molecular Dynamics Modeling of the Sliding Performance of an Amorphous Silica Nano-Layer—The Impact of Chosen Interatomic Potentials*. Lubricants, vol. 6, no. 2, page 43, 2018.

[Drelich 2019] Jaroslaw W Drelich. *Contact angles: From past mistakes to new developments through liquid-solid adhesion measurements*. Advances in colloid and interface science, vol. 267, pages 1–14, 2019.

[Du *et al.* 2016] BX Du, ZY He, Qiang Du and YG Guo. *Effects of water absorption on surface charge and dielectric breakdown of polyimide/Al 2 O 3 nanocomposite films*. IEEE Transactions on Dielectrics and Electrical Insulation, vol. 23, no. 1, pages 134–141, 2016.

[Duan & Lieber 2000] Xiangfeng Duan and Charles M Lieber. *General synthesis of compound semiconductor nanowires*. Advanced Materials, vol. 12, no. 4, pages 298–302, 2000.

[Duki & Tsige 2018] Solomon F Duki and Mesfin Tsige. *Volume analysis of supercooled water under high pressure*. MRS Advances, vol. 3, no. 41, pages 2467–2478, 2018.

[Duong *et al.* 2019] Thuy-Quynh Duong, Carlo Massobrio, Guido Ori, Mauro Boero and Evelyne Martin. *Thermal conductivity and transport modes in glassy GeTe 4 by first-principles molecular dynamics*. Physical Review Materials, vol. 3, no. 10, page 105401, 2019.

[Ehle *et al.* 2011] Angelika Ehle, Steffen Feja and Matthias H Buschmann. *Temperature dependency of ceramic nanofluids shows classical behavior*. Journal of thermophysics and heat transfer, vol. 25, no. 3, pages 378–385, 2011.

[Emami *et al.* 2014] Fateme S Emami, Valeria Puddu, Rajiv J Berry, Vikas Varshney, Siddharth V Patwardhan, Carole C Perry and Hendrik Heinz. *Force*

field and a surface model database for silica to simulate interfacial properties in atomic resolution. Chemistry of Materials, vol. 26, no. 8, pages 2647–2658, 2014.

[Erlebacher 2018] Jonah Erlebacher. *DE-SC0008686: Control of Reactivity in Nanoporous Metal/Ionic Liquid Composite Catalysts*. Technical report, Johns Hopkins Univ., Baltimore, MD (United States), 2018.

[Esfe & Afrand 2020] Mohammad Hemmat Esfe and Masoud Afrand. *Mathematical and artificial brain structure-based modeling of heat conductivity of water based nanofluid enriched by double wall carbon nanotubes*. Physica A: Statistical Mechanics and its Applications, vol. 540, page 120766, 2020.

[Fang & Pilon 2011] Jin Fang and Laurent Pilon. *Scaling laws for thermal conductivity of crystalline nanoporous silicon based on molecular dynamics simulations*. Journal of Applied Physics, vol. 110, no. 6, page 064305, 2011.

[Fang *et al.* 2006] Kuan-Chuan Fang, Cheng-I Weng and Shin-Pon Ju. *An investigation into the structural features and thermal conductivity of silicon nanoparticles using molecular dynamics simulations*. Nanotechnology, vol. 17, no. 15, page 3909, 2006.

[Farmahini & Bhatia 2016] Amir H Farmahini and Suresh K Bhatia. *Effect of structural anisotropy and pore-network accessibility on fluid transport in nanoporous Ti3SiC2 carbide-derived carbon*. Carbon, vol. 103, pages 16–27, 2016.

[Felix & Pereira 2018] Isaac M Felix and Luiz Felipe C Pereira. *Thermal conductivity of graphene-hBN superlattice ribbons*. Scientific reports, vol. 8, no. 1, pages 1–10, 2018.

[Fogarty *et al.* 2010] Joseph C Fogarty, Hasan Metin Aktulga, Ananth Y Grama, Adri CT Van Duin and Sagar A Pandit. *A reactive molecular dynamics simulation of the silica-water interface*. The Journal of chemical physics, vol. 132, no. 17, page 174704, 2010.

[Furchner *et al.* 2017] Andreas Furchner, Annika Kroning, Sebastian Rauch, Petra Uhlmann, Klaus-Jochen Eichhorn and Karsten Hinrichs. *Molecular interactions and hydration states of ultrathin functional films at the solid–liquid interface*. Analytical chemistry, vol. 89, no. 6, pages 3240–3244, 2017.

[Futamura *et al.* 2017] Ryusuke Futamura, Taku Iiyama, Yuma Takasaki, Yury Gogotsi, Mark J Biggs, Mathieu Salanne, Julie Segalini, Patrice Simon and Katsumi Kaneko. *Partial breaking of the Coulombic ordering of ionic liquids confined in carbon nanopores*. Nature materials, vol. 16, no. 12, pages 1225–1232, 2017.

[Ge & Li 2001] Wei Ge and Jinghai Li. *Macro-scale pseudo-particle modeling for particle-fluid systems*. Chinese Science Bulletin, vol. 46, no. 18, pages 1503–1507, 2001.

[GHASEMI & Kord 2009] ESMAEIL GHASEMI and Behzad Kord. *Long-term water absorption behaviour of polypropylene/wood flour/organoclay hybrid nanocomposite*. 2009.

[Gingold & Monaghan 1977] Robert A Gingold and Joseph J Monaghan. *Smoothed particle hydrodynamics: theory and application to non-spherical stars*. Monthly notices of the royal astronomical society, vol. 181, no. 3, pages 375–389, 1977.

[Giovambattista *et al.* 2006] Nicolas Giovambattista, Peter J Rossky and Pablo G Debenedetti. *Effect of pressure on the phase behavior and structure of water confined between nanoscale hydrophobic and hydrophilic plates*. Physical Review E, vol. 73, no. 4, page 041604, 2006.

[Giri & Hopkins 2014] Ashutosh Giri and Patrick E Hopkins. *Spectral analysis of thermal boundary conductance across solid/classical liquid interfaces: A molecular dynamics study*. Applied Physics Letters, vol. 105, no. 3, page 033106, 2014.

[Glassbrenner & Slack 1964] C Jo Glassbrenner and Glen A Slack. *Thermal conductivity of silicon and germanium from 3 K to the melting point*. Physical Review, vol. 134, no. 4A, page A1058, 1964.

[Glicksman & Schaefer 1967] ME Glicksman and RJ Schaefer. *Investigation of solid/liquid interface temperatures via isenthalpic solidification*. Journal of Crystal Growth, vol. 1, no. 5, pages 297–310, 1967.

[Goicochea *et al.* 2011] Javier V Goicochea, Ming Hu, Bruno Michel and Dimos Poulikakos. *Surface functionalization mechanisms of enhancing heat transfer at solid-liquid interfaces*. Journal of heat transfer, vol. 133, no. 8, 2011.

[Gravelle *et al.* 2016] Simon Gravelle, Hiroaki Yoshida, Laurent Joly, Christophe Ybert and Lydéric Bocquet. *Carbon membranes for efficient water-ethanol separation*. The Journal of chemical physics, vol. 145, no. 12, page 124708, 2016.

[Guevara-Carrion *et al.* 2008] Gabriela Guevara-Carrion, Carlos Nieto-Draghi, Jadran Vrabec and Hans Hasse. *Prediction of transport properties by molecular simulation: methanol and ethanol and their mixture*. The Journal of Physical Chemistry B, vol. 112, no. 51, pages 16664–16674, 2008.

[Guillot 2002] Bertrand Guillot. *A reappraisal of what we have learnt during three decades of computer simulations on water*. Journal of molecular liquids, vol. 101, no. 1-3, pages 219–260, 2002.

[Guo *et al.* 2002] J-H Guo, Yi Luo, Andreas Augustsson, J-E Rubensson, Conny Såthe, Hans Ågren, Hans Siegbahn and Joseph Nordgren. *X-ray emission spectroscopy of hydrogen bonding and electronic structure of liquid water*. Physical review letters, vol. 89, no. 13, page 137402, 2002.

[Guo *et al.* 2021] Pu Guo, Zubin Wang, Xiao Han and Liping Heng. *Nepenthes pitcher inspired isotropic/anisotropic polymer solid–liquid composite interface: preparation, function, and application*. Materials Chemistry Frontiers, vol. 5, no. 4, pages 1716–1742, 2021.

[Hafskjold *et al.* 1993] Bjørn Hafskjold, Tamio Ikeshoji and Signe Kjelstrup Ratkje. *On the molecular mechanism of thermal diffusion in liquids*. Molecular Physics, vol. 80, no. 6, pages 1389–1412, 1993.

[Han *et al.* 2010] Sungho Han, MY Choi, Pradeep Kumar and H Eugene Stanley. *Phase transitions in confined water nanofilms*. Nature Physics, vol. 6, no. 9, pages 685–689, 2010.

[Harikrishna *et al.* 2013] Hari Harikrishna, William A Ducker and Scott T Huxtable. *The influence of interface bonding on thermal transport through solid–liquid interfaces*. Applied Physics Letters, vol. 102, no. 25, page 251606, 2013.

[Hashin & Shtrikman 1962] Z am Hashin and S Shtrikman. *On some variational principles in anisotropic and nonhomogeneous elasticity*. Journal of the Mechanics and Physics of Solids, vol. 10, no. 4, pages 335–342, 1962.

[He *et al.* 2001] Mingyan He, Amy Szuchmacher Blum, D Eric Aston, Cynthia Buenviaje, René M Overney and Reto Luginbühl. *Critical phenomena of water bridges in nanoasperity contacts*. The Journal of Chemical Physics, vol. 114, no. 3, pages 1355–1360, 2001.

[He *et al.* 2018] Wenqing He, Peng Liu, Jieke Jiang, Meijin Liu, Hualin Li, Jianqiang Zhang, Yan Luo, Hon-Yeung Cheung and Xi Yao. *Development of multifunctional liquid-infused materials by printing assisted functionalization on porous nanocomposites*. Journal of Materials Chemistry A, vol. 6, no. 9, pages 4199–4208, 2018.

[Heim & Bonaccurso 2013] Lars-Oliver Heim and Elmar Bonaccurso. *Measurement of line tension on droplets in the submicrometer range*. Langmuir, vol. 29, no. 46, pages 14147–14153, 2013.

[Hemmati & Angell 1998] M Hemmati and CA Angell. *Physics meets geology, edited by M. Aoki, R. Hemley*, 1998.

[Henry & Chen 2008] Asegun S Henry and Gang Chen. *Spectral phonon transport properties of silicon based on molecular dynamics simulations and lattice dynamics*. Journal of Computational and Theoretical Nanoscience, vol. 5, no. 2, pages 141–152, 2008.

[Hienola *et al.* 2007] Anca I Hienola, PM Winkler, PE Wagner, Hanna Vehkamäki, Antti Lauri, Ismo Napari and Markku Kulmala. *Estimation of line tension and contact angle from heterogeneous nucleation experimental data*. The Journal of chemical physics, vol. 126, no. 9, page 094705, 2007.

[Hopkins *et al.* 2011] Patrick E Hopkins, Charles M Reinke, Mehmet F Su, Roy H Olsson III, Eric A Shaner, Zayd C Leseman, Justin R Serrano, Leslie M Phinney and Ihab El-Kady. *Reduction in the thermal conductivity of single crystalline silicon by phononic crystal patterning*. Nano letters, vol. 11, pages 107–112, 2011.

[Horn *et al.* 2004] Hans W Horn, William C Swope, Jed W Pitera, Jeffry D Madura, Thomas J Dick, Greg L Hura and Teresa Head-Gordon. *Development of an improved four-site water model for biomolecular simulations: TIP4P-Ew*. The Journal of chemical physics, vol. 120, no. 20, pages 9665–9678, 2004.

[Hu & Jia 2021] Ying Hu and Guozhu Jia. *Non-thermal effect of microwave in supercritical water: A molecular dynamics simulation study*. Physica A: Statistical Mechanics and its Applications, vol. 564, page 125275, 2021.

[Hu *et al.* 2011] Ming Hu, Konstantinos P Giapis, Javier V Goicochea, Xiaoliang Zhang and Dimos Poulikakos. *Significant reduction of thermal conductivity in Si/Ge core- shell nanowires*. Nano letters, vol. 11, no. 2, pages 618–623, 2011.

[Hu *et al.* 2016] Yanwei Hu, Haoran Li, Yurong He and Lidong Wang. *Role of nanoparticles on boiling heat transfer performance of ethylene glycol aqueous solution based graphene nanosheets nanofluid*. International Journal of Heat and Mass Transfer, vol. 96, pages 565–572, 2016.

[Huang *et al.* 2018] Dezhao Huang, Ruimin Ma, Teng Zhang and Tengfei Luo. *Origin of Hydrophilic Surface Functionalization-Induced Thermal Conductance Enhancement across Solid–Water Interfaces*. ACS applied materials & interfaces, vol. 10, no. 33, pages 28159–28165, 2018.

[Huber *et al.* 2012] Marcia L Huber, Richard A Perkins, Daniel G Friend, Jan V Sengers, Marc J Assael, Ifigenia N Metaxa, Kiyoshi Miyagawa, Robert Hellmann and Eckhard Vogel. *New international formulation for the thermal conductivity of H2O*. Journal of Physical and Chemical Reference Data, vol. 41, no. 3, page 033102, 2012.

[Hui *et al.* 1999] PM Hui, X Zhang, AJ Markworth and D Stroud. *Thermal conductivity of graded composites: Numerical simulations and an effective medium approximation*. Journal of materials science, vol. 34, no. 22, pages 5497–5503, 1999.

[Isaiev *et al.* 2016] Mykola Isaiev, Sergii Burian, Leonid Bulavin, Michel Gradeck, Fabrice Lemoine and Konstantinos Termentzidis. *Efficient tuning of potential parameters for liquid–solid interactions*. Molecular Simulation, vol. 42, pages 910–915, 2016.

[Isaiev *et al.* 2018] Mykola Isaiev, Sergii Burian, Leonid Bulavin, William Chaze, Michel Gradeck, Guillaume Castanet, Samy Merabia, Pawel Keblinski and Konstantinos Termentzidis. *Gibbs adsorption impact on a nanodroplet shape: modification of Young–Laplace equation*. The Journal of Physical Chemistry B, vol. 122, no. 12, pages 3176–3183, 2018.

[Isaiev *et al.* 2020] Mykola Isaiev, Xiaorui Wang, Konstantinos Termentzidis and David Lacroix. *Thermal transport enhancement due to confined water in hybrid nanocomposite*. arXiv preprint arXiv:2004.04121, 2020.

[Isaifan *et al.* 2019] Rima J Isaifan, Daniel Johnson, Luis Ackermann, Benjamin Figgis and Mohammed Ayoub. *Evaluation of the adhesion forces between dust particles and photovoltaic module surfaces*. Solar Energy Materials and Solar Cells, vol. 191, pages 413–421, 2019.

[Issa *et al.* 2020] Hasan K Issa, Aboozar Taherizadeh and Ali Maleki. *Atomistic-level study of the mechanical behavior of amorphous and crystalline silica nanoparticles*. Ceramics International, vol. 46, no. 13, pages 21647–21656, 2020.

[Jean *et al.* 2014] V Jean, Sébastien Fumeron, K Termentzidis, S Tutashkonko and David Lacroix. *Monte Carlo simulations of phonon transport in nanoporous silicon and germanium*. Journal of Applied Physics, vol. 115, no. 2, page 024304, 2014.

[Ji 2004] Shaocheng Ji. *A generalized mixture rule for estimating the viscosity of solid-liquid suspensions and mechanical properties of polyphase rocks and composite materials*. Journal of Geophysical Research: Solid Earth, vol. 109, no. B10, 2004.

[Jiang *et al.* 2015] Haifeng Jiang, Qianghui Xu, Chao Huang and Lin Shi. *The role of interfacial nanolayer in the enhanced thermal conductivity of carbon nanotube-based nanofluids*. Applied Physics A, vol. 118, no. 1, pages 197–205, 2015.

[Jorgensen & Tirado-Rives 1988] William L Jorgensen and Julian Tirado-Rives. *The OPLS [optimized potentials for liquid simulations] potential functions for proteins, energy minimizations for crystals of cyclic peptides and crambin*. Journal of the American Chemical Society, vol. 110, no. 6, pages 1657–1666, 1988.

[Ju & Yang 2018] Shin-Pon Ju and Cheng-Chia Yang. *Understanding the structural, mechanical, thermal, and electronic properties of MgCa bulk metallic glasses by molecular dynamics simulation and density functional theory calculation*. Computational Materials Science, vol. 154, pages 256–265, 2018.

[Kang *et al.* 2012] Dun-Yen Kang, Ho Ming Tong, Ji Zang, Rudra Prosad Choudhury, David S Sholl, Haskell W Beckham, Christopher W Jones and Sankar Nair. *Single-walled aluminosilicate nanotube/poly (vinyl alcohol) nanocomposite membranes*. ACS Applied Materials & Interfaces, vol. 4, no. 2, pages 965–976, 2012.

[Karuso *et al.* 2012] Peter Karuso*et al. Quasicrystals or quasiscience: 2011 Nobel prize in chemistry II*. Chemistry in Australia, no. Mar 2012, page 16, 2012.

[Kasahara *et al.* 2020] Kota Kasahara, Yuki Takimoto, Ryoi Ashida and Takuya Takahashi. *Effects of ion–water Lennard-Jones potentials on the hydration dynamics around a monovalent atomic ion in molecular dynamics simulations*. Molecular Simulation, vol. 46, no. 2, pages 83–91, 2020.

[Kazan *et al.* 2010] Michel Kazan, G Guisbiers, Susana Pereira, MR Correia, P Masri, Aurélien Bruyant, Sebastian Volz and Pascal Royer. *Thermal conductivity of silicon bulk and nanowires: Effects of isotopic composition, phonon confinement, and surface roughness*. Journal of Applied Physics, vol. 107, no. 8, page 083503, 2010.

[Keating 1966] PN Keating. *Effect of invariance requirements on the elastic strain energy of crystals with application to the diamond structure*. Physical Review, vol. 145, no. 2, page 637, 1966.

[Keblinski *et al.* 2002] P Keblinski, MZ Bazant, RK Dash and MM Treacy. *Thermodynamic behavior of a model covalent material described by the environment-dependent interatomic potential*. Physical Review B, vol. 66, no. 6, page 064104, 2002.

[Keblinski *et al.* 2005] Pawel Keblinski, Jeffrey A Eastman and David G Cahill. *Nanofluids for thermal transport*. Materials today, vol. 8, no. 6, pages 36–44, 2005.

[Kerrache *et al.* 2006] A Kerrache, Victor Teboul and Andre Monteil. *Screening dependence of the dynamical and structural properties of BKS silica.* Chemical physics, vol. 321, no. 1-2, pages 69–74, 2006.

[Khan *et al.* 2017] Mohammed Mumtaz A Khan, R Saidur and Fahad A Al-Sulaiman. *A review for phase change materials (PCMs) in solar absorption refrigeration systems*. Renewable and sustainable energy reviews, vol. 76, pages 105–137, 2017.

[Kim *et al.* 2009] Ho Jin Kim, In Cheol Bang and Jun Onoe. *Characteristic stability of bare Au-water nanofluids fabricated by pulsed laser ablation in liquids*. Optics and Lasers in Engineering, vol. 47, no. 5, pages 532–538, 2009.

[Kim *et al.* 2019] Taeyeong Kim, Dong-min Kim, Bong Jae Lee and Jungchul Lee. *Soft and deformable sensors based on liquid metals*. Sensors, vol. 19, no. 19, page 4250, 2019.

[Kio 2014] Michael Tamuno Elekima Kio. *Molecular Dynamics of Kapitza Resistance at the Solid-Liquid Interface of Nanofluidic Channels*. 2014.

[Kittel *et al.* 1996] Charles Kittel, Paul McEuen and Paul McEuen. Introduction to solid state physics, volume 8. Wiley New York, 1996.

[Ko *et al.* 2010] Jeong-Ahn Ko, Ho-Jin Choi, Man-Yeong Ha, Seung-Do Hong and Hyun-Sik Yoon. *A study on the behavior of water droplet confined between an atomic force microscope tip and rough surfaces*. Langmuir, vol. 26, no. 12, pages 9728–9735, 2010.

[Kokate & Sonawane 2019] Yogesh Kokate and Sandipkumar Sonawane. *Investigation of Particle Size Effect on Thermal Conductivity Enhancement of Distilled Water-Al2O3 Nanofluids*. In ICTEA: International conference on thermal engineering, volume 2019, 2019.

[Konashi *et al.* 2003] Kenji Konashi, Tamio Ikeshoji, Yoshiyuki Kawazoe and Hideki Matsui. *A molecular dynamics study of thermal conductivity of zirconium hydride*. Journal of Alloys and compounds, vol. 356, pages 279–282, 2003.

[Korayem *et al.* 2018] AH Korayem, M Taghizadeh, M Abdi and MH Korayem. *Experimental analysis of rough surface topography and modifying the humidity effect in AFM images to improve the topography quality*. The International Journal of Advanced Manufacturing Technology, vol. 94, no. 1-4, pages 1229–1241, 2018.

[Ladhari *et al.* 2010] Aouatef Ladhari, Hachmi Ben Daly, Hedi Belhadjsalah, Kenneth C Cole and Johanne Denault. *Investigation of water absorption in clay-reinforced polypropylene nanocomposites*. Polymer Degradation and Stability, vol. 95, no. 4, pages 429–439, 2010.

[Lampin *et al.* 2013] E Lampin, PL Palla, P-A Francioso and F Cleri. *Thermal conductivity from approach-to-equilibrium molecular dynamics*. Journal of Applied Physics, vol. 114, no. 3, page 033525, 2013.

[Lee & Kim 2019] Song Hi Lee and Jahun Kim. *Transport properties of bulk water at 243–550 K: a Comparative molecular dynamics simulation study using SPC/E, TIP4P, and TIP4P/2005 water models*. Molecular Physics, vol. 117, no. 14, pages 1926–1933, 2019.

[Lee *et al.* 2007] J-H Lee, JC Grossman, J Reed and G Galli. *Lattice thermal conductivity of nanoporous Si: Molecular dynamics study*. Applied Physics Letters, vol. 91, page 223110, 2007.

[Legon & Millen 1987] AC Legon and DJ Millen. *Angular geometries and other properties of hydrogen-bonded dimers: A simple electrostatic interpretation of the success of the electron-pair model*. Chemical Society Reviews, vol. 16, pages 467–498, 1987.

[Lennard-Jones 1924] John Edward Lennard-Jones. *On the determination of molecular fields. II. From the equation of state of gas*. Proc. Roy. Soc. A, vol. 106, pages 463–477, 1924.

[Li *et al.* 1998] Ju Li, Lisa Porter and Sidney Yip. *Atomistic modeling of finite-temperature properties of crystalline β-SiC: II. Thermal conductivity and effects of point defects*. Journal of Nuclear Materials, vol. 255, pages 139–152, 1998.

[Li *et al.* 2017] Xiang Li, Yuan Zhou, Hongen Nian, Xinxing Zhang, Ouyang Dong, Xiufeng Ren, Jinbo Zeng, Chunxi Hai and Yue Shen. *Advanced nanocomposite phase change material based on calcium chloride hexahydrate with aluminum oxide nanoparticles for thermal energy storage*. Energy & Fuels, vol. 31, no. 6, pages 6560–6567, 2017.

[Li *et al.* 2018] Jia-Sheng Li, Yong Tang, Zong-Tao Li, Long-Shi Rao, Xin-Rui Ding and Bin-Hai Yu. *High efficiency solid–liquid hybrid-state quantum dot light-emitting diodes*. Photonics Research, vol. 6, no. 12, pages 1107–1115, 2018.

[Li *et al.* 2019] Xiying Li, Jia Ming Zhang, Xin Yi, Zhongyi Huang, Pengyu Lv and Huiling Duan. *Multimaterial microfluidic 3D printing of textured composites with liquid inclusions*. Advanced Science, vol. 6, no. 3, page 1800730, 2019.

[Li *et al.* 2020] Xiaoke Li, Guangyong Zeng and Xinyu Lei. *The stability, optical properties and solar-thermal conversion performance of SiC-MWCNTs hybrid nanofluids for the direct absorption solar collector (DASC) application*. Solar Energy Materials and Solar Cells, vol. 206, page 110323, 2020.

[Li *et al.* 2021] Zhen Li, Lin Frank Song, Pengfei Li and Kenneth M Merz Jr. *Parametrization of Trivalent and Tetravalent Metal Ions for the OPC3, OPC, TIP3P-FB, and TIP4P-FB Water Models*. Journal of chemical theory and computation, vol. 17, no. 4, pages 2342–2354, 2021.

[Lishchuk *et al.* 2015] Pavlo Lishchuk, Dmytro Andrusenko, Mykola Isaiev, Vladimir Lysenko and Roman Burbelo. *Investigation of thermal transport properties of porous silicon by photoacoustic technique*. International Journal of Thermophysics, vol. 36, pages 2428–2433, 2015.

[Liu *et al.* 2020] Changqing Liu, Wei Yu, Cheng Chen, Huaqing Xie and Bingyang Cao. *Remarkably reduced thermal contact resistance of graphene/olefin block copolymer/paraffin form stable phase change thermal interface material*. International Journal of Heat and Mass Transfer, vol. 163, page 120393, 2020.

[Liu *et al.* 2021] Shanliangzi Liu, Dylan S Shah and Rebecca Kramer-Bottiglio. *Highly stretchable multilayer electronic circuits using biphasic gallium-indium*. Nature Materials, vol. 20, no. 6, pages 851–858, 2021.

[Liu *et al.* 2022] Hongshen Liu, Huseyin Kaya, Yen-Ting Lin, Andrew Ogrinc and Seong H Kim. *Vibrational spectroscopy analysis of silica and silicate glass networks*. Journal of the American Ceramic Society, vol. 105, no. 4, pages 2355–2384, 2022.

[Lo *et al.* 2005] Chih-Hung Lo, Tsing-Tshih Tsung, Liang-Chia Chen, Chun-His Su and Hong-Ming Lin. *Fabrication of copper oxide nanofluid using submerged arc nanoparticle synthesis system (SANSS)*. Journal of Nanoparticle Research, vol. 7, no. 2, pages 313–320, 2005.

[Loulijat *et al.* 2015] Hamid Loulijat, Hicham Zerradi, Soufiya Mizani, El mehdi Achhal, Aouatif Dezairi and Said Ouaskit. *The behavior of the thermal conductivity near the melting temperature of copper nanoparticle*. Journal of Molecular Liquids, vol. 211, pages 695–704, 2015.

[Lu & Berkowitz 2006] L Lu and ML Berkowitz. *Hydration force between model hydrophilic surfaces: Computer simulations*, 2006.

[Lugger *et al.* 2018] Jody Lugger, Dirk Jan Mulder, Rint Sijbesma and Albert Schenning. *Nanoporous polymers based on liquid crystals*. Materials, vol. 11, no. 1, page 104, 2018.

[Luo *et al.* 1997] K Luo, Z Shi, J Varesi and A Majumdar. *Sensor nanofabrication, performance, and conduction mechanisms in scanning thermal microscopy*. Journal of Vacuum Science & Technology B: Microelectronics and Nanometer Structures Processing, Measurement, and Phenomena, vol. 15, no. 2, pages 349–360, 1997.

[Luu *et al.* 2019] Son DN Luu, Taras Parashchuk, Artur Kosonowski, Thang B Phan and Krzysztof T Wojciechowski. *Structural and Thermoelectric Properties of Solid–Liquid In4Se3-In Composite*. Journal of Electronic Materials, vol. 48, no. 9, pages 5418–5427, 2019.

[Luzar & Chandler 1996] Alenka Luzar and David Chandler. *Effect of environment on hydrogen bond dynamics in liquid water*. Physical review letters, vol. 76, no. 6, page 928, 1996.

[Machrafi *et al.* 2016] Hatim Machrafi, Georgy Lebon and D Jou. *Thermal rectifier efficiency of various bulk–nanoporous silicon devices*. International Journal of Heat and Mass Transfer, vol. 97, pages 603–610, 2016.

[Malakooti *et al.* 2020] Mohammad H Malakooti, Michael R Bockstaller, Krzysztof Matyjaszewski and Carmel Majidi. *Liquid metal nanocomposites*. Nanoscale Advances, vol. 2, no. 7, pages 2668–2677, 2020.

[Mantisi *et al.* 2012] B Mantisi, Arnaud Tanguy, G Kermouche and E Barthel. *Atomistic response of a model silica glass under shear and pressure*. The European Physical Journal B, vol. 85, no. 9, pages 1–13, 2012.

[Mao & Zhang 2012] Yijin Mao and Yuwen Zhang. *Thermal conductivity, shear viscosity and specific heat of rigid water models*. Chemical Physics Letters, vol. 542, pages 37–41, 2012.

[Márquez-García *et al.* 2018] Lourdes Márquez-García, Braulio Beltrán-Pitarch, Damian Powell, Gao Min and Jorge García-Cañadas. *Large Power Factor Improvement in a Novel Solid–Liquid Thermoelectric Hybrid Device*. ACS Applied Energy Materials, vol. 1, no. 2, pages 254–259, 2018.

[Masuduzzaman & Kim 2020] Md Masuduzzaman and BoHung Kim. *Scale effects in nanoscale heat transfer for fourier's law in a dissimilar molecular interface*. ACS omega, vol. 5, no. 41, pages 26527–26536, 2020.

[Matsumoto & Kimura 1998] S Maruyama T Kurashige S Matsumoto and Y Yamaguchi T Kimura. *Liquid droplet in contact with a solid surface*. Microscale Thermophysical Engineering, vol. 2, no. 1, pages 49–62, 1998.

[McBride & Law 2012] Sean P McBride and Bruce M Law. *Influence of line tension on spherical colloidal particles at liquid-vapor interfaces*. Physical review letters, vol. 109, no. 19, page 196101, 2012.

[Melillo *et al.* 2011] Matthew Melillo, Fangqiang Zhu, Mark A Snyder and Jeetain Mittal. *Water transport through nanotubes with varying interaction strength between tube wall and water*. The journal of physical chemistry letters, vol. 2, no. 23, pages 2978–2983, 2011.

[Melis *et al.* 2014] Claudio Melis, Riccardo Dettori, Simon Vandermeulen and Luciano Colombo. *Calculating thermal conductivity in a transient conduction regime: theory and implementation*. The European Physical Journal B, vol. 87, no. 4, pages 1–9, 2014.

[Merlin *et al.* 2016] Kevin Merlin, Jérôme Soto, Didier Delaunay and Luc Traonvouez. *Industrial waste heat recovery using an enhanced conductivity latent heat thermal energy storage*. Applied energy, vol. 183, pages 491–503, 2016.

[Minnich & Chen 2007] Austin Minnich and Gang Chen. *Modified effective medium formulation for the thermal conductivity of nanocomposites*. Applied Physics Letters, vol. 91, no. 7, page 073105, 2007.

[Mintsa *et al.* 2009] Honorine Angue Mintsa, Gilles Roy, Cong Tam Nguyen and Dominique Doucet. *New temperature dependent thermal conductivity data for water-based nanofluids*. International journal of thermal sciences, vol. 48, no. 2, pages 363–371, 2009.

[Mirmohammadi *et al.* 2018] Seyed Aliakbar Mirmohammadi, Luming Shen and Yixiang Gan. *A reliable approach for calculating thermophysical properties of liquid using molecular dynamics simulations*. Chemical Physics Letters, vol. 712, pages 44–53, 2018.

[Molinari *et al.* 2019] Alan Molinari, Horst Hahn and Robert Kruk. *Voltage-Control of Magnetism in All-Solid-State and Solid/Liquid Magnetoelectric Composites*. Advanced Materials, vol. 31, no. 26, page 1806662, 2019.

[Montazeri *et al.* 2020] Kimia Montazeri, Mohammad Javad Abdolhosseini Qomi and Yoonjin Won. *Solid-like behaviors govern evaporative transport in adsorbed water nanofilms*. ACS Applied Materials & Interfaces, vol. 12, no. 47, pages 53416–53424, 2020.

[Mortazavi *et al.* 2016] Bohayra Mortazavi, Obaidur Rahaman, Timon Rabczuk and Luiz Felipe C Pereira. *Thermal conductivity and mechanical properties of nitrogenated holey graphene*. Carbon, vol. 106, pages 1–8, 2016.

[Mortazavi *et al.* 2019] Bohayra Mortazavi, Mohamed E Madjet, Masoud Shahrokhi, Said Ahzi, Xiaoying Zhuang and Timon Rabczuk. *Nanoporous graphene: a 2D semiconductor with anisotropic mechanical, optical and thermal conduction properties*. Carbon, vol. 147, pages 377–384, 2019.

[Mosaddeghi *et al.* 2012] Hamid Mosaddeghi, Saman Alavi, MH Kowsari and Bijan Najafi. *Simulations of structural and dynamic anisotropy in nano-confined water between parallel graphite plates*. The Journal of chemical physics, vol. 137, no. 18, page 184703, 2012.

[Mu *et al.* 2009] Lijuan Mu, Qunzhi Zhu and Leilei Si. *Radiative properties of nanofluids and performance of a direct solar absorber using nanofluids*. In International Conference on Micro/Nanoscale Heat Transfer, volume 43895, pages 549–553, 2009.

[Mukherjee *et al.* 2007] Biswaroop Mukherjee, Prabal K Maiti, Chandan Dasgupta and AK Sood. *Strong correlations and Fickian water diffusion in narrow carbon nanotubes*. The Journal of chemical physics, vol. 126, no. 12, page 124704, 2007.

[Munetoh *et al.* 2007] Shinji Munetoh, Teruaki Motooka, Koji Moriguchi and Akira Shintani. *Interatomic potential for Si–O systems using Tersoff parameterization*. Computational Materials Science, vol. 39, no. 2, pages 334–339, 2007.

[Nada 2016] Hiroki Nada. *Anisotropy in geometrically rough structure of ice prismatic plane interface during growth: Development of a modified six-site model of H2O and a molecular dynamics simulation*. The Journal of chemical physics, vol. 145, no. 24, page 244706, 2016.

[Nagayama & Cheng 2004] Gyoko Nagayama and Ping Cheng. *Effects of interface wettability on microscale flow by molecular dynamics simulation*. International Journal of Heat and Mass Transfer, vol. 47, no. 3, pages 501–513, 2004.

[Nakabe *et al.* 1999] Kazuyoshi Nakabe, Kosuke Yamanaka and Kenjiro Suzuki. *An MD simulation on micro droplet behaviors affected by solid surface conditions*. Technical report, Kyoto Univ.(JP), 1999.

[Nan *et al.* 1997] Ce-Wen Nan, R Birringer, David R Clarke and H Gleiter. *Effective thermal conductivity of particulate composites with interfacial thermal resistance*. Journal of Applied Physics, vol. 81, no. 10, pages 6692–6699, 1997.

[Narankhishig *et al.* 2021] Zoljargal Narankhishig, Jeonggyun Ham, Hoseong Lee and Honghyun Cho. *Convective heat transfer characteristics of nanofluids including the magnetic effect on heat transfer enhancement-a review*. Applied Thermal Engineering, vol. 193, page 116987, 2021.

[Ndour *et al.* 2021] Mbaye Ndour, Laurent Chaput and Philippe Jund. *Classical molecular dynamics study of small samples of amorphous silica: structural and dynamical properties*. Journal of Non-Crystalline Solids, vol. 569, page 120995, 2021.

[Neek-Amal *et al.* 2016] Mehdi Neek-Amal, Francois M Peeters, Irina V Grigorieva and Andre K Geim. *Commensurability effects in viscosity of nanoconfined water*. ACS nano, vol. 10, no. 3, pages 3685–3692, 2016.

[Nieto de Castro *et al.* 1986] CA Nieto de Castro, SFY Li, A Nagashima, RD Trengove and WA Wakeham. *Standard reference data for the thermal conductivity of liquids*. Journal of physical and chemical reference data, vol. 15, no. 3, pages 1073–1086, 1986.

[Ogwu *et al.* 2012] AA Ogwu, TIT Okpalugo and JAD McLaughlin. *The effect of PECVD plasma decomposition on the wettability and dielectric constant changes in silicon modified DLC films for potential MEMS and low stiction applications*. AIP Advances, vol. 2, no. 3, page 032128, 2012.

[Ohira *et al.* 1994] Tatsuya Ohira, Takaji Inamuro and Takeshi Adachi. *Molecular dynamics simulation of amorphous silicon with Tersoff potential*. Solar energy materials and solar cells, vol. 34, no. 1-4, pages 565–570, 1994.

[Ohta *et al.* 2008] Hiromichi Ohta, Rong Huang and Yuichi Ikuhara. *Large enhancement of the thermoelectric Seebeck coefficient for amorphous oxide semiconductor superlattices with extremely thin conductive layers*. physica status solidi (RRL)–Rapid Research Letters, vol. 2, pages 105–107, 2008.

[Ong & Liow 2019] Ernest ES Ong and Jong-Leng Liow. *The temperature-dependent structure, hydrogen bonding and other related dynamic properties of the standard TIP3P and CHARMM-modified TIP3P water models*. Fluid Phase Equilibria, vol. 481, pages 55–65, 2019.

[Ong & Pop 2010] Zhun-Yong Ong and Eric Pop. *Molecular dynamics simulation of thermal boundary conductance between carbon nanotubes and SiO 2*. Physical Review B, vol. 81, no. 15, page 155408, 2010.

[Owens & Daniels 2013] Eli T Owens and Karen E Daniels. *Acoustic measurement of a granular density of modes*. Soft Matter, vol. 9, no. 4, pages 1214–1219, 2013.

[Ozcelik *et al.* 2020] H Gokberk Ozcelik, Yigit Sozen, Hasan Sahin and Murat Barisik. *Parametrizing nonbonded interactions between silica and water from first principles*. Applied Surface Science, vol. 504, page 144359, 2020.

[Ozkanlar & Clark 2014] Abdullah Ozkanlar and Aurora E Clark. *ChemNetworks: a complex network analysis tool for chemical systems*. Journal of computational chemistry, vol. 35, no. 6, pages 495–505, 2014.

[Ozkanlar *et al.* 2014] Abdullah Ozkanlar, Morgan P Kelley and Aurora E Clark. *Water organization and dynamics on mineral surfaces interrogated by graph theoretical analyses of intermolecular chemical networks*. Minerals, vol. 4, no. 1, pages 118–129, 2014.

[Palla *et al.* 2019] Pier Luca Palla, Sonia Zampa, Evelyne Martin and Fabrizio Cleri. *Interface thermal behavior in nanomaterials by thermal grating relaxation*. International Journal of Heat and Mass Transfer, vol. 131, pages 932–943, 2019.

[Pan *et al.* 2020a] Bin Pan, Xia Yin and Stefan Iglauer. *A review on clay wettability: From experimental investigations to molecular dynamics simulations*. Advances in Colloid and Interface Science, page 102266, 2020.

[Pan *et al.* 2020b] Cong Pan, Chengwen Liu, Junhui Peng, Pengyu Ren and Xuhui Huang. *Three-site and five-site fixed-charge water models compatible with AMOEBA force field*. Journal of computational chemistry, vol. 41, no. 10, pages 1034–1044, 2020.

[Park *et al.* 2019] Young-Geun Park, Hyegi Min, Hyobeom Kim, Anar Zhexembekova, Chang Young Lee and Jang-Ung Park. *Three-dimensional, high-resolution printing of carbon nanotube/liquid metal composites with mechanical and electrical reinforcement*. Nano letters, vol. 19, no. 8, pages 4866–4872, 2019.

[Perlin & Schultz 2000] Marc Perlin and William W Schultz. *Capillary effects on surface waves*. Annual review of fluid mechanics, vol. 32, no. 1, pages 241–274, 2000.

[Pham *et al.* 2014] An Truong Pham, Murat Barisik and Bohung Kim. *Molecular dynamics simulations of Kapitza length for argon-silicon and water-silicon interfaces*. International journal of precision engineering and manufacturing, vol. 15, no. 2, pages 323–329, 2014.

[Pia *et al.* 2016] Giorgio Pia, Ludovica Casnedi and Ulrico Sanna. *Porosity and pore size distribution influence on thermal conductivity of yttria-stabilized zirconia: experimental findings and model predictions*. Ceramics International, vol. 42, no. 5, pages 5802–5809, 2016.

[Pîslaru-Dănescu *et al.* 2013] Lucian Pîslaru-Dănescu, Alexandru M Morega, Gabriela Telipan, Mihaela Morega, Jean Bogdan Dumitru and Virgil Marinescu. *Magnetic nanofluid applications in electrical engineering*. IEEE Transactions on magnetics, vol. 49, no. 11, pages 5489–5497, 2013.

[Pizzagalli *et al.* 2013] Laurent Pizzagalli, J Godet, Julien Guénolé, Sandrine Brochard, E Holmstrom, K Nordlund and dan T Albaret. *A new parametrization of the Stillinger–Weber potential for an improved description of defects and plasticity of silicon*. Journal of Physics: Condensed Matter, vol. 25, no. 5, page 055801, 2013.

[Plimpton 1995a] Steve Plimpton. *Fast parallel algorithms for short-range molecular dynamics*. Journal of computational physics, vol. 117, no. 1, pages 1–19, 1995.

[Plimpton 1995b] Steve Plimpton. *Fast parallel algorithms for short-range molecular dynamics*. Journal of computational physics, vol. 117, no. 1, pages 1–19, 1995.

[Poetzsch & Böttger 1994] Reinhard HH Poetzsch and Harald Böttger. *Interplay of disorder and anharmonicity in heat conduction: molecular-dynamics study*. Physical Review B, vol. 50, no. 21, page 15757, 1994.

[Press & Teukolsky 1990] William H Press and Saul A Teukolsky. *Savitzky-Golay smoothing filters*. Computers in Physics, vol. 4, no. 6, pages 669–672, 1990.

[Qiao *et al.* 2006] Yu Qiao, Venkata K Punyamurtula, Aijie Han, Xinguo Kong and Falgun B Surani. *Temperature dependence of working pressure of a nanoporous liquid spring*. Applied physics letters, vol. 89, no. 25, page 251905, 2006.

[Qvist *et al.* 2011] Johan Qvist, Helmut Schober and Bertil Halle. *Structural dynamics of supercooled water from quasielastic neutron scattering and molecular simulations*. The Journal of chemical physics, vol. 134, no. 14, page 144508, 2011.

[Rajabpour *et al.* 2019] Ali Rajabpour, Roham Seif, Saeed Arabha, Mohammad Mahdi Heyhat, Samy Merabia and Ali Hassanali. *Thermal transport at a nanoparticle-water interface: A molecular dynamics and continuum modeling study*. The Journal of chemical physics, vol. 150, no. 11, page 114701, 2019.

[Rao *et al.* 2000] CN Ramachandra Rao, Giridhar U Kulkarni, P John Thomas and Peter P Edwards. *Metal nanoparticles and their assemblies*. Chemical Society Reviews, vol. 29, no. 1, pages 27–35, 2000.

[Rao *et al.* 2013] Zhonghao Rao, Shuangfeng Wang and Feifei Peng. *Molecular dynamics simulations of nano-encapsulated and nanoparticle-enhanced thermal energy storage phase change materials*. International Journal of Heat and Mass Transfer, vol. 66, pages 575–584, 2013.

[Rivas *et al.* 2018] Bernabé L Rivas, Bruno F Urbano and Julio Sánchez. *Water-soluble and insoluble polymers, nanoparticles, nanocomposites and hybrids with ability to remove hazardous inorganic pollutants in water*. Frontiers in chemistry, vol. 6, page 320, 2018.

[Roduner 2006] Emil Roduner. *Size matters: why nanomaterials are different*. Chemical Society Reviews, vol. 35, no. 7, pages 583–592, 2006.

[Römer *et al.* 2012] Frank Römer, Anders Lervik and Fernando Bresme. *Nonequilibrium molecular dynamics simulations of the thermal conductivity of water: A systematic investigation of the SPC/E and TIP4P/2005 models*. The Journal of chemical physics, vol. 137, no. 7, page 074503, 2012.

[Rousset *et al.* 1995] JL Rousset, AM Cadrot, FJ Cadete Santos Aires, A Renouprez, P Mélinon, A Perez, M Pellarin, JL Vialle and M Broyer. *Study of bimetallic Pd–Pt clusters in both free and supported phases*. The Journal of chemical physics, vol. 102, no. 21, pages 8574–8585, 1995.

[Roy Chowdhury *et al.* 2021] Prabudhya Roy Chowdhury, Jingjing Shi, Tianli Feng and Xiulin Ruan. *Prediction of Bi2Te3-Sb2Te3 interfacial conductance and superlattice thermal conductivity using molecular dynamics simulations*. ACS Applied Materials & Interfaces, vol. 13, no. 3, pages 4636–4642, 2021.

[Russo *et al.* 2011] Daniela Russo, Jose Teixeira, Larry Kneller, John RD Copley, Jacques Ollivier, Stefania Perticaroli, Eric Pellegrini and Miguel Angel Gonzalez. *Vibrational density of states of hydration water at biomolecular sites: hydrophobicity promotes low density amorphous ice behavior*. Journal of the American Chemical Society, vol. 133, no. 13, pages 4882–4888, 2011.

[Sachdeva 2009] Parveen Sachdeva. *Molecular dynamics study of thermal conductivity enhancement of water based nanofluids*. 2009.

[Sadeghi & Parsafar 2013] M Sadeghi and GA Parsafar. *Density-induced molecular arrangements of water inside carbon nanotubes*. Physical Chemistry Chemical Physics, vol. 15, no. 19, pages 7379–7388, 2013.

[Sadeghinezhad *et al.* 2016] Emad Sadeghinezhad, Mohammad Mehrali, R Saidur, Mehdi Mehrali, Sara Tahan Latibari, Amir Reza Akhiani and Hendrik Simon Cornelis Metselaar. *A comprehensive review on graphene nanofluids: recent research, development and applications*. Energy Conversion and Management, vol. 111, pages 466–487, 2016.

[Sarkisov & Monson 2000] L Sarkisov and PA Monson. *Hysteresis in Monte Carlo and molecular dynamics simulations of adsorption in porous materials*. Langmuir, vol. 16, no. 25, pages 9857–9860, 2000.

[Schelling *et al.* 2002] Patrick K Schelling, Simon R Phillpot and Pawel Keblinski. *Comparison of atomic-level simulation methods for computing thermal conductivity*. Physical Review B, vol. 65, no. 14, page 144306, 2002.

[Schneider & Stoll 1978] T Schneider and E Stoll. *Molecular-dynamics study of a three-dimensional one-component model for distortive phase transitions*. Physical Review B, vol. 17, no. 3, page 1302, 1978.

[Sedighi & Mohebbi 2014] Mina Sedighi and Ali Mohebbi. *Investigation of nanoparticle aggregation effect on thermal properties of nanofluid by a combined equilibrium and non-equilibrium molecular dynamics simulation*. Journal of Molecular Liquids, vol. 197, pages 14–22, 2014.

[Sellan *et al.* 2010] Daniel P Sellan, Eric S Landry, JE Turney, Alan JH McGaughey and Cristina H Amon. *Size effects in molecular dynamics thermal conductivity predictions*. Physical Review B, vol. 81, no. 21, page 214305, 2010.

[Selvakumar & Suresh 2012] Ponnusamy Selvakumar and Sivan Suresh. *Use of*

{

\rm Al} _ {2}{\rm O} _ {3}\hbox {–}{\rm Cu} /Water Hybrid Nanofluid in an Electronic Heat Sink. IEEE transactions on components, packaging and manufacturing technology, vol. 2, no. 10, pages 1600–1607, 2012.

[Senthilraja *et al.* 2010] S Senthilraja, M Karthikeyan and R Gangadevi. *Nanofluid applications in future automobiles: comprehensive review of existing data*. Nano-Micro Letters, vol. 2, no. 4, pages 306–310, 2010.

[Sharma 2018] Shubham Sharma. *Fabricating an experimental setup to investigate the performance of an automobile car radiator by using aluminum/water nanofluid*. Journal of Thermal Analysis and Calorimetry, vol. 133, no. 3, pages 1387–1406, 2018.

[Sharp 2001] Kim A Sharp. *Water: Structure and properties*. e LS, 2001.

[Sheng *et al.* 2011] HW Sheng, MJ Kramer, A Cadien, T Fujita and MW Chen. *Highly optimized embedded-atom-method potentials for fourteen fcc metals*. Physical Review B, vol. 83, no. 13, page 134118, 2011.

[Sheng *et al.* 2022] Yufei Sheng, Yue Hu, Zheyong Fan and Hua Bao. *Size effect and transient phonon transport mechanism in approach-to-equilibrium molecular dynamics simulations*. Physical Review B, vol. 105, no. 7, page 075301, 2022.

[Shi & Majumdar 2002] Li Shi and Arunava Majumdar. *Thermal transport mechanisms at nanoscale point contacts*. J. Heat Transfer, vol. 124, no. 2, pages 329–337, 2002.

[Sikkenk *et al.* 1987] JH Sikkenk, JO Indekeu, JMJ Van Leeuwen and EO Vossnack. *Molecular-dynamics simulation of wetting and drying at solid-fluid interfaces*. Physical review letters, vol. 59, no. 1, page 98, 1987.

[Sinha 2004] Shashank Sinha. Molecular dynamics simulation of interfacial tension and contact angle of lennard-jones fluid. University of California, Los Angeles, 2004.

[Sirghi *et al.* 2000] Lucel Sirghi, Nobuyuki Nakagiri, Katsumi Sugisaki, Hiroyuki Sugimura and Osamu Takai. *Effect of sample topography on adhesive force in atomic force spectroscopy measurements in air*. Langmuir, vol. 16, no. 20, pages 7796–7800, 2000.

[Smith *et al.* 2014] Alexander M Smith, Michael A Parkes and Susan Perkin. *Molecular friction mechanisms across nanofilms of a bilayer-forming ionic liquid*. The journal of physical chemistry letters, vol. 5, no. 22, pages 4032–4037, 2014.

[Soltani *et al.* 2017] Shohreh Soltani, Alibakhsh Kasaeian, Hamid Sarrafha and Dongsheng Wen. *An experimental investigation of a hybrid photovoltaic/thermoelectric system with nanofluid application*. Solar Energy, vol. 155, pages 1033–1043, 2017.

[Speedy *et al.* 1987] Robin J Speedy, Jeffry D Madura and William L Jorgensen. *Network topology in simulated water*. Journal of Physical Chemistry, vol. 91, no. 4, pages 909–913, 1987.

[Stillinger & Weber 1985] Frank H Stillinger and Thomas A Weber. *Computer simulation of local order in condensed phases of silicon*. Physical review B, vol. 31, no. 8, page 5262, 1985.

[Structures 1963] Crystal Structures. *RWG Wyckoff, Vol. 1*. Interscience Publishers, Wiley and Sons, New York, page 160, 1963.

[Stukowski 2009] Alexander Stukowski. *Visualization and analysis of atomistic simulation data with OVITO–the Open Visualization Tool*. Modelling and Simulation in Materials Science and Engineering, vol. 18, no. 1, page 015012, 2009.

[Su & Zhang 2018] Ruixia Su and Xing Zhang. *Size effect of thermal conductivity in monolayer graphene*. Applied Thermal Engineering, vol. 144, pages 488–494, 2018.

[Su *et al.* 2015] Weiguang Su, Jo Darkwa and Georgios Kokogiannakis. *Review of solid–liquid phase change materials and their encapsulation technologies*. Renewable and Sustainable Energy Reviews, vol. 48, pages 373–391, 2015.

[Sun & Ebner 1992] M Sun and C Ebner. *Molecular dynamics study of flow at a fluid-wall interface*. Physical Review Letters, vol. 69, no. 24, page 3491, 1992.

[Suresh *et al.* 2011] S Suresh, KP Venkitaraj, P Selvakumar and M Chandrasekar. *Synthesis of Al2O3–Cu/water hybrid nanofluids using two step method and its thermo physical properties*. Colloids and Surfaces A: Physicochemical and Engineering Aspects, vol. 388, no. 1-3, pages 41–48, 2011.

[Tang & Zhang 2004] CY Tang and LC Zhang. *A molecular dynamics analysis of the mechanical effect of water on the deformation of silicon monocrystals subjected to nano-indentation*. Nanotechnology, vol. 16, no. 1, page 15, 2004.

[Tarazona *et al.* 1987] P Tarazona, U Marini Bettolo Marconi and R Evans. *Phase equilibria of fluid interfaces and confined fluids: non-local versus local density functionals*. Molecular Physics, vol. 60, no. 3, pages 573–595, 1987.

[Tejedor *et al.* 2010] Vincent Tejedor, Olivier Bénichou, Raphael Voituriez, Ralf Jungmann, Friedrich Simmel, Christine Selhuber-Unkel, Lene B Oddershede and Ralf Metzler. *Quantitative analysis of single particle trajectories: mean maximal excursion method*. Biophysical journal, vol. 98, no. 7, pages 1364–1372, 2010.

[Termentzidis *et al.* 2018] Konstantinos Termentzidis, Valentina M Giordano, Maria Katsikini, Eleni Paloura, Gilles Pernot, Maxime Verdier, David Lacroix, Ioannis Karakostas and Joseph Kioseoglou. *Enhanced thermal*

conductivity in percolating nanocomposites: a molecular dynamics investigation. Nanoscale, vol. 10, no. 46, pages 21732–21741, 2018.

[Tersoff 1988] Jerry Tersoff. *New empirical approach for the structure and energy of covalent systems*. Physical review B, vol. 37, no. 12, page 6991, 1988.

[Thomas *et al.* 2010] John A Thomas, Ryan M Iutzi and Alan JH McGaughey. *Thermal conductivity and phonon transport in empty and water-filled carbon nanotubes*. Physical Review B, vol. 81, no. 4, page 045413, 2010.

[Thompson & Robbins 1989] Peter A Thompson and Mark O Robbins. *Simulations of contact-line motion: slip and the dynamic contact angle*. Physical review letters, vol. 63, no. 7, page 766, 1989.

[Timofeeva *et al.* 2009] Elena V Timofeeva, Jules L Routbort and Dileep Singh. *Particle shape effects on thermophysical properties of alumina nanofluids*. Journal of applied physics, vol. 106, no. 1, page 014304, 2009.

[Touloukian 1970] Yeram Sarkis Touloukian. *Thermal conductivity-metallic elements and alloys*. Thermophysical properties of matter, vol. 1, 1970.

[Tyson & Miller 1977] WR Tyson and WA Miller. *Surface free energies of solid metals: Estimation from liquid surface tension measurements*. Surface Science, vol. 62, no. 1, pages 267–276, 1977.

[Van Beest *et al.* 1990] BWH Van Beest, Gert Jan Kramer and RA Van Santen. *Force fields for silicas and aluminophosphates based on ab initio calculations*. Physical review letters, vol. 64, no. 16, page 1955, 1990.

[Van Duin *et al.* 2003] Adri CT Van Duin, Alejandro Strachan, Shannon Stewman, Qingsong Zhang, Xin Xu and William A Goddard. *ReaxFFSiO reactive force field for silicon and silicon oxide systems*. The Journal of Physical Chemistry A, vol. 107, no. 19, pages 3803–3811, 2003.

[Van Honschoten *et al.* 2010] Joost W Van Honschoten, Nataliya Brunets and Niels R Tas. *Capillarity at the nanoscale*. Chemical society reviews, vol. 39, no. 3, pages 1096–1114, 2010.

[Van Norren *et al.* 2009] K Van Norren, A Van Helvoort, JM Argilés, S Van Tuijl, Karin Arts, M Gorselink, A Laviano, D Kegler, HP Haagsman and EM Van Der Beek. *Direct effects of doxorubicin on skeletal muscle contribute to fatigue*. British journal of cancer, vol. 100, no. 2, pages 311–314, 2009.

[Vera & Bayazitoglu 2015] Jerry Vera and Yildiz Bayazitoglu. *Temperature and heat flux dependence of thermal resistance of water/metal nanoparticle interfaces at sub-boiling temperatures*. International Journal of Heat and Mass Transfer, vol. 86, pages 433–442, 2015.

[Verdier *et al.* 2016] Maxime Verdier, Konstantinos Termentzidis and David Lacroix. *Crystalline-amorphous silicon nano-composites: Nano-pores and nano-inclusions impact on the thermal conductivity*. Journal of Applied Physics, vol. 119, no. 17, page 175104, 2016.

[Verdier *et al.* 2017] Maxime Verdier, Roman Anufriev, Aymeric Ramiere, Konstantinos Termentzidis and David Lacroix. *Thermal conductivity of phononic membranes with aligned and staggered lattices of holes at room and low temperatures*. Physical Review B, vol. 95, page 205438, 2017.

[Verdier *et al.* 2018] Maxime Verdier, Yang Han, David Lacroix, Pierre-Olivier Chapuis and Konstantinos Termentzidis. *Radial dependence of thermal transport in silicon nanowires*. Journal of Physics: Materials, vol. 2, no. 1, page 015002, 2018.

[Vink *et al.* 2001] RLC Vink, GT Barkema, WF Van der Weg and Normand Mousseau. *Fitting the Stillinger–Weber potential to amorphous silicon*. Journal of non-crystalline solids, vol. 282, no. 2-3, pages 248–255, 2001.

[Vo & Kim 2015] Truong Quoc Vo and BoHung Kim. *Interface thermal resistance between liquid water and various metallic surfaces*. International Journal of Precision Engineering and Manufacturing, vol. 16, no. 7, pages 1341–1346, 2015.

[Vogelsang *et al.* 1987] R Vogelsang, C Hoheisel and G Ciccotti. *Thermal conductivity of the Lennard-Jones liquid by molecular dynamics calculations*. The Journal of chemical physics, vol. 86, pages 6371–6375, 1987.

[Vollmayr *et al.* 1996] Katharina Vollmayr, Walter Kob and Kurt Binder. *Cooling-rate effects in amorphous silica: A computer-simulation study*. Physical Review B, vol. 54, no. 22, page 15808, 1996.

[Wagemann *et al.* 2017] Enrique Wagemann, Elton Oyarzua, Jens H Walther and Harvey A Zambrano. *Slip divergence of water flow in graphene nanochannels: the role of chirality*. Physical Chemistry Chemical Physics, vol. 19, no. 13, pages 8646–8652, 2017.

[Walsh *et al.* 2000] Tiffany R Walsh, Mark Wilson and Adrian P Sutton. *Hydrolysis of the amorphous silica surface. II. Calculation of activation barriers and mechanisms*. The Journal of Chemical Physics, vol. 113, no. 20, pages 9191–9201, 2000.

[Wang *et al.* 2014] Chun-Hung Wang, Peng Bai, J Ilja Siepmann and Aurora E Clark. *Deconstructing hydrogen-bond networks in confined nanoporous materials: implications for alcohol–water separation*. The Journal of Physical Chemistry C, vol. 118, no. 34, pages 19723–19732, 2014.

[Wang *et al.* 2016] Sen Wang, Farzam Javadpour and Qihong Feng. *Molecular dynamics simulations of oil transport through inorganic nanopores in shale*. Fuel, vol. 171, pages 74–86, 2016.

[Wang *et al.* 2018] Changhong Wang, Qian Sun, Yulong Liu, Yang Zhao, Xia Li, Xiaoting Lin, Mohammad Norouzi Banis, Minsi Li, Weihan Li, Keegan R Adair*et al. Boosting the performance of lithium batteries with solid-liquid hybrid electrolytes: Interfacial properties and effects of liquid electrolytes*. Nano Energy, vol. 48, pages 35–43, 2018.

[Wei *et al.* 2020] Qiangbing Wei, Mingkang Sun, Zongyu Wang, Jiajun Yan, Rui Yuan, Tong Liu, Carmel Majidi and Krzysztof Matyjaszewski. *Surface engineering of liquid metal nanodroplets by attachable diblock copolymers*. ACS nano, vol. 14, no. 8, pages 9884–9893, 2020.

[Weil 1984] KG Weil. *JS Rowlinson and B. Widom: Molecular Theory of Capillarity, Clarendon Press, Oxford 1982. 327 Seiten, Preis:£ 30,–*. Berichte der Bunsengesellschaft für physikalische Chemie, vol. 88, no. 6, pages 586–586, 1984.

[Wemp & Carey 2019] Claire K Wemp and Van P Carey. *Heat transport for evaporating droplets on superhydrophilic, thin, nanoporous layers*. International Journal of Heat and Mass Transfer, vol. 132, pages 34–51, 2019.

[Wen *et al.* 2009] Dongsheng Wen, Guiping Lin, Saeid Vafaei and Kai Zhang. *Review of nanofluids for heat transfer applications*. Particuology, vol. 7, no. 2, pages 141–150, 2009.

[Wirnsberger *et al.* 2015] Peter Wirnsberger, Daniel Frenkel and C Dellago. *An enhanced version of the heat exchange algorithm with excellent energy conservation properties*. The Journal of chemical physics, vol. 143, no. 12, page 124104, 2015.

[Wolf *et al.* 1999] D Wolf, P Keblinski, SR Phillpot and J Eggebrecht. *Exact method for the simulation of Coulombic systems by spherically truncated, pairwise r- 1 summation*. The Journal of chemical physics, vol. 110, no. 17, pages 8254–8282, 1999.

[Wolf 1992] Dieter Wolf. *Reconstruction of NaCl surfaces from a dipolar solution to the Madelung problem*. Physical Review Letters, vol. 68, no. 22, page 3315, 1992.

[Wong & De Leon 2010] Kaufui V Wong and Omar De Leon. *Applications of nanofluids: current and future*. Advances in mechanical engineering, vol. 2, page 519659, 2010.

[Woodward & Zasadzinski 1994] John T Woodward and Joseph A Zasadzinski. *Height amplifications of scanning tunneling microscopy images in air*. Langmuir, vol. 10, no. 5, pages 1340–1344, 1994.

[Wu *et al.* 2019] Qi Wu, Hui Xiong, Yan Peng, Yi Yang, Jian Kang, Guangsu Huang, Xiancheng Ren and Jinrong Wu. *Highly Stretchable and Self-Healing "Solid–Liquid" Elastomer with Strain-Rate Sensing Capability*. ACS applied materials & interfaces, vol. 11, no. 21, pages 19534–19540, 2019.

[Xie *et al.* 2018] Ganhua Xie, Pei Li, Zhiju Zhao, Zhongpeng Zhu, Xiang-Yu Kong, Zhen Zhang, Kai Xiao, Liping Wen and Lei Jiang. *Light-and electric-field-controlled wetting behavior in nanochannels for regulating nanoconfined mass transport*. Journal of the American Chemical Society, vol. 140, no. 13, pages 4552–4559, 2018.

[Xing *et al.* 2006] Zhang Xing, Gu Hua and Motoo Fujii. *Effective thermal conductivity and thermal diffusivity of nanofluids containing spherical and cylindrical nanoparticles*. Journal of Applied Physics, vol. 100, no. 4, pages 044325–044325–5, 2006.

[Xiong *et al.* 2020] Yeyue Xiong, Parviz Seifpanahi Shabane and Alexey V Onufriev. *Melting Points of OPC and OPC3 Water Models*. ACS omega, vol. 5, no. 39, pages 25087–25094, 2020.

[Xue *et al.* 2003a] L. Xue, P. Keblinski, S. R. Phillpot, U. S. Choi and J. A. Eastman. *Two regimes of thermal resistance at a liquid–solid interface*. Journal of Chemical Physics, vol. 118, no. 1, pages 337–339, 2003.

[Xue *et al.* 2003b] L Xue, P Keblinski, SR Phillpot, SU-S Choi and JA Eastman. *Two regimes of thermal resistance at a liquid–solid interface*. The Journal of chemical physics, vol. 118, no. 1, pages 337–339, 2003.

[Xue *et al.* 2004] L Xue, P Keblinski, SR Phillpot, SU-S Choi and JA Eastman. *Effect of liquid layering at the liquid–solid interface on thermal transport*. International Journal of Heat and Mass Transfer, vol. 47, no. 19-20, pages 4277–4284, 2004.

[Yagasaki *et al.* 2020] Takuma Yagasaki, Masakazu Matsumoto and Hideki Tanaka. *Lennard-Jones parameters determined to reproduce the solubility of NaCl and KCl in SPC/E, TIP3P, and TIP4P/2005 water*. Journal of chemical theory and computation, vol. 16, no. 4, pages 2460–2473, 2020.

[Yamakiri *et al.* 2011] Hiroki Yamakiri, Shinya Sasaki, Tsuneo Kurita and Nagayoshi Kasashima. *Effects of laser surface texturing on friction behavior of silicon nitride under lubrication with water*. Tribology International, vol. 44, no. 5, pages 579–584, 2011.

[Yang & Dames 2013] Fan Yang and Chris Dames. *Mean free path spectra as a tool to understand thermal conductivity in bulk and nanostructures*. Physical Review B, vol. 87, no. 3, page 035437, 2013.

[Yang & Liu 2011] Xue-Fei Yang and Zhen-Hua Liu. *Application of functionalized nanofluid in thermosyphon*. Nanoscale research letters, vol. 6, no. 1, pages 1–12, 2011.

[Yang *et al.* 2019a] Shujin Yang, Yanping Zhang and Li Chen. *Molecular dynamics study on the effect of surface wettability on the performance of water vapor condensation*. AIP Advances, vol. 9, no. 2, page 025031, 2019.

[Yang *et al.* 2019b] Xianchao Yang, Lianqing Zhu, Ying Lu and Jianquan Yao. *Ultrasharp LSPR Temperature Sensor Based on Grapefruit Fiber Filled with a Silver Nanoshell and Liquid*. Journal of Lightwave Technology, 2019.

[Yang *et al.* 2019c] Xiaohu Yang, Pan Wei, Xin Cui, Liwen Jin and Ya-Ling He. *Thermal response of annuli filled with metal foam for thermal energy storage: an experimental study*. Applied Energy, vol. 250, pages 1457–1467, 2019.

[Yang *et al.* 2022] MY Yang, Q Sheng, H Zhang and GH Tang. *Water molecular bridge undermines thermal insulation of Nano-porous silica aerogels*. Journal of Molecular Liquids, vol. 349, page 118176, 2022.

[Yeh & Hummer 2004] In-Chul Yeh and Gerhard Hummer. *System-size dependence of diffusion coefficients and viscosities from molecular dynamics simulations with periodic boundary conditions*. The Journal of Physical Chemistry B, vol. 108, no. 40, pages 15873–15879, 2004.

[Yeo *et al.* 2013] Jing Jie Yeo, ZS Liu and TY Ng. *Enhanced thermal characterization of silica aerogels through molecular dynamics simulation*. Modelling and Simulation in Materials Science and Engineering, vol. 21, no. 7, page 075004, 2013.

[Young 1805] Thomas Young. *III. An essay on the cohesion of fluids*. Philosophical transactions of the royal society of London, no. 95, pages 65–87, 1805.

[Yousefi *et al.* 2020a] Farrokh Yousefi, Farhad Khoeini and Ali Rajabpour. *Thermal conductivity and thermal rectification of nanoporous graphene: A molecular dynamics simulation*. International Journal of Heat and Mass Transfer, vol. 146, page 118884, 2020.

[Yousefi *et al.* 2020b] Farrokh Yousefi, Farhad Khoeini and Ali Rajabpour. *Thermal conductivity and thermal rectification of nanoporous graphene: A molecular dynamics simulation*. International Journal of Heat and Mass Transfer, vol. 146, no. Jan., pages 118884.1–118884.7, 2020.

[Yu & Leitner 2005] Xin Yu and David M Leitner. *Thermal transport coefficients for liquid and glassy water computed from a harmonic aqueous glass*. The Journal of chemical physics, vol. 123, no. 10, page 104503, 2005.

[Yu & Xie 2012] Wei Yu and Huaqing Xie. *A review on nanofluids: preparation, stability mechanisms, and applications*. Journal of nanomaterials, vol. 2012, 2012.

[Yu *et al.* 2018a] Tongfei Yu, Lifei Bai, Zhijun Xu and Xiaoning Yang. *Molecular simulation of permeation behaviour of ethanol/water molecules with single-layer graphene oxide membranes*. Molecular Simulation, vol. 44, no. 10, pages 840–849, 2018.

[Yu *et al.* 2018b] Tongfei Yu, Lifei Bai, Zhijun Xu and Xiaoning Yang. *Molecular simulation of permeation behaviour of ethanol/water molecules with*

single-layer graphene oxide membranes. Molecular Simulation, vol. 44, no. 10, pages 1–10, 2018.

[Yu *et al.* 2021] Chengbin Yu, Jae Ryoun Youn and Young Seok Song. *Enhancement of Thermo-Electric Energy Conversion Using Graphene Nanoplatelets Embedded Phase Change Material*. Macromolecular Research, vol. 29, no. 8, pages 534–542, 2021.

[Yuan & Huang 2012] Fenglin Yuan and Liping Huang. *Molecular dynamics simulation of amorphous silica under uniaxial tension: From bulk to nanowire*. Journal of non-crystalline solids, vol. 358, no. 24, pages 3481–3487, 2012.

[Yuan & Sundén 2013] Jinliang Yuan and Bengt Sundén. *On continuum models for heat transfer in micro/nano-scale porous structures relevant for fuel cells*. International Journal of Heat and Mass Transfer, vol. 58, no. 1-2, pages 441–456, 2013.

[Yuan *et al.* 2018] Dengsen Yuan, Tao Zhang, Qing Guo, Fengxian Qiu, Dongya Yang and Zhongping Ou. *Superhydrophobic hierarchical biomass carbon aerogel assembled with TiO2 nanorods for selective immiscible oil/water mixture and emulsion separation*. Industrial & Engineering Chemistry Research, vol. 57, no. 43, pages 14758–14766, 2018.

[Zambrano *et al.* 2014] HA Zambrano, Jens Honore Walther and RL Jaffe. *Molecular dynamics simulations of water on a hydrophilic silica surface at high air pressures*. Journal of Molecular Liquids, vol. 198, pages 107–113, 2014.

[Zaoui *et al.* 2016] Hayat Zaoui, Pier Luca Palla, Fabrizio Cleri and Evelyne Lampin. *Length dependence of thermal conductivity by approach-to-equilibrium molecular dynamics*. Physical Review B, vol. 94, no. 5, page 054304, 2016.

[Zarudi *et al.* 2004] I Zarudi, LC Zhang and MV Swain. *Cyclic microindentations on monocrystalline silicon in air and in water*. Proceedings of the Institution of Mechanical Engineers, Part C: Journal of Mechanical Engineering Science, vol. 218, no. 6, pages 591–593, 2004.

[Zhang Jun 2017] Reese Jason M Zhang Jun Borg Matthew K. *Multiscale simulation of dynamic wetting*. International Journal of Heat and Mass Transfer, vol. 115, pages 886–896, 2017.

[Zhang *et al.* 2016] Chao Zhang, Zhen Liu and Peng Deng. *Contact angle of soil minerals: A molecular dynamics study*. Computers and Geotechnics, vol. 75, pages 48–56, 2016.

[Zhang *et al.* 2018a] Haohao Zhang, Guihuan Chen, Bing Yu and Hailin Cong. *Emerging advanced nanomaterials for cancer photothermal therapy*. Reviews on Advanced Materials Science, vol. 53, no. 2, pages 131–146, 2018.

[Zhang *et al.* 2018b] Meijie Zhang, Miaolin He, Huazhi Gu, Ao Huang and Wuguo Xiang. *Influence of pore distribution on the equivalent thermal conductivity of low porosity ceramic closed-cell foams*. Ceramics International, vol. 44, no. 16, pages 19319–19329, 2018.

[Zhang *et al.* 2019] Xiqi Zhang, Hongliang Liu and Lei Jiang. *Wettability and applications of nanochannels*. Advanced Materials, vol. 31, no. 5, page 1804508, 2019.

[Zhang *et al.* 2020] Xinrui Zhang, Guangfan Meng and Zhaoliang Wang. *Experimental study on flow and heat transfer characteristics of SiC-water nanofluids in micro-cylinder-groups*. International Journal of Heat and Mass Transfer, vol. 147, page 118971, 2020.

[Zhao & Li 2008] Hongxia Zhao and Robert KY Li. *Effect of water absorption on the mechanical and dielectric properties of nano-alumina filled epoxy nanocomposites*. Composites Part A: Applied Science and Manufacturing, vol. 39, no. 4, pages 602–611, 2008.

[Zhao *et al.* 2019] Jinfu Zhao, Zhanqiang Liu, Qingqing Wang and Jiaming Jiang. *Measurement of temperature-dependent thermal conductivity for PVD Ti0. 55Al0. 45N ceramic coating by time domain thermo-reflectance method*. Ceramics International, vol. 45, no. 7, pages 8123–8129, 2019.

[Zhao *et al.* 2020] Zhixiang Zhao, Chengzhen Sun and Runfeng Zhou. *Thermal conductivity of confined-water in graphene nanochannels*. International Journal of Heat and Mass Transfer, vol. 152, page 119502, 2020.

[Zhou *et al.* 2017] Yucun Zhou, Zhejun Li and Yi-Chun Lu. *A stable lithium–selenium interface via solid/liquid hybrid electrolytes: Blocking polyselenides and suppressing lithium dendrite*. Nano Energy, vol. 39, pages 554–561, 2017.

[Zhu *et al.* 2020] Haochen Zhu, Fengrui Yang, Yunjie Zhu, Aihua Li, Wenzhi He, Juwen Huang and Guangming Li. *Investigation of dielectric constants of water in a nano-confined pore*. RSC Advances, vol. 10, no. 15, pages 8628–8635, 2020.

FOLIO ADMINISTRATIF

THESE DE L'INSA LYON, MEMBRE DE L'UNIVERSITE DE LYON

NOM : WANG
(avec précision du nom de jeune fille, le cas échéant)

DATE de SOUTENANCE : 06/10/2022

Prénoms : Xiaorui

TITRE : Thermal Properties of Solid-Liquid Nanocomposites.

NATURE : Doctorat

Numéro d'ordre : 2022ISAL0085

Ecole doctorale : Mécanique, Energétique, Génie Civil, Acoustique de Lyon

Spécialité : Thermique Energétique

RESUME : À l'échelle nanométrique, la conductivité thermique des nanocomposites hybrides solide-liquide est étudiée, en particulier pour le silicium cristallin nanoporeux sec et humide avec l'eau confinée. Plusieurs paramètres ont été étudiés en détail. La conductivité thermique (TC) est calculée à l'aide de simulations de dynamique moléculaire, qui sont réalisées avec LAMMPS. Premièrement, une cellule de simulation de silicium cristallin avec un pore sphérique au centre est étudiée. Les cas d'échantillons secs et humides sont comparés. En utilisant les simulations de dynamique moléculaire à l'équilibre, les effets de la température et de la densité effective sur la TC sont examinés, séparément. Pour une certaine température (à 300 K) ou une certaine densité effective (0,8 g/cm^3), une valeur maximale de la TC a été obtenue. De plus, une stratification des molécules d'eau près de l'interface solide/liquide est observée et confirmée dans la littérature. Pour clarifier les mécanismes physiques derrière le transport thermique aux interfaces et l'interaction intermoléculaire de l'eau nanoconfinée, plusieurs paramètres structurels et dynamiques de l'eau nanoconfinée ont été explorés, la fonction de distribution radiale, les déplacements carrés moyens, l'orientation des molécules d'eau et les réseaux de liaisons hydrogène. De plus, l'existence de nouveaux canaux de flux thermique entre une matrice solide et un liquide nanoconfiné a été prouvée, par la densité d'états des phonons. Deuxièmement, les effets de la distribution spatiale, de la taille et de la combinaison espace/taille du silicium nanoporeux humide sont étudiés. La nouvelle cellule de simulation est produite en répliquant le silicium nanoporeux cubique le long de la direction longitudinale. Cette partie de l'étude, en raison des demandes de modélisation, a été réalisée en utilisant les simulations de dynamique moléculaire hors-équilibre.

MOTS-CLÉS : Dynamique Moléculaire, Conductivité Thermique, Silicium Nanoporeux, Eau Nanoconfinée, Interface Solide/liquide, Réseaux de Liaisons Hydrogène

Laboratoire (s) de recherche :CETHIL

Directeur de thèse: Konstantinos TERMENTZIDIS

Président de jury : Evelyne MARTIN, Directrice de Recherche, Université de Strasbourg, CNRS

Composition du jury :

Jérôme SAINT-MARTIN,	Directeur de Recherche,	Université Paris-Saclay, CNRS,	Rapporteur,
Gilles PERNOT,	Professeur des Universités,	Université de Lorraine, CNRS,	Examinateur,
Samy MERABIA,	Directeur de Recherche,	Université Claude Bernard Lyon 1, CNRS,	Examinateur,
Séverine GOMES,	Directrice de Recherche,	INSA-Lyon, CNRS,	Co-Directrice de thèse,
Konstantinos TERMENTZIDIS,	Directeur de Recherche,	INSA-Lyon, CNRS,	Directeur de thèse.